Université de Montréal

Diagnostics spectroscopiques de plasmas d'argon à la pression atmosphérique en présence d'espèces réactives

par

Antoine Durocher-Jean

Département de physique
Faculté des arts et des sciences

Thèse présentée à la Faculté des études supérieures et postdoctorales
en vue de l'obtention du grade de
Philosophiæ Doctor (Ph.D.)
en Physique

mars 2019

© Antoine Durocher-Jean, 2019

Université de Montréal

Faculté des études supérieures et postdoctorales

Cette thèse intitulée

Diagnostics spectroscopiques de plasmas d'argon à la pression atmosphérique en présence d'espèces réactives

présentée par

Antoine Durocher-Jean

a été évaluée par un jury composé des personnes suivantes :

Michel Moisan
(président-rapporteur)

Luc Stafford
(directeur de recherche)

Ahmad Hamdan
(membre du jury)

Gaétan Laroche
(membre du jury)

María Dolores Calzada
(examinateur externe)

Christian Reber
(représentant du doyen des ESP)

Sommaire

Les travaux réalisés dans le cadre de cette thèse de doctorat caractérisent de manière cohérente la physique des plasmas d'argon à la pression atmosphérique en présence d'espèces réactives. Ces travaux sont motivés par les lacunes manifestes de la compréhension des plasmas froids à la pression atmosphérique, celles-ci étant en grande partie dues au nombre restreint de techniques de diagnostic permettant de les caractériser.

Dans ce contexte, des diagnostics optiques permettant l'obtention des propriétés fondamentales (température du gaz et des électrons, densité d'états excités) sont d'abord développés et validés tant pour les plasmas microonde que pour les décharges à barrière diélectriques d'argon à la pression atmosphérique. En particulier, une méthode couplant des mesures d'émission optique des transitions 2p-1s de l'argon à un modèle collisionnel-radiatif décrivant la population des niveaux émetteurs 2p permettant d'obtenir la température des électrons est présentée, de même qu'un moyen d'obtenir la température du gaz à l'aide de mesures d'élargissement spectral de raies et la densité d'états métastables de l'argon à l'aide de mesures de spectroscopie d'absorption par diode laser accordable en longueur d'onde.

Par la suite, ces diagnostics optiques sont employés pour étudier l'influence de l'ajout de gaz diatomiques dans un plasma microonde, mettant en évidence l'efficacité avec laquelle ils en viennent à dominer la cinétique de la décharge en absorbant la majorité de la puissance fournie au plasma. Une comparaison entre le bilan de puissance des électrons qu'ils permettent de calculer à celui d'un diagnostic électrique est également effectué dans le cas d'une décharge à barrière diélectrique d'argon en présence de précurseurs d'anhydrides.

Finalement, les propriétés fondamentales de deux configurations de jets de plasmas s'écoulant dans l'air ambiant, l'une radiofréquence, l'autre microonde, sont également examinées. Dans le premier cas, les effets de l'air ambiant sur ces propriétés sont mis de l'avant, alors que dans le second cas, la position d'injection du précurseur organosilicié HMDSO dans le jet de plasma est évaluée pour le dépôt de revêtements fonctionnels sur des substrats de

verre. Ces derniers travaux révèlent l'obtention d'un revêtement antibuée dans des conditions opératoires spécifiques, un résultat fort prometteur pour l'industrie du verre.

Mots-clés : Plasmas à la pression atmosphérique, jets de plasma, diagnostics spectroscopiques des plasmas, modèle collisionnel-radiatif, température électronique, température des neutres, densité d'états métastables, bilan de puissance des électrons

Summary

The research done in this Ph.D. thesis consistently characterizes the physics of argon plasmas at atmospheric pressure in the presence of reactive species. This work is motivated by the obvious deficiencies in the understanding of cold plasmas at atmospheric pressure, which are largely due to the limited number of diagnostic techniques used to characterize them.

In this context, optical diagnostics allowing the obtaining of fundamental properties (gas and electron temperature, number density of excited species) are first developed and validated in a microwave argon plasma as well as in a dielectric barrier discharge in argon at atmospheric pressure. In particular, a method coupling optical emission measurements of argon 2p-1s transitions to collisional-radiative modelling of the emitting 2p levels is presented in order to get the electron temperature, as well as a means to obtain the gas temperature by the spectral broadening of emission lines and the number density of argon metastable states from tunable laser diode absorption spectroscopy measurements.

Subsequently, these optical diagnostics are used to study the influence adding diatomic gases in microwave argon plasmas, highlighting the efficiency with which they start dominating the discharge kinetics by absorbing most of the supplied power. A comparison between the electron power balance calculated from such optical diagnostics to that obtained from electrical diagnostics is also made in the case of an argon-based dielectric barrier discharge with anhydride precursors.

Finally, the fundamental properties of two plasmas jet configurations (one radio-frequency, the other microwave) expanding in ambient air are also examined. In the first case, the effects of ambient air on these properties are featured, while in the second case, the injection position of the organosilicon precursor HMDSO in the plasma jet is studied for the deposition of functionnal coatings on glass substrates. The latter reveals the obtaining of an antifog coating under specific operating conditions, a very promising result for the glass industry.

Keywords: Atmospheric pressure plasmas, plasma jets, spectroscopic plasma diagnostics, collisional-radiative modelling, electron temperature, neutral gas température, number density of metastable atoms, electron power balance

Table des matières

Sommaire iii

Summary v

Liste des tableaux xii

Liste des figures xiii

Liste des abréviations xviii

Liste des symboles xix

Remerciements xxii

Introduction générale 1

Chapitre 1. Principes généraux et revue de la littérature 5

1.1. Survol des principales sources de plasma froid à la pression atmosphérique 5

1.2. Caractérisation des plasmas froids à la pression atmosphérique dans les gaz rares 10

1.3. Plasmas dans les gaz rares à la pression atmosphérique avec espèces réactives. 22

Chapitre 2. Développement et validation de diagnostics optiques dans les plasmas d'argon 28

2.1. Introduction 28

2.2. Article 1 : Caractérisation d'un plasma microonde d'argon à la pression atmosphérique par spectroscopie optique d'émission et d'absorption couplée à un modèle collisionnel-radiatif 29

2.2.1. Introduction 33
2.2.2. Experimental setup and data analysis 34
2.2.2.1. Plasma source 34
2.2.2.2. Optical emission spectroscopy 35
2.2.2.3. Optical absorption spectroscopy 37
2.2.3. Collisional radiative model 40
2.2.3.1. General considerations 41
2.2.3.2. Excitation and de-excitation mechanisms 42
2.2.3.3. Theoretical spectrum 47
2.2.3.4. Experimental spectrum 47
2.2.3.5. Comparison of the spectra 48
2.2.4. Validation of the method 48
2.2.5. Axial profiles of $\mathbf{T_g}$, $\mathbf{n_{1s_5}}$ and $\mathbf{T_e}$ along the microwave plasma column 51
2.2.6. Conclusion 55
Acknowledgments 55
References 55

2.3. Article 2 : Étude résolue temporellement de la température des électrons et de la densité d'atomes d'argon excités dans les DBDs à base d'argon 60

Chapitre 3. Plasmas d'argon en présence d'espèces réactives 62

3.1. Introduction 62

3.2. Article 3 : Influence de l'ajout de molécules diatomiques sur le bilan de puissance électronique et le chauffage des neutres dans les plasmas microonde d'argon à la pression atmosphérique 63
3.2.1. Introduction 67
3.2.2. Experimental Setup 68
3.2.3. Data acquisition and analysis 69

3.2.3.1. Optical emission spectroscopy combined with collisional-radiative modelling ... 69
3.2.3.2. High-resolution optical emission spectroscopy ... 73
3.2.3.3. Tunable laser diode optical absorption spectroscopy ... 73
3.2.3.4. Hydrogen H_β broadening and argon line ratio analysis ... 75
3.2.4. Results ... 76
3.2.5. Discussion ... 81
3.2.5.1. Electron power balance ... 81
3.2.5.2. Neutral gas heating ... 83
3.2.6. Conclusion ... 87
Acknowledgments ... 88
References ... 88
3.3. Article 4 : Comparaison des diagnostics optiques et électriques quant au bilan énergétique du précurseur dans la DBD d'argon à la pression atmosphérique ... 92
3.4.1. Introduction ... 95
3.4.2. Description of the electrical method ... 96
3.4.3. Description of the optical method ... 96
3.4.4. Results and discussion ... 101
3.4.5. Conclusion ... 105
Acknowledgments ... 106
References ... 106
Chapitre 4. Plasmas d'argon en configuration jet ... 109
4.1. Introduction ... 109
4.2. Article 5 : Diagnostics optiques d'un jet de plasma RF d'argon en contact avec l'air ambiant ... 110
4.3. Introduction ... 114
4.4. Experimental setup and methods ... 115

4.4.1. Setup configuration 115
4.4.2. Optical Emission Spectroscopy 116
4.4.3. Optical Absorption Spectroscopy 117
4.4.4. Collisional Radiative Model 120

4.5. Results and Discussion 123
4.5.1. Gas Temperature and Fluid Flow 123
4.5.2. Spatially-resolved Ar 1s level populations 124
4.5.3. Spatially-resolved Electron Temperature 127

4.6. Conclusion 129
Acknowledgements 130
References 130

4.7. Article 6 : Diagnostics optiques d'un jet de plasma microonde d'argon appliqué au dépôt d'un revêtement antibuée sur verre 134
4.4.1. Introduction 137
4.4.2. Experimental details and data analysis methods 138
4.4.2.1. Experimental setup and operating conditions 138
4.4.2.2. Methods for surface characterization of plasma-coated glass substrates 141
4.4.2.3. Methods for plasma jet characterization 143
4.4.3. Experimental results and discussion 147
4.4.3.1. Surface characterization 147
4.4.3.2. Plasma jet characterization 155
4.4.4. Conclusion 161
Acknowledgments 162
References 162

Conclusion générale et perspectives 167

Références 171

Annexe : Article 2 179

A.1.1. Introduction ... 181
A.1.2. Experimental conditions ... 181
A.1.3. Description of the model ... 183
A.1.4. Experimental results and discussion ... 188
A.1.5. Conclusion ... 195
Acknowledgments ... 195
References ... 195

Liste des tableaux

1.1 Caractéristiques et densités d'espèces énergétiques pour différentes décharges à la pression atmosphérique 12

1.2 Sommaire des propriétés obtenues par diffusion Thomson de différentes sources de plasma à la pression atmosphérique 17

2.1 Excitation and de-excitation mechanisms considered for the particle balance equation of the argon $2p_i$ level. 42

4.1 Comparison of Ar 1s level densities available in the literature. 127

4.2 Comparison of electron temperature available in the literature. 129

4.3 Calculation of the Si, C and O atomic percentages in the plasma-deposited coatings for experiments realized at the 16 mm and 24 mm injection positions according to the high-resolution spectra 154

Liste des figures

0.1 Plasmas froids en contact avec du bois et des doigts ... 2

1.1 Quelques configurations possibles de DBDs ... 6

1.2 Courbe courant-tension typique d'une DBD ... 6

1.3 Famille d'excitateurs de plasmas d'onde de surface ... 8

1.4 Exemples de jets de plasma ... 9

1.5 Courbe I-V d'une DBD en régime filamentaire ... 11

1.6 Spectre d'émission optique d'un plasma RF d'argon ... 13

1.7 Diagramme des niveaux d'énergie de l'argon ... 13

1.8 Température rotationnelle en fonction de l'intensité maximale des pics de courant dans un plasma RF d'argon ... 14

1.9 Diagramme de Boltzmann permettant le calcul d'une température d'excitation dans un POS d'argon ... 15

1.10 Obtention de la température et de la densité des électrons à partir d'une mesure de continuum d'émission dans un plasma RF ... 16

1.11 Distribution axiale de la densité électronique dans un POS d'argon ... 18

1.12 Évolution de la densité d'états métastables d'hélium dans une décharge capacitive entretenue selon différents régimes ... 20

1.13 Évolution temporelle de la température électronique dans une DBD d'hélium ... 21

1.14 Profils axiaux des températures du gaz et des électrons dans un POS d'argon ... 21

1.15 Dynamique de conversion du précurseur HMDSO dans une DBD d'Ar/O_2 ... 23

1.16 Consommation du précurseur SiH_4 en fonction de la position dans une DBD ... 24

1.17 Mise en évidence de la fragmentation d'HMDSO par spectroscopie optique d'émission d'un plasma d'onde de surface 26
1.18 Spectrométrie de masse des espèces résultantes de la fragmentation d'HMDSO dans un jet de plasma RF 26
1.19 Énergie électrique absorbée par les électrons par cycle de la tension appliquée pour trois fréquences 27
2.1 Schematic of the experimental setup and picture of the microwave plasma column 35
2.2 Typical optical emission spectrum of the microwave argon plasma at atmospheric pressure 36
2.3 Typical fit of the two argon emission lines used for the determination of T_g 38
2.4 Experimental setup for the OAS and OES measurements 39
2.5 I_0 and I_t signals as well as the corresponding laser frequency. Resulting absorption spectrum with the corresponding Voigt profile 40
2.6 Schematic of the reactions considered in the CR model of argon 2p states 43
2.7 Relative standard deviation as a function of T_e 49
2.8 Comparison of the optimal theoretical spectra with the experimental one and percentage of radiation trapping for the optimal electron temperature 50
2.9 Contribution of the different mechanisms to the excitation and de-excitation of the argon 2p levels 51
2.10 Ar $1s_5$, n_e, T_e and T_g axial profiles 52
3.1 Schematic of the experimental setup used to sustain the microwave argon plasmas in presence of N_2, O_2 or H_2 admixtures 69
3.2 Typical optical emission spectra of the microwave argon plasmas, without and with 0.5% O_2 70
3.3 Schematic of the reactions considered in the CR model 71
3.4 Experimental setup for the OAS and OES measurements 74

3.5 Electron number density as a function of the axial position with respect to the wave launcher ... 76

3.6 Axial profiles of n_e, n_{1s_5}, T_g and T_e along the microwave plasma column for an increased amount of the three diatomic admixtures ... 78

3.7 Correlation between the population of argon 1s$_5$ atoms and the predictions of a simple particle balance equation ... 80

3.8 Power dissipated per molecule and percentage of the power taken by the admixture for the different concentration fractions of N_2, O_2, and H_2 ... 84

3.9 Neutral gas temperature as a function of the power transferred per neutral atom 87

3.10 Schematics of the power absorption and dissipation in Ar-based DBDs. ... 100

3.11 Electrical measurements of E_g as a function of the precursor flow rate. ... 101

3.12 Influence of the precursor flow rate on the electron temperature, argon 1s number density and relative electron number density obtained from optical emission spectroscopy combined with collisional-radiative modelling of argon 2p$_i$-to-1s$_j$ transitions ... 102

3.13 Optical and electrical value of ΔE_g as a function of the flow rate for both precursors ... 104

4.1 Schematics of the APPJ and OES setup. ... 116

4.2 Emission spectrum of the Ar APPJ flowing afterglow region, 0.6 mm from the nozzle exit, integrated over 200 ms between 300 and 680 nm, and over 20 ms between 680 and 880 nm. ... 117

4.3 Schematic diagram of the optical absorption spectroscopy setup. ... 118

4.4 Global absorption coefficients as a function of k_0L at the nozzle exit plane (z=0). 119

4.5 Radial profile of the absorption for the 751.5 nm line, 1 cm away from the nozzle exit plane. ... 120

4.6 Schematic of the reactions considered in the CR model ... 122

4.7 Axial distribution of the rotational temperature of OH(A) and N_2(C) obtained using Specair and gas temperature measured with a thermocouple, at 5 L/min of Ar and 40 W. 123

4.8 Argon mole fraction at 5 slm and temperature from measurement and CFD 125

4.9 Axial distribution of the measured absorption at 5 L/min and 40 W. 125

4.10 Axial distribution of Ar 1s level population at 5 L/min and 40 W. 126

4.11 Axial distribution of T_e at 5 L/min and 40 W. 128

4.12 Schematics of the apparatus used for the production of an open-to-air argon plasma at atmospheric pressure sustained by microwave electromagnetic fields ... 139

4.13 Picture of the microwave plasma jet along with the precursor injection system .. 140

4.14 Transmittance of different glass samples as a function of time when exposed to a warm, humid atmosphere. 143

4.15 Typical OES spectra along the jet of the open-to-air microwave argon plasma .. 144

4.16 OH emission used for the calculation of T_{rot}, N_2 emission used in the calculation of T_{vib}, Ar emission used in the calculation of T_{exc} and Ar line broadenings used for the calculation of T_g 146

4.17 Optical images of the plasma-deposited coatings for various precursor injection positions 148

4.18 Transmittance plots of the coatings for various precursor injection positions and reference transmittance of the glass substrate 150

4.19 Minimal transmittance during the anti-fog test and apparent contact angle of the coatings 151

4.20 XPS high-resolution scans of Si2p and C1s peaks of the plasma-deposited coatings for experiments realized at 2 injection positions 152

4.21 Normalized emission intensity from various excited species as a function of position along the jet 156

4.22 Ar $1s_5$, electron number density and gas, rotational, vibrational and excitation temperature profiles 159

A.1 Schematic of the DBD used in this study 182

A.2 Typical optical emission spectrum of Ar/NH3 DBDs 183

A.3 Schematics of the population and depopulation mechanisms considered for Ar 2p levels. 185

A.4 Typical surface plot of the percentage standard error 187

A.5 Comparison of normalized emission intensities obtained from the experiment and the model 189

A.6 Time evolution of T_e and Ar $1s_2$ population during the negative half cycles for an Ar/NH_3 DBD 190

A.7 Time evolution of T_e and Ar $1s_2$ population during the negative half cycles for an Ar/ethyl lactate DBD 191

A.8 Discharge current, integrated emission intensity and the electron temperature for an Ar/ethyl lactate DBD 192

A.9 Percent contribution of each populating mechanism for Ar 2p levels during the negative half-cycle of an Ar/ethyl lactate DBD 193

A.10 Relation between T_e and $n_{(1s)}$ for Ar/ ethyl lactate and Ar/NH_3 DBDs 194

Liste des abréviations

CR	Collisionnel-radiatif
DBD	Décharge à barrière diélectrique
FWHM	*Full width at half maximum*
HMDSO	Hexaméthyldisiloxane
ID	*Inner diametre*
OAS	*Optical absorption spectroscopy*
OD	*Outer diametre*
OES	*Optical emission spectroscopy*
POS	Plasma d'onde de surface
RF	Radio-fréquence
sccm	*Standard cubic centimetre per minute*
slm	*Standard litre per minute*
UV	Ultraviolet

Liste des symboles

A_{ij}	Cœfficient d'Einstein pour l'émission spontanée d'une raie spectrale
$\mathcal{A}$	Cœfficient d'absorption global d'une raie spectrale
a_0	Rayon de Bohr (5.29×10^{-11} m)
c	Vitesse de la lumière dans le vide (299792458 m/s)
$\Delta\nu$	Élargissement en fréquence d'une raie spectrale
e	Charge élémentaire ($1.60217662 \times 10^{-19}$ C) ; facteur de conversion électronvolt $\Rightarrow$ joule
ϵ_0	Permittivité du vide ($8.85418782 \times 10^{-12}$ F/m)
f_{gj}	Force d'oscillateur entre les niveaux électroniques g et j
$f(\lambda)$	Fonction de réponse de l'appareillage
g_i	Poids statistique du niveau i
I_d	Courant de décharge
I_λ	Intensité d'une raie spectrale centrée sur la longeur d'onde λ
I_0	Intensité initiale d'un faisceau lumineux
I_t	Intensité transmise d'un faisceau lumineux
k_B	Constante de Boltzmann ($1.38064852 \times 10^{-23}$ J/K)
k_{i-j}	Taux de réaction pour l'excitation du niveau i vers le niveau j
h	Constante de Planck ($6.62607004 \times 10^{-34}$ J·s)
ℓ	Longueur d'absorption
λ	Longueur d'onde
m_e	Masse d'un électron ($9.10938356 \times 10^{-31}$ kg)
M_{Ar}	Masse d'un atome d'argon ($6.6335209 \times 10^{-26}$ kg)
n_e	Densité électronique
n_g	Densité de neutres à l'état fondamental
P	Pression
R	Constante des gaz parfaits (8.314462 J/mol K)

θ_{ij} Facteur d'échappement d'une transition optique du niveau i vers le niveau j

T_g Température du gaz

T_e Température électronique

V Volume

V_{gap} Tension au gaz

ν_0 Fréquence centrale d'une raie spectrale

À mon grand-père Aurèle qui, jusqu'à la toute fin, m'aura demandé
« Pis, qu'est-ce que t'as appris de bon à l'école aujourd'hui ? »

Remerciements

Mon premier et plus grand remerciement va évidemment à Luc, et particulièrement à la personne derrière le directeur de thèse. Dès le début, ta confiance en moi, ta patience et ton ouverture à mes idées m'ont permis de m'approprier mon projet et d'en faire ce qu'il est finalement aujourd'hui. Merci de ton écoute, pour toutes nos discussions sur le sens profond de la physique ou d'autres sujets moins fondamentaux..! Merci d'avoir été un rêveur, à toujours vouloir en faire plus, mieux, à aller plus loin. Des physiciens comme toi, je me rends compte que ça ne court pas les rues et assurément j'en suis devenu un bien meilleur grâce à toi.

Ensuite, je remercie Danielle d'avoir été un pilier infaillible sur lequel j'ai toujours pu m'appuyer. Ton aide inestimable pour faire rouler le labo et ton support moral dans mes (quelques) moments de découragement ont quotidiennement embelli ces folles années.

Je remercie aussi les gens du groupe, actuels et anciens, que j'ai eu le plaisir de côtoyer. Tout particulièrement, merci à Vincent, mon bro qui a été là du début du bac à la fin du doc. Ta présence, ton appui, ta rigueur, ta vision des choses, name it ! ça a fait du bien de t'avoir durant toute cette épopée universitaire. Merci aussi à Olivier, Jean-Sébastien B., Germain, Simon et Edouard de m'avoir aidé chacun à votre manière.

Merci également à Jean-Sébastien M. et à Véronique pour le support technique impeccable ; à l'armée de stagiaires que j'ai eue (9 !) et particulièrement à Nicolas, qui m'ont tous aidé dans l'avancement de mon projet.

Sur une note plus personnelle, je dois aussi remercier ma famille, Johanne et Denis (merci pour l'aide en labo !), Etienne et Amélie ainsi que mes amis pour leur soutien et leurs encouragements durant toutes ces années (et même celles d'avant !). Merci Antoine pour ton aide transdisciplinaire, et merci les cocos et coccinelles, j'ai réussi en grande partie grâce à vous !

Finalement, mon merci le plus important et le plus ressenti est pour ma Pichu, ma meilleure amie, ma complice au quotidien, le bonheur dans ma vie. Merci pour ton écoute, ton support, ta patience et ta compréhension. Comme à maintes reprises auparavant, on a traversé ce bout-là ENSEMBLE mais, encore une fois, ce n'était que le début du reste. Idziemy, mkéla ?

Introduction générale

L'utilisation des plasmas dans de nombreux secteurs technologiques a aujourd'hui le vent dans les voiles. Parmi les applications désormais couramment rencontrées, beaucoup concernent la science des matériaux, par exemple la gravure [1, 2], le dépôt de couches minces [3, 4] ou encore la modification des propriétés d'une surface par un dépôt, une texturation, une incorporation d'atomes ou une activation [5, 6]. Historiquement, les plasmas employés pour ces procédés étaient généralement entretenus à des pressions réduites, c'est à dire de l'ordre du millitorr à celui du torr. Comme ces réacteurs peuvent encore parfois être très onéreux, les applications visées concernent principalement les produits à très haute valeur ajoutée comme ceux de la microélectronique, de l'optique et de la photonique. Cependant, de nos jours, les plasmas à la pression atmosphérique (PA) prennent de plus en plus d'importance grâce à certains de leurs avantages indéniables, notamment la possibilité de faire des traitements en continu plutôt que par lots. Ceci permet de rendre viables des technologies impliquant des cadences de production élevées ou la mise en marché de gros volumes de produits avec une faible valeur ajoutée comme ceux des industries alimentaires, agroalimentaires, agricoles et forestières.

Bien qu'il existe actuellement une panoplie de sources à plasmas à la PA, toutes peuvent être classées en deux grandes catégories : celles produisant des plasmas thermiques et celles produisant des plasmas hors équilibre thermodynamique, aussi appelés plasmas froids. Les plasmas thermiques sont ainsi nommés car l'équilibre thermodynamique qui les caractérise en fait des plasmas où même les espèces lourdes (atomes et ions) possèdent beaucoup d'énergie. Ainsi, ils sont d'intérêt pour des applications nécessitant ou pouvant supporter de forts degrés d'ionisation et de hautes températures (soudure, traitement des déchets, ... [7, 8]). À l'inverse, les plasmas hors équilibre thermodynamique se distinguent du fait que ce sont des milieux faiblement ionisés dans lesquels ce sont principalement les électrons qui véhiculent l'énergie ; les espèces lourdes et donc le gaz plasmagène en général étant beaucoup plus froids, voire même à la température ambiante. Cette propriété les rend donc attractifs pour

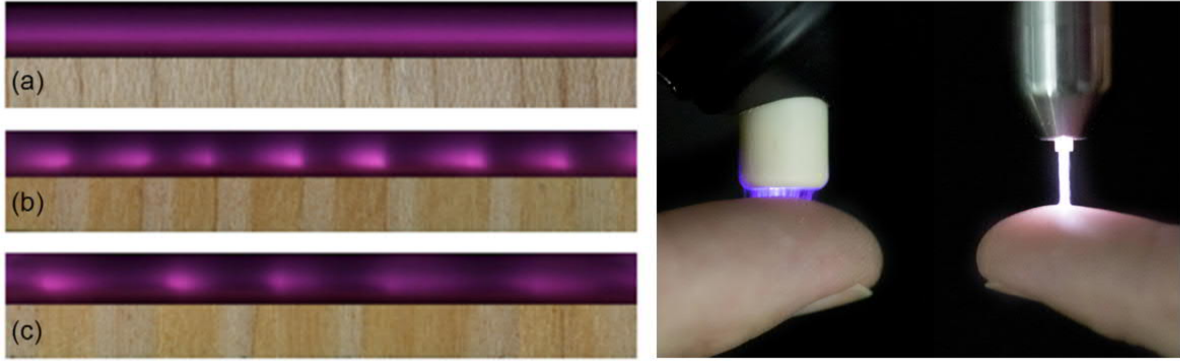

FIGURE 0.1. Plasmas froids en contact avec diverses espèces de bois (gauche) et des doigts (droite). Images respectivement tirées de [10, 11]

le traitement des matériaux sensibles à la chaleur comme les polymères destinés au domaine du biomédical et les matériaux cellulosiques dérivés de la biomasse forestière [3, 9]. Deux exemples sont illustrés à la Figure 0.1.

Parmi l'ensemble des sources permettant de créer et d'entretenir des plasmas froids, trois types se démarquent particulièrement dans la littérature. On note tout d'abord les décharges à barrière diélectrique (DBDs) qui reposent sur l'application d'une différence de potentiel alternative de basse fréquence entre deux électrodes métalliques recouvertes d'un diélectrique. Ces décharges possèdent l'avantage de pouvoir être mises à une échelle industrielle relativement facilement puisqu'à priori il ne suffit que d'agrandir la taille des électrodes pour traiter des substrats de plus grandes dimensions. Ensuite, on note les plasmas produits par des champs électriques radiofréquence (RF) en mode capacitif ou inductif. Ces sources sont faciles et robustes d'utilisation en plus d'être relativement abordables à concevoir sur une gamme étendue de conditions opératoires. Finalement, les plasmas microonde possèdent une souplesse remarquable à l'égard des conditions d'opération (pression, fréquence, puissance, etc.) qui les rend polyvalents pour de nombreuses applications. Ceci inclut évidemment la science et l'ingénierie des matériaux mais aussi le traitement des gaz et des effluents gazeux pour l'épuration, la conversion, la dépollution, le reformage, etc.

Dans tous les cas, les deux images de la Figure 0.1 résument bien les avenues actuellement possibles lorsqu'il s'agit d'utiliser une variante de l'une de ces trois sources à plasmas froids en science des matériaux : soit le matériau est exposé directement au plasma en étant inséré dans le réacteur, soit l'interaction se produit via un jet de plasma. Par ailleurs, tant pour l'une que pour l'autre option, le traitement de la surface se fait typiquement via l'ajout

d'espèces réactives dans le gaz plasmagène, celui-ci étant habituellement un gaz rare tel que l'argon ou l'hélium (l'hélium étant beaucoup plus coûteux, l'argon est habituellement privilégié lorsque possible). Or, il s'avère que peu d'études dans la littérature actuelle portent sur les effets de l'insertion de ces espèces sur les propriétés fondamentales du plasma, notamment les températures du gaz, des ions et des électrons ainsi que les densités d'espèces réactives (électrons, ions, neutres excités). Pourtant, c'est dans la connaissance et le contrôle de ces propriétés fondamentales que réside l'amélioration des procédés puisqu'elles influencent directement la physique et la chimie des interactions entre le plasma et les surfaces exposées au plasma.

Dans ce contexte, il est primordial de préciser que l'éventail réduit de diagnostics disponibles pour les plasmas hors équilibre thermodynamique à la PA entrave considérablement le comblement de ces lacunes, autant en ce qui concerne la phase gazeuse que les interactions plasma-surface. Dans le même ordre d'idées, les jets de plasma impliquent aussi une interaction avec l'environnement, celui-ci étant généralement ou ayant pour but d'être l'air ambiant. Ainsi, une caractérisation adéquate de l'influence de cet environnement sur les propriétés physico-chimiques du plasma est nécessaire pour permettre de mieux adapter celui-ci selon l'application envisagée. Par conséquent, les objectifs principaux pour ce travail de thèse sont :

1- De développer un ensemble cohérent de diagnostics permettant d'obtenir un portrait complet des densités et des températures de l'ensemble des espèces actives dans les plasmas hors équilibre thermodynamique d'argon à la pression atmosphérique ;

2- D'étudier l'influence de l'ajout d'espèces réactives dans un plasma d'argon sur ses propriétés fondamentales ;

3- D'examiner des plasmas hors équilibre thermodynamique d'argon à la pression atmosphérique en configuration jet dans l'objectif d'établir des liens entre ses propriétés fondamentales et les propriétés physiques et chimiques des matériaux traités par plasma, par exemple au cours du dépôt par plasma de couches minces.

De ce fait, ce document est divisé en quatre chapitres. Dans le chapitre 1, un survol des sources de plasmas froids à la PA et certaines de leurs propriétés sera présenté. En particulier, l'accent sera d'abord mis sur les propriétés fondamentales des plasmas dans les gaz rares et sur les différents diagnostics actuellement disponibles pour les caractériser. Un

aperçu de l'état des connaissances en ce qui a trait aux plasmas incluant des espèces réactives pertinentes pour la synthèse, la gravure et la modification de matériaux sera aussi abordé.

Le chapitre 2 présentera les diagnostics optiques mis au point dans cette thèse pour obtenir des valeurs de densités et de températures des espèces actives dans les plasmas hors équilibre thermodynamique d'argon à la PA. Ceci comprend des mesures d'élargissement de raie pour obtenir la température du gaz (élargissements Doppler, van der Waals et résonnant) et la densité de particules chargées (élargissement Stark), mais aussi des mesures de spectroscopie optique d'absorption avec une diode laser pour obtenir la densité des niveaux métastables et résonnants. Ce chapitre décrira également les détails du modèle collisionnel-radiatif (CR) développé pour obtenir la température des électrons dans les plasmas d'argon à partir de mesures de spectroscopie optique d'émission. Par le biais de deux articles, l'un concernant les plasmas produits par des champs microonde (onde de surface) et l'autre les décharges à barrière diélectrique en régime diffus (ou homogène), les capacités et la fiabilité de cette méthode seront démontrées.

Dans le chapitre 3, il sera question d'utiliser ces différents diagnostics optiques dans les cas où les plasmas sont produits en présence d'espèces réactives. D'une part, l'impact de l'ajout de molécules diatomiques (N_2, O_2 et H_2) dans un plasma microonde d'argon sera étudié via un troisième article. D'autre part, un quatrième article s'intéressera à l'ajout de précurseurs de la famille des anhydrides dans des DBDs d'argon. Dans ce cas, l'intérêt sera surtout porté à comparer ce que de tels diagnostics optiques donnent comme résultats par rapport à ceux obtenus par des diagnostics électriques largement utilisés dans la littérature.

Finalement, le chapitre 4 abordera les plasmas d'argon en configuration jet. D'une part, un cinquième article se concentrera sur les effets de l'air ambiant sur certaines propriétés fondamentales des jets de plasma produits par des champs RF. D'autre part, un sixième et dernier article abordera les caractéristiques d'un jet de plasma ouvert à l'air ambiant produit par un champ microonde. En ayant recours à une injection d'un précurseur organosilicié dans le jet de plasma, des applications à la synthèse de couches minces antibuée seront aussi explorées.

Chapitre 1

Principes généraux et revue de la littérature

1.1. Survol des principales sources de plasma froid à la pression atmosphérique

La règle générale pour produire un plasma est de fournir suffisamment d'énergie à un gaz neutre pour en arriver à former des porteurs de charges libres (électrons et ions). Pour y parvenir, la méthode souvent privilégiée en laboratoire est de soumettre le gaz à un champ électrique pouvant être issu d'une différence de potentiel entre deux électrodes, d'une induction magnétique ou encore de la propagation et de l'atténuation d'une onde. De ce fait, la classification des sources de plasma froid se base généralement sur le type de couplage de l'énergie électrique vers le plasma (capacitif, inductif, interactions ondes-particules) ou encore selon la fréquence d'oscillation du champ par rapport à certaines grandeurs caractéristiques du plasma (fréquence plasma des ions et des électrons, fréquence de collisions des ions et des électrons).

À très basses fréquences (typiquement entre 3 et 30 kHz) la pulsation du champ électrique est inférieure à la pulsation propre des ions et des électrons de sorte que les deux espèces répondent au champ électrique instantané. C'est le cas des DBDs, dont quelques configurations possibles sont présentées à la Figure 1.1. Dans ces réacteurs, selon l'excursion des ions et des électrons dans l'espace interélectrodes, la multiplication électronique peut résulter des processus α (ionisation dans le volume et au voisinage des électrodes) et/ou γ (génération d'électrons secondaires par bombardement ionique de la cathode). De plus, comme le montre la Figure 1.1, un ou plusieurs diélectriques doivent être placés stratégiquement dans le réacteur afin de prévenir l'apparition d'arcs électriques. Plus spécifiquement, l'accumulation de charges sur les diélectriques au cours de chaque demi-période permet d'écranter progressivement le potentiel appliqué, mettant astucieusement fin à la décharge avant le passage à l'arc. En régime diffus ou homogène (plutôt que filamentaire) dans les gaz rares comme

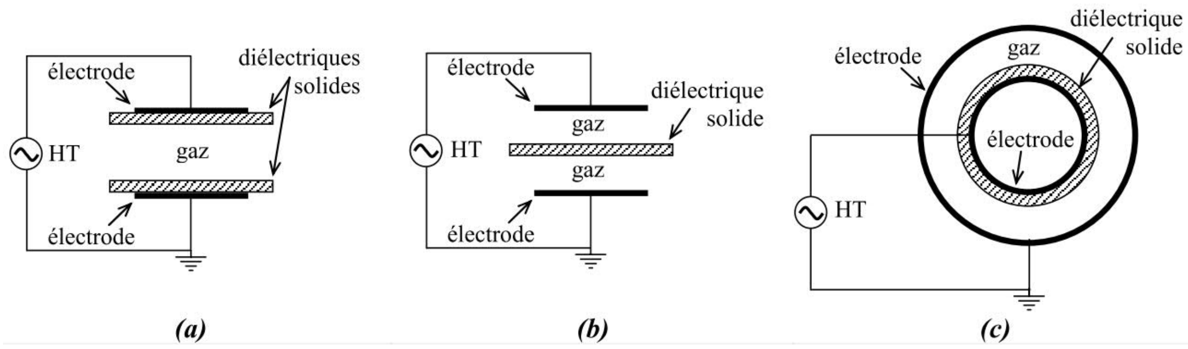

FIGURE 1.1. Quelques configurations possibles de DBDs : (a) plan-plan ; (b) plan simple ; (c) cylindrique. Schémas tirés de [12].

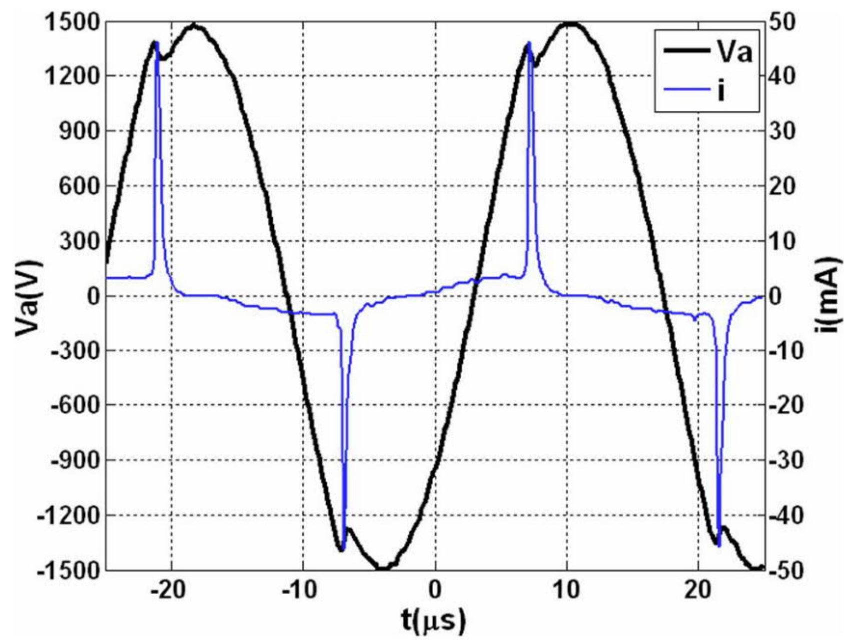

FIGURE 1.2. Courbe courant-tension typique d'une DBD. Graphique tiré de [14].

l'hélium , ceci donne lieu à des pics de courant bien définis temporellement comme le montre la Figure 1.2. Dans ces conditions, comme la fréquence de collisions des électrons avec les particules neutres ν est largement supérieure à la pulsation du champ ω, le transfert d'énergie du champ avec les particules lourdes via les électrons s'effectue à chaque instant de la période du champ. Les propriétés fondamentales du plasma deviennent alors tributaires de la valeur instantanée de l'amplitude du champ électrique et varient donc en fonction du temps. Dans les DBDs, les densités de puissance absorbées par les électrons du champ électrique (moyenne sur un cycle) sont typiquement de l'ordre de 0.1-1 W/cm^3 [13].

À plus hautes fréquences (typiquement entre 3 et 30 MHz), les ions des plasmas radiofréquence (RF) peinent à suivre l'oscillation rapide du champ électrique ($\omega > \omega_{pi}$) de sorte que sur un cycle, peu parcourent une distance considérable. Quant aux électrons, ils répondent toujours au champ instantané. De plus, comme $\nu < \omega$, les propriétés fondamentales du plasma peuvent toujours varier en fonction du temps. Cependant, contrairement aux DBDs, la décharge demeure allumée sur tout le cycle de la tension appliquée et la présence des diélectriques entre les deux électrodes n'est plus nécessaire pour empêcher l'apparition d'arcs. En effet, l'inversion rapide de polarisation minimise intrinsèquement les risques d'accumulations de charges. Dans les plasmas RF en régime capacitif, c'est-à-dire avec des électrodes internes comme dans les DBDs, les densités de puissance absorbée par les électrons du champ électrique (moyenne sur un cycle) sont typiquement de l'ordre de 1-10 W/cm^3 [13]. Ces valeurs augmentent grandement en régime inductif (200 - 400 W/cm^3 [15]), c'est-à-dire lorsque le plasma devient alimenté par le champ électrique induit associé aux variations temporelles d'un champ magnétique. Les propriétés de tels plasmas se rapprochent généralement plus de celles des plasmas thermiques que de celles des plasmas froids.

Finalement, les ultra et super hautes fréquences (300 MHz - 30 GHz) servent à produire les plasmas microonde. Dans ces conditions, les ions demeurent immobiles ($\omega > \omega_{pi}$) tandis que les électrons répondent toujours au champ instantané ($\omega < \omega_{pe}$). Comme $\nu \sim \omega$, les collisions peuvent survenir à des moments différents de la période d'un cycle à l'autre, rendant les propriétés de tels plasmas tributaires de la valeur moyenne du champ électrique et donc indépendantes du temps. Au fil des années, une grande variété de méthodes ont été proposées pour créer et entretenir des plasmas microonde [16, 17]. Parmi l'ensemble de ces méthodes, les plasmas d'onde de surface (POS) présentent une souplesse remarquable à l'égard des conditions opératoires (fréquence, puissance, dimension de tube, débit de gaz, etc.), ce qui en fait des candidats idéaux pour l'étude de la physique des plasmas froids à la PA ainsi que leurs principales applications [18]. Dans ce contexte, une famille complète d'excitateurs a été mise au point dans les laboratoires de l'Université de Montréal, comme le montre la Figure 1.3. Dans ces systèmes, les microondes sont apportées par un câble coaxial ou un guide d'onde à un lanceur, où elles sont couplées à un diélectrique. L'onde se sert alors de l'interface diélectrique-plasma pour se lancer et en se propageant, elle entretient le plasma en lui transférant de son énergie (milieu dissipatif) [18]. De ce fait, une caractéristique typique

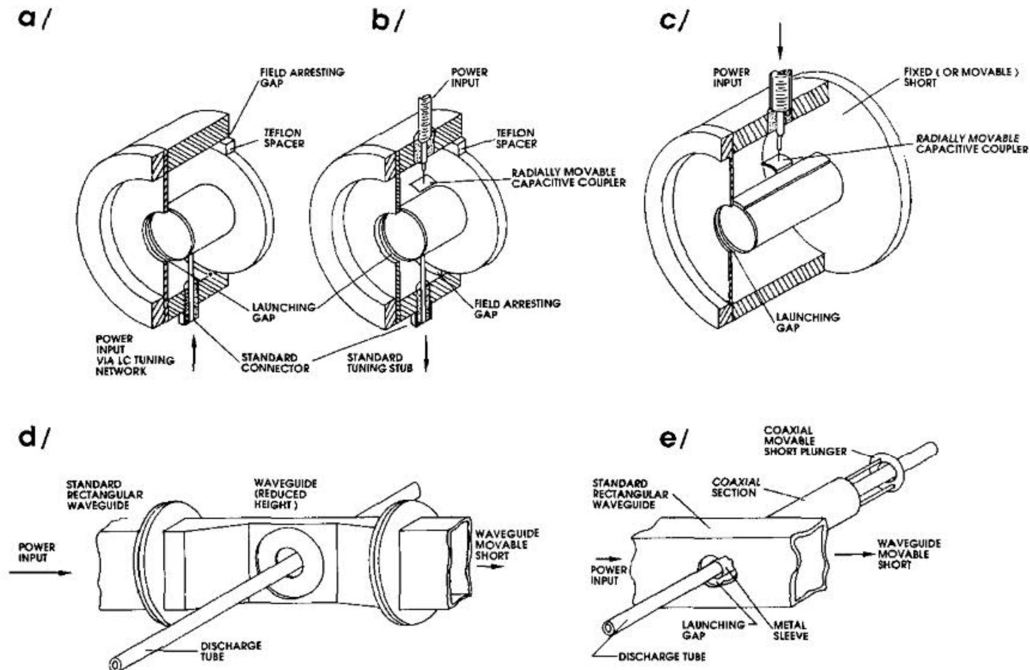

FIGURE 1.3. Famille d'excitateur de plasmas d'onde de surface. a) et b) Ro-box ; c) surfatron ; d) surfaguide et e) surfatron-guide. Schémas tirés de [16].

des POS est un allongement de la colonne à plasma avec l'augmentation de la puissance totale absorbée. Dans les POS, les densités de puissance absorbée par les électrons du champ microonde sont typiquement de l'ordre de 100 - 200 W/cm^3 [18], ce qui est nettement plus grand que celles des DBDs et des plasmas RF en mode capacitif.

Par ailleurs, certaines configurations des sources mentionnées précédemment peuvent permettre d'obtenir des jets de plasma, c'est-à-dire un plasma en partie ou totalement à l'extérieur d'une enceinte, par exemple dans l'air ambiant. Il existe aujourd'hui pratiquement autant de ces configurations qu'il y a de laboratoires à les étudier, chacun ayant ses besoins particuliers selon l'application envisagée. Cependant, les deux configurations apparaissant dans la Figure 1.4 présentent un exemplaire générique de celles qui sont populaires dans la littérature. La première est un jet RF connue sous le nom de *COST Reference Microplasma Jet* dans la communauté scientifique. Il s'agit d'un système formé de deux électrodes symétriques séparées par 1 mm et de plaques de quartz permettant à un gaz (ou un mélange de gaz) de circuler dans le canal ainsi formé. Dans ce cas-ci, la décharge se forme donc à l'intérieur du réacteur et c'est le débit de gaz qui pousse les espèces réactives à l'extérieur, créant le jet. Cette configuration est le résultat d'une concertation internationale afin de

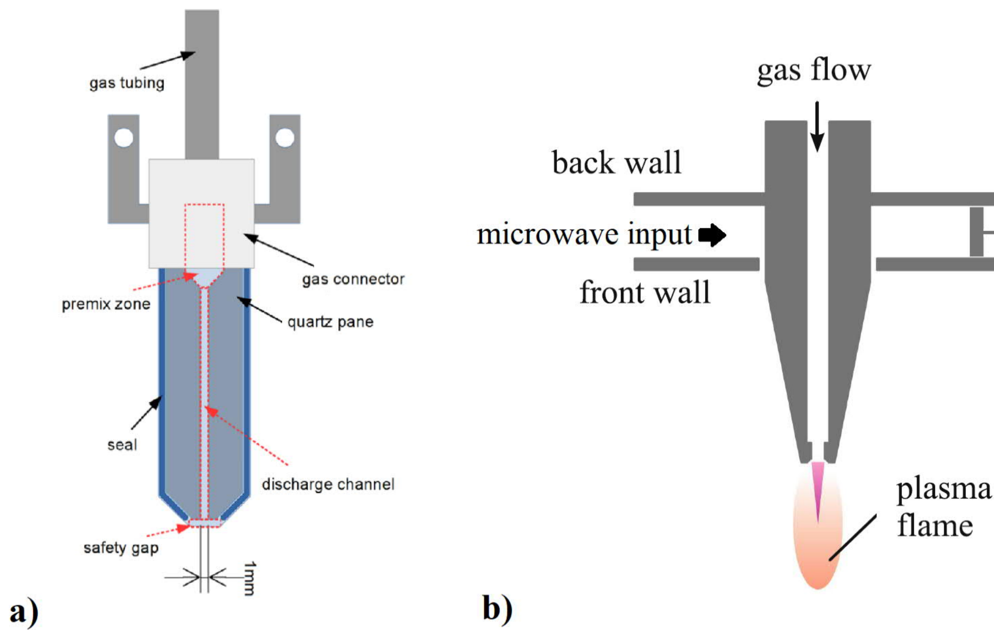

FIGURE 1.4. Exemples de jets de plasma : a) Plasma RF ; b) TIAGO . Schémas respectivement tirés de [19] et [18].

standardiser les études de différents groupes puisque les variantes de cette configuration et la multitude d'applications résultantes (surtout en médecine par plasma) empêchaient toute comparaison entre elles [19].

La seconde configuration porte le nom de torche à injection axiale sur guide d'onde (TIAGO) [20] et consiste en un guide coaxial creux inséré dans un guide d'onde apportant des microondes. Le gaz est inséré dans la partie creuse de cette partie coaxiale, dont l'extrémité est terminée par une buse qui concentre l'intensité des microondes en sortie. Ainsi, c'est à cet endroit et non à l'intérieur du guide qu'est créé le plasma, ce qui fait que le jet peut d'ailleurs atteindre plusieurs centimètres de long simplement en fournissant une puissance de quelques dizaines de watts. Comme il en sera question dans la prochaine section, le plasma issu de cette source est habituellement beaucoup plus chaud et plus dense en espèces actives que le jet RF, ce qui le rend plus adapté pour le dépôt de couche mince que pour le traitement de tissus humains.

1.2. Caractérisation des plasmas froids à la pression atmosphérique dans les gaz rares

Puisque leur apparition dans la littérature est relativement récente, les plasmas à la PA sont à ce jour beaucoup moins bien documentés quant à leurs propriétés fondamentales que le sont ceux à basse pression. Ceci s'explique en partie par le fait que plusieurs des diagnostics développés pour étudier les plasmas à pression réduite ne sont pas directement applicables à la caractérisation des plasmas à la PA. À titre d'exemple, les mesures électriques avec une sonde de Langmuir sont très utilisées à basse pression mais nettement moins à la PA. Ceci est dû aux théories sous-jacentes qui sont beaucoup plus complexes à haute pression et donc ne permettent pas encore d'interprétations satisfaisantes des caractéristiques courant-tension. Dans d'autres cas comme celui de la spectroscopie, ce sont plutôt les importants gradients spatio-temporels des différents paramètres qui nuisent à son application, puisqu'au mieux ceci demande de l'équipement beaucoup plus sophistiqué (et donc dispendieux) pour obtenir des résolutions spatiales et temporelles adéquates, et au pire de poser des hypothèses sur les profils spatio-temporels qui ne sont pas toujours justifiées et donc loin d'être sans conséquence. Malgré tout, plusieurs études rapportent aujourd'hui quelques-unes des propriétés fondamentales des plasmas dans les gaz rares à la PA et le but de cette section est d'en donner un aperçu.

Tout d'abord, les diagnostics électriques sont certainement les plus répandus dans les analyses des DBDs et certaines des décharges RF. Dans le cas des DBDs, les mesures I-V (courant-tension) permettent d'emblée de savoir si la décharge est entretenue dans un régime homogène ou filamentaire [22]. En effet, bien qu'ils limitent le passage au régime d'arc à proprement dit, les diélectriques n'empêchent pas la formation de canaux localisés ou microdécharges (*streamers* dans la littérature) associés à des taux d'ionisation très élevés et donnant lieu dans certains plasmas à de forts pics de courant très courts temporellement, tel que présenté à la Figure 1.5. D'ailleurs, une DBD en argon pur à la PA est généralement en régime filamentaire[23]. Pour obtenir une décharge en régime homogène, il faut typiquement ajouter des traces d'un gaz dont l'énergie d'ionisation est inférieure à celui de l'argon de telle sorte à obtenir un mélange Penning. Ainsi, en favorisant l'ionisation via des mécanismes à plusieurs atomes comme l'ionisation Penning plutôt que l'ionisation directe par les électrons, il devient possible de ralentir l'ionisation pour éviter que l'avalanche électronique atteigne

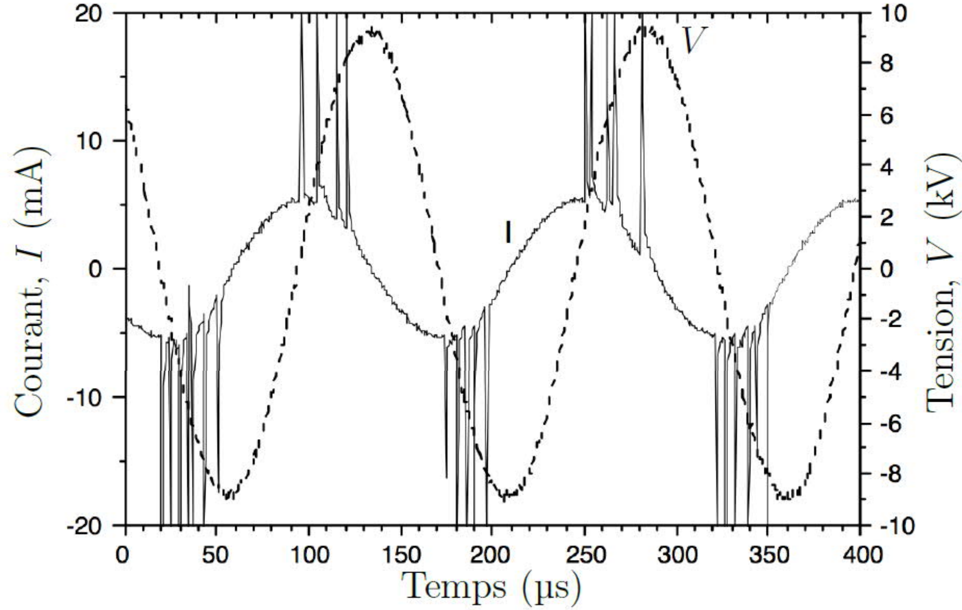

FIGURE 1.5. Courbe I-V d'une DBD en régime filamentaire. Graphique tiré de [21].

la taille critique associée à la formation des microdécharges. Pour l'argon, l'ammoniac est généralement utilisé. Dans ces conditions, un seul pic de courant par demi-cycle de la tension appliquée est obtenu, comme le montre la Figure 1.2.

Le Tableau 1.1 présente un sommaire des propriétés fondamentales des DBDs pour plusieurs régimes de décharge. En régime filamentaire, comme le plasma est formé d'une multitude de microdécharges, les densités électroniques peuvent être très élevées (jusqu'à 10^{20} m^{-3}) mais sur de très courts laps de temps (typiquement 10 - 100 ns). Dans le cas du régime homogène, la densité d'électrons peut être estimée de la mesure du courant de décharge [24]. Comme le montre le Tableau 1.1, les densités de courant de ce régime peuvent atteindre 10 mA/cm^2, ce qui correspond à des maximums de densités de charges de l'ordre de 10^{16} - 10^{17} m^{-3}. Finalement, dans les plasmas RF, comme le plasma demeure toujours allumé, les densités de courant sont plus élevées ce qui fait en sorte que les densités de charges peuvent atteindre les 10^{17} - 10^{18} m^{-3}.

Les diagnostics optiques sont également fort populaires pour caractériser les plasmas froids à la PA. Ces diagnostics peuvent se décliner en deux grandes catégories que sont la spectroscopie d'émission et la spectroscopie d'absorption. La spectroscopie d'émission est probablement la plus polyvalente des méthodes puisqu'elle est pour une grande part indépendante du type de plasma étudié : il ne suffit que de posséder un spectromètre et de

Tableau 1.1. Caractéristiques et densités d'espèces énergétiques pour différentes décharges à la pression atmosphérique. Tableau adapté de [24].

Type de décharge	DBD en régime filamentaire	DBD en régime homogène	DBD en régime de Townsend	Plasma RF
Durée de la décharge	10-100 ns	1-5μs	Moitié de la période	Allumée en tout temps
Densité de courant maximale [mA/cm^2]	10^3 - 10^4	1-10	0.1-5	50
Densité de puissance maximale [W/cm^2]	10	1	5	5
Densité électronique maximale [m^{-3}]	10^{20}	10^{16} - 10^{17}	10^{13} - 10^{14}	10^{18}
Densité d'états métastables maximale [m^{-3}]	10^{19}	10^{17}	10^{19}	10^{18}
Densité ionique maximale [m^{-3}]	10^{20}	10^{17}	10^{17}	10^{17} - 10^{18}

pointer une fibre optique sur le plasma pour en faire une mesure du spectre. Qui plus est, une telle technique permet d'avoir accès à une quantité impressionnante d'information, mais ceci se ne fait pas sans heurts puisque les subtilités sont nombreuses.

Un exemple de spectre est présenté à la Figure 1.6 pour un plasma RF d'argon en régime capacitif. Entre 690 et 850 nm, le spectre est dominé par les transitions 2p-1s (notation de Paschen) de l'argon. Le diagramme des niveaux d'énergie de l'argon est illustré à la Figure 1.7. À la Figure 1.6, des bandes ro-vibrationnelles de l'azote entre 300 et 550 nm, une bande rotationnelle de OH à 309 nm, ainsi que des raies atomiques de l'oxygène à 777 et 844 nm sont également observables ; ceci dénote la présence d'impuretés dans le mélange gazeux.

À partir de l'analyse détaillée du spectre rotationnel de OH, les auteurs ont rapporté des températures rotationnelles (et donc des températures du gaz en admettant un équilibre entre les niveaux de rotation et de translation, voir détails plus loin) entre 400 et 600 K selon l'intensité maximale des pics de courant. Ces données sont illustrées à la Figure 1.8. Dans les

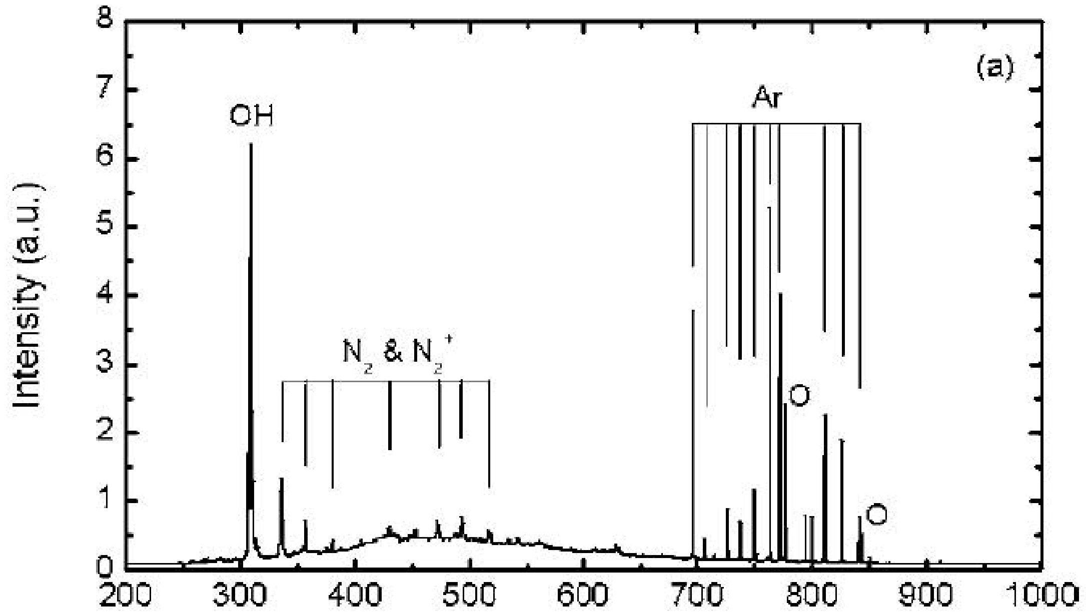

FIGURE 1.6. Spectre d'émission optique d'un plasma RF d'argon. Graphique tiré de [25].

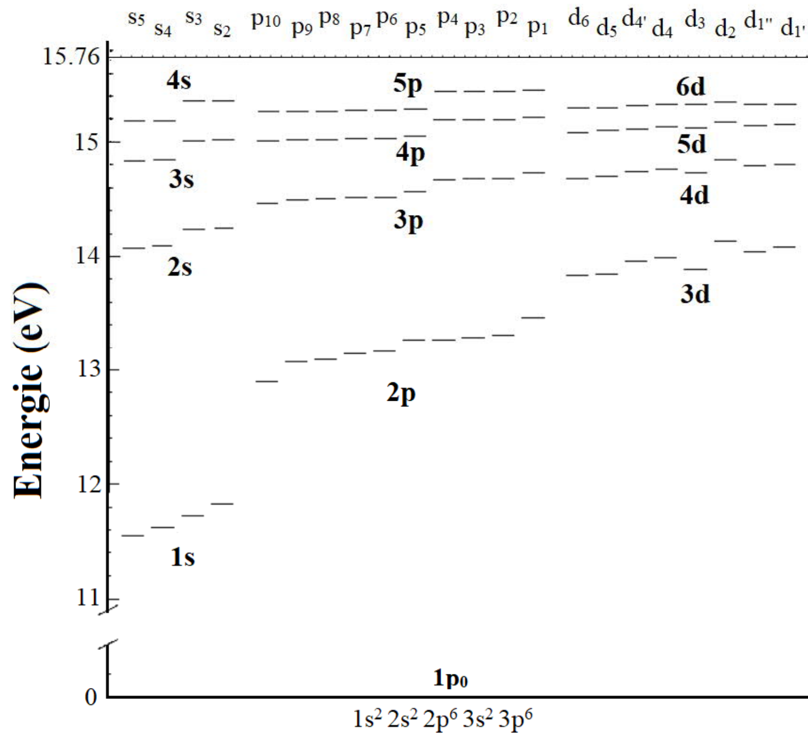

FIGURE 1.7. Diagramme des niveaux d'énergie de l'argon.

DBDs, comme les densités de courant et donc les densités de puissance sont considérablement plus faibles, les températures du gaz sont généralement beaucoup plus près de 300 K [26].

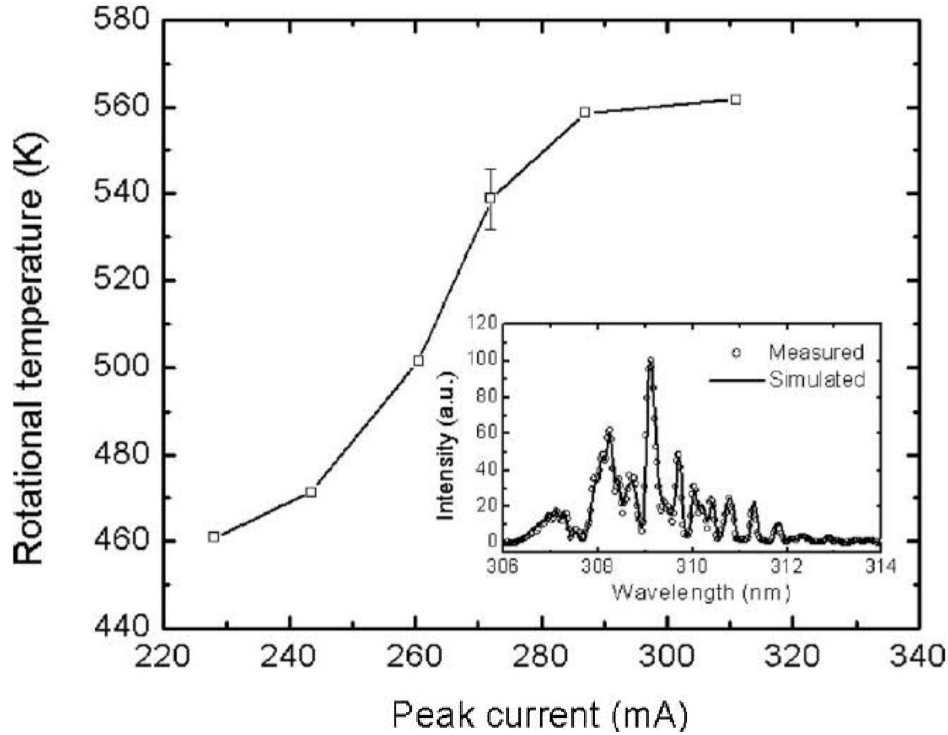

FIGURE 1.8. Température rotationnelle en fonction de l'intensité maximale des pics de courant dans un plasma RF d'argon. Graphique tiré de [25].

Dans certains plasmas, il est également possible d'observer des raies d'émission issues des niveaux électroniques élevés en énergie (3s, 4p, 5d, etc.), soit près du seuil d'ionisation. Bien que ces raies ne soient jamais vraiment observables dans les plasmas de basse puissance comme les DBDs, elles peuvent le devenir dans les plasmas plus fortement ionisés comme les plasmas RF et microonde. Dans ces conditions, les niveaux électroniques élevés en énergie peuvent satisfaire des conditions d'équilibre d'excitation et de désexcitation de sorte qu'en traçant un diagramme de Boltzmann à partir de l'intensité de ces raies tel que celui à la Figure 1.9, il devient possible d'obtenir une valeur de température, dite température d'excitation. Cependant, cette température n'est représentative que des niveaux à partir desquels elle a été calculée, d'où sa désignation de température d'excitation. Pour pouvoir porter le nom de température électronique, la droite du diagramme de Boltzmann à partir de laquelle elle est calculée devrait décrire tous les niveaux de l'argon. Or, il est maintenant bien connus que les niveaux les plus bas en énergie (1s et 2p) font rarement partie de cet équilibre, et donc ne sont pas représentés par ce T_{exc} [27].

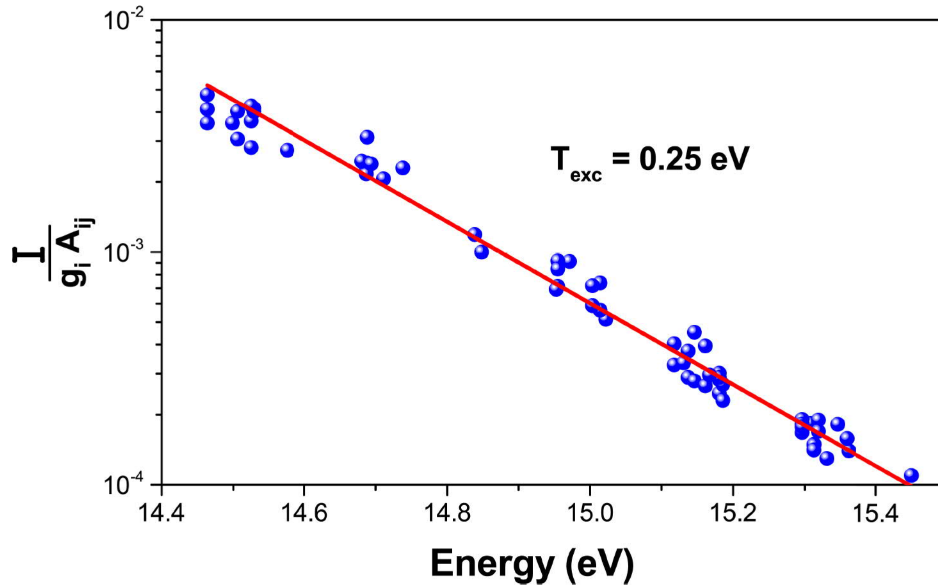

FIGURE 1.9. Diagramme de Boltzmann permettant le calcul d'une température d'excitation dans un POS d'argon.

Pour effectivement obtenir la température des électrons, certains se sont basés sur le continuum d'émission électron-neutre parfois visible en plus des raies d'émission sur un spectre [28]. Cette technique, habituellement employée dans le cas des plasmas RF, permet aussi d'obtenir la densité des électrons puisque l'intensité et l'aspect du continuum dépendent de ces deux paramètres. Un exemple, illustré à la Figure 1.10, présente des densités électroniques maximales de l'ordre de 10^{17} m^{-3} et des températures électroniques de quelques électronvolts, résultats qui sont conformes à ceux du Tableau 1.1. Cependant, cette technique d'analyse du continuum d'émission ne se transfère pas facilement dans le cas des plasmas plus faiblement ionisés comme les DBDs puisqu'un tel continuum y est rarement observé.

Similairement, des mesures de diffusion Thomson peuvent aussi permettre d'obtenir simultanément la température et la densité des électrons [29]. Toutefois, le recours à ce diagnostic nécessite des densités électroniques assez élevées pour diffuser suffisamment de lumière. En plus, de telles mesures requièrent de l'équipement hautement sophistiqué (et généralement fait sur mesure) de sorte qu'il s'agit d'un diagnostic peu accessible. Qui plus est, l'alignement du laser et la taille de son faisceau étant critiques dans ce genre de mesures, ce sont surtout des jets qui ont été caractérisés par diffusion Thomson, ceux-ci évitant d'avoir à tout aligner en considérant le réacteur. Le Tableau 1.2 présente un sommaire de plusieurs mesures de

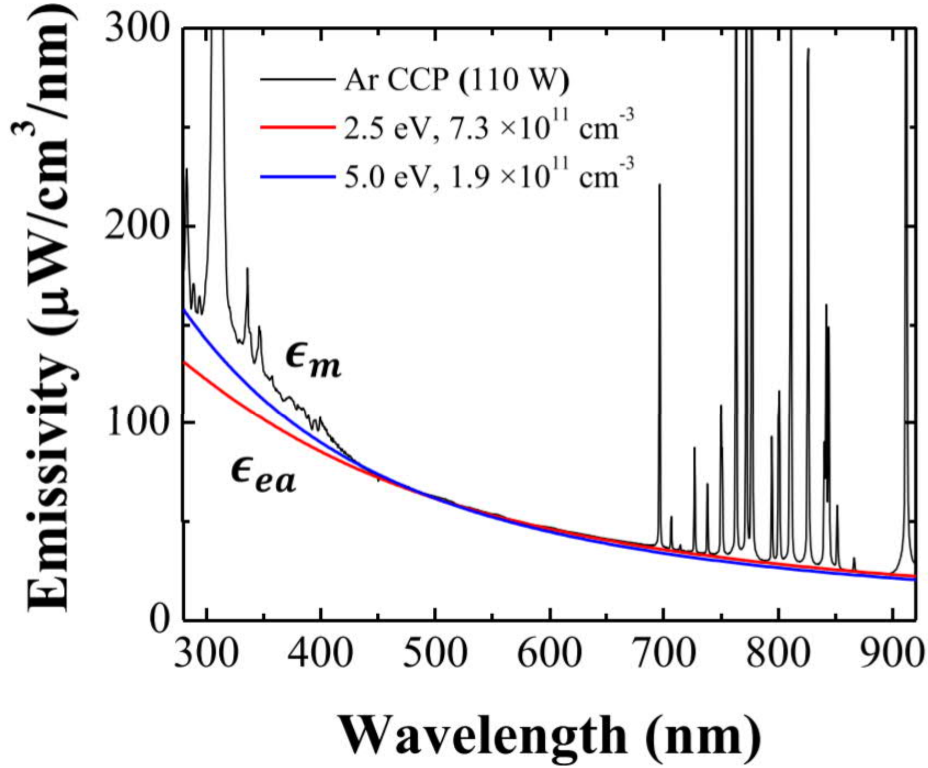

FIGURE 1.10. Obtention de la température et de la densité des électrons à partir d'une mesure de continuum d'émission dans un plasma RF. Graphique tiré de [28].

la densité et de la température des électrons par diffusion Thomson. On y voit cette fois des températures électroniques entre 0.1 et 5 eV selon les conditions opératoires. Quant aux densités électroniques, elles sont plus faibles dans les plasmas de basse fréquence comme les DBDs et plus élevées dans les plasmas de haute fréquence comme les plasmas microonde. À nouveau, ces données sont conformes à celles du Tableau 1.1.

Toujours dans la thématique des électrons, des mesures de spectroscopie d'émission à haute résolution ont aussi fréquemment permis d'obtenir la densité électronique dans les plasmas fortement ionisés. Par exemple, les densités électroniques élevées, caractéristiques des plasmas microonde, se traduisent en un élargissement Stark considérable pour certaines raies. C'est particulièrement le cas de la raie H_β de l'hydrogène, expliquant pourquoi tant de littérature existe aujourd'hui à son sujet et qu'il s'agit probablement du diagnostic le plus employé et accepté dans la communauté pour obtenir la densité électronique. Dans le cas de la H_β comme dans celui de toutes les autres raies, l'élargissement mesuré par un spectromètre à haute résolution possède un profil généralement bien décrit par une fonction

Tableau 1.2. Sommaire des propriétés obtenues par diffusion Thomson de différentes sources de plasma à la pression atmosphérique. Tableau adapté de [30].

Plasma	Gaz	n_e [10^{20}m^{-3}]	T_e	Référence
DBD-jet 20kHz	He	0.005–0.15	0.1–1.6	Hübner *et al* [31]
RF-jet 14.5 MHz, pulsé	Ar, Ar/air	0.05–0.2	0.2–2	Van Gessel *et al* [32]
RF ICP 27 MHz	Ar, Ar/H2O	1–20	0.3–0.7	Huang *et al* [33]
Microonde-jet 2.45 GHz	Ar	0.2–8	1.2–5	Van Gessel *et al* [29]
Microonde-torche 2.45 GHz	Ar	1–22	0.8–1.9	van der Mullen *et al* [34]

Voigt et est le résultat d'une convolution de nombreux élargissements. Parmi ceux-ci, les élargissements Stark, van der Waals et résonnant possèdent un profil lorentzien alors que l'élargissement Doppler ainsi que celui dû à l'appareillage de mesure en ont un gaussien, d'où le profil de Voigt. Or, l'avantage de la H_β réside dans le fait qu'à densité électronique donnée, l'élargissement Stark est davantage significatif vis-à-vis des autres que pour de nombreuses autres raies susceptibles d'être observées, réduisant ainsi l'erreur commise lors des calculs. Cependant, puisqu'une telle technique nécessite généralement l'ajout au gaz plasmagène d'une trace contenant de l'hydrogène (par exemple de l'eau), il est légitime de se demander à quel point le résultat est représentatif du plasma tel qu'il était sans la trace. Malgré tout, cette technique a permis de démontrer à de nombreuses reprises que le profil de densité électronique dans les plasmas produits par une onde électromagnétique de surface présente une décroissance linéaire à partir de l'excitateur (illustré à la Figure 1.11), mettant ainsi en évidence même un dépôt de puissance de l'onde de surface dans le milieu dissipatif décroissant linéairement [18].

Sinon, dans les dernières années, certains ont semblablement cherché à utiliser la spectroscopie d'émission à haute résolution pour obtenir la température des neutres dans les plasmas à la PA [36, 37]. La méthode développée a été appliquée en particulier aux plasmas microonde dont la température du gaz est connue pour être beaucoup plus élevée (plusieurs centaines de kelvins) que celle des DBDs et des plasmas RF. Elle repose sur l'analyse de l'élargissement van der Waals de certaines raies spécialement sélectionnées (par exemple à

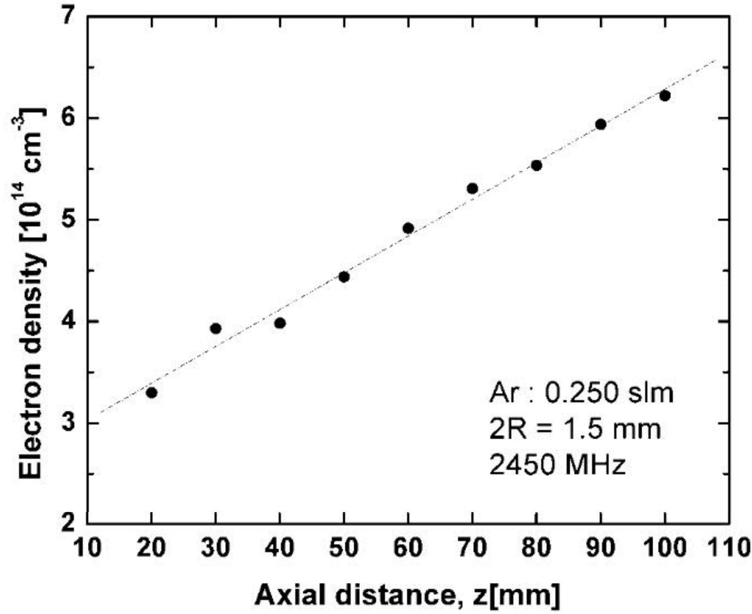

FIGURE 1.11. Profil axial de la densité électronique dans un POS d'argon obtenu à partir de l'élargissement Stark de la raie H_β de l'hydrogène. Graphique tiré de [35].

549.6 nm et 603.2 nm pour l'argon), mais le fait que ce choix soit uniquement basé sur des observations expérimentales jette un doute sur l'exactitude des résultats. En effet, elles ont été sélectionnées suite à l'observation que leur élargissement lorentzien total changeait peu en fonction de la densité électronique dans un POS, et donc par hypothèse qu'elles sont peu sujettes à un élargissement Stark. Or, des calculs théoriques montrent au contraire que les niveaux desquels proviennent ces deux raies sont fortement affectés tant par l'élargissement van der Waals que Stark. De plus, puisqu'il s'avère qu'une diminution de la densité électronique réduit effectivement l'élargissement Stark, mais qu'elle s'accompagne généralement aussi d'une décroissance de la température du gaz qui elle augmente l'élargissement van der Waals, il est alors logique que l'élargissement lorentzien total change effectivement peu avec un changement de la densité électronique. Cependant, ce n'est pas parce que les raies sont affranchies de tout élargissement Stark : une erreur est donc systématiquement commise en ne le considérant pas dans les calculs.

Pour circonvenir à ceci et néanmoins obtenir la température du gaz de manière optique, beaucoup ont plutôt opté pour le calcul d'une température de rotation à partir de l'émission ro-vibrationnelle d'espèces moléculaires thermométriques comme OH ou N_2. Dans ces cas, comme mentionné précédemment, il est supposé que la PA favorise suffisamment un équilibre

rotation-translation pour que cette température rotationnelle soit représentative de celle du gaz. Cependant, cette hypothèse impose que l'excitation électronique des niveaux émetteurs se fasse en conservant intacte la structure rotationnelle des molécules à l'état fondamental, et qu'aucun autre mécanisme d'excitation (par exemple via un pompage collisionnel dû à des espèces métastables) ne doive avoir lieu. Or, puisque ces deux hypothèses sont difficiles à vérifier sur une gamme étendue de conditions opératoires, cette méthode est elle aussi alambiquée et controversée.

Concernant les diagnostics optiques basés sur l'absorption plutôt que l'émission, ceux-ci sont pour leur part généralement utilisés afin de cibler les neutres excités (métastables ou non) présents dans le plasma. L'intérêt de ces niveaux provient du fait qu'à la PA, ils peuvent, selon les conditions, contribuer de manière significative aux différents processus d'excitation et d'ionisation inhérents au plasma. D'ailleurs, la distinction entre niveaux métastables et niveaux résonnants perd pratiquement sa signification pour une telle pression puisque la très grande quantité de neutre à l'état fondamental ($\sim 10^{25}$ m^{-3}) résulte en une auto absorption quasi totale des photons issus des niveaux résonnants. Ceci justifie que les uns comme les autres peuvent jouer un rôle dans la cinétique réactionnelle. Tant si la technique d'absorption implique une lampe spectrale ou une diode laser accordable en longueur d'onde, la quantité de lumière absorbée permet de calculer la densité de ces neutres excités. Pour cette raison, Boisvert *et al.* ont par exemple combiné les deux méthodes afin d'observer l'évolution temporelle de la densité de niveaux métastables d'une décharge capacitive en hélium, ainsi que l'influence qu'a sur elle la fréquence d'excitation [13]. Ces derniers résultats sont présentés à la Figure 1.12 et montrent que de passer d'un régime DBD (courbes bleues) à RF (courbes brunes, vertes et rouge) influence peu cette densité, celle-ci étant davantage sensible aux différents régimes de décharge et, implicitement, à la puissance. Les valeurs observées peuvent alors couvrir deux ordres de grandeur, allant de 10^{16} à 10^{18} m^{-3}. Semblablement, Castaños-Martinez *et al.* ont aussi utilisé une lampe spectrale pour obtenir la densité d'états métastables dans un POS d'argon [38]. Dans leur cas, ils ont obtenu des résultats de l'ordre de 10^{18} - 10^{19} m^{-3}.

Finalement, en lien avec les mesures expérimentales des propriétés fondamentales des plasmas à la PA, les modélisations sont elles aussi populaires peu importe le type de plasma considéré. Par exemple, dans le cas d'une DBD d'hélium, un modèle CR couplé à des mesures

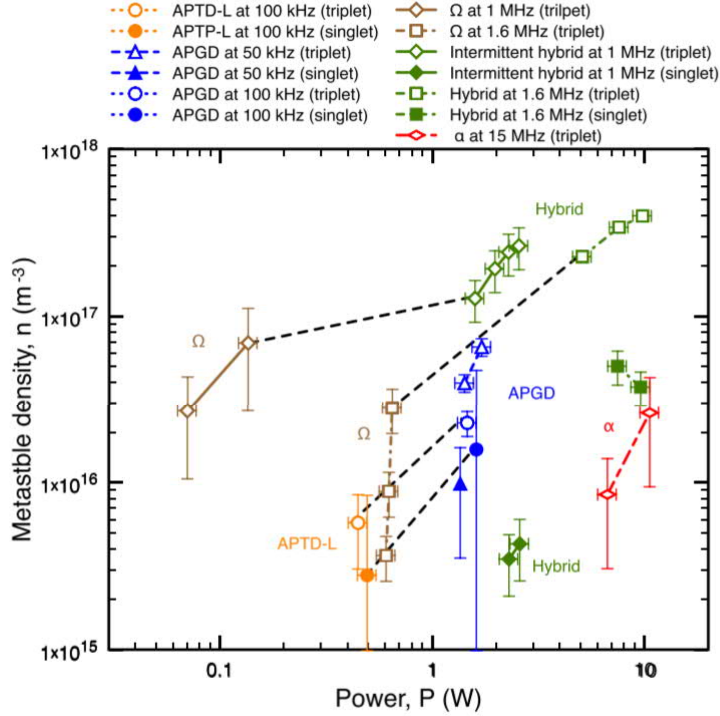

FIGURE 1.12. Évolution de la densité d'états métastables d'hélium dans une décharge capacitive entretenue selon différents régimes. Graphique tiré de [13].

de spectroscopie d'émission ont permis à Gangwar *et al.* de suivre l'évolution temporelle de la température des électrons [39]. Tel que montré à la Figure 1.13, il a alors été observé qu'un pic de T_e caractérisait les premiers instants de la décharge, passant de 1.2 eV jusqu'à 0.2 eV à mesure que la décharge passait d'un régime non entretenu (régime de Townsend) à celui d'une décharge luminescente.

Dans le même ordre d'idées, différents groupes ont également développé des modèles concernant les plasmas d'argon. Zhu et Pu ainsi que Castaños-Martinez *et al.* ont élaboré eux aussi un modèle CR [38, 40], permettant entre autres aux seconds de prédire que la température des électrons dans un POS d'argon devrait avoisiner 0.9 eV tout au long de la colonne. Pour leur part, Kabouzi *et al.* ont réalisé un modèle fluide 2D couplé aux équations électromagnétiques, obtenant ainsi les profils résolus spatialement de différents paramètres d'intérêt comme les températures du gaz et des électrons reportés à la Figure 1.14 et dont les valeurs s'approchent de celles de Castaños-Martinez et *al.*

Toutefois, il est important de mentionner que tous ces modèles pour l'argon sont auto cohérents, ne se basant que sur des équations et non sur des données expérimentales pour

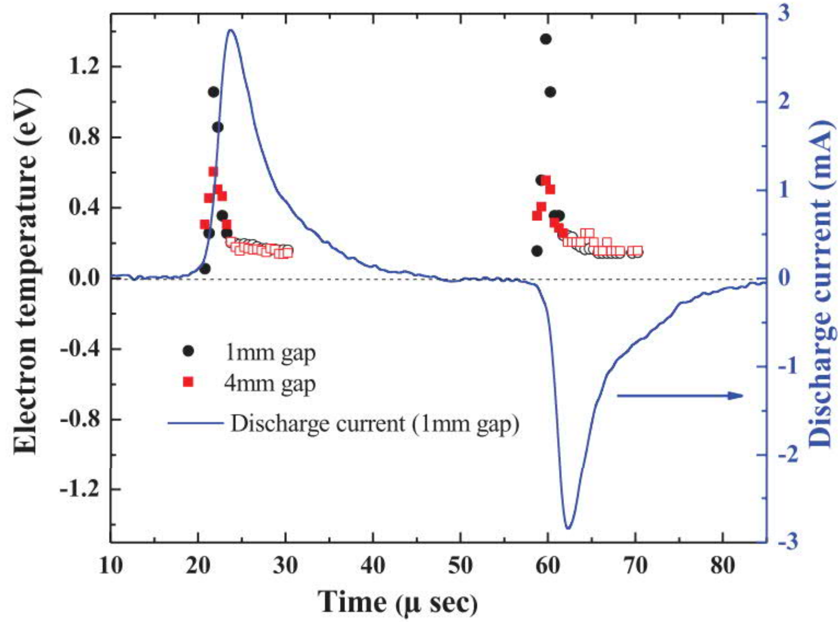

FIGURE 1.13. Évolution temporelle de la température électronique dans une DBD d'hélium. Graphique tiré de [39].

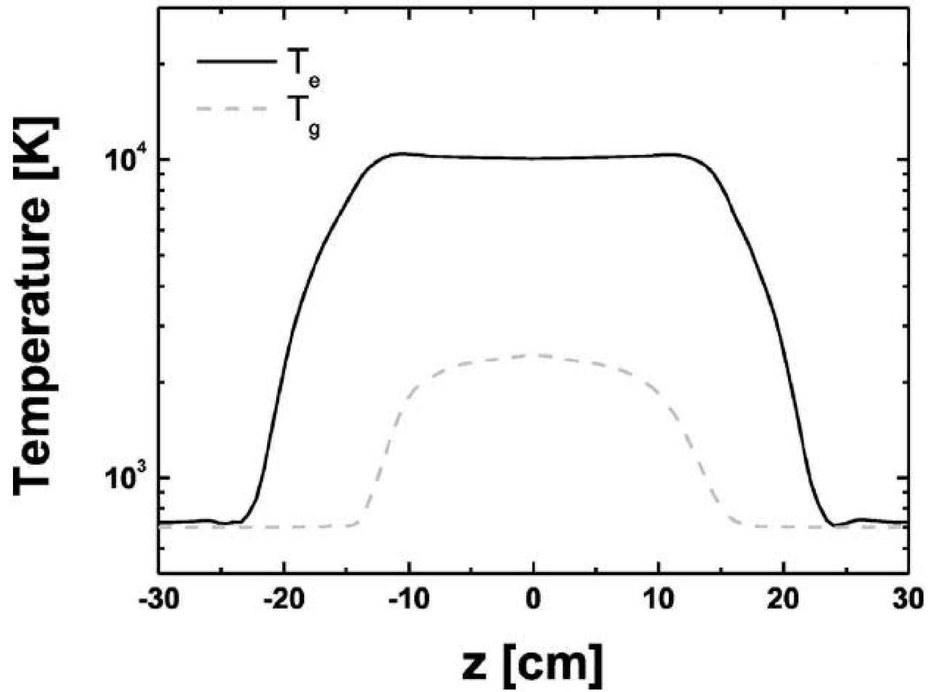

FIGURE 1.14. Profils axiaux des températures du gaz et des électrons dans un POS d'argon, obtenus à partir d'une modélisation fluide du plasma couplé aux équations électromagnétiques. Graphique tiré de [41].

prédire les propriétés des plasmas. Or, tous possèdent un certain nombre de lacunes puisque chacun à leur façon ne tient pas suffisamment compte des particularités de l'argon (plus complexe à modéliser que l'hélium) ainsi que de celles de la PA pour donner des résultats vraisemblables. Par exemple, les transferts d'excitation entre niveaux 2p de l'argon suite à des collisions avec les atomes neutres peuvent devenir importants dans les plasmas à la PA. De manière similaire, la présence d'impuretés liées à la contamination par le milieu environnant ou encore à la pureté du gaz utilisé peut jouer un rôle prépondérant dans la désexcitation collisionnelle (quenching) des niveaux 2p de l'argon. C'est d'ailleurs ces processus qui gouvernent l'obtention du régime homogène plutôt que filamentaire dans les DBD [23] et l'obtention d'une décharge diffuse plutôt que contractée dans les plasmas produits par des champs électromagnétiques de haute fréquence [42]. Comme ces changements dans les populations des niveaux 1s peuvent jouer un rôle critique sur la cinétique d'ionisation du plasma, ils peuvent également modifier les valeurs de densités et de température des électrons. Pour ces raisons, les résultats fournis par ces modèles sont à considérer avec prudence. De ceci, la conclusion est également qu'il est primordial d'obtenir un portrait cohérent de l'ensemble des propriétés fondamentales des plasmas hors équilibre à la PA, ce qui inclut n_e, T_e, T_g et n_{1s}, pour maîtriser toute la subtilité de l'ensemble des processus physiques mis en jeu. Ces aspects seront couverts au Chapitre 2.

1.3. Plasmas dans les gaz rares à la pression atmosphérique avec espèces réactives

Les plasmas produits dans des gaz rares tels que tout juste décrits permettent peu d'applications dans les différents domaines d'intérêt comme ceux mentionnés dans l'introduction. En effet, c'est plutôt avec l'ajout de composés réactifs dans le plasma (qu'ils soient délibérément injectés ou simplement issus de l'environnement ambiant) que surviennent toutes les possibilités, bien que ce soit au détriment d'une cinétique réactionnelle beaucoup plus complexe. Dans les cas impliquant la synthèse de revêtements, le choix du précurseur dépend en grande partie de la composition chimique et des propriétés de ce qui souhaite être synthétisé. Ceci explique que les précurseurs les plus couramment étudiés dans la littérature actuelle vont de l'acétylène (C_2H_2) aux précurseurs organosiliciés tels que HMDSO ($(CH_3)_3SiOSi(CH_3)_3$) et TEOS ($Si(OC_2H_5)_4$), en passant par le silane (SiH_4) [43–47]. Dans les cas où ce sont surtout

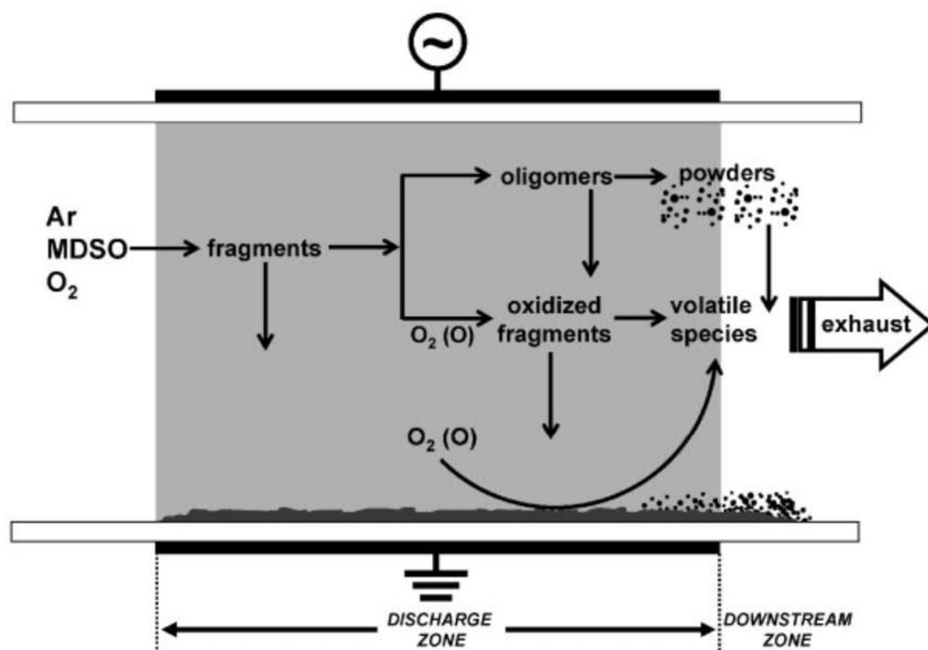

FIGURE 1.15. Dynamique de conversion du précurseur HMDSO dans une DBD d'Ar/O_2. Schéma tiré de [47].

les espèces réactives en phase gaz qui intéressent, comme c'est le cas en médecine par plasma, ce sont alors des gaz comme N_2, O_2 et H_2 qui sont ajoutés.

Évidemment, plus le composé réactif est une molécule complexe, plus les cinétiques de fragmentation et de recombinaison des fragments sont difficiles à comprendre et donc l'impact du composé sur les propriétés du plasma laborieux à étudier. En effet, puisque tous les liens chimiques sont caractérisés par une énergie de liaison, ceci implique que certains sont plus propices à se rompre que d'autres suivant leur interaction avec les espèces de haute énergie du plasma, par exemple les électrons et les espèces métastables. De plus, certains atomes ont des affinités particulières avec d'autres, de sorte que temporellement et spatialement, le plasma doit maintenant être caractérisé non seulement par une densité et une température électroniques, une température du gaz porteur et la densité de certains de ses états excités, mais aussi par des concentrations de fragments de toute sorte et potentiellement de nanoparticules en croissance dont les dynamiques de formation et de transport sont encore loin d'être parfaitement compris. De manière simplifiée, la conversion des composés réactifs dans les plasmas peut se représenter par le schéma de la Figure 1.15 concernant l'insertion du précurseur HMDSO dans une DBD d'Ar/O_2, dépeignant les phénomènes de fragmentation, de dépôt, de désorption de produits volatils et de recombinaison en phase gazeuse.

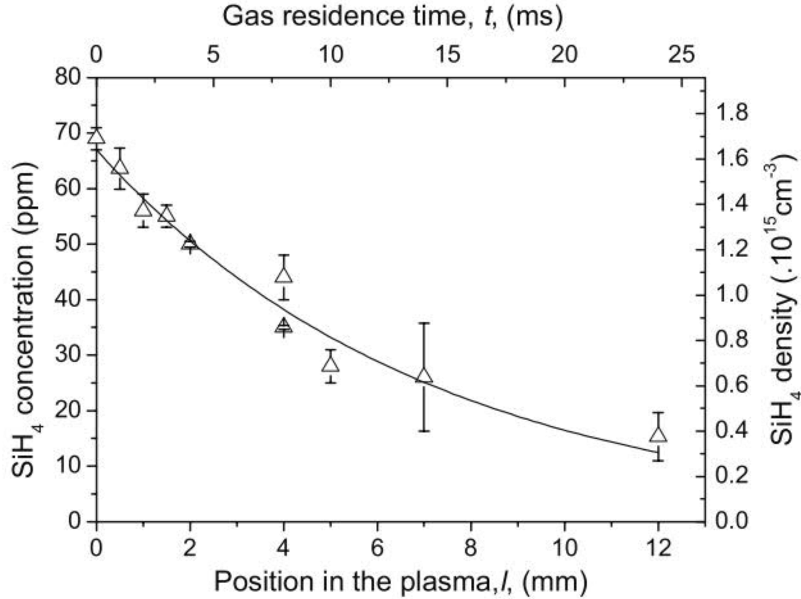

FIGURE 1.16. Consommation du précurseur SiH_4 en fonction de la position dans une DBD. Graphique tiré de [48].

En théorie, un plasma peut morceler un précurseur en autant de fragments qu'il y a d'atomes le composant. Aussi, toute espèce du plasma possédant davantage que l'énergie d'une liaison chimique peut contribuer à la cinétique de fragmentation. Ceci implique donc certainement les électrons, mais aussi potentiellement des métastables, des photons UV et des neutres ayant une grande énergie cinétique. S'il est plausible d'assumer que dans le cas de la majorité des plasmas froids, ces derniers n'ont pas l'énergie thermique nécessaire pour participer à la fragmentation, les rôles respectifs des métastables et des photons n'ont jamais vraiment été étudiés non plus. Ainsi, avec raison ou non, il est généralement considéré que ce sont essentiellement les électrons et les métastables qui dictent la cinétique de fragmentation [24].

Ceci étant dit, parmi le peu d'études qui se sont intéressées plus fondamentalement aux plasmas réactifs, Vallade et Massines ont retenu la spectroscopie infrarouge d'absorption à transformée de Fourier pour étudier l'injection de silane dans une DBD d'argon [48]. À partir du passage d'un faisceau infrarouge a large bande dans la décharge, ils ont pu suivre un pic d'absorption caractéristique du précurseur en fonction de la position et ainsi mettre en lumière sa disparition, donc sa fragmentation au profit de quelque chose d'autre. Ces résultats sont présentés à la Figure 1.16.

Pour leur part, Kilicaslan *et al.* ont eu recours à une autre technique spectroscopique pour mettre en évidence la fragmentation des espèces réactives dans un plasma, celle de la spectroscopie optique d'émission[49]. En prenant le spectre d'émission d'un POS d'argon dans lequel ils ont injecté le précurseur HMDSO (Figure 1.17b) et en le comparant à un spectre pris en argon pur (Figure 1.17a) ou a celui d'une DBD dans laquelle de l'HMDSO était aussi injecté (Figure 1.17d), ils ont vu apparaitre des raies et des systèmes de bandes qui n'étaient pas visibles auparavant. Ceci leur a permis de conclure que non seulement le POS est beaucoup plus agressif qu'une DBD quant à la fragmentation, un effet naturellement lié aux densités de puissance tel que discuté précédemment, il est surtout suffisamment agressif pour laisser croire à une fragmentation quasi totale vu l'apparition d'une raie de silicium (391.5nm) dans le spectre. De plus, en ajoutant de l'oxygène dans leur expérience, ils ont observé que le carbone, entre autres les molécules C_2 visibles par leur signature de bande entre 400nm et 600nm, disparaissait, démontrant par le fait même une plus grande affinité de recombinaison avec l'oxygène qu'avec d'autres carbones, formant ainsi des produits volatils.

Dans le même ordre d'idée, Benedikt *et al.* ont utilisé la spectrométrie de masse afin d'avoir spécifiquement de l'information sur les fragments produits dans un jet de plasma RF suite à l'insertion du même précurseur HMDSO [50]. Un exemple de leur spectre de masse est présenté à la Figure 1.18. Ils ont ainsi pu observer que dans leurs conditions c'est la liaison Si-O du précurseur qui était la plus sujette à se rompre et que l'ajout intentionnel d'oxygène dans la décharge influençait la nature et la densité des fragments produits.

Finalement, Nisol *et al* ont entrepris de caractériser une multitude de précurseurs quant à leur bilan énergétique dans une DBD d'argon [26, 51–55]. Pour ce faire, ils ont développé un modèle de circuit équivalent leur permettant de déterminer la quantité d'énergie prise par chaque molécule durant son temps de résidence dans la décharge. Ils ont ainsi mis en lumière des caractéristiques communes à des familles de précurseurs simplement à partir de mesures électriques. Un exemple de mesures d'énergie électrique absorbée par les électrons par cycle de la tension appliquée est présenté à la Figure 1.19. Afin d'obtenir l'énergie relative prise par le précurseur, les auteurs ont ensuite calculé la différence relative entre l'énergie absorbée par les électrons dans le plasma d'argon ($E_g(\mathrm{Ar})$) et celle en présence du précurseur

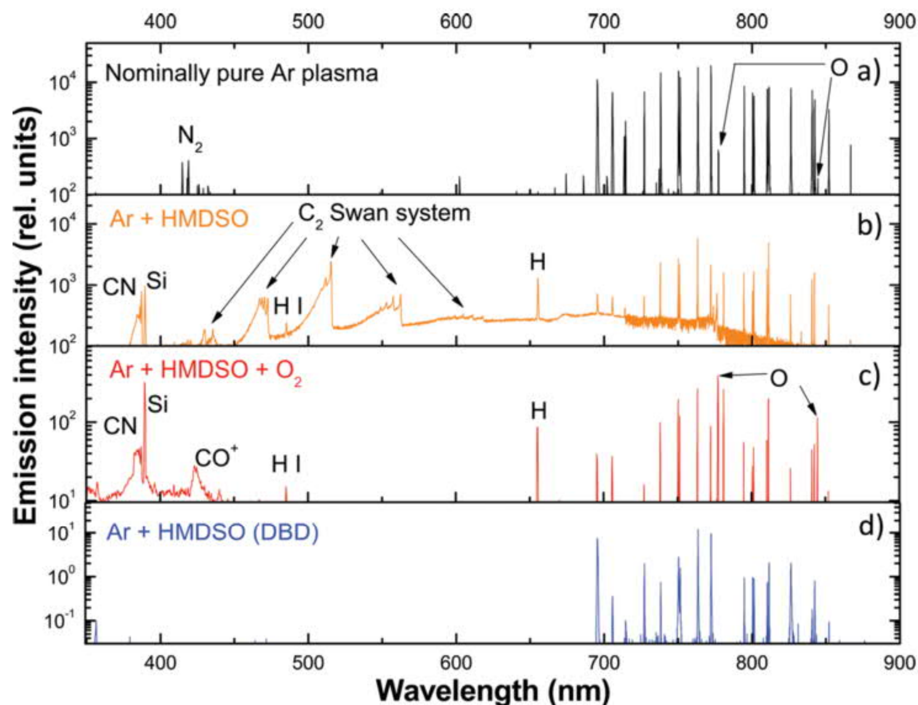

Figure 1.17. Mise en évidence de la fragmentation d'HMDSO par spectroscopie optique d'émission d'un plasma d'onde de surface : a) Plasma d'argon pur ; b) Plasma d'argon avec HMDSO ; c) Plasma d'argon avec oxygène et HMDSO ; d) Comparaison avec une DBD. Graphiques tirés de [49].

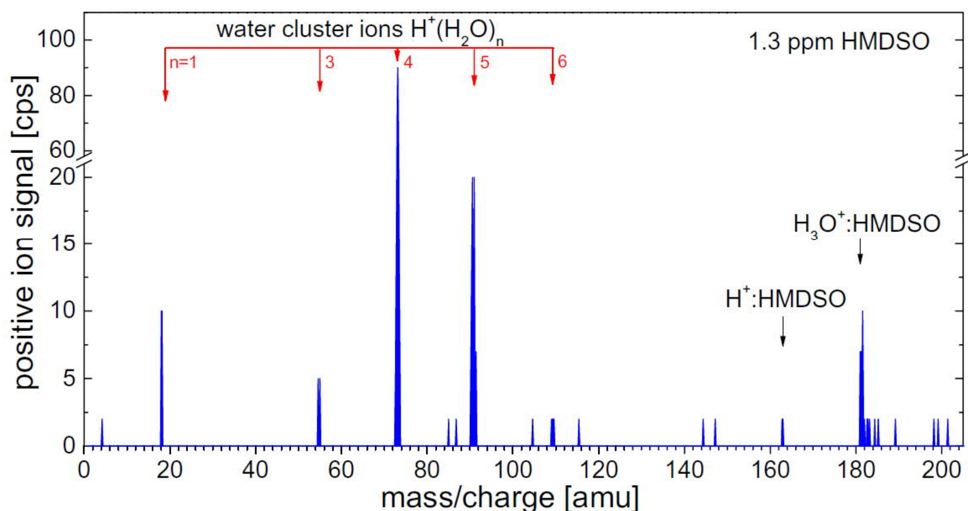

Figure 1.18. Spectrométrie de masse des espèces résultantes de la fragmentation d'HMDSO dans un plasma microonde. Graphique tiré de [50].

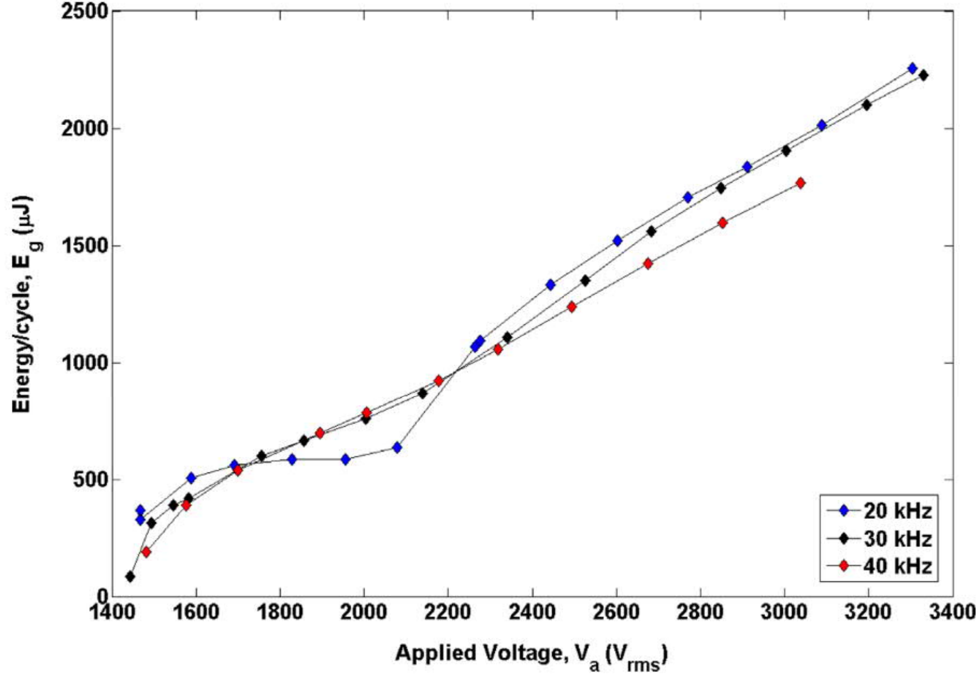

FIGURE 1.19. Énergie électrique absorbée par les électrons par cycle de la tension appliquée pour trois fréquences. Graphique tiré de [26].

(E_g(Ar+Prec)) :

$$\Delta E_g^{electrical}(\%) = \frac{E_g(Ar) - E_g(Ar + Prec)}{E_g(Ar)} \times 100 \quad (1)$$

Dans cette équation, il est néanmoins important de préciser qu'il est implicitement supposé que le plasma d'argon demeure inaltéré suite à l'ajout du précurseur de telle sorte que la différence en énergie devient alors complètement disponible pour le précurseur. Un retour sur cet aspect sera fait au Chapitre 3.

Manifestement, la multitude et l'originalité des approches qui viennent d'être mentionnées ont permis à plusieurs groupes de recherche d'étudier chacun à leur façon divers plasmas réactifs. Cependant, toutes ces études ont en commun qu'elles se sont principalement intéressées à l'impact du plasma sur les espèces réactives, et non l'inverse. En effet, aucune ou presque ne s'est réellement intéressée à l'impact des espèces réactives sur les propriétés fondamentales du plasma et ce constat justifie pourquoi il en sera question dans les Chapitres 3 et 4.

Chapitre 2

Développement et validation de diagnostics optiques dans les plasmas d'argon

2.1. Introduction

À la lumière du précédent chapitre, les diagnostics optiques apparaissent aujourd'hui comme le choix de prédilection pour obtenir un bon nombre des propriétés nécessaires aux études de la physique des plasmas froids à la PA. Néanmoins, il est aussi évident que certaines lacunes persistent, particulièrement en ce qui a trait à la température électronique dans les plasmas d'argon. En effet, les techniques existantes sont soit limitées quant à leur applicabilité (continuum d'émission), soit onéreuses et difficiles à mettre en place (diffusion Thomson), ou encore uniquement développées pour l'hélium (spectre d'émission optique couplé à un modèle CR). Force est aussi de constater que les techniques optiques permettant l'obtention de la température du gaz ne font pas non plus l'unanimité, chacune ayant des faiblesses plus ou moins criticables. Ainsi, l'objectif de ce chapitre est de mettre au point un ensemble cohérent de diagnostics optiques pour la caractérisation des plasmas froids d'argon à la PA. Ceci comprend des diagnostics optiques pour la densité et la température électroniques, la température du gaz ainsi que la densité des états 1s de l'argon.

En particulier, inspiré par ce qui a déjà été fait dans l'hélium [39], une méthode a été développée pour les plasmas d'argon afin d'obtenir la température des électrons en couplant des mesures d'émission optique des transitions 2p-1s à un modèle CR décrivant la population des niveaux 2p. Faisant l'objet d'un premier article inclus dans cette thèse, ce modèle a été spécifiquement adapté aux particularités de la PA puisqu'il permet de prendre en compte les phénomènes d'autoabsorption des raies, les collisions d'excitation/désexcitation induites par les molécules neutres et ne dépend pas de la résolution des équations permettant d'obtenir la densité des états 1s. Au contraire, pour des raisons explicitées dans le texte, cette densité

est plutôt fournie comme paramètre d'entrée au modèle, au même titre que la température du gaz et autres données expérimentales liées aux conditions opératoires. D'ailleurs, et pour cette raison, ce premier article traite également de nouvelles méthodes proposées pour obtenir optiquement cette densité des états 1s ainsi que la température du gaz. Il y est aussi question de la validation de toutes ces nouvelles techniques, réalisée dans le cas particulier d'une étude le long de l'axe d'un POS d'argon puisque les propriétés de ce type de plasma ont fait l'objet de plusieurs publications et offrent donc un excellent point de comparaison.

Similairement, une validation additionnelle a été effectuée dans le contexte d'une DBD d'argon, cette fois-ci en suivant l'évolution temporelle de la température électronique au cours d'une période complète de la tension appliquée. Les résultats de cette étude, résumés au point 2.3, sont également compilés sous la forme d'un second article, joint en annexe. Dans le cas de ces deux articles comme dans celui des autres à venir au cours des prochains chapitres, une brève description du montage expérimental utilisé sera faite dans la présentation. Ce traitement au cas par cas est dû au fait que la majorité des articles ont un montage qui leur est propre et donc qu'il ne s'avérait pas judicieux de faire une section de la thèse spécifiquement consacrée à la portion expérimentale.

2.2. Article 1 : Caractérisation d'un plasma microonde d'argon à la pression atmosphérique par spectroscopie optique d'émission et d'absorption couplée à un modèle collisionnel-radiatif

Ce premier article présente les grandes lignes de la méthode développée pour obtenir la température électronique d'un plasma froid d'argon à la PA à partir d'un spectre d'émission des transitions 2p-1s couplé à un modèle CR décrivant la population des niveaux émetteurs 2p. Les diagnostics connexes permettant d'obtenir, d'une part, la température du gaz à partir de l'élargissement des raies $2p_2$-$1s_2$ et $2p_3$-$1s_2$ de l'argon et, d'autre part, la densité d'états $1s_5$ par spectroscopie d'absorption employant une diode laser accordable en longueur d'onde y sont également exposés. Ils ont eux aussi été développés pour l'occasion car le modèle nécessite justement comme paramètres d'entrée entre autres ces deux données pour simuler l'intensité des raies 2p-1s de l'argon, celles-ci étant habituellement les plus intenses et donc faciles à observer dans un plasma d'argon. Utilisant alors la température électronique comme seul paramètre ajustable, le modèle a pour but de reproduire le spectre mesuré et la valeur de

T_e résultant du meilleur accord théorie/expérience est supposée être la véritable température électronique caractéristique du volume de plasma sondé par le spectre.

Suite à la présentation des détails de la méthode, tant en ce qui concerne les équations de bilan des niveaux émetteurs 2p que de la manière dont l'expérience est comparée à la théorie, une validation de la méthode est effectuée dans le cas d'un POS d'argon. Pour ce faire, l'accord théorie/expérience est d'une part démontré avec à l'appui un graphique montrant qu'il n'existe qu'une seule valeur de température électronique permettant d'obtenir ce spectre théorique optimal. D'autre part, la distribution de la température électronique le long de l'axe du plasma microonde tel qu'obtenu par le couplage du modèle à des spectres d'émission optique est comparé à ceux déjà rapportés dans la littérature utilisant diverses approches mentionnées au chapitre précédent. Afin de parvenir à ce résultat, le profil axial de la température du gaz ainsi que celui de la densité d'états $1s_5$ sont eux aussi présentés et validés. Dans tous les cas, les comportements de même que les valeurs obtenues concordent bien avec la littérature, c'est-à-dire qu'une chute de température du gaz est observée du lanceur vers la fin de la colonne ($\sim$1600 K à $\sim$1300 K), la température électronique demeure stable autour de 1.4 eV tout au long de la colonne et la densité de niveaux métastables demeure elle aussi stable, oscillant entre 1-2$\times 10^{18}$ m^{-3}.

Quant au POS dont il est question dans cet article, il a été produit dans un tube de silice fondue ayant 2 mm de diamètre interne et 6 mm de diamètre externe afin de s'affranchir des phénomènes de contraction et de filamentation [42]. Ces dimensions ont aussi permis d'éviter la propagation de modes autres que le mode fondamental puisque les microondes, couplées au tube à l'aide d'un surfaguide, avaient une fréquence de 2.45 GHz [56]. Une puissance constante de 300 W, mesurée à partir d'une ligne bidirective et d'un bolomètre, était transférée au plasma d'argon et toute puissance réfléchie était dissipée dans une charge adaptée refroidie à l'eau. Bien que le tube était ouvert à l'air ambiant en aval du flux, sa longue taille et le débit d'argon utilisés ont permis de faire en sorte qu'aucune trace significative d'impureté n'était visible dans les spectres. Les résultats peuvent donc être considérés comme typiques d'un plasma d'argon pur.

Characterization of a microwave argon plasma column at atmospheric pressure by optical emission and absorption spectroscopy coupled with collisional-radiative modelling

par

Antoine Durocher-Jean[1], Edouard Desjardins[1] et Luc Stafford[1]

([1]) Département de physique, Université de Montréal, Montréal, Québec, Canada

Cet article a été publié dans la revue *Physics of Plasmas* :

Phys. Plasmas, 26, 063516 (2019) .

Les contributions des différents auteurs à cet article sont :

— Antoine Durocher-Jean : Réalisation du montage expérimental, élaboration des diagnostics et des analyses (modèle CR, absorption par diode laser, élargissement des raies), prise des mesures, analyse des résultats, validation par rapport à la littérature et écriture du premier jet du manuscrit

— Edouard Desjardins : Révision du modèle CR

— Luc Stafford : Supervision des travaux, révision du manuscrit

Abstract.

Optical emission and absorption spectroscopy of argon 2p-1s transitions (Paschen notation) combined with collisional-radiative (CR) modeling of argon 2p states are developed and used to determine the neutral gas temperature, the Ar 1s number density, and the electron temperature along a microwave argon plasma column at atmospheric pressure. The CR model, designed specifically for atmospheric pressure and optically thick plasma conditions, is fully detailed and validated by comparing the relative line emission intensities of argon 2p-to-1s transitions measured experimentally with the ones predicted by the CR model using the electron temperature as the only adjustable parameter. Subsequently, the neutral gas temperature ($\tilde{1}300$–1600 K; obtained from the broadening of argon $2p_2$-$1s_2$ and $2p_3$-$1s_2$ emission lines), the Ar $1s_5$ number density (1–2×10^18 m^{-3}; obtained from absorption spectroscopy of the argon $2p_9$-$1s_5$ transition using a tunable laser diode), and the electron temperature $\tilde{1}.4$ eV; obtained from the comparison between the measured and simulated 2p-to-1s emission line intensities) are reported as a function of the axial distance along the microwave plasma column. The values and behaviors reveal a good agreement with those reported in previous experimental and modeling studies.

Keywords: microwave plasma at atmospheric pressure, optical emission spectroscopy, tunable laser diode absorption spectroscopy, collisional-radiative modelling, electron temperature, number density of metastable atoms, neutral gas temperature

2.2.1. Introduction

Nonthermal plasmas at atmospheric pressure are being increasingly studied for their ability to produce active species useful in a wide variety of applications such as gas treatment (methane or CO_2 conversion, greenhouse gas abatement) [1–3] and thin film deposition (hydrophilic/hydrophobic coatings, anti-UV or antireflective layers) [4–7]. While they offer significant benefits over their low-pressure counterparts (absence of vacuum pumping systems, low costs, ease of use, continuous in-line processing, etc.), they are not without disadvantages such as their usually small size and their important spatial gradients. Consequently, the steps to follow are not always easy to establish when it comes to develop or improve processes based on nonthermal plasmas at atmospheric pressure through fine tuning of their spatially resolved and often temporally resolved plasma properties. This gets even worse when one realizes that the physics involved in optical and electrical diagnostics of nonthermal plasmas at atmospheric pressure is much less documented than the one involved in low-pressure plasmas. For these reasons, accurate and trustworthy plasma diagnostic techniques are needed more than ever to understand the physics driving nonthermal plasmas at atmospheric pressure; such information is required to cleverly improve plasma-based processes through the use of more fundamental methods rather than traditional trial and error methods.

As of today, electrical measurements and their corresponding electrical models have been largely exploited to gain insights into some of the physical properties of nonthermal plasmas at atmospheric pressure, including the power absorbed and/or dissipated by electrons and the electron density [8,9]. Diagnostic techniques involving lasers have also been developed and used to provide additional parameters such as the electron density and temperature by Thomson scattering [10] or the number density of reactive neutral species using laser induced fluorescence (LIF) [11,12]. Similarly, plasma sampling mass spectrometry has lately gained an increased interest for its ability to qualitatively and quantitatively describe plasma-generated fragments in complex reactive plasmas [13,14]. Finally, self-consistent models have also been developed and used over the years to predict the aforementioned plasma properties [15–17].

Of the remaining few techniques used nowadays, optical emission spectroscopy (OES) is, in addition to being nonintrusive, one of the easiest and relatively inexpensive ways to acquire

information about a plasma. OES can be used, for example, to probe rotational, vibrational, and excitation temperatures through the use of Boltzmann plots for rotational, vibrational, and electronic levels, respectively. It can also be used to analyze line broadening of selected transitions to gather data on the neutral gas temperature or the electron density [18,19].

In this work, a method to obtain the electron temperature T_e from emission and absorption spectroscopy measurements of argon 2p-1s transitions (Paschen notation) combined with the predictions of a collisional-radiative (CR) model of argon 2p states is described. This method is first validated by comparing the OES plot in the 690–930 nm wavelength range measured in an argon plasma column at atmospheric pressure sustained by a propagating electromagnetic surface wave in the microwave regime with the one predicted by the CR model. Afterwards, the axial profiles of the neutral gas temperature, as found from the line broadening of selected argon 2p-1s transitions, as well as the population of argon $1s_5$ level (n_{1s_5}), as found from tunable laser diode optical absorption spectroscopy (OAS), are used as input parameters in the model to obtain the axially resolved electron temperature from the comparison between measured and simulated optical emission spectra. The article is divided as follows: in Sec. 2.2.2, the experimental setup used to produce the microwave plasma column in addition to how OAS and OES data were recorded and analyzed are presented; in Sec. 2.2.3, the CR model is detailed by a description of all the considered reactions and how the theoretical spectra are compared to the experimental one; in Sec. 2.2.4, the method is validated, and in Sec. 2.2.5 the axial profiles of T_g , n_{1s_5}, and T_e along the microwave plasma column are presented and discussed.

2.2.2. Experimental setup and data analysis

2.2.2.1. *Plasma source*

Figure 2.1 a) and b) show a schematic of the experimental setup and an image of the resulting plasma column, respectively. A constant power of 300W(incident minus reflected) was delivered to the plasma by a 2 kW Sairem microwave generator operating at 2.45GHz. Wave coupling was ensured by a surfaguide-type wave launcher. The discharge tube made of fused silica (2 mm inner diameter, 6 mm OD) was connected to the gas inlet on one end and was open to ambient air on the other end. This relatively small tube diameter was chosen to avoid propagation of high-order surface-wave modes as well as filamentation and

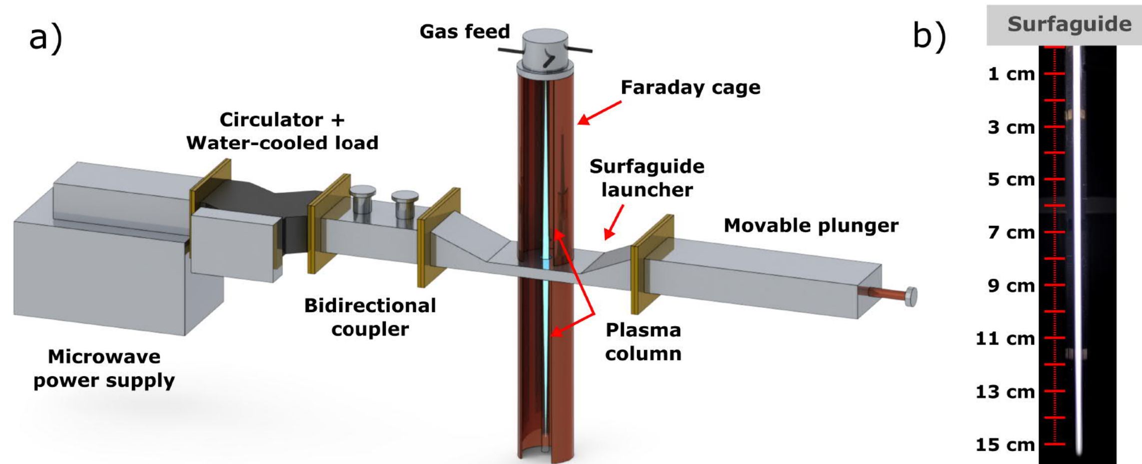

Figure 2.1. a) Schematic of the experimental setup. b) Picture of the microwave plasma column below the surfaguide wave launcher.

contraction phenomena often seen in microwave plasmas at atmospheric pressure [20]. High purity argon was used, and its mass flow rate, directed downward, was maintained at 500 SCCM (cubic centimeters per minute at standard temperature and pressure) using a mass flow controller. In such experimental conditions, the resulting plasma column was sustained symmetrically both above and below the wave launcher [21] and visually stable over short and long periods of time. Furthermore, a circulator placed between the microwave power supply and the surfaguide directed unwanted reflections to a water-cooled load. A movable plunger was also used to transfer the maximal power to the plasma, and a bidirectional coupler paired to a bolometer was used to measure the incident and reflected powers.

2.2.2.2. *Optical emission spectroscopy*

Optical emission spectroscopy measurements were performed in part using a 320 mm focal length spectrometer (Princeton Instruments IsoPlane SCT-320) equipped with a 600 lines/mm grating and an intensified charged coupled device (ICCD) camera (Princeton Instruments PI-MAX4 1024x256). This system provided a spectral resolution (full width at half maximum) of ~0.26 nm across the whole wavelength range investigated in this study (690-930 nm), allowing to distinguish most of the closely separated Ar 2p-to-1s emission lines. The only exception was at ~772.4 nm where the two emission lines were measured as a single peak and, for this reason, these were excluded from the analysis with the CR model. Each spectrum recorded between 690 and 930 nm provided access to 20 of the 26 remaining

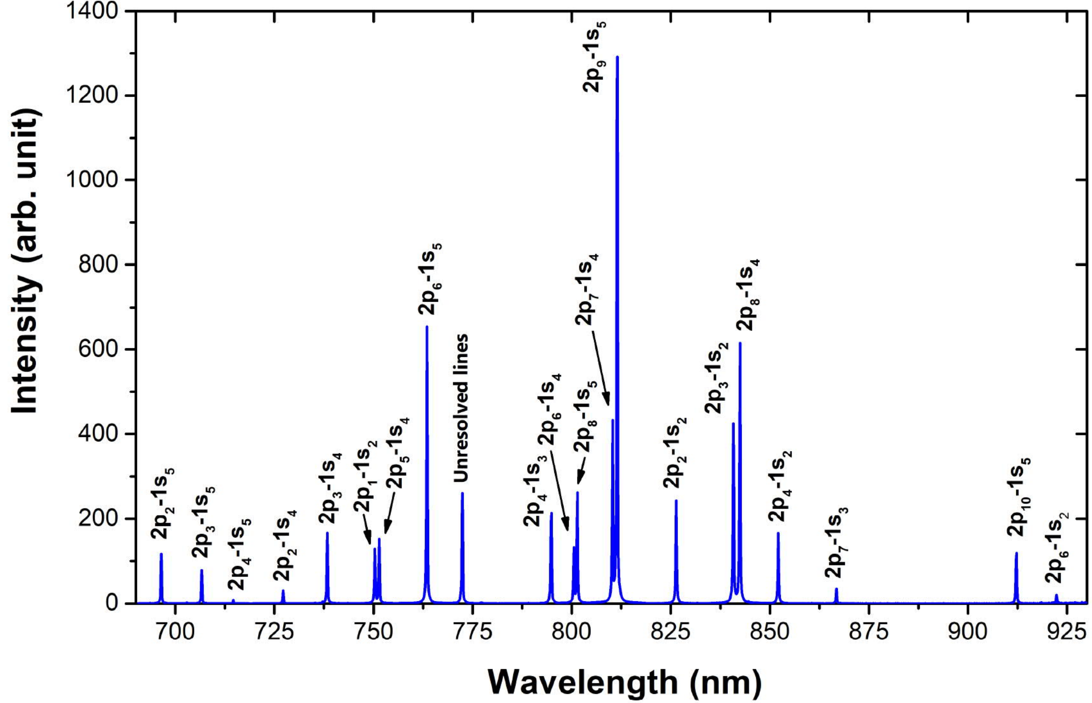

Figure 2.2. Typical optical emission spectrum of the microwave argon plasma at atmospheric pressure.

Ar 2p-to-1s emission lines. Lines outside of this spectral range were too weak to be worth considering in the present analysis. A pinhole (0.5mm wide $\times$ 15mm long) placed in front of the optical fiber allowed spatially resolved measurements. For the plasma-to-optical fiber distance used in this study, the axial resolution was estimated to 0.8mm. A typical broad spectrum of the microwave argon plasma column for the conditions described in Sec 2.2.2 is presented in Figure 2.2. As for every broad spectrum used in the forthcoming analysis, it is the average of 100 measurements and has been corrected for optical response of the apparatus and optical fiber (previously calculated using the known spectrum of a broadband calibration lamp) after background removal.

Additionally, line broadening measurements were recorded using a high-resolution spectrometer (HORIBA Jobin Yvon THR1000) equipped with a 1800 lines/mm holographic grating and a photomultiplier tube (Hamamatsu R636–10). This system provided a spectral resolution (full width at half maximum) of 21.5 pm for the Ar 2p-to-1s emission lines at 826 nm and 841 nm. This value was obtained from the broadening of the same lines emitted by a low-pressure, low-temperature plasma source for which any physical broadening mechanism was negligible compared to the experimental one. These two lines were specifically chosen

because, in nonthermal plasmas at atmospheric pressure, they are strongly affected by resonance broadening. Therefore, the Lorentzian part of their total line broadening becomes completely dominated by mechanisms linked to the neutral gas temperature (resonance and van der Waals broadening). Indeed, as usual, natural broadening can be neglected, and even with electron densities in the 10^{20}–10^{21} m^{-3} range (see, for example, Refs. 19, 22, and 23), Stark broadening can also be neglected with respect to the two aforementioned mechanisms. For these reasons, the equation for the total Lorentzian full width at half-maximum (FWHM), in frequency units and for a given Ar 2p$_i$-to-1s$_j$ transition, is reduced to [24]

$$\Delta\nu_{Lor_{ij}} = \Delta\nu_{Res_{ij}} + \Delta\nu_{VdW_{ij}}$$

$$= \frac{1.04}{16\pi\varepsilon_0}\frac{e^2}{m_e}\sqrt{\frac{g_g}{g_j}}\frac{f_{gj}}{\nu_{0_{jg}}}\frac{P}{k_B T_g} + \left(\frac{e^2}{2\varepsilon_0 h}\alpha\left|\left\langle\overline{R}_i^2\right\rangle - \left\langle\overline{R}_j^2\right\rangle\right|a_0^2\right)^{2/5}\left(\frac{16}{\pi M_{Ar}}\right)^{3/10}\frac{P}{(k_B T_g)^{7/10}} \quad (1)$$

where ε_0 is the vacuum permittivity, e is the elementary charge, m_e is the electron mass, g_g and g_j are the statistical weights of the ground and 1s$_j$ states, f_{gj} and $\nu_{0_{jg}}$ are the oscillator strength and central frequency of the resonant transition, P is the operating pressure, k_B is the Boltzmann constant, h is the Planck constant, α is the polarizability of the emitting atom, $\left\langle\overline{R}_i^2\right\rangle$ and $\left\langle\overline{R}_j^2\right\rangle$ are the mean square radius of the atom in its 2p$_i$ and 1s$_j$ excited states, a_0 is the Bohr radius, and M_{Ar} is the argon mass.

As such, for every emission line broadening measurement recorded in this study, the Lorentzian component of the broadening was deconvoluted from the Gaussian one by least-squares fitting of a Voigt function. A minimal Gaussian width, dictated by the instrumental broadening at both the emission lines central frequency, was always imposed. Typical measurements along with their Voigt fits are presented in Figure 2.3. The approach developed and used in this study is further validated by the fact that for most measurements, the individual neutral gas temperature values that were found from both lines agree to within a few kelvins. Consequently, any T_g value reported in this article (and used as an input parameter in the CR model, see details below) is the mean of the temperatures found from both lines, and the error is defined as the standard deviation.

2.2.2.3. *Optical absorption spectroscopy*

The population of argon 1s$_5$ atoms was analyzed by OAS measurements using a tunable laser diode (Sacher Lasertechnik Pilot PZ 500) in a Littman/Metcalf configuration (laser

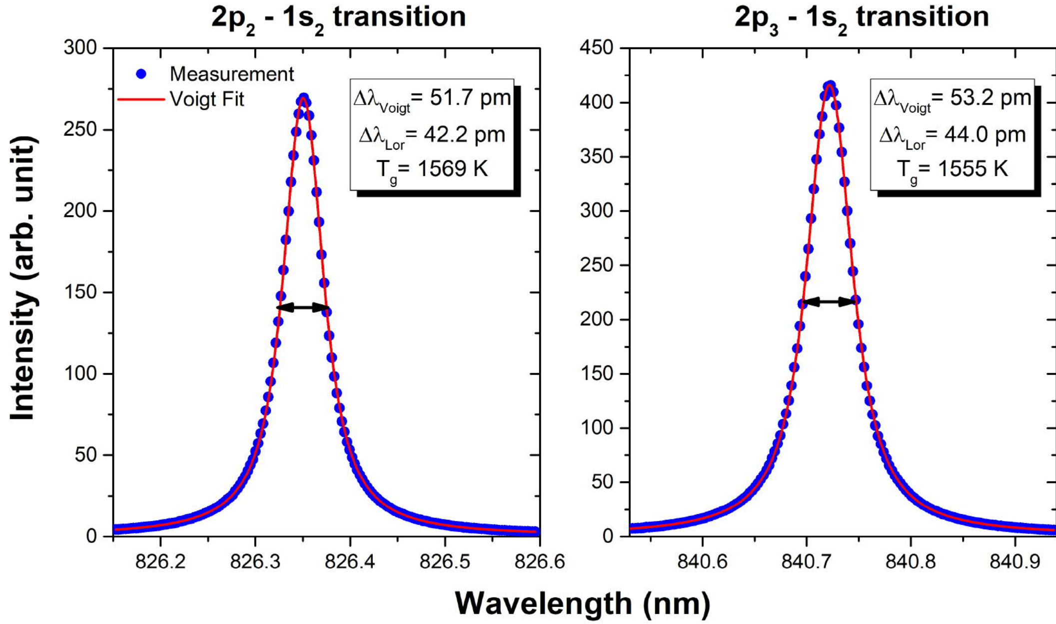

Figure 2.3. Typical fit of the two argon emission lines used for the determination of T_g.

linewidth <100 kHz). For all experiments, the laser power was low enough to prevent any significant alteration of the plasma properties, for example, through photonionization and photoexcitation. A triangular signal on a piezoelectric actuator enabled a periodical frequency sweep of the laser centred on the Ar $2p_9$-$1s_5$ transition. The built-in current-coupling feature enabled a large and continuous (mode hop free) tuning range (>30 GHz). The sweeping process was monitored using a WS-6 wavelength meter (WLM) from HighFinesse GmbH. As shown in Figure 2.4, two photodiode detectors connected to a Teledyne-Lecroy HDO6104 oscilloscope were used to record both the reference (unabsorbed) laser intensity I_0 and the absorbed laser intensity I_t as a function of time. Longpass filters were placed right before the detectors to reduce as much as possible the detection of any unwanted light but a background measurement (laser off, plasma on) was always taken and subtracted nonetheless. For every position investigated along microwave plasma column, the laser path was always carefully realigned with regard to the tube axis using the alignment camera. Also shown in Figure 2.4 are the positions of the optical fiber sending light to the low-resolution and high-resolution spectrometers. They were placed perpendicularly to the laser beam path in order to only collect the light emitted by the plasma and not any laser light scattered by the tube.

A typical OAS measurement (averaged over 50 scans) and the resulting absorption spectrum are presented in Figure 2.5 a) and b) respectively. Since the optical transition was

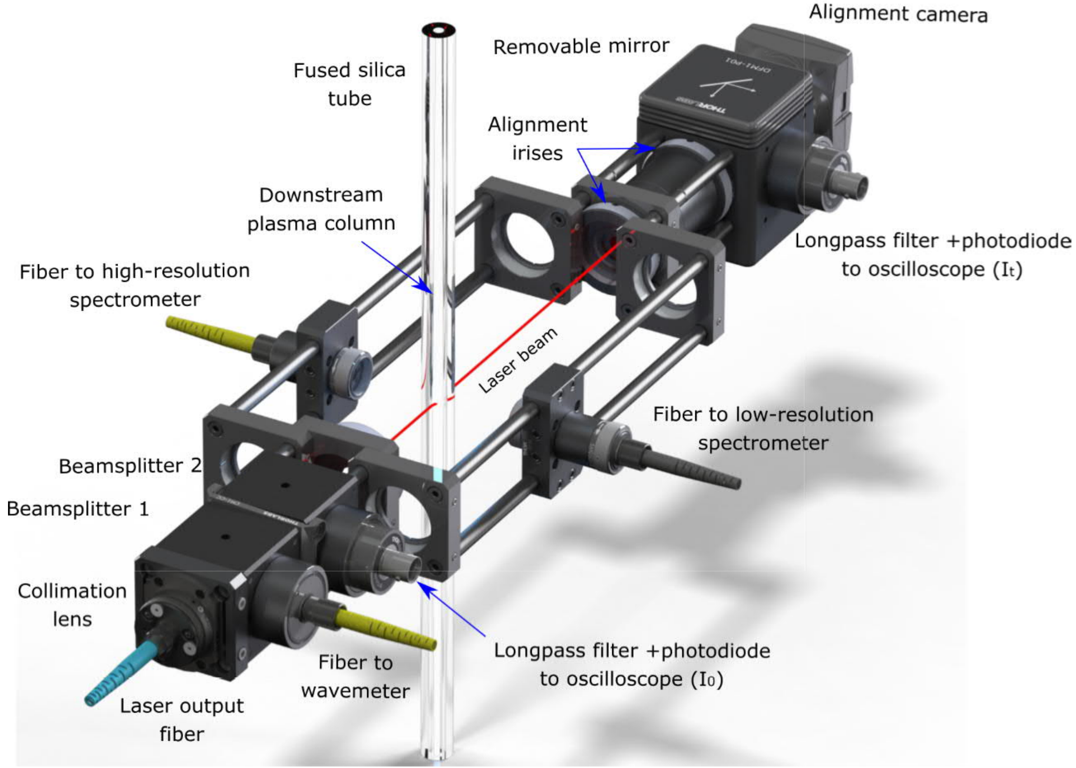

Figure 2.4. Experimental setup for the OAS and OES measurements.

periodically swept with the laser frequency first decreasing and then increasing, two absorption spectra were obtained for each measurement. Thus, similarly to the high-resolution OES procedure, the n_{1s_5} values reported later in this work are the average of these two spectra and the error is defined as the standard deviation. In order to get optimal results, a Voigt function was again least squares fitted to each of the absorption spectrum, and the total absorption coefficient was calculated using the following formula [25]:

$$\mathcal{A}(\nu) = \ln\left(\frac{I_0(\nu)}{I_t(\nu)}\right) \tag{2}$$

Since OAS measurements did not reach unabsorbed frequencies on either side of the transition (see example in Figure 2.5 b)), this procedure allowed a better description of the wings of the Voigt profile. The argon $1s_5$ level number density could then be calculated using:

$$n_{1s_5} = \frac{8\pi}{A_{2p_9-1s_5}} \frac{g_{1s_5}}{g_{2p_9}} \frac{\nu_0^2}{c^2} \frac{1}{\ell} \int_{-\infty}^{\infty} \mathcal{A}(\nu)\, d\nu \tag{3}$$

where $A_{2p_9-1s_5}$ is the spontaneous emission Einstein coefficient of the argon $2p_9$-$1s_5$ transition, c is the speed of light and ℓ is the length of the plasma along the line of sight. This last

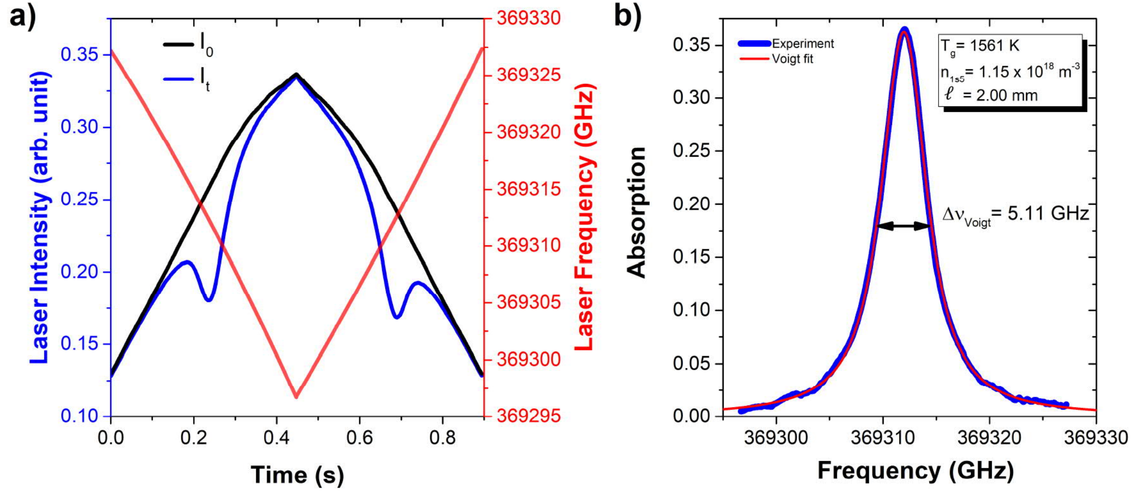

Figure 2.5. a) Typical measured I_0 and I_t signals as well as the corresponding laser frequency. b) Resulting absorption spectrum with the corresponding Voigt profile.

parameter was taken as the inner diameter of the tube (2 mm), since, as it was already mentioned, the plasma filled the whole discharge tube (no filamentation and no contraction).

2.2.3. Collisional radiative model

Inspired by the OES studies of Malyshev and Donnelly [26] performed in low-pressure plasmas, one of the objectives of this work is to compare the measured OES line intensities from argon 2p-to-1s transitions to those predicted by a CR model of argon 2p states in order to extract the electron temperature (assuming Maxwell-Boltzmann electron energy probability function) from the best fit using a set of input parameters (see details below). In this framework, the model relies on the well-known equation for the line emission intensity (I_λ):

$$I_\lambda = A_{ij}\, n_i\, \theta_{ij} \tag{4}$$

where A_{ij} is the Einstein coefficient of the argon 2p$_i$-to-1s$_j$ transition, n_i is the number density of the emitting level i, and θ_{ij} is the escape factor of the 2p$_i$-to-1s$_j$ transition. In optically thin plasmas, $\theta_{ij} = 1$ for all transitions. However, in optically thick media, both n_i and θ_{ij} must be calculated from the CR model. In this context, the approach relies on calculating line emission intensities, and thus n_i and θ_{ij} values for all argon 2p$_i$-to-1s$_j$ transitions, over a wide range of T_e values, and then comparing these intensities with those

measured experimentally. The value of T_e that provides the best fit of the experimental data can therefore be assumed to represent the actual electron temperature in the plasma. Since OES measurements are averaged over the line of sight, the values of T_e obtained from this method are thus also averaged over the tube diameter.

2.2.3.1. *General considerations*

The CR model developed and used in this study is zero dimensional, assumes steady-state, and uses as input parameters the operating pressure, the neutral gas temperature, the number density of argon $1s_5$ atoms, and the plasma length along the line of sight. Since the argon 2p-to-1s transitions are generally the most intense emission lines observed in nominally pure argon plasmas, the main objective of the model is therefore to solve, for each value of T_e, the particle balance equations of the ten 2p levels of argon. T_e being the only adjustable parameter in the CR model, the other three number densities of argon 1s states can be calculated relatively to n_{1s_5} by assuming that either they are distributed according to the Boltzmann distribution or all strictly equals (treated as a block); this choice depends on the very specific experimental conditions. Moreover, as shown in Sec. 2.2.3, relative line emission intensities of argon 2p-to-1s transitions are mostly independent of the electron number density since this parameter only influences Stark broadening (if significant) of simulated emission lines (see details below).

Regarding the population of argon 1s atoms involved in a number of excitation processes of argon 2p states, including stepwise electron-impact excitation and radiation trapping (see details below), two approaches can be used. Inspired by previous studies in low pressure plasmas [28], the first one relies on a detailed resolution of the particle balance equations of all argon 1s states [23,27,28]. However, in nonthermal plasmas at atmospheric pressure, it is generally well established that many reactions involving argon 1s states are poorly described in the scientific literature. For example, the dissociative recombination (DR) of the molecular ion Ar_2^+ mainly results in the creation of argon 1s levels [29]. However, precise knowledge of the creation and destruction mechanisms of this dimer ion remains to be studied such that an accurate determination of the population of dimer ions prior to the calculation of the population of argon 1s levels likely leads to significant uncertainties in the CR model. Also, argon 1s levels lie between 11.55 eV and 11.83 eV above ground state argon atoms. These

Table 2.1. Excitation and de-excitation mechanisms considered in the CR model for the particle balance equation of the argon $2p_i$ level.

	Mechanism	Equation	Reference
Excitation	1- $Ar + e^- \rightarrow Ar_{2p_i} + e^-$	$k_{g-2p_i}\ n_g\ n_e$	[32]
	2- $Ar_{1s_j} + e^- \rightarrow Ar_{2p_i} + e^-$	$k_{1s_j-2p_i}\ n_{1s_j}\ n_e$	[33]
	3- $Ar_{1s_j} + h\nu \rightarrow Ar_{2p_i}$	$A_{ij}\ n_i\ (1 - \theta_{ij})$	[34]
	4- $Ar + Ar_{2p_k} \rightarrow Ar + Ar_{2p_i}$	$k_{2p_k-2p_i}\ n_g\ n_{2p_k}$	[35]
De-excitation	5- $Ar_{2p_i} \rightarrow Ar_{1s_j} + h\nu$	$A_{ij}\ n_i$	[34]
	6- $Ar + Ar_{2p_i} \rightarrow Ar + Ar_{2p_k}$	$k_{2p_i-2p_k}\ n_g\ n_{2p_i}$	[35]
	7- $Ar + Ar_{2p_i} \rightarrow Ar + Ar_{1s_j}$	$k_{2p_i-1s_j}\ n_g\ n_{2p_i}$	[36]

excited species can thus readily be quenched by almost any species either involuntary present in the argon plasma as a result of impurities in the gas bottle or the open-to-air configuration (for example, nitrogen, oxygen, carbon dioxide, water vapors) or voluntary injected in the gas mixture for technological applications (for example, organosilicon species for materials synthesis) [30,31]. In this context, even if some of the corresponding quenching reaction rates are documented in the scientific literature, the number densities of these quenching species are extremely difficult to assess. In such conditions, the predictions of CR models for argon 1s states become questionable. To circumvent this limitation, the particle balance equations of argon 1s states were not systematically resolved; values obtained from the OAS measurements described above were used as input parameters in the CR model.

2.2.3.2. *Excitation and de-excitation mechanisms*

Table 1 contains a list of all the considered excitation and de-excitation mechanisms along with their equations. Sections 2.2.3.2 describe these reactions in more details and define the relevant variables accordingly. A schematic of all the considered reactions is also presented in Figure 2.6.

2.2.3.2.1. Mechanisms involving electrons

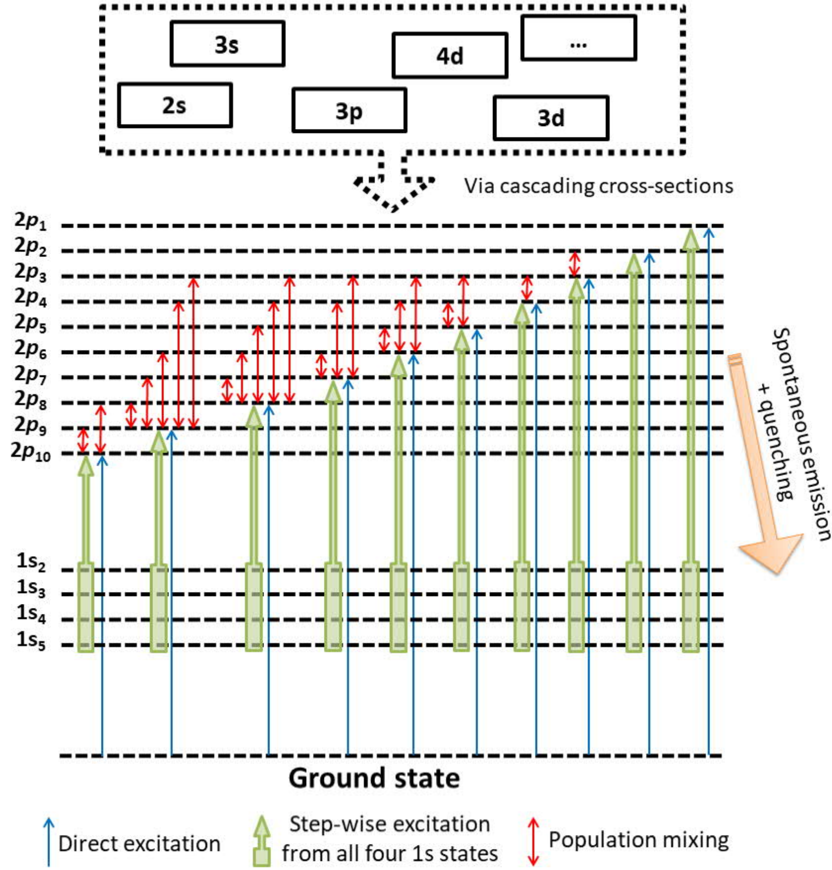

Figure 2.6. Schematic of the reactions considered in the CR model of argon 2p states.

Mechanisms 1 and 2 are excitation mechanisms involving electrons colliding with argon neutral atoms respectively in the ground state (direct excitation) and 1s states (stepwise excitation). The ground state number density (n_g) is calculated by the ideal gas law since the pressure and the neutral gas temperature are given as input parameters in the CR model. As for the reaction rates, they are calculated from the corresponding cross sections σ(E) according to:

$$k_{g,1s\rightarrow 2p}(T_e) = \sqrt{\frac{2}{m_e}} \frac{\int_0^\infty \sigma\left(E\right)\ f\left(E,T_e\right)\ E\ dE}{\int_0^\infty f\left(E,T_e\right)\ E^{1/2}\ dE} \tag{5}$$

where *f(E,* T_e*)* is assumed to be the Maxwell-Boltzmann electron energy probability function. Since these reaction rates are calculated for every T_e value, this is where the electron temperature dependence comes from. As represented with the dotted box in Figure 2.6, the cross sections used are always apparent (cascading) cross sections [37]; this method therefore

implicitly considers cascading effects from higher energy levels without solving the particle balance equation for each of these levels. For direct electron impact excitation, the cross sections are also multiplied by a high-pressure correction formula [38], which takes into account radiation trapping from above-2p levels that have radiative transitions to the ground state. Indeed, because of the high ground state number density at atmospheric pressure, radiation trapping forces those above-2p levels to radiate to other levels than the ground state, among which are the 2p. This explains why this particular set of cross sections was preferred instead of the more recent ones since, to our knowledge, it is the only one available with this correction. For the 1s$_j$-2p$_i$ cross sections (stepwise electron-impact excitation), a high-pressure correction is not needed since, according to Donnelly [37], levels higher than the argon 2p levels are weakly populated by the 1s levels.

2.2.3.2.2. Mechanisms involving photons

Mechanisms 3 and 5 are, respectively, radiation trapping and spontaneous photon emission. As discussed above, radiation trapping can be significant over the range of experimental conditions investigated since the populations of both the ground state and 1s levels can become significant to achieve optically thick plasma conditions, at least for some transitions. The consequence is a reduction (partial or total) of the importance of spontaneous emission in the particle balance equations of argon 2p states. In addition, it can also reduce the theoretical line emission intensities due to the corresponding decrease of θ_{ij} in Equation (3).

According to the literature, there are quite a few ways to calculate the escape factor (fraction of emitted photons that are not reabsorbed in the plasma) of a given transition, with Mewe's version being arguably the most widespread one [39]. However, since it is an empirical equation intended for lines that as mostly affected by Doppler broadening, a different version is developed here for any kind of broadening. Starting with the definition of θ_{ij} and using the Beer-Lambert law, one finds:

$$\theta_{ij} = \frac{I_T}{I_0} = \frac{\int_{-\infty}^{\infty} I_{\nu_T} d\nu}{\int_{-\infty}^{\infty} I_{\nu_0} d\nu} = \frac{\int_{-\infty}^{\infty} I_{\nu_0} \exp\left(-k(\nu)\ell\right) d\nu}{\int_{-\infty}^{\infty} I_{\nu_0} d\nu} \tag{6}$$

where $k(\nu)$ is the absorption coefficient at frequency ν. Without loss of generality, the initial intensity can be normalized such that the bottom integral is equal to unity. Moreover, since

OES measurements are averaged over the line of sight, Equation (5) can be refined as:

$$\overline{\theta}_{ij} = \frac{1}{\ell}\int_0^{\ell}\int_{-\infty}^{\infty} I_{\nu_0}\exp\left(-k(\nu)\ell'\right)d\nu\ d\ell' = \int_{-\infty}^{\infty}\frac{I_{\nu_0}\left(1-\exp(-k(\nu)\ell)\right)}{k(\nu)\ell}\ d\nu \tag{7}$$

The right-hand side of Equation 7 is only valid in plasmas homogeneous along the line of sight (zero-dimensional model). Similar approximations were performed in other formulas for the escape factor, including Mewe's [39]. While more robust methods for the calculation of the escape factor can be found in the literature, they require at least a 1D model [40] and thus obviously come at a much higher computer resource price. Still, according to Boffard et al. [41], if both emitting and absorbing particles have a similar spatial distribution, any departure from a constant value for one can be somehow compensated by the other such that in the end the homogeneous plasma approximation remains valid. In this zero-dimensional CR model, Equation 7 was used to describe all the mechanisms involving photons.

In Equation 7, the plasma length along the line of sight ℓ directly corresponds to the tube dimension. As for $k(\nu)$, it must be calculated for every emission line with the corresponding broadening mechanisms (Doppler, van der Waals, resonant, Stark) being convoluted into a Voigt absorption profile [42,43]:

$$k_{ij}(\nu) = \frac{g_i}{g_j}\frac{A_{ij}n_j}{8\pi}\frac{c^2}{\nu_{0_{ij}}^2}\frac{2\ln(2)}{\pi^{3/2}}\frac{\Delta\nu_{Lor_{ij}}}{\Delta\nu_{Dop_{ij}}}\int_{-\infty}^{\infty}\frac{\exp\left(-y^2\right)}{\left(\frac{\sqrt{ln(2)}\Delta\nu_{Lor_{ij}}}{\Delta\nu_{Dop_{ij}}}\right)^2+\left(\frac{2\sqrt{ln(2)}\left(\nu-\nu_{0_{ij}}\right)}{\Delta\nu_{Dop_{ij}}}-y\right)^2}dy \tag{8}$$

In equation (7), n_j is the population of the absorbing level and $\Delta\nu_{Dop_{ij}}$ and $\Delta\nu_{Lor_{ij}}$ are the Doppler and Lorentzian full widths at half maximum. Since Doppler broadening is the only mechanism with a Gaussian profile, it can be included as is in Equation (7) and can be calculated according to [24]:

$$\Delta\nu_{Dop_{ij}} = \nu_{0_{ij}}\sqrt{\frac{8\ln(2)\quad R\ T_g}{M_{Ar}c^2}} \tag{9}$$

where R is the universal gas constant. As discussed in section 2.2.2, the case of the Lorentzian component is more complex due to the contributions of van der Waals, Stark and resonant broadening. Nonetheless, the total full width at half maximum is simply the sum of each

individual contribution:

$$\Delta\nu_{Lor_{ij}} = \Delta\nu_{Res_{ij}} + \Delta\nu_{VdW_{ij}} + \Delta\nu_{Stark_{ij}} \tag{10}$$

The respective full widths at half maximums are calculated according to Equation 1 and Ref 24:

$$\Delta\nu_{Stark_{ij}} = 2\left(1 + 1.75\alpha_G\left[1 - 0.75r_d\right]\right)w_G \tag{11}$$

where r_d is the Debye shielding parameter and $\alpha_G(T_e, n_e)$ and $w_G(T_e, n_e)$ are two parametric functions tabulated by Griem [44]. Equation (11) is the only equation where n_e has an influence on the relative emission intensities computed from the CR model. In non-thermal plasmas characterized by relatively small ionization degrees, Stark broadening is at most comparable to the other mechanisms such that its relative contribution to the whole model is very small.

2.2.3.2.3. Mechanisms involving argon atoms in the ground state

Mechanisms 4 and 6 are excitation transfer reactions or population mixing reactions between two argon 2p levels following the collision of an argon 2p state with an argon atom in the ground state. Indeed, when the population of ground state argon atoms becomes high enough (as in atmospheric-pressure plasmas), excitation transfer reactions play a significant role in the excitation as well as in the deexcitation kinetics of argon 2p states since both the initial and final states are among the 2p states. Due to these reactions, the number density of every 2p level is closely related to the density of the other 2p levels such that the particle balance equations of the argon 2p states are coupled and must absolutely be solved self-consistently. This is a major difference from the low-pressure plasma models in which each 2p level can generally be solved individually. The reaction rates ($k_{2p_i-2p_k}$) for excitation transfer reactions were mostly taken from Ref. 35. For those unavailable, detailed balancing was used [45]. Since all of these reaction rates were reported at 300 K, a $\sqrt{T_g/300}$ dependence was added to account for possible variations of the neutral gas temperature.

Finally, mechanism 7 is a quenching reaction of an argon 2p level by collision with a ground state argon atom resulting in a 1s level. The reaction rates ($k_{2p_i-1s_j}$) used in the CR model are summed over all 1s states for every 2p level. As for the excitation transfer reactions, a $\sqrt{T_g/300}$ dependence was added to account for possible neutral gas heating effects.

2.2.3.3. *Theoretical spectrum*

When considering all the reactions provided in Table 1 and highlighted in Figure 2.6, the population of argon 2p$_i$ level can be written as

$$n_{2p_i} = \frac{n_e \left(k_{g-2p_i} n_g + \sum_j k_{1s_j-2p_i} \; n_{1s_j} \right) + \sum_{k \neq i} k_{2p_k-2p_i} \; n_g \; n_{2p_k}}{\sum_j A_{ij}\theta_{ij} + k_{2p_i-1s_j} \; n_g + \sum_{k \neq i} k_{2p_i-2p_k} \; n_g \; n_{2p_k}} \qquad (12)$$

It is here noteworthy to realize that the electron number density appears in every term of the numerator. Indeed, its presence was emphasized in the first two terms, and since the excitation transfer terms contains n_{2p_k} ; it implicitly contains a direct n_e dependence. Therefore, this parameter mostly acts as a scaling factor for the absolute number density of the argon 2p levels and thus for the absolute line emission intensity. In the approach described below, relative emission intensities are computed from the CR model as a function of the electron temperature using Eqs. (4), (7), and (12). These relative emission intensities are then compared to the relative emission intensities obtained from the experiments. Since only relative emission intensities, and not absolute emission intensities, are compared, the method developed and used in this study to extract the electron temperature in microwave argon plasma columns at atmospheric pressure is thus independent of the electron number density.

2.2.3.4. *Experimental spectrum*

Building the most accurate CR model for argon 2p states is not the only challenge in finding T_e from an experimental spectrum of argon 2p-to-1s transitions since how the experimental spectrum itself is measured, analyzed, and then compared to the simulated ones is as crucial as the precision of the CR model itself. It is clear that the better the resolution of the measuring apparatus is, the more accurate the experimental spectrum will be. Still, in cases where emission line convolution occurs or if the experimental broadening is large, it is best to fit all the lines with at least a Gaussian profile in order to extract the exact peak intensity for each transition by calculating the area under the curve. Indeed, this will compensate for when the resolution is limited by the size of the detector's pixels or when the convolution is such that the wings of two or more lines contribute to the intensity of each

other. Moreover, the relative sensitivity of all the optical elements (optical fiber, grating, detector) over the range of wavelengths examined must absolutely be taken into account before any comparison between measured and theoretical spectra can be performed.

2.2.3.5. *Comparison of the spectra*

To compare the experimental and theoretical spectra, an approach based on Donnelly's work in low-pressure plasmas was used [26]. More precisely, the goodness of the fit was analyzed by calculating a weighed relative standard deviation (RSD). For a given T_e value and for every line that could be seen in the experimental spectra, a ratio (R_i) of the measured intensity over the theoretical one can be calculated. In this framework, the model thus only considers relative emission intensities instead of absolute emission intensities. A weight (w_i) is then associated with each ratio and calculated from the sum of relative experimental and theoretical uncertainties, with large uncertainties resulting in small weights:

$$RSD\,(T_e) = \frac{100}{\overline{R}_i}\sqrt{\frac{1}{N-1}\sum_{i=1}^{N}\left|R_i - \overline{R}_i\right|^2 w_i} \tag{13}$$

The experimental uncertainties come from how each line distinguishes itself from the background (signal to noise ratio) and how accurately the Gaussian fit reproduced the experimental broadening. The theoretical uncertainties come directly from the input parameters (P, T_g, ℓ, n_{1s_5}) or from those of the published cross sections and reaction rates. As mentioned above, the value of Te in the theoretical spectrum that best matches the experimental spectrum, thus resulting in the lowest RSD over all the scanned values, is assumed to represent the actual electron temperature in the microwave argon plasma column. We defined the uncertainty on T_e based on all the T_e values resulting in a RSD less than 5%higher than the optimal RSD.

2.2.4. Validation of the method

When developing a CR model of argon 2p states to be paired with OES measurements of argon 2p-to-1s transitions, it is crucial to be able to trust the results and therefore a rather detailed validation is of prime importance. The first way to attest the reliability of the method is by looking at what the RSD looks like when scanning over a wide range of T_e values. To do so, the experimental spectrum presented in Figure 2.2 (recorded at 2 cm

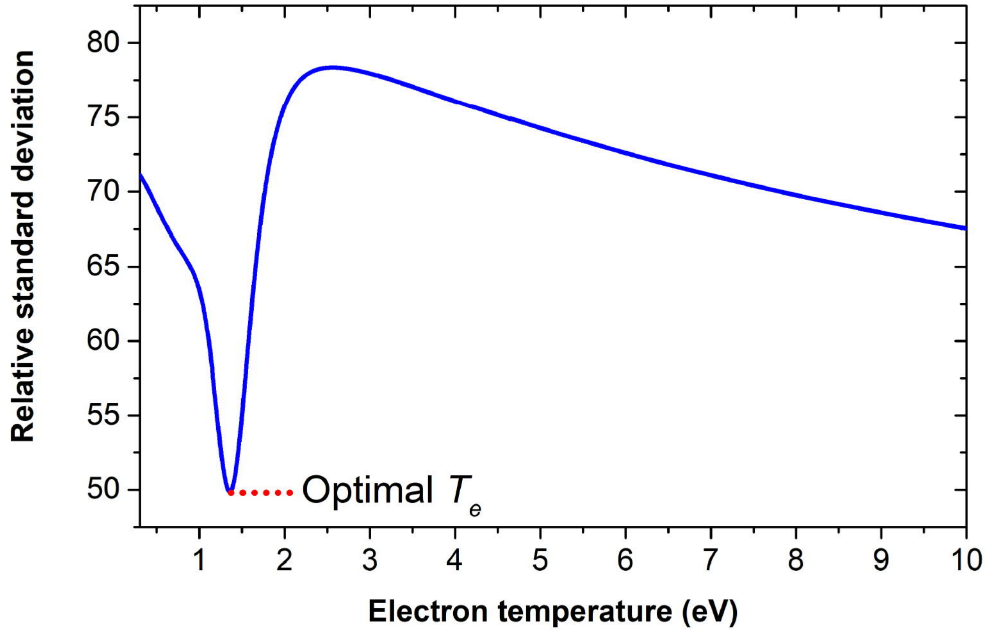

Figure 2.7. Relative standard deviation as a function of T_e.

below the surfaguide) was compared to the predictions of the CR using the following input parameters: P= 760 Torr, T_g= 1561 K, ℓ= 2 mm, n_{1s}=1.15 × 10^{18} m^{-3} (all levels treated as a block). The result is presented in Figure 2.7, where only one, sharply-defined minimum can be seen.

Another way to validate the approach is to look at how accurately the model is able to reproduce the experimental spectrum with the optimal T_e. This is shown in Figure 2.8 a), where one can see that the agreement for most of the analyzed emission lines is excellent, specifically considering the large and numerous uncertainties in the theoretical data and the amount of missing reaction rates for excitation transfer reactions by collisions with ground state argon atoms. Digging for more information provided by the model with the optimal T_e value also confirms the significant contribution of radiation trapping (optically thick plasma). This is illustrated in Figure 2.8 b) that presents the percentage of radiation trapping for each emission line. Even with an absorption length of 2mm, radiation trapping can go above 15%. Moreover, when completely removing radiation trapping effects from the CR model, no optimal T_e could be determined from the comparison between measured and simulated OES spectra (no minimum could be observed in the RSD plots).

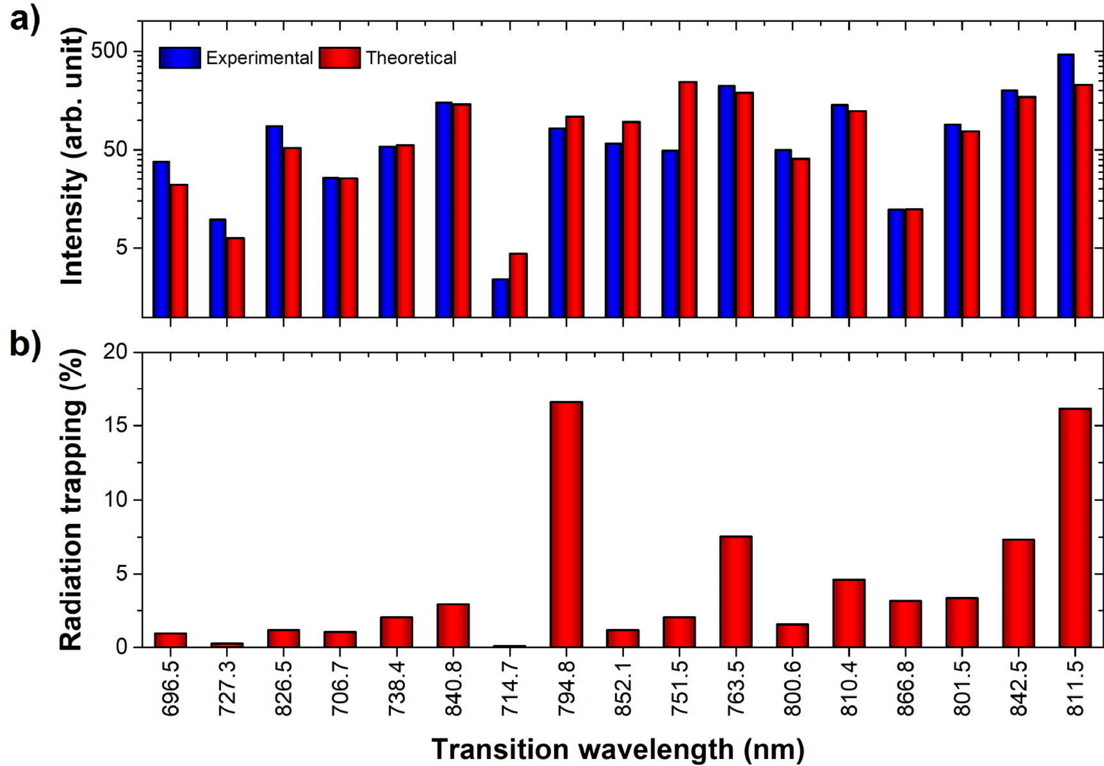

Figure 2.8. a) Comparison of the optimal theoretical spectra with the experimental one. b) Percentage of radiation trapping for the optimal electron temperature.

The contribution of each excitation and de-excitation mechanisms in the particle balance equation of argon 2p states in the same conditions as in Figures 2.2, 2.7 and 2.8 are plotted in Figure 2.9. For the optimal value of T_e determined in Figure 2.7, it can be seen in Figure 9a) that the excitation of every 2p level is dominated neither by direct nor stepwise electron impact excitation. In addition, excitation transfer reactions (mechanism 4) are responsible for more than 50% of the creation of some levels whereas the quenching by neutral atoms towards 1s levels (mechanism 7) is the dominant de-excitation mechanism. Similar results were reported by Li *et al.* for an RF discharge at atmospheric pressure using a simple line ratio method [46]. From such data, one readily concludes that the contribution of these excitation transfer and quenching reactions is quite significant in the modeling of nonthermal argon plasmas at atmospheric pressure such that erroneous results for T_e could easily be obtained when neglecting these reactions in the particle balance equations of argon 2p states.

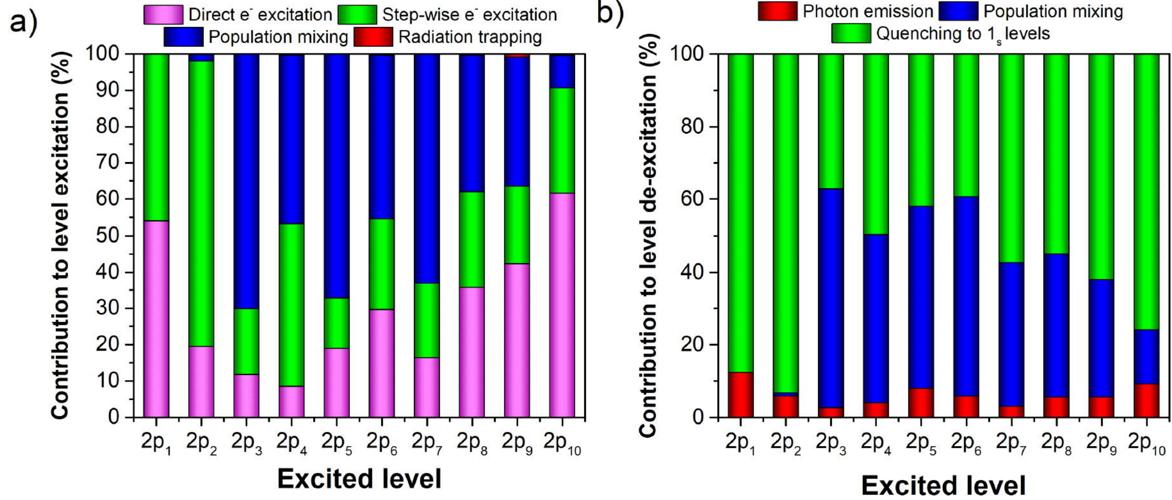

Figure 2.9. Contribution of the different mechanisms to the a) excitation and b) de-excitation of the argon 2p levels.

2.2.5. Axial profiles of T_g, n_{1s_5} and T_e along the microwave plasma column

With the validity of the method attested, OES and OAS measurements combined with the predictions of the CR model were used to examine the axial distribution of the neutral gas temperature (obtained from line broadening of OES measurements), the number density of argon $1s_5$ atoms (obtained from OAS measurements), and the electron temperature (obtained from the comparison between measured and simulated OES spectra) along the microwave argon plasma column. All these results are presented in Figure 2.10 and, for the purpose of understandings the trends, the electron densities calculated following the results reported by Christova *et al.* [19] in comparable conditions are also presented. It can be seen that the n_{1s_5} values are of the order of 1-2 $\times$ 10^{18} m^{-3} and are more or less constant along the column axis. The same behaviour is obtained for T_e, with values in the range of 1.4 eV. As for T_g, the values decrease from 1600 K to 1300 K when n_e decreases somewhat linearly from 8 to $2.5\times$ 10^{20} m^{-3} when moving away from the surfaguide wave launcher [19,23,47,48].

Although the electron temperature in surface-wave plasmas in the microwave regime has been the subject of quite a few research works, with many different diagnostic techniques resulting in different results, the values and trend reported in Figure 2.10 are nonetheless consistent with those reported in previous experimental and modeling studies. For example, the models proposed by Kabouzi et al. [16] and Castaños-Martínez and Moisan [23] have predicted an electron temperature slightly increasing from ~0.8 eV close to the wave launcher

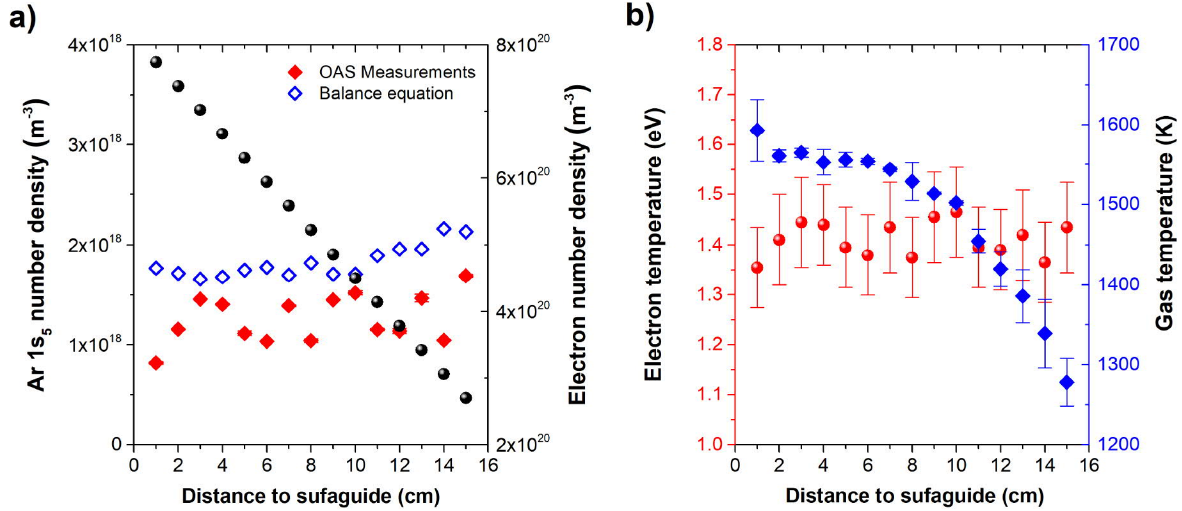

Figure 2.10. a) Ar 1s$_5$ and electron number density axial profiles and b) T$_e$ and T$_g$ axial profiles.

to ~0.9 eV near the end of the plasma column for a microwave frequency of 915 MHz. Part of this small difference can be linked to the omission of excitation transfer and quenching reactions which, as demonstrated above, play a very significant role in the population and depopulation kinetics of argon excited states. Over the range of experimental conditions investigated, the influence of these reactions in the CR model was mostly to increase T_e values, as seen from the comparison between the results presented in Figure 2.10 and the modeling studies of Kabouzi *et al.* [16] and Castaños-Martínez and Moisan [23]. Hubner *et al.* [49] and Palomares *et al.* [50] have also examined the electron temperature in microwave plasma columns using Thomson scattering measurements. The authors have reported an increase in T_e from 1.2 eV to 1.4–1.6 eV but for an intermediate pressure of 20 mbar. Carbone *et al.* [51] have also found, using the same technique, an on-axis T_e value of 1.2 eV at 88 mbar but have more importantly reported an increase up to 2.2 eV when moving barely 2 mm radially off axis. Since the approach developed and used in this study only provides values averaged over the line-of-sight, the data presented in Figure 2.10 are somewhere in the middle of what has been reported in the literature.

Some authors have suggested that the axial trend of T_e along the microwave argon plasma column is linked to the behavior of the argon dimer [23,52]. Indeed, this molecule ion has been shown to be an important channel not only for electron losses by dissociative recombination

(DR) reactions but also in the radial contraction of surface-wave plasmas [20]. As such, the more DR reactions there are at a given position, the hotter the electrons need to be at this position to sustain the plasma. However, over the range of experimental conditions examined, the plasma fills radially the whole discharge tube from the beginning to the end (no radial contraction), suggesting that the electrons are mainly lost by diffusion and recombination on the reactor walls (DR reactions thus only play a negligible role). In such conditions, the electron temperature becomes linked to the diffusion length. This latter value being constant along the whole microwave plasma column, constant T_e values would be expected, as seen in Figure 2.10.

Regarding the behaviour of the population of argon 1s atoms, a slight increase towards the end of the plasma column is generally reported in the literature. This feature was observed, for example, by Lao *et al.* [53] and by Hubner *et al.* [54] at reduced pressures and by Santiago and Calzada [55] at atmospheric pressure for a microwave frequency of 2.45 GHz. It was also observed through zero-dimensional modeling by Castaños-Martínez and Moisan [23] at atmospheric pressure for a microwave frequency of 915 MHz. However, the rise in n_{1s} is generally lower than a factor of two between the wave launcher and the column end; this very small variation is somehow close to the rather constant behaviour reported in Figure 2.10. Moreover, the number densities in the $\sim 10^{18}$ m^{-3} range are consistent with those reported in other studies (between 10^{17} m^{-3} and 10^{19} m^{-3} depending on the experimental conditions).

It was also suggested by Castaños-Martínez and Moisan [23] that the behaviour of the population of argon 1s atoms along the microwave plasma column could be, just like T_e, closely linked to that of the argon dimer ions since DR reactions produce argon 1s levels [29]. However, a quick calculation of Equations 11 and 15 found in Ref 52 and applied to the conditions displayed in Figure 2.10 reveals that this channel produces three orders of magnitude less 1s levels than electron impact collisions on ground state argon atoms. Furthermore, a simple balance equation for these levels considering only electron impact excitation on ground-state argon atoms as the population mechanism and stepwise excitation of the argon 2p levels as the de-population mechanism (the contributing of stepwise ionization has been

calculated to be at least 10^3 times less important) yields

$$n_{1s} = \frac{k_{g-1s}(T_e)\ n_g(T_g)\ n_e}{k_{1s-2p}\,(T_e)\ n_e} \tag{14}$$

As shown with the blue dots in Figure 2.10 a), this simple balance equation for argon 1s state results in an Ar 1s number density having the same profile and order of magnitude than the one obtained by OAS measurements. Thus, it evidences that this mechanism and not DR reactions are the main source of 1s levels production over the range of experimental conditions investigated. The trend along the microwave plasma column can therefore be explained as follows: while n_e decreases along the axis, its presence is in both the excitation and de-excitation term, thus effectively vanishing from the equation. Combined to the fact that T_e remains fairly constant and n_g only slightly increases due to the corresponding decrease of T_g, no significant variations of n_{1s} are expected between the wave launcher and the end of the plasma column, as seen in the experiments presented in Figure 2.10.

As for the neutral gas temperatures, the values reported in Figure 2.10 are also consistent with previous modeling and experimental studies published in the literature. Indeed, many authors have reported a decrease of the neutral gas temperature when moving towards the end of the plasma column. This decreasing trend is generally ascribed to a decrease in neutral gas heating through electron-neutral collisions due to the corresponding decrease of n_e along the microwave plasma column (see Figure 2.10). In some studies, T_g was assumed to be equal to the rotational temperature determined from either N_2^+ or OH emission bands and this resulted in neutral gas temperatures ranging from 1500 K to 3000 K depending on the experimental conditions and the thermometric species [19,23,55]. In some other cases, line broadening measurements similar to the ones used in this study but with other argon 2p-to-1s transitions yielded values ranging from 1600 K to 1000 K [19,56]. However, it was shown by Juana Martínez *et al.* that the gas mass flow rate is a key factor influencing the axial profile of T_g [21], and that one has to be careful when comparing values to what has been reported by other authors. Indeed, in conditions similar to the ones used in Figure 2.10 and for a position close to the wave-launcher, the authors reported a drop in T_g from ~1700 K when using a gas mass flow rate of 0.25 SLM to ~900 K using 10 SLM. Nonetheless, the values of T_g displayed in Figure 2.10 are comparable to the one reported by Juana Martínez *et al.* [21] when using comparable mass flow rates.

2.2.6. Conclusion

A method to obtain the electron temperature from OES and OAS measurements of argon 2p-1s transitions combined with the predictions of a collisional-radiative model for argon 2p states has been presented and validated. Each of the considered reaction in the model has been described, as well as how the theoretical spectra are compared to experimental ones. The axial profiles of the electron temperature as well as the neutral gas temperature found from line broadening measurements and Ar $1s_5$ number density found from OAS measurements were then studied along the axis of a microwave plasma column at atmospheric pressure. For the very small tube radius examined in this study, a rather constant T_e value (~1.4 eV) was observed. On the other hand, a significant decrease of the neutral gas temperature (1600 K to 1300 K) was observed and linked to a drop in the gas heating by electron-neutral collisions due to the corresponding decrease of n_e. This in turn explains the rather constant axial profile for the argon 1s population (1-2 $\times$ 10^{18} m^{-3}) since its creation mechanism appears dominated by electron impact on ground state argon atoms and its loss mechanism appears to be driven by stepwise electron-impact excitation of the argon 2p levels. All trends and values were found to be consistent with other experimental and modeling studies reported in the literature. Further research exploiting the potential of the presented method is under way, among which is the study of the influence of contaminants on the neutral gas temperature, the argon 1s number density, the electron temperature, and the electron number density.

Acknowledgments

The equipment used in this work was acquired through the Leaders Opportunity Fund of the Canadian Foundation for Innovation (CFI). Financial support from the National Science and Engineering Research Council (NSERC) of Canada is also acknowledged.

References

[1] C. De Bie, J. Van Dijk, and A. Bogaerts, J. Phys. Chem. C 119, 22331 (2015).

[2] C. M. Mitsingas, R. Rajasegar, S. Hammack, H. Do, and T. Lee, IEEE Trans. Plasma Sci. 44, 651 (2016).

[3] Y. Kabouzi, M. Moisan, J. C. Rostaing, C. Trassy, D. Guérin, D. Kéroack, and Z. Zakrzewski, J. Appl. Phys. 93, 9483 (2003).

[4] F. Massines, C. Sarra-Bournet, F. Fanelli, N. Naudé, and N. Gherardi, Plasma Processes Polym. 9, 1041 (2012).

[5] O. Levasseur, L. Stafford, N. Gherardi, N. Naudé, V. Blanchard, P. Blanchet, B. Riedl, and A. Sarkissian, Plasma Processes Polym. 9, 1168 (2012).

[6] O. Levasseur, L. Stafford, N. Gherardi, N. Naudé, E. Beche, J. Esvan, P. Blanchet, B. Riedl, and A. Sarkissian, Surf. Coat. Technol. 234, 42 (2013).

[7] O. Levasseur, M. Vlad, J. Profili, N. Gherardi, A. Sarkissian, and L. Stafford, Wood Sci. Technol. 51, 1339 (2017).

[8] G. Wei, C. Ren, M. Qian, and Q. Nie, IEEE Trans. Plasma Sci. 39, 1842 (2011).

[9] R. Bazinette, R. Subileau, J. Paillol, and F. Massines, Plasma Sources Sci. Technol. 23, 035008 (2014).

[10] A. F. H. van Gessel, E. A. D. Carbone, P. J. Bruggeman, and J. J. A. M. van der Mullen, Plasma Sources Sci. Technol. 21, 15003 (2012).

[11] A. F. H. van Gessel, B. Hrycak, M. Jasinski, J. Mizeraczyk, J. J. A. M. van der Mullen, and P. J. Bruggeman, J. Phys. D: Appl. Phys. 46, 095201 (2013).

[12] T. Verreycken, R. Mensink, R. Van Der Horst, N. Sadeghi, and P. J. Bruggeman, Plasma Sources Sci. Technol. 22, 55014 (2013).

[13] Z. Abd-Allah, D. A. G. Sawtell, K. McKay, G. T. West, P. J. Kelly, and J. W. Bradley, J. Phys. D: Appl. Phys. 48, 085202 (2015).

[14] J. Benedikt, D. Ellerweg, S. Schneider, K. Rugner, R. Reuter, H. Kersten, and T. Benter, J. Phys. D: Appl. Phys. 46, 464017 (2013).

[15] X.-M. Zhu and Y.-K. Pu, J. Phys. D: Appl. Phys. 40, 2533 (2007).

[16] Y. Kabouzi, D. B. Graves, E. Castanos-Martınez, and M. Moisan, Phys. Rev. E 75, 16402 (2007).

[17] M. Dors, H. Nowakowska, M. Jasinski, and J. Mizeraczyk, Plasma Chem. Plasma Process. 34, 313 (2014).

[18] C. Yubero, M. C. Garcıa, M. Varo, and P. Martınez, Spectrochim. Acta, Part B 90, 61 (2013).

[19] M. Christova, E. Castanos-Martinez, M. D. Calzada, Y. Kabouzi, J. M. Luque, and M.

Moisan, Appl. Spectrosc. 58, 1032 (2004).
[20] E. Castanos-Martınez, M. Moisan, and Y. Kabouzi, J. Phys. D: Appl. Phys. 42, 12003 (2009).
[21] J. Martınez, E. Castanos-Martınez, C. Gonzalez-Gago, R. Rincon, M. D. Calzada, and J. Munoz, Plasma Sources Sci. Technol. 27, 077001 (2018).
[22] S. Y. Moon, W. Choe, H. S. Uhm, Y. S. Hwang, and J. J. Choi, Phys. Plasmas 9, 4045 (2002).
[23] E. Castanos-Martınez and M. Moisan, Spectrochim. Acta, Part B 65, 199 (2010).
[24] T. Belmonte, C. Noel, T. Gries, J. Martin, and G. Henrion, Plasma Sources Sci. Technol. 24, 064003 (2015).
[25] E. A. D. Carbone, S. Hubner, M. Jimenez-Diaz, J. M. Palomares, E. Iordanova, W. A. A. D. Graef, A. Gamero, and J. J. A. M. van der Mullen, J. Phys. D: Appl. Phys. 45, 475202 (2012).
[26] M. V. Malyshev and V. M. Donnelly, Phys. Rev. E 60, 6016 (1999).
[27] X.-M. Zhu and Y.-K. Pu, J. Phys. D: Appl. Phys. 43, 015204 (2009).
[28] W. Van Gaens and A. Bogaerts, J. Phys. D: Appl. Phys. 46, 275201 (2013).
[29] A. Sainz, J. Margot, M. C. Garcıa, and M. D. Calzada, J. Appl. Phys. 97, 113305 (2005).
[30] O. Levasseur, R. K. Gangwar, J. Profili, N. Naude, N. Gherardi, and L. Stafford, Plasma Processes Polym. 14, 1600172 (2017).
[31] V. Garofano, R. Berard, S. Boivin, C. Joblin, K. Makasheva, and L. Stafford, Plasma Sources Sci. Technol. 28, 055019 (2019).
[32] J. E. Chilton, J. B. Boffard, R. S. Schappe, and C. C. Lin, Phys. Rev. A 57, 267 (1998).
[33] R. K. Gangwar, L. Sharma, R. Srivastava, and A. D. Stauffer, J. Appl. Phys. 111, 053307 (2012).
[34] A. Kramida, Yu. Ralchenko, and J. Reader, and NIST ASD Team (2015) NIST Atomic Spectra Database (Version 5.3). National Institute of Standards and Technology, Gaithersburg, MD. http://physics.nist.gov/asd.
[35] T. D. Nguyen and N. Sadeghi, Phys. Rev. A 18, 1388 (1978).
[36] R. S. F. Chang and D. W. Setser, J. Chem. Phys. 69, 3885 (1978).
[37] V. M. Donnelly, J. Phys. D: Appl. Phys. 37, R217 (2004).

[38] M. J. Schabel, V. M. Donnelly, A. Kornblit, and W. W. Tai, J. Vac. Sci. Technol., A 20, 555 (2002).

[39] R. Mewe, Br. J. Appl. Phys. 18, 107 (1967).

[40] X.-M. Zhu, T. V. Tsankov, D. Luggenholscher, and U. Czarnetzki, J. Phys. D: Appl. Phys. 48, 085201 (2015).

[41] J. B. Boffard, R. O. Jung, C. C. Lin, A. E. Wendt, B. B. John, R. O. Jung, C. L. Chun, and A. E. Wendt, Plasma Sources Sci. Technol. 18, 035017 (2009).

[42] M. Moisan, D. Keroack, and L. Stafford, Physique Atomique et Spectroscopie Optique, 1st ed. (EDP Sciences, 2016).

[43] H. O. Di Rocco, D. I. Iriarte, and J. Pomarico, Appl. Spectrosc. 55, 822 (2001).

[44] H. R. Griem, Spectral Line Broadening by Plasmas (New York; London: Academic Press, 1974).

[45] M. A. Lieberman and A. J. Lichtenberg, Principles of Plasma Discharges and Materials Processing (Wiley, 2005).

[46] L. Li, A. Nikiforov, N. Britun, R. Snyders, and C. Leys, Spectrochim. Acta, Part B 107, 75 (2015).

[47] M. Moisan and H. Nowakowska, Plasma Sources Sci. Technol. 27, 073001 (2018).

[48] M. Moisan and J. Pelletier, Physique Des Plasmas Collisionnels (EDP Sciences, 2006).

[49] S. Hubner, E. Iordanova, J. M. Palomares, E. A. D. Carbone, and J. J. A. M. van der Mullen, Eur. Phys. J.: Appl. Phys. 58, 20802 (2012).

[50] J. M. Palomares, E. Iordanova, E. M. van Veldhuizen, L. Baede, A. Gamero, A. Sola, and J. J. A. M. van der Mullen, Spectrochim. Acta, Part B 65, 225 (2010).

[51] E. A. D. Carbone, S. Hubner, J. M. Palomares, and J. J. A. M. van der Mullen, J. Phys. D: Appl. Phys. 45, 345203 (2012).

[52] J. Jonkers, M. Van De Sande, A. Sola, A. Gamero, A. Rodero, and J. Van Der Mullen, Plasma Sources Sci. Technol. 12, 464 (2003).

[53] C. Lao, A. Gamero, A. Sola, T. Petrova, E. Benova, G. M. Petrov, and I. Zhelyazkov, J. Appl. Phys. 87, 7652 (2000).

[54] S. Hubner, N. Sadeghi, E. A. D. Carbone, and J. J. A. M. van der Mullen, J. Appl. Phys. 113, 143306 (2013).

[55] I. Santiago and M. D. Calzada, IEEE Trans. Plasma Sci. 37, 790 (2009).

[56] M. C. Garcıa, M. Varo, and P. Martınez, Plasma Chem. Plasma Process. 30, 241 (2010).
[57] C. Yubero, M. S. Dimitrijevi, M. C. Garcıa, and M. D. Calzada, Spectrochim. Acta, Part B 62, 169 (2007).

2.3. Article 2 : Étude résolue temporellement de la température des électrons et de la densité d'atomes d'argon excités dans les DBDs à base d'argon

Pour tester la robustesse de la méthode développée pour obtenir T_e, une validation supplémentaire a été réalisée en étudiant une DBD d'argon en régime homogène. Afin de ne pas alourdir inutilement le texte, l'article correspondant à cette seconde validation a été joint en annexe et les prochaines lignes se contentent d'en résumer les informations pertinentes. Tout d'abord, le réacteur était pourvu de deux électrodes recouvertes d'alumine et séparées d'une distance de 1 mm, résultant en un volume de décharge de $\sim$1.2 cm^3. Une tension sinusoïdale d'une fréquence de 35 kHz a été appliquée sur les électrodes, transférant une puissance moyenne de 1.5 W/cm^3 au gaz. Des traces d'ammoniac ou d'éthyl lactate ont été ajoutées à l'argon afin d'opérer la décharge en régime homogène plutôt que filamentaire, évitant par conséquent d'avoir affaire à une physique beaucoup plus complexe. Tel que discuté au Chapitre 1, ces mélanges dits Penning sont maintenant perçus comme les conditions typiques lorsqu'il est question d'une DBD d'argon en régime homogène.

Dans le cadre de cette étude, plutôt que de regarder l'évolution spatiale de la température électronique comme c'était le cas pour l'article précédent, c'est son évolution temporelle en un endroit donné au cours d'une période complète de la tension appliquée qui a été analysée. Cependant, puisque les mesures ont été réalisées dans le laboratoire de collaborateurs et que ceux-ci n'avaient pas la possibilité d'obtenir expérimentalement la densité des états 1s, le modèle a dû être modifié conséquemment. Plus spécifiquement, alors que cette densité était précédemment utilisée comme paramètre d'entrée, elle a plutôt été traitée dans le cas du présent article comme un second paramètre ajustable, au même titre que la température électronique. La validité de cette modification est d'ailleurs démontrée en cours de route puisqu'un graphique tout aussi éloquent que dans le premier article montre qu'il n'existe cette fois qu'un seul couple de température électronique / densité d'états 1s permettant d'obtenir le spectre théorique optimal.

Quant aux résultats en tant que tels, ils montrent que dans le cas des deux mélanges (ammoniac et éthyl lactate), les valeurs de T_e sont plus élevées en début de décharge ($\sim$0.8 eV). Ensuite, à mesure que le courant de décharge augmente, elles diminuent jusqu'à $\sim$0.35

eV et demeurent alors constantes autour de cette valeur jusqu'à l'extinction de la décharge sur le demi-cycle étudié. Une telle évolution temporelle démontre ainsi à nouveau la validité de la méthode puisqu'il s'agit d'un résultat très similaire à celui rapporté pour une DBD dans l'hélium[39]. Par ailleurs, un comportement inverse à T_e a été observé pour la densité des états 1s, ceux-ci passant de $\sim 4 \times 10^{16}$ à $\sim 2 \times 10^{17}$ m^{-3} au cours d'un demi-cycle. Puisque ces valeurs concordent aussi avec d'autres rapportées dans la littérature[57], ce résultat a permis de conclure en un fort lien entre T_e et n_{1s}, probablement via l'importance de l'ionisation Penning qui permet à la température électronique de diminuer lorsque la densité d'états 1s est grande.

Chapitre 3

Plasmas d'argon en présence d'espèces réactives

3.1. Introduction

Le précédent chapitre a permis de mettre au point un ensemble cohérent de diagnostics pour déterminer la densité et la température des électrons, la température du gaz ainsi que la densité des états 1s de l'argon dans les plasmas froids d'argon à la PA. En particulier, il a permis de valider le potentiel d'une nouvelle méthode pour obtenir la température des électrons couplant les prédictions d'un modèle CR décrivant la population des niveaux émetteurs 2p à des mesures d'émissions optiques des transitions 2p-1s. Cette méthode est utilisable peu importe les conditions expérimentales et donc s'avère très polyvalente quant à la variété de plasmas qu'elle permet de caractériser. De ces travaux, il devient maintenant possible de s'intéresser à l'effet de l'ajout d'espèces réactives dans les plasmas d'argon à la PA. Tel que discuté au Chapitre 1, un tel intérêt se trouve justifié dans la mesure où la grande majorité des études impliquant l'ajout d'espèces réactives dans les plasmas d'argon avaient pour but d'examiner l'impact du plasma sur ces espèces. Or, l'inverse demeure très peu documenté, bien qu'il s'agisse de la pierre angulaire permettant l'amélioration des procédés basés sur les plasmas froids via notamment la compréhension des mécanismes de fragmentation des espèces réactives et de la recombinaison de ces fragments en phase gazeuse.

Conséquemment, dans ce troisième chapitre, il est d'abord question d'étudier l'influence de molécules ajoutées à dessein au plasma, par opposition aux espèces tacitement incorporées comme dans le cas des jets de plasma (ces derniers aspects seront abordés au Chapitre 4). En particulier, l'impact de l'ajout de molécules diatomiques (N_2, O_2 et H_2) sur le bilan de puissance électronique ainsi que sur le chauffage des neutres dans un POS d'argon à la PA est présenté dans un troisième article. Les variations spatiales de la température électronique et du gaz, de même que de la densité électronique et celle des états 1s de l'argon y sont analysées pour une quantité croissante de ces molécules. Les profils spatiaux révèlent les

similitudes et différences que présente l'ajout de ces gaz réactifs et permettent de mettre en lumière qu'ils en viennent à rapidement dominer la cinétique de la décharge en absorbant la majorité de la puissance fournie au plasma. De plus, des liens physiques entre les différentes propriétés fondamentales de ces plasmas sont étudiés de plus près, ce qui conduit à des études approfondies des mécanismes physiques gouvernant la température du gaz et la densité des états 1s de l'argon.

Par ailleurs, au cours de ce troisième article, une méthode entièrement basée sur des mesures optiques et permettant le calcul de la puissance absorbée par les molécules réactives est présentée. Ce calcul a été motivé par les articles dans la littérature qui, depuis l'article pionnier de Yasuda et Hirotsu [58], ont établi des liens entre l'énergie absorbée par une molécule réactive dans le plasma et, par exemple, les propriétés physiques et chimiques d'un revêtement obtenu par dépôt chimique en phase vapeur assisté par plasma [59–62]. Qui plus est, si la majorité de ces articles traitaient autrefois des plasmas à pression réduite, ce n'est plus le cas aujourd'hui, comme le démontrent les articles récents ayant recours à une méthode de calcul basée sur des diagnostics électriques pour établir ce genre de corrélation dans une DBD à base d'argon à la PA [26, 51–54, 63, 64]. Dans ce contexte, un quatrième article ayant pour but de comparer les résultats obtenus de la méthode optique développée dans le cadre de cette thèse à ceux issus de cette méthode électrique est présenté. Pour les fins de cette comparaison, les mesures optiques et électriques ont été prises dans une DBD d'argon à la PA dans laquelle des précurseurs anhydrides (acétique et isobutyrique) pertinents pour le dépôt de groupements carboxyliques étaient insérés.

3.2. Article 3 : Influence de l'ajout de molécules diatomiques sur le bilan de puissance électronique et le chauffage des neutres dans les plasmas microonde d'argon à la pression atmosphérique

Dans ce troisième article, le même montage expérimental que pour le premier a été utilisé. Pour le rappeler brièvement, un POS était produit à l'aide d'un surfaguide dans un tube de silice fondue (2 mm ID, 6 mm OD) ouvert à l'air ambiant en aval. Pour le cas présent, de petites quantités ($\leqslant 1\%$) de gaz diatomiques tels que N_2, O_2 et H_2 ont été ajoutées à l'argon en amont du plasma. Pour s'assurer d'un bon mélange, l'injection des gaz dans le tube s'est faite à l'aide d'un vortex. En augmentant progressivement la part de ces gaz

dans l'admixtion, il a alors été possible d'étudier leurs impacts respectifs sur les propriétés fondamentales du plasma résultant. N_2, O_2 et H_2 ont été spécialement sélectionnés afin de simplifier l'analyse des résultats et conséquemment de bien pouvoir cerner les conclusions, ce qui aurait été plus difficilement le cas en ajoutant des molécules complexes telles que celles typiquement utilisées lors des procédés de dépôt chimique en phase vapeur assisté par plasma (acétylène, silane, précurseurs organosiliciés (TEOS, HMDSO), etc. [43–47]).

Les résultats de cette étude traitent à nouveau de la température électronique (obtenue avec la méthode du modèle CR décrivant la population des niveaux 2p combiné à des mesures d'émission optique des transitions 2p-1s), de la température du gaz (obtenue via l'élargissement des transitions radiatives $2p_2$-$1s_2$ et $2p_3$-$1s_2$ de l'argon), de la densité des états $1s_5$ de l'argon (obtenue par spectroscopie d'absorption résolue spectralement à l'aide d'une diode laser accordable) et de la densité électronique (obtenue via l'élargissement Stark de la raie H_β de l'hydrogène et d'un ratio d'intensité de raies). D'abord, les profils de ces paramètres le long de l'axe de la colonne de plasma montrent que l'ajout de molécules diatomiques n'affecte pas leur comportement, c'est-à-dire que la densité électronique et la température du gaz chutent toujours vers la fin de colonne alors que la densité des états $1s_5$ et la température électronique varient peu. Cependant, pour une position donnée et une concentration croissante de molécules diatomiques, une augmentation de la température du gaz et une diminution de la densité électronique sont observées. Quant à la température électronique et la densité des états 1s de l'argon, ils chutent d'abord puis remontent.

Par ailleurs, à partir de toutes ces informations, une analyse détaillée du bilan de puissance électronique révèle que la grande majorité de la puissance fournie au plasma ($>80\%$) va aux molécules diatomiques, bien que celles-ci représentent au plus 1% de l'admixtion. Cette absorption significative de puissance par les électrons et transmise aux molécules diatomiques par collisions concorde bien avec l'augmentation de la température des neutres observée. Par ailleurs, l'article démontre qu'un tel résultat est principalement dû à l'excitation de niveaux rotationnels par impacts électroniques.

Influence of N_2, O_2, and H_2 admixtures on the electron power balance and neutral gas heating in microwave Ar plasmas at atmospheric pressure

par

Antoine Durocher-Jean[1], Nicolas Delnour[1] et Luc Stafford[1]

([1]) Département de physique, Université de Montréal, Montréal, Québec, Canada

Cet article a été publié dans la revue *Journal of Physics D : Applied Physics* :

J. Phys. D : Appl. Phys. 52 (2019) 475201 .

Les contributions des différents auteurs à cet article sont :

— Antoine Durocher-Jean : Réalisation du montage expérimental, prise des mesures, analyse des résultats et écriture du premier jet du manuscrit

— Nicolas Delnour : Aide à la prise de mesures, révision du manuscrit

— Luc Stafford : Supervision des travaux, révision du manuscrit

ABSTRACT.

A combination of optical emission and absorption spectroscopy of argon 2p –1s transitions (Paschen notation) combined with collisional-radiative (CR) modelling of argon 2p states was used to characterize microwave argon plasmas at atmospheric pressure in presence of N_2, O_2, and H_2 admixtures. In particular, the neutral gas temperature (obtained from the broadening of argon $2p_2$–$1s_2$ and $2p_3$–$1s_2$ emission lines), the number density of argon $1s_5$ atoms (obtained from absorption spectroscopy of the argon $2p_9$–$1s_5$ transition using a tunable laser diode), the electron temperature (obtained from the comparison between measured and simulated argon 2p-to-1s relative line emission intensities), and the electron density (obtained from the Stark broadening of the H_β line and argon relative line emission intensities) were recorded as a function of the axial distance along the microwave plasma column. The results show that, for a given position in the plasma and a higher amount of admixture in the nominally pure argon plasma, the neutral gas temperature increases and the electron number density decreases, while the electron temperature and the population of argon metastable atoms first decreases and then increases at higher concentrations. With such information, a detailed analysis of the electron power balance was performed. It is found that less than 1% of the admixture in the argon plasma already absorbed more than 80% of the microwave power. Part of this energy is used for neutral gas heating, mostly through electron-impact excitation of rotational levels.

Keywords: microwave plasmas at atmospheric pressure, optical emission spectroscopy, tunable laser diode absorption spectroscopy, collisional-radiative modelling, electron temperature, number density of metastable atoms, neutral gas temperature

3.2.1. Introduction

The plasma state is increasingly seen and used as a means to induce physical and chemical reactions. For example, plasma-generated electrons are an ideal source of energy to transform molecules or compounds. In recent years, numerous articles have reported the use of non-thermal plasmas at atmospheric pressure to convert complex molecules into fragments for deposition purposes. The variety of results sought range from the creation of hydrophobic/hydrophilic surfaces for biocompatible or anti-fog materials [1–4] to ultra-hard, wear-resistant layers for the semiconductor and aeronautic industries [5–7]. Other applications of non-thermal plasmas at atmospheric pressure include the production of nanostructures using organosilicon and organotitanium precursors [8], the abatement of harmful greenhouse effect gases such as perfluorinated compounds [9], the conversion of CO_2 molecules into valued products [10–12] or the generation of reactive neutral species for plasma medicine [13, 14].

In all of these applications, understanding the kinetics driving the plasma and its interaction with surfaces holds the key to increasing the efficiency of the processes. Therefore, over the years, many have worked towards this goal. Among others, the link between operating conditions and the physical and chemical pathways converting methane (CH_4) into several free-standing carbon nanostructures was investigated [15]; the impact of aerosol particles on the flowing afterglow of an atmospheric pressure plasma was studied to improve the properties of plasma-synthesized ceramics or boron nitride particles [16]; the influence of the wood microstructure and wood outgassing was investigated to better understand the plasma deposition dynamics of water-repellent coatings in dielectric barrier discharges [17]; and the physics driving Ar/ethyl lactate dielectric barrier discharge relevant for the growth of biodegradable plasma polymers was investigated to gain insights into the precursor fragmentation kinetics [18]. More related to the present work, effect of air or air-related species on the electron kinetics of argon plasmas jets or glow discharges, relevant to many surface-treatment or biomedical applications, were also studied [19, 20].

With a similar objective in mind, the present article reports on how the presence of admixtures, with their own particular physical and chemical properties, contribute to the overall kinetics driving non-thermal microwave argon plasmas at atmospheric pressure. To do so, small amounts of common diatomic species (N_2, O_2 and H_2) were added to the microwave argon plasma column. Their influence on the axial profile of the electron number

density (n_e), electron temperature (T_e), neutral gas temperature (T_g) and number density of argon 1s$_5$ (Paschen notation) atoms (n_{1s_5}) was studied. This was realized using a combination of optical emission and absorption spectroscopy of argon 2p–1s transitions combined with collisional-radiative (CR) modelling of argon 2p states. While the chosen molecules may not be representative of the larger and more complex precursors used in the aforementioned applications, their impacts are nonetheless probably the simplest to single out and understand. As such, it is hoped that these results can be used as building blocks for the understanding of the impact of the injection of larger compounds such as organosilicon and organotitanium precursors in microwave argon plasma columns for the synthesis of SiOCH and TiOCH materials [8]. In this context, the article has been organized as follows: in section 3.2.2, the experimental setup used to produce the microwave argon plasma column in presence of N_2, O_2 and H_2 admixtures is described; in section 3.2.3, the different plasma diagnostics are detailed; in section 3.2.4, the axial profiles of n_e, T_e, T_g and n_{1s_5} along the microwave plasma column are presented; in section 3.2.5, these results are discussed with respect to the electron power balance and neutral gas heating dynamics. Finally, section 3.2.6 presents a summary of the main findings.

3.2.2. Experimental Setup

Figure 3.1 shows a schematic of the experimental setup with an image of the resulting plasma column when sustained in nominally pure argon conditions. For every experiment, a constant power of 300 W (incident minus reflected) was delivered to the plasma by a 2 kW Sairem microwave generator operating at 2.45 GHz. While a movable plunger was used and set for maximal power transfer to the plasma, a circulator directed unwanted reflections to a water-cooled load. A bidirectional coupler paired to a bolometer was used to measure the incident and reflected powers (to determine the absorbed power). Wave coupling was ensured by a surfaguide-type wave launcher. The discharge tube made of fused silica (2 mm inner diameter, 6 mm OD) was connected to the gas inlet on one end and was open to ambient air on the other end. This relatively small tube diameter was chosen to avoid propagation of high-order surface-wave modes as well as filamentation and contraction phenomena often seen in such plasmas [21]. High purity argon was used and its mass flow rate, directed downward, maintained at 500 SCCM (cubic centimetres per minute at standard temperature

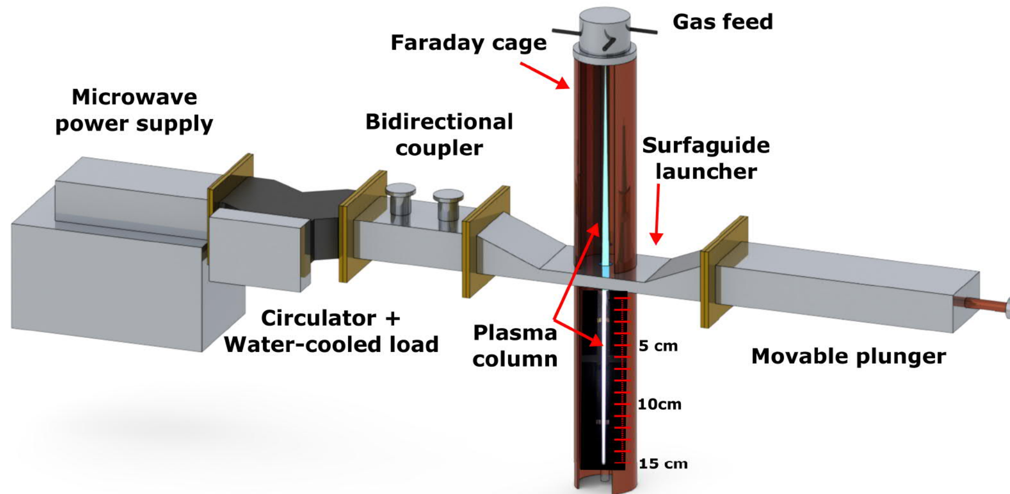

Figure 3.1. Schematic of the experimental setup used to sustain the microwave argon plasmas in presence of N_2, O_2 or H_2 admixtures. Over the range of experimental conditions investigated, the resulting plasma column was sustained symmetrically both above and below the wave launcher [22]. All optical emission and absorption spectroscopy measurements were performed below the surfaguide wave launcher.

and pressure) using a mass flow controller. An independent mass flow controller was used for selective control of the concentration fraction (0.25%, 0.5% or 1%) of the N_2, O_2 or H_2 admixture.

3.2.3. Data acquisition and analysis

3.2.3.1. *Optical emission spectroscopy combined with collisional-radiative modelling*

Optical emission spectroscopy measurements were performed in part using a 320 mm focal length spectrometer (Princeton Instruments IsoPlane SCT-320) equipped with a 600 lines/mm grating and an intensified charged coupled device (ICCD) camera (Princeton Instruments PI-MAX4 1024x256). This system provided a spectral resolution (full width at half maximum) of ~ 0.26 nm across the 690-930 nm wavelength range, allowing to distinguish most of the closely separated Ar 2p-to-1s emission lines. Typical OES spectra of the microwave argon plasma column without and with 0.5% O_2 are shown in Figure 3.2. These and the others used in the forthcoming analysis are the average of 100 measurements and have

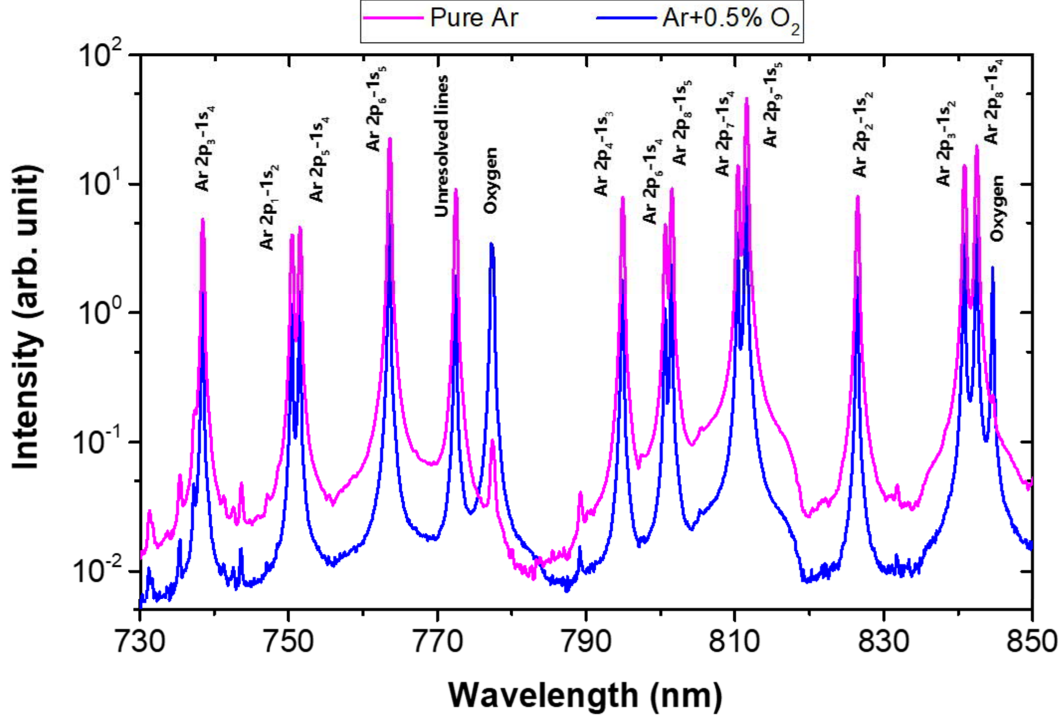

Figure 3.2. Typical optical emission spectra of the microwave argon plasmas, without and with 0.5% O_2.

been corrected for the optical response of the apparatus and optical fibre after background removal.

The Ar 2p -to-1s emission line intensities obtained from the OES spectra displayed in Figure 3.2 were used together with the predictions of a 0D CR model for argon 2p states to obtain the electron temperature (T_e) assuming a Maxwell–Boltzmann electron energy distribution function. Details on this CR model can be found in a previous publication [23], only a brief summary is given here. The method for T_e determination relies on a direct comparison between measured and simulated emission line intensities for argon 2p-to-1s transitions. In this context, the intensity of a given Ar I line (I_λ) emanating from a 2p$_i$ level can be written as

$$I_\lambda = A_{ij}\ n_{2p_i}\ \theta_{ij} \tag{1}$$

where A_{ij} is the Einstein coefficient of the argon 2p$_i$-to-1s$_j$ transition, n_{2pi} is the number density of the emitting 2p$_i$ level, and θ_{ij} is the escape factor of the 2p$_i$-to-1s$_j$ transition. As such, the role of the CR model is to find the optimal n_{2p_i} values that fit the experimental data by solving the particle balance equations of the argon 2p levels in optically thick plasma

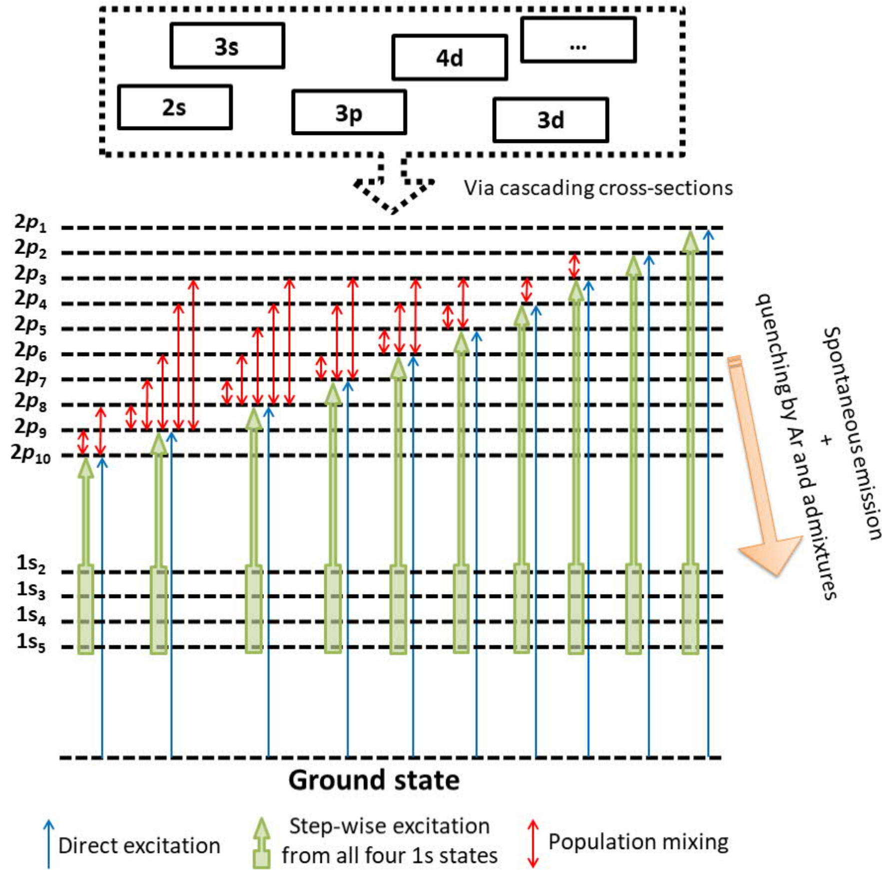

Figure 3.3. Schematic of the reactions considered in the CR model.

conditions ($\theta_{ij} < 1$). Figure 3.3 summarizes the different mechanisms that were considered in the excitation and de-excitation of argon 2p states [23].

Excitation mechanisms include electron impact from either ground [24] or 1s metastable and resonant states [25], excitation transfer reactions between 2p levels induced by a collision with ground state argon atoms [26] as well as radiation trapping (see detailed expression for the escape factor θ_{ij} in [23]). As represented by the dotted box above figure 3.3, apparent cross-sections for electron collisions are used to calculate the reaction rates; this method therefore implicitly considers cascading effects from higher energy levels without solving the particle balance equation for each of these levels. Furthermore, de-excitation mechanisms include radiative decay [27], quenching by neutrals [28, 29] and N_2, O_2, or H_2 admixtures [30], as well as excitation transfer reactions between 2p levels induced by a collision with ground state argon atoms [26]. Radiation trapping and excitation transfer reactions involving

ground state neutral atoms make the CR model developed in [23] particularly well suited for detailed investigations of the electron temperature in non-thermal argon plasmas at atmospheric pressure. Based on this framework, the steady-state particle balance equation of the argon 2p$_i$ levels can be expressed as

$$n_{2p_i} = \frac{n_e\left(k_{g-2p_i}\; n_g \; + \sum_j k_{1s_j-2p_i} \;\; n_{1s_j}\right) + \sum_{k\neq i} k_{2p_k-2p_i}\; n_g\; n_{2p_k}}{\sum_j A_{ij}\; \theta_{ij} + k_{2p_i-1s_j}\; n_g + \sum_{k\neq i} k_{2p_i-2p_k}\; n_g \; + \sum_{Quench} k_{Quench}\; n_{Quench}} \tag{2}$$

where n_e and n_g are the electron and argon ground-state number densities, k_{g-2p_i} are the reaction rates for the electron-impact excitation of the 2p$_i$ level from ground state, $k_{1s_j-2p_i}$ are the reaction rates for the stepwise electron-impact excitation of the 2p$_i$ level from 1s$_j$ levels, $k_{2p_k-2p_i}$ and $k_{2p_i-2p_k}$ are the reaction rates for excitation transfer reactions (from level i to level k), $k_{2p_i-1s_j}$ and k_{Quench} are the quenching rates by Ar atoms and by N_2, O_2, or H_2 admixtures, and n_{Quench} are the number densities of the quenching species (Ar, N_2, O_2, and H_2).

In Equation (2), it is worth highlighting that only k_{g-2p_i} and $k_{1s_j-2p_i}$ depend on the electron temperature. In addition, n_e appears in every term of the numerator (implicit in all the n_{2p_k} terms). Therefore, the electron number density mostly acts as a scaling factor for the absolute number density of the argon 2p levels and thus for the absolute line emission intensity (see Equation (1)). It would not have been the case if the number density of Ar 1s levels or the neutral gas temperature were solved instead of being inputted in the model, since these quantities depend on n_e [31]. Consequently, in the approach described, relative emission intensities are computed from the CR model as a function of the electron temperature using n_g, n_{1s_j}, and n_{quench} as input parameters. These relative emission intensities are then compared to the relative emission intensities obtained from the experiments. Since only relative emission intensities, and not absolute emission intensities, are compared, the method used in this study to extract the electron temperature from the best fit of the experimental data is independent of n_e.

The ground state number density n_g used as input parameter in the CR model is calculated by the ideal gas law, with the neutral gas temperature T_g obtained from broadening analysis of the argon 2p$_2$–1s$_2$ and 2p$_3$–1s$_2$ emission lines (see details below). As for the populations of argon 1s states, also used as input parameters in the CR model, the number density of the Ar 1s$_5$ state is determined from optical absorption spectroscopy measurements

of the argon $2p_9$–$1s_5$ transition using a tunable laser diode (see details below). For this work, based on the results from Santiago and Calzada [32],the number density of the other three Ar 1s states ($1s_2$, $1s_3$ and $1s_4$) are all considered equal to n_{1s_5}. Finally, n_{quench} is calculated with respect to n_g from the concentration fraction of the quenching species. For example, in nominally pure argon plasmas with 0.5% O_2, n_{quench} = 0.5% n_g for the oxygen admixture. For each experimental spectrum, and thus for each experimental condition, the value of T_e that yields the most accurate fit of the measured line emission intensities is assumed to be the actual electron temperature in the plasma.

3.2.3.2. *High-resolution optical emission spectroscopy*

Line broadening measurements were also recorded using a high-resolution spectrometer (HORIBA Jobin Yvon THR1000) equipped with a 1800 lines mm^{-1} holographic grating and a photomultiplier tube (Hamamatsu R636-10). This system provided a spectral resolution (full width at half maximum) of 21.5 pm for the argon $2p_2$-$1s_2$ and $2p_3$-$1s_2$ emission lines at 826 nm and 841 nm. These two lines were specifically chosen because, in non-thermal argon plasmas at atmospheric pressure, they are strongly affected by resonance broadening. Therefore, the Lorentzian part of their total line broadening becomes completely dominated by mechanisms linked to the neutral gas temperature (resonance and van der Waals broadening). More details on T_g determination from line broadening analysis of the argon $2p_2$-$1s_2$ and $2p_3$-$1s_2$ transitions are provided in [23]. Here, all T_g values reported (and used as input in the CR model) are the mean of the temperatures obtained from both lines and the error is defined as the standard deviation.

3.2.3.3. *Tunable laser diode optical absorption spectroscopy*

The population of argon $1s_5$ atoms was determined by optical absorption spectroscopy measurements using a tunable laser diode (Sacher Lasertechnik Pilot PZ 500) in a Littman/Metcalf configuration (laser linewidth $<$100 kHz). The optical path of the laser as well as the position of the optical fibres sending light to the low-resolution and highresolution spectrometers (placed perpendicularly to the laser beam path to only collect the light emitted by the plasma) is presented in figure 3.4. A triangular signal on a piezoelectric actuator enabled a periodical sweep of the laser frequency centred on the argon $2p_9$–$1s_5$ transition. The built-in current coupling feature enabled a large and continuous (mode

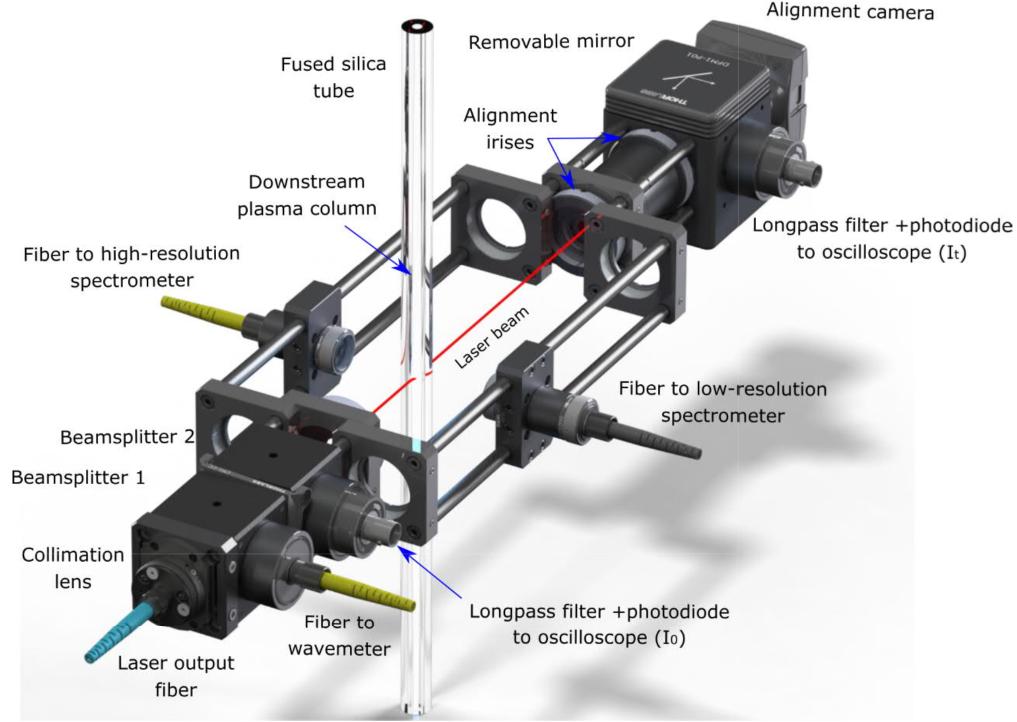

Figure 3.4. Experimental setup for the OAS and OES measurements.

hop free) tuning range (>30 GHz). The sweeping process was monitored using a WS-6 wavelength meter (WLM) from HighFinesse GmbH. As shown in figure 3.4, two photodiode detectors connected to a Teledyne-Lecroy HDO6104 oscilloscope were used to record both the reference (unabsorbed) laser intensity I_0 and the absorbed laser intensity I_t as a function of time. Longpass filters were placed right before the detectors to reduce as much as possible the detection of any unwanted light. Still, a background measurement (laser off, plasma on) was always taken and subtracted nonetheless. For every axial position investigated along the microwave plasma column, the laser path was always carefully realigned with regard to the tube axis using the alignment camera. More details on optical absorption spectroscopy analysis are provided in [23].

The number density of the argon $1s_5$ atom was determined from the measured absorption spectrum of the argon $2p_9$-$1s_5$ transition using [25]

$$n_{1s_5} = \frac{8\pi}{A_{2p_9-1s_5}} \frac{g_{1s_5}}{g_{2p_9}} \frac{\nu_0^2}{c^2} \frac{1}{l} \int_{-\infty}^{\infty} \ln\left(\frac{I_0(\nu)}{I_t(\nu)}\right) d\nu \tag{3}$$

where $A_{2p_9-1s_5}$ is the spontaneous emission Einstein coefficient, c is the speed of light, g_{2p_9} and g_{1s_5} are the statistical weights of the $2p_9$ and $1s_5$ states, and l is the length of the

plasma along the line of sight (2 mm). In Equation (3), the integral is performed over the total absorption coefficient $\mathcal{A}(\nu) = \ln\left(\frac{I_0(\nu)}{I_t(\nu)}\right)$. Since the optical transition was periodically swept with the laser frequency first decreasing and then increasing, two absorption spectra were obtained for each measurement. Thus, similarly to the high-resolution OES procedure described above, the n_{1s_5} values reported later in this work are the average of these two spectra and the error is defined as the standard deviation.

3.2.3.4. *Hydrogen H_β broadening and argon line ratio analysis*

According to Equations (1) and (2), the intensity of a given Ar I line can be assumed proportional to the electron number density. Consequently, the intensity ratio of the same line for two different experimental conditions becomes proportional to the ratio of their electron number density provided that the geometric factors (plasma volume seen by the fibre, distance between the plasma and fibre, etc) remain the same for both conditions; this aspect was fulfilled for all measurements. As such, the electron number density as a function of the axial distance from the wave launcher and as a function of the concentration fraction of the admixture in the microwave argon plasma was obtained by a two-step analysis. First, using the high-resolution spectrometer described above, the hydrogen H_β broadening was measured with a 1% H_2 admixture in the nominally pure argon plasma. The Lorentzian component was then deconvoluted from the Voigt profile using the same procedure as for T_g [23] and the electron number density was calculated from the Stark broadening using the data reported by Griem [33]. This result is shown as the red curve in figure 3.5 and the first data point (x = 1 cm) was taken as the reference electron number density ($n_{e_{Ref}}$). Afterwards, the emission intensity I_i of the Ar $2p_2$-$1s_2$ transition at 826 nm was recorded for every axial position along the microwave plasma column and for a number of experimental conditions. These emission intensities were then normalized to the reference intensity I_{Ref} at (x = 1 cm, 1% H2) of the same transition. Using the results of the CR model and the parameters found from the other optical emission and absorption spectroscopy diagnostics, the corresponding ratios of the escape factors (θ_{Ref}/θ_i) and $2p_i$ number densities ($n'_{2p_2-i}/n'_{2p_2-Ref}$) were calculated such that the electron density n_{e_i} could be obtained for every axial position and experimental condition according to

$$n_{e_i} = \frac{I_i}{I_{Ref}} \frac{\theta_{Ref}}{\theta_i} \frac{n'_{2p_2-Ref}}{n'_{2p_2-i}} n_{e_{Ref}} \tag{4}$$

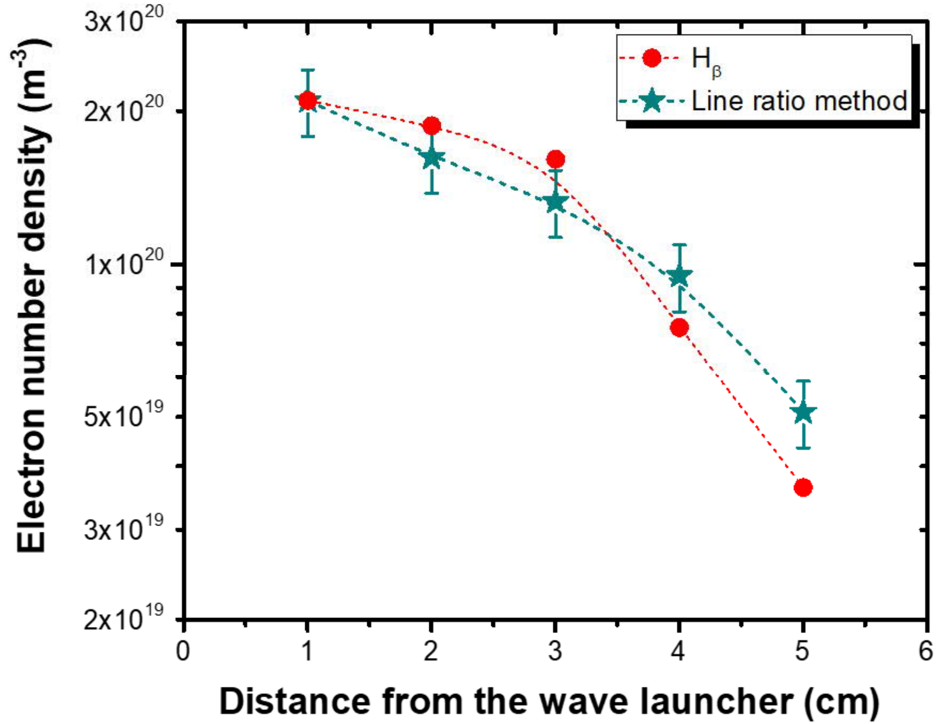

Figure 3.5. Electron number density as a function of the axial position with respect to the wave launcher. Data were obtained using the H_β broadening and the two-step argon line ratio analysis in argon plasmas with 1% H_2.

To assess the reliability of this simple argon line-ratio method with respect to the more complicated broadening analysis of the hydrogen H_β line, figure 3.5 compares the results from both techniques obtained with 1% H_2 in the argon plasma (blue-green plot). A very good agreement is observed between the two methods. One of the main advantages of this argon line ratio technique is that absolute values of n_e can easily be obtained over a wide range of experimental conditions, including in plasmas without any hydrogen such as Ar/N_2 and Ar/O_2.

3.2.4. Results

The values of the electron number density, electron temperature, neutral gas temperature, and number density of argon $1s_5$ atoms are presented in figure 3.6 as a function of the axial distance with respect to the surfaguide wave launcher. The first result to notice is that, compared to the nominally pure argon plots, the axial profiles are not significantly changed by the addition of any admixture: for all experimental conditions examined in this study, n_e

and T_g decrease from the wave launcher towards the end of the plasma column whereas T_e and n_{1s_5} remain more or less constant. These trends were already reported for nominally pure argon plasma columns sustained by microwave electromagnetic fields and were explained as follows [23, 34]: n_e decreases because as the surface wave propagates along the discharge tube, it gradually transfers its energy to the electrons and as such has progressively less energy to create new ones. Consequently, there is less energy being transferred from electrons to the neutral gas atoms through elastic collisions such that T_g also decreases. As for the electron temperature, it is dictated by the particle balance equation of charged species. Over the range of experimental conditions investigated here, for every axial position along the tube, the creation of charged species is dominated by direct electron-impact ionization of ground state neutral argon atoms whereas losses are controlled by diffusion and recombination on the plasma reactor walls (the plasma is neither contracted nor filamented in such a small tube, hence volume recombination reactions involving argon dimer ions is negligible [21]). In such conditions, fairly constant values of T_e are expected, as seen in the experiments (figure 3.6). Similarly, in nominally pure argon plasmas, argon 1s atoms are predominantly created by electron impact excitation of ground-state argon atoms and are predominantly lost by stepwise electron impact excitation of argon 2p levels. In such conditions, the populations of argon 1s atoms become independent of n_e and mostly linked to T_e through the reaction rates for electron impact excitation of ground-state argon atoms and stepwise electron impact excitation of argon 2p levels. As such, given the fairly constant T_e values along the microwave plasma column, rather constant number densities for argon 1s atoms are expected, as seen in the experiments (figure 3.6).

This being said, figure 3.6 also reveals that the addition of N_2, O_2, and H_2 admixtures in the argon plasma reduces the length of the microwave plasma column and moreover affects the absolute values of the studied plasma parameters. More specifically, for an increased amount of admixture at a given position, n_e steadily decreases while T_g steadily increases. These changes are most and least notable with the H_2 and N_2 admixtures. Such trends were also observed by other authors in different plasma conditions and configurations, for example in the jet of argon plasmas expanding in ambient air [16, 35–39]. The cases of n_{1s_5} and T_e are a bit less obvious but still present a clear signature in the presence of N_2, O_2, and H_2 admixtures. On the one hand, the behaviour of T_e is marked first by a decrease

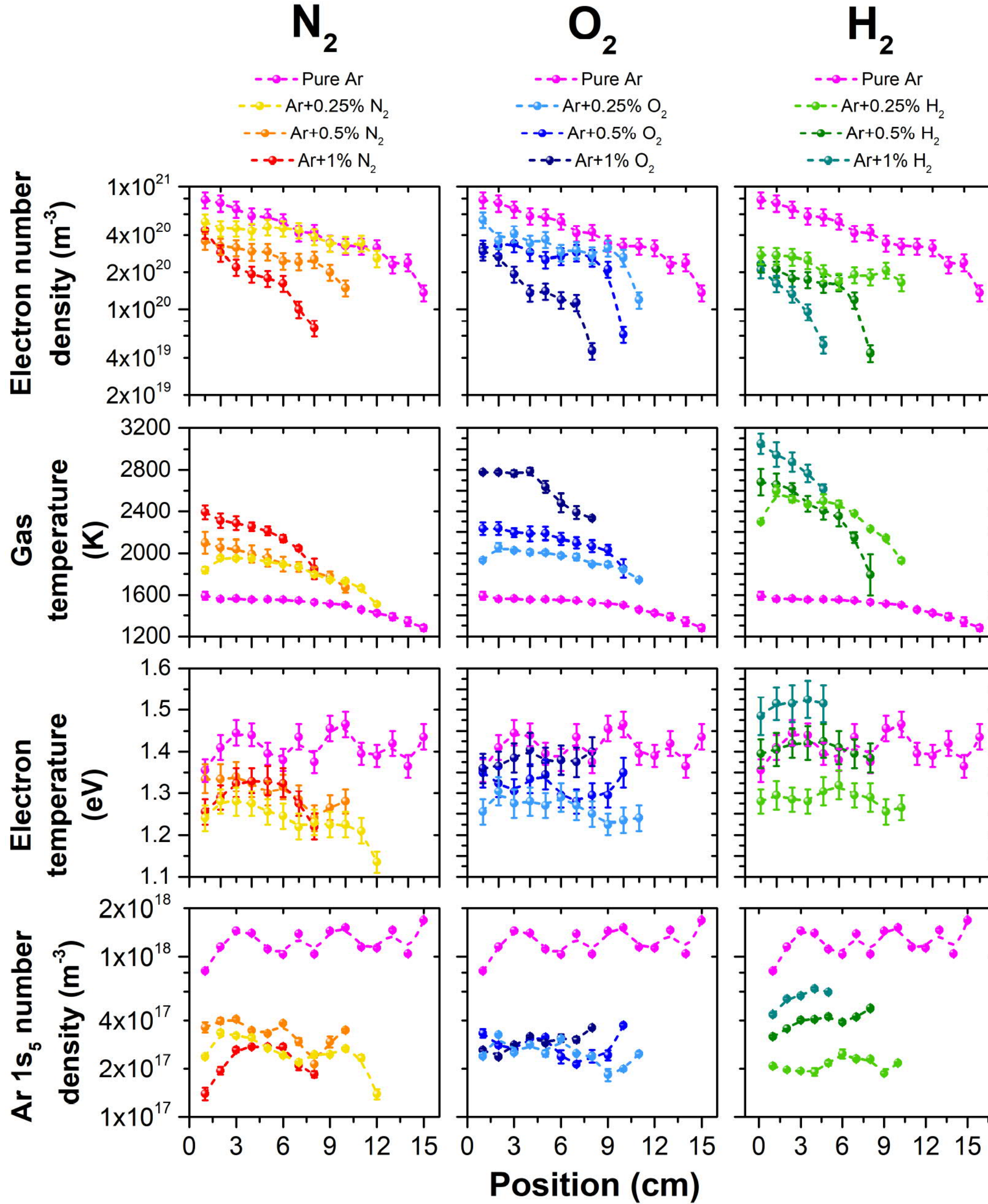

Figure 3.6. Axial profiles of n_e, n_{1s_5}, T_g and T_e along the microwave plasma column for an increased amount of the three diatomic admixtures. Error bars are present on all data points; in some conditions, error bars are below the marker size which makes them almost invisible.

compared to the pure argon case, followed by an increase as the concentration fraction of the admixture increases. Once more, this behaviour is most and least accentuated in the respective cases of H_2 and N_2 admixtures. Such rises in T_e with the addition of admixtures have already been reported by Levasseur *et al* in dielectric barrier discharges in helium with

N_2, O_2, and air admixtures [40] or by Chen and Phillips following the addition of aerosol particles into a microwave plasma torch [16]. On the other hand, the n_{1s_5} values with the admixtures are always lower than those achieved in the nominally pure argon plasma column. However, where the n_{1s_5} values decrease with an increased amount of N_2, they increase with an increased amount of H_2. Oxygen is again the intermediate case since no significant variation is observed for all concentration fractions investigated.

As mentioned before, in nominally pure argon plasmas, argon 1s atoms are predominantly created by electron impact excitation of ground-state argon atoms and are predominantly lost by stepwise electron impact excitation of argon 2p levels [21]. In such conditions, the particle balance of argon 1s atoms is

$$k_{1s_5}\ n_e\ n_g = \sum_k k_{1s-2p_k}\ n_e\ n_{1s_5} \tag{5}$$

where k_{1s_5} is the reaction rate for electron impact excitation of argon $1s_5$ atoms [22] and k_{1s-2p_k} are the reaction rates for stepwise electron impact excitation of argon 2p levels from the argon $1s_5$ level [23]. Equation (5) can also be rewritten as

$$1/n_{1s_5} = \sum_k k_{1s-2p_k}\ /k_{1s_5} n_g \tag{6}$$

The predictions of Equation (6) were verified by plotting all values of $1/n_{1s_5}$ presented in Figure 3.6 as a function of $\sum_k k_{1s-2p_k}\ /k_{1s_5} n_g$, where the values of $k_{1s_5} = k_{1s_5}(T_e)$, $k_{1s_5} = k_{1s_5}(T_e)$, and $n_g = n_g(T_g)$ were obtained from the corresponding values of the electron temperature and neutral gas temperature presented in Figure 3.6. The results are shown in Figure 3.7. In nominally pure argon plasmas, $1/n_{1s_5}$ increases with $\sum_k k_{1s-2p_k}\ /k_{1s_5} n_g$, in very good agreement with the predictions of Equation (6). Figure 3.7 further reveals that this correlation remains in presence of the N_2, O_2, and H_2 admixtures. However, even if all concentration fractions of admixtures obey a similar growth, they are all vertically shifted upwards from the plot obtained in nominally pure argon plasmas. This means that for a given ration of $\sum_k k_{1s-2p_k}\ /k_{1s_5} n_g$, n_{1s_5} will be lower in presence of the admixture; a feature that can be ascribed to the quenching of argon 1s states by collisions with diatomic molecules [34,35,37]. Addition of this loss mechanism in the right-hand side of Equation 6 would probably have shifted all the data points in the presence of admixtures to the right (higher losses) such that they would most likely have become aligned with the values achieved

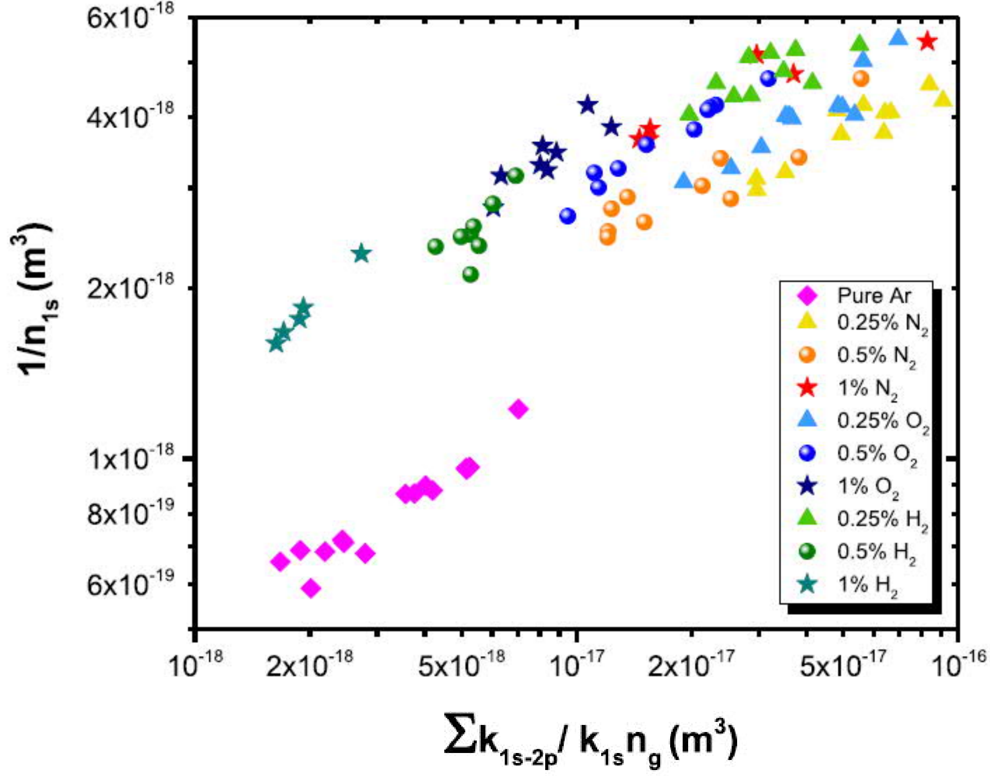

Figure 3.7. Correlation between the population of argon $1s_5$ atoms and the predictions of a simple particle balance equation involving the reaction rate for electron impact excitation of argon $1s_5$ atoms k_{1s_5}, the reaction rates for stepwise electron impact excitation of argon 2p levels from the argon $1s_5$ level k_{1s-2p_k}, and the neutral gas number density n_g. The results are shown for different concentration fractions of admixtures.

in nominally pure argon plasmas. This could not be realized since some of the quenching reaction rates could not be found in the literature.

It is worth highlighting that the vertical shift for the data point obtained in presence of N_2, O_2, and H_2 admixtures in Figure 3.7 does not seem to significantly increase with the concentration fraction of the admixture. This can probably be ascribed to the concurrent rise of the concentration fraction and the neutral gas temperature. More precisely, the collision frequency for a quenching reaction can be written as $k_{Quench}\, n_{Quench}$, where $k_{Quench} \propto \sqrt{T_g/300}$ and $n_{Quench} = \%_{Adm}\, n_g \propto \%_{Adm}/T_g$, such that $k_{Quench}\, n_{quench}$ varies like $\%_{Adm}/\sqrt{T_g}$. Therefore, since T_g always rises along with $\%_{Adm}$ (see Figure 3.6), no significant variation of $k_{Quench}\, n_{Quench}$ are expected, in good agreement with the set of data plotted in Figure 3.7.

3.2.5. Discussion

3.2.5.1. *Electron power balance*

The complete set of data presented in Figure 3.6 was used to perform a detailed analysis of the electron power balance in microwave plasmas. More specifically, the values of the electron number density, electron temperature, neutral gas temperature, and number density of argon $1s_5$ atoms as a function of the axial distance and concentration fraction of the N_2, O_2, and H_2 admixture were used to calculate the axially resolved power being dissipated by the electrons P_{diss} though collisions with neutral argon atoms. The following collisions were considered: elastic collisions, direct and stepwise ionization, direct excitation of the argon 1s and argon 2p levels, and stepwise excitation of the argon 2p levels via the argon 1s levels:

$$P_{diss} = n_e V \left(k_{el}\, n_g \frac{2m_e M_{Ar}}{(m_e + M_{Ar})^2} \left(\frac{3}{2} T_e - \frac{3}{2} T_g \right) + k_{ion-d}\, n_g\, \Delta E_{ion-d} + \right.$$
$$+ \sum_j \left(k_{ion-s}\, n_{1s_j} \left(\Delta E_{ion-d} - \Delta E_{1s_j} \right) + k_{1s_j}\, n_g\, \Delta E_{1s_j} \right) +$$
$$\left. \sum_k \left(k_{2p_k}\, n_g\, \Delta E_{2p_k} + \sum_j k_{1s_j-2p_k}\, n_{1s} \left(\Delta E_{2p_k} - \Delta E_{1s_j} \right) \right) \right) \quad (7)$$

where $k_i = k_i(T_e)$ are the reaction rates calculated from the corresponding cross-sections [24,25,42], ΔE_{ion-d}, ΔE_{1s} and ΔE_{2p} are the threshold energies for electron-impact ionization of argon atoms, electron-impact excitation of argon atoms leading to 1s atoms, and electron-impact excitation of argon atoms leading to 2p atoms, respectively, and V is the plasma volume in which the power was dissipated. For all the experimental conditions examined in this work, measurements were recorded every centimetre along the downstream plasma column. Consequently, the plasma volume for each axial position investigated can be represented as a cylinder with a height of 1 cm and a diameter of 2 mm (tube inner diameter). Afterwards, the axially resolved values of P_{diss} (one value per cylinder) in the downstream plasma zone were summed and the result was multiplied by a factor of 2 to account for both the upstream and downstream plasma columns (both upstream and downstream plasmas were assumed identical [22]). These values of the total power dissipated by electrons through collisions were then compared to the corresponding value achieved in nominally pure argon plasmas. Since all power that could have gone to the

argon atoms was accounted for, any difference between the two can readily be attributed to the electrons dissipating the remaining power on the admixture molecules. Designating the percentage of power taken by the admixture as $\%P_{Adm}$, it was calculated according to:

$$\%P_{Adm} = \frac{\sum P_{diss}^{Ar} - \sum P_{diss}^{Ar+admixture}}{\sum P_{diss}^{Ar}} \times 100 \quad (8)$$

This procedure is valid and legitimate only because all significant changes in the plasma properties have been correctly been taken into account through the corresponding variation of n_e, T_e, T_g, and n_{1s_5}. The results are shown in Figure 3.8 as a function of the concentration of the N_2, O_2, and H_2 admixture in the microwave argon plasma. Inspired by previous studies [43-45], the values of the power dissipated per molecule (P_{Mol}) are also plotted in Figure 3.8. This parameter was calculated according to

$$P_{Mol} = \frac{\%P_{Adm} \times \ 300\ W}{\sum n_g V \ \times \ \%_{Adm}} \quad (9)$$

where 300 W (1.9×10^{21} eV/s) is the total microwave power absorbed by the plasma (incident minus reflected power), and $n_g V$ is the total number of atoms in the plasma volume V. In Equation (9), the summation is performed over the upstream and downstream plasma zones with the small plasma volumes V represented as a cylinder with a height of 1 cm height and a diameter of 2 mm (tube inner diameter).

Figure 3.8 reveals that the percentage of the microwave power taken by the admixture increases with the concentration of N_2, O_2, and H_2 in the microwave argon plasma. Another interesting feature is that even with a 0.25% amount of admixture, the different gases absorb more than 80% of the microwave power. This amount rises to values above 90% for the 1% conditions. Consequently, in such conditions, the plasmas can hardly be considered as an argon-dominated plasma but rather as an admixture-dominated plasma with the latter acting as the principal energy recipient. A similar conclusion was reached by Niermann *et al* [46]: the authors noticed that as little as 0.5% of argon into a helium RF plasma at atmospheric pressure was enough to dominate the discharge physics. Similar results were reported by Castanos-Martinez in a neon microwave plasma at atmospheric pressure with small amounts of argon [21].

Over the range of experimental conditions investigated, it can also be seen in Figure 3.8 that the values of the power dissipated per molecule are in the 10^5 eV/s range. Considering

that in non-thermal argon plasmas at atmospheric pressure the collision frequency for elastic electron-neutral collisions is in the range of 10^9 - 10^{10} collisions per second [47], this yields to a mere ~10^{-5} - 10^{-4} eV per collision. If other collisions (rotation, vibration, dissociation, ionization, etc.) were to be added in presence of admixtures, this value would be even lower. This result underlines that only a very small fraction of the electron collisions actually results in an electronic excitation, dissociation, or ionization. Therefore, one has to be careful when trying to link a measured value of the power per molecule or energy per molecule to an excitation, dissociation, or ionization energy.

Moreover, the values displayed in Figure 3.8 are interestingly much higher than the ones that can be calculated from the set of data presented in other studies. For example, in argon-based dielectric barrier discharge with 1% of N_2 in the nominally pure argon gas, detailed analysis of the current-voltage characteristics have resulted in an absorbed power by the nitrogen molecules of 8 W distributed over a plasma volume of 43.2 cm^3. Assuming a neutral gas temperature of 300 K, this yields 5 eV/s. This value of the power dissipated per molecule is obviously much lower the ones presented in Figure 3.8; a feature that can be ascribed to the much lower number density of charged species in dielectric barrier discharges with respect to those obtained in microwave plasmas.

Figure 3.8 also suggests that there is a maximal power that can be transferred to a molecule since, starting from 0, the plot rises abruptly and then drops as the amount of admixture increases. This trend was also observed in [48] and can be ascribed to the fact that, starting from the 0% concentration, the admixture rapidly takes most of the injected power. As such, adding more admixtures still results in more absorption of the input power but at a lower rate since there is only a fraction of the injected power remaining. In our case, it is important to mention that the dashed lines are only there to help understanding the graphs. Therefore, the percentage of admixture for which the power per molecule is maximal could very well be prior to the 0.25% value. Again, these trends are most and least noticeable respectively for H_2 and N_2.

3.2.5.2. *Neutral gas heating*

As mentioned earlier, previous studies have already shown a close link between the axial profiles of T_g and n_e along microwave plasma columns in nominally pure argon [23,49].

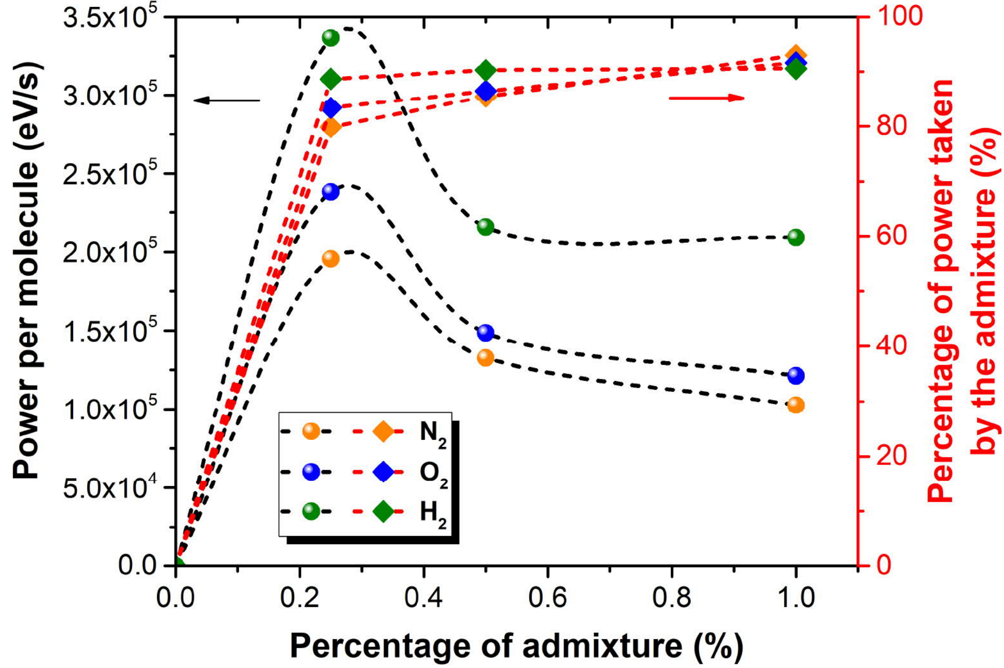

Figure 3.8. Power dissipated per molecule and percentage of the power taken by the admixture for the different concentration fractions of N_2, O_2, and H_2 in the microwave argon plasma.

Such feature still holds for the axial profiles displayed in figure 3.6: when n_e drops, so does T_g. However, the opposite behaviour can also be observed in presence of N_2, O_2, and H_2 admixtures in the microwave argon plasma: while n_e decreases, T_g increases. This counter-intuitive trend seems even more puzzling considering that the less numerous electrons are also characterized by lower electron temperatures (see figure 3.6). Therefore, local energy transfers through elastic electron-neutral collisions (involving both argon and admixture molecules) can no longer solely explain the observed trends in T_g along the microwave plasma column. This result can be visualized in figure 3.9(a), where no global correlation can be seen between T_g and the local power transferred per neutral atom through elastic collisions $W_{elastic}$ in the plasma volume V along the plasma column, calculated by

$$W_{elastic} = k_{el}\ n_e \frac{2m_e M_{Ar}}{(m_e + M_{Ar})^2} \left(\frac{3}{2}T_e - \frac{3}{2}T_g\right) V \tag{10}$$

However, in presence of admixture molecules, neutral gas heating can also arise as a result of electron-impact dissociation reactions and energy transfer collisions from excited rotational

states [50, 51]. Therefore, using the set of data presented in figure 3.6, the contributions of these two mechanisms were also calculated. On the one hand, the local power transferred per neutral atom through electron-impact dissociation W_{diss} in the plasma volume V along the plasma column can be written as

$$W_{diss} = k_{diss}\, n_e\, (\Delta E_{diss})\, V \tag{11}$$

where k_{diss} is the reaction rate for electron-impact dissociation of the admixture molecule and ΔE_{diss} is the threshold energy for the corresponding electron-impact dissociation (9.79 eV for N_2, 5.15 eV for O_2, and 4.52 eV for H_2). The cross sections used for calculations of the rate constants for electron-impact dissociation of N_2, O_2, and H_2 as a function of the electron temperature were taken from [52–54].

On the other hand, according to Kutz and Meyer [55], two different mechanisms of molecular rotational excitation can occur: the "low energy", or "normal", excitation and the "high energy", or "rotational rainbow", excitation. Since, according to their calculations, the rotational rainbow starts being an important excitation channel only for electrons having energies above 10–20 eV, this mechanism was neglected over the range of experimental conditions examined. Moreover, the selection rule for the "normal" excitation allows only $\Delta j = 0, 2, 4$, etc, where j is the rotational quantum number. Consequently, the local power transferred per neutral atom through electron impact excitation of rotational levels W_{rot} in the plasma volume V along the plasma column was calculated as:

$$W_{rot} = n_e V \sum_j \left(k_{rot_{j+2\leftarrow j}} \Delta E_{rot_{j+2\leftarrow j}} + k_{rot_{j+4\leftarrow j}} \Delta E_{rot_{j+4\leftarrow j}} + ...\right) \tag{12}$$

where $k_{rot_{j+2/4/...\leftarrow j}}$ are the reaction rate for electron-impact excitation of the jth to the $j + 2/4/$th rotational level of the admixture molecule, n_j is the relative number density of admixture atoms in the jth rotational state and $\Delta E_{rot_{j+2/4/...\leftarrow j}}$ is the energy transferred into rotation, assumed equal to the energy difference between the final and initial rotational levels. Following the rigid rotator approximation formula, the energy of each rotational level was calculated using:

$$E_{rot_j} = B_0 j(j + 1) \tag{13}$$

where B_0 is the rotational constant proper to each gas and found in [52–54]. From equation (10), the relative number density of admixture atoms in the jth rotational state was

calculated assuming a Boltzmann distribution:

$$n_j = \frac{(2j+1)\exp\left(-\frac{E_j}{T_g}\right)}{\sum_j \exp\left(-\frac{E_j}{T_g}\right)} \tag{14}$$

In this equation, the rotational temperature was assumed equal to the gas temperature, an hypothesis often made for microwave plasmas at atmospheric pressure and justified by the very efficient energy exchange between translation and rotation [56,57]. Based on high resolution OES measurements of the N_2 rovibrational second positive system, a total of 25 rotational levels were considered in our calculations. Finally, due to the limited availability of cross sections, only the reaction rates of the $j = 2 \leftarrow 0$ rotational transitions ($k_{rot_{2\leftarrow 0}}$) were calculated as a function of the electron temperature using the cross section reported by Itikawa for N_2 [54] and by Yoon *et al* for H_2 [53]. O_2 could not be included in the figures since no similar reliable experimental rotational cross sections were found [52]. Consequently, the rate constants of the other rotational transitions were calculated using an Arrhenius equation [50]:

$$k_{rot_{j+2/4/\ldots\leftarrow j}} = k_{rot_{2\leftarrow 0}} \exp\left(-\frac{\Delta E_{rot_{j+2/4/\ldots\leftarrow j}} - E_{rot_2}}{T_e}\right) \tag{15}$$

This approximation is justified by the fact that, according to Kutz and Meyer [55], the cross sections fall off exponentially with increasing Δj.

As presented in figure 3.9(b), a global trend is now observed for neutral gas heating when T_g values are linked to the total power transferred per neutral atom calculated from the sum of equations (7)–(9). In addition, electron-impact excitation of rotational levels appears as a key mechanism for neutral gas heating over the range of experimental conditions investigated. Indeed, these collisions are responsible for more than 80% of the total microwave energy transferred from electrons to neutral species while dissociation reactions play a negligible role. Other mechanisms such as electron-impact excitation of vibrational levels and diatomic molecule dissociation by Ar metastable states and ions were also investigated but found to be negligible with regards to neutral gas heating. This conclusion is due to the numerous rotational levels (not only the ground state one) being significantly populated for the range of gas temperature of interest here. As such, they all contribute significantly to the overall energy transferred and the sum of their contribution is what makes rotation the dominant

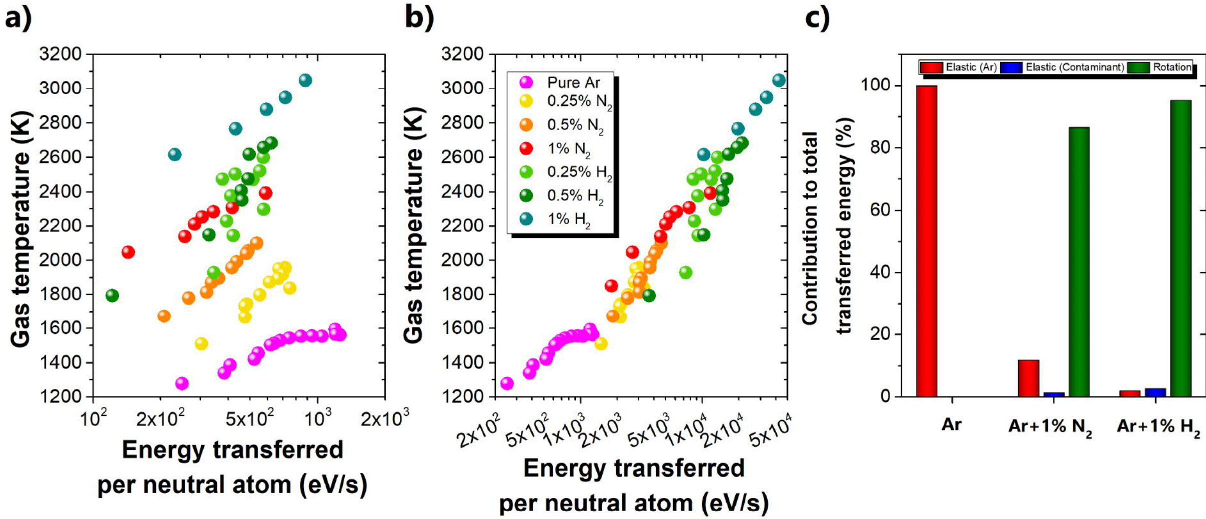

Figure 3.9. Neutral gas temperature as a function of the power transferred per neutral atom when considering (a) only elastic collisions with neutrals and (b) elastic collisions as well as dissociation and rotation excitation reactions. (c) Relative contribution to neutral gas heating of the various mechanisms.

mechanism. Figure 3.9(c) also shows that hydrogen species are able to transfer more energy through rotational states than nitrogen.

In figure 3.9, it can be concluded that most of the power leading to neutral gas heating involves excitation of rotational levels by electron impact. However, this certainly does not mean this power is the only mechanism involved in the >80% of microwave power absorbed by the N_2, O_2 and H_2 admixtures observed in figure 3.8. In fact, in addition to rotational excitation, power dissipation also occur through electron-impact excitation of vibrational and electronic states, electron-impact ionization and dissociation, etc. Moreover, inspired by the results in nominally pure argon plasmas, these inelastic reactions are expected to dominate for electron temperature above the 1 eV range [58]. As a consequence, one readily expects much higher values of the power dissipated per electron in presence of N_2, O_2, and H_2 admixtures [59,60]; this explains the lower plasma column lengths observed in this study with N_2, O_2, and H_2 at fixed absorbed power (see figure 3.6).

3.2.6. Conclusion

The axial profiles of the neutral gas temperature, electron temperature, electron number density, and argon metastable number density were analyzed along atmospheric pressure plasma columns sustained by microwave electromagnetic fields. This study was realized by

means of optical emission and absorption spectroscopy coupled with collisional radiative modelling. The influence of diatomic molecules, namely N_2, O_2, and H_2, was examined in details. The results show that the axial behaviours of the plasma parameters along the microwave plasma column remain fairly the same in nominally pure argon plasmas and in presence of N_2, O_2, and H_2 admixtures: from the wave launcher to the column end, n_e and T_g decrease while n_{1s_5} and T_e remain constant. However, their values at a given position are strongly modified when increasing the amount of admixture. Indeed, with the addition of N_2, O_2, and H_2, T_g increases, n_e decreases, n_{1s_5} and T_e first decreases and then increases. Furthermore, an electron power balance analysis has revealed that fewer than 1% of contaminants took more than 80% of the input power. In addition, an investigation of the neutral gas heating has indicated the rise of Tg in presence of N_2, O_2, and H_2 was mostly linked to electron-impact excitation of rotational levels.

The N_2, O_2, and H_2 admixtures examined in this study were chosen because of their simplicity, helping in the understanding of their individual impacts on the plasma physics and chemistry. However, since nitrogen, oxygen, and hydrogen atoms are present in numerous precursors used in a wide variety of applications, in particular in materials processing, the obtained results can now be used as building blocks in the understanding of the impacts of such precursors on the plasma properties. Further studies involving the injection of some of these larger precursors are now under way.

Acknowledgments

The equipment used in this work was acquired through the Leaders Opportunity Fund of the Canadian Foundation for Innovation (CFI). Financial supports from the National Science and Engineering Research Council (NSERC) of Canada are also acknowledged.

References

[1] Levasseur O, Stafford L, Gherardi N, Naudé N, Blanchard V, Blanchet P, Riedl B and Sarkissian A 2012 Plasma Process. Polym. 9 1168

[2] Yi J W, Moon M W, Faruque Ahmed S, Kim H, Cha T G, Kim H Y, Kim S S and Lee K R 2010 Langmuir 26 17203

[3] Chevallier P, Turgeon S, Sarra-Bournet C, Turcotte R and Laroche G 2011 ACS Appl. Mater. Interfaces 3 750

[4] Wu Y, Bekke M, Inoue Y, Sugimura H, Kitaguchi H, Liu C and Takai O 2004 Thin Solid Films 457 122

[5] Vennekamp M, Bauer I, Groh M, Sperling E, Ueberlein S, Myndyk M, Mäder G and Kaskel S 2011 Beilstein J. Nanotechnol. 2 665

[6] Hassani S, Klemberg-Sapieha J E and Martinu L 2010 Surf. Coat. Technol. 205 1426

[7] Pougoum F, Qian J, Laberge M, Martinu L, Klemberg-Sapieha J, Zhou Z, Li K Y, Savoie S and Schulz R 2018 Surf. Coat. Technol. 350 699

[8] Kilicaslan A, Levasseur O, Roy-Garofano V, Profili J, Moisan M, Cote C, Sarkissian A and Stafford L 2014 J. Appl. Phys. 115 113301

[9] Kabouzi Y, Moisan M, Rostaing J C, Trassy C, Guérin D, Kéroack D and Zakrzewski Z 2003 J. Appl. Phys. 93 9483

[10] Silva T, Britun N, Godfroid T, Van Der Mullen J and Snyders R 2016 J. Appl. Phys. 119 173302

[11] Mitsingas C M, Rajasegar R, Hammack S, Do H and Lee T 2016 IEEE Trans. Plasma Sci. 44 651

[12] Van Rooij G J, Van Den Bekerom D C M, Den Harder N, Minea T, Berden G, Bongers W A, Engeln R, Graswinckel M F, Zoethout E and Van De Sanden M C M 2015 Faraday Discuss. 183 233

[13] Park G Y, Hong Y J, Lee H W, Sim J Y and Lee J K 2010 Plasma Process. Polym. 7 281

[14] Uhm H S, Lim J P and Li S Z 2007 Appl. Phys. Lett. 90 261501

[15] Bundaleska N, Tsyganov D, Dias A, Felizardo E, Henriques J, Dias F M, Abrashev M, Kissovski J and Tatarova E 2018 Phys. Chem. Chem. Phys. 20 13810

[16] Chun-Ku C and Jonathan P 2002 J. Phys. D: Appl. Phys. 35 998

[17] Levasseur O, Stafford L, Gherardi N, Naudé N, Beche E, Esvan J, Blanchet P, Riedl B and Sarkissian A 2013 Surf. Coat. Technol. 234 42

[18] Desjardins E, Laurent M, Durocher-Jean A, Laroche G, Gherardi N, Naudé N and Stafford L 2018 Plasma Sources Sci. Technol. 27 015015

[19] Park G, Lee H, Kim G and Lee J K 2008 Plasma Process. Polym. 5 569

[20] Van Gessel B, Brandenburg R and Bruggeman P 2013 Appl. Phys. Lett. 103 1

[21] Castaños-Martínez E, Moisan M and Kabouzi Y 2009 J. Phys. D: Appl. Phys. 42 12003

[22] Martínez J, Castaños-Martínez E, González-Gago C, Rincón R, Calzada M D and Muñoz J 2018 Plasma Sources Sci. Technol. 27 077001

[23] Durocher-Jean A, Desjardins E and Stafford L 2019 Phys. Plasmas 26 063516

[24] Chilton J E, Boffard J B, Schappe R S and Lin C C 1998 Phys. Rev. A 57 267

[25] Gangwar R K, Sharma L, Srivastava R and Stauffer A D 2012 J. Appl. Phys. 111 053307

[26] Nguyen T D and Sadeghi N 1978 Phys. Rev. A 18 1388

[27] Kramida A, Ralchenko Yu, Reader J and NIST ASD Team 2015 NIST Atomic Spectra Database (ver. 5.6.1)

[28] Chang R S F and Setser D W 1978 J. Chem. Phys. 69 3885

[29] Zhu X-M and Pu Y-K 2009 J. Phys. D: Appl. Phys. 43 015204

[30] Van Gaens W and Bogaerts A 2013 J. Phys. D: Appl. Phys. 46 275201

[31] Zhu X M, Pu Y K, Balcon N and Boswell R 2009 J. Phys. D: Appl. Phys. 42 142003

[32] Santiago I and Calzada M D 2009 IEEE Trans. Plasma Sci. 37 790

[33] Griem H R 1964 Plasma Spectroscopy (New York: McGraw-Hill)

[34] Christova M, Castanos-Martinez E, Calzada M D, Kabouzi Y, Luque J M and Moisan M 2004 Appl. Spectrosc. 58 1032

[35] Timmermans E A H, Jonkers J, Thomas I A J, Rodero A, Quintero M C, Sola A, Gamero A and Van Der Mullen J A M 1998 Spectrochim. Acta B 53 1553

[36] Potocnáková L, Hnilica J and Kudrle V 2014 Open Chem. 13 541

[37] Moon S Y and Choe W 2006 Phys. Plasmas 13 103503

[38] Palomares J M, Iordanova E I, Gamero A, Sola A and v d Mullen J J A M 2010 J. Phys. D: Appl. Phys. 43 395202

[39] Bravo J A, Rincón R, Muñoz J, Sánchez A and Calzada M D 2015 Plasma Chem. Plasma Process. 35 993

[40] Levasseur O, Kumar Gangwar R, Profili J, Naudé N, Gherardi N and Stafford L 2017 Plasma Process. Polym. 14 1600172

[41] Massines F, Sarra-Bournet C, Fanelli F, Naudé N and Gherardi N 2012 Plasma Process. Polym. 9 1041

[42] Yanguas-Gil A, Cotrino J and Alves L L 2005 J. Phys. D: Appl. Phys. 38 1588

[43] Yasuda H and Hirotsu T 1978 J. Polym. Sci. 16 743

[44] Nisol B, Gagnon H, Lerouge S and Wertheimer M R 2016 Plasma Process. Polym. 13 366

[45] Hegemann D, Hossain M M, Körner E and Balazs D J 2007 Plasma Process. Polym. 4 229

[46] Niermann B, Böke M, Sadeghi N and Winter J 2010 Eur. Phys. J. D 60 489

[47] Benova E, Marinova P and Atanasova M 2018 J. Phys. D: Appl. Phys. 51

[48] Watson S, Nisol B, Lerouge S and Wertheimer M R 2015 Langmuir 31 10125

[49] Kabouzi Y, Graves D B, Castaños-Martínez E and Moisan M 2007 Phys. Rev. E 75 16402

[50] Lieberman M A and Lichtenberg A J 2005 Principles of Plasma Discharges and Materials Processing (New York: Wiley)

[51] Donnelly V M and Malyshev M V 2000 Appl. Phys. Lett. 77 2467

[52] Itikawa Y 2009 J. Phys. Chem. Ref. Data 38 1

[53] Yoon J-S, Song M-Y, Han J-M, Hwang S H, Chang W-S, Lee B and Itikawa Y 2008 J. Phys. Chem. Ref. Data 37 913

[54] Itikawa Y 2006 J. Phys. Chem. Ref. Data 35 31

[55] Kutz H and Meyer H-D 1995 Phys. Rev. A 51 3819

[56] Castaños-Martínez E and Moisan M 2010 Spectrochim. Acta B 65 199

[57] Rincón R, Muñoz J and Calzada M D 2015 Spectrochim. Acta B 103–4 14

[58] Moisan M and Pelletier J 2012 Physics of Collisional Plasmas: Introduction to High-Frequency Discharges (Berlin: Springer)

[59] Ferreira C M and Moisan M 1988 Phys. Scr. 38 382

[60] Margot J, Vidal F, Chaker M, Johnston T W, Aliouchouche A, Tabbal M, Delprat S, Pauna O and Benhabib D 2001 Plasma Sources Sci. Technol. 10 556

3.3. Article 4 : Comparaison des diagnostics optiques et électriques quant au bilan énergétique du précurseur dans la DBD d'argon à la pression atmosphérique

Le bilan de puissance dont il a été question dans la section 3.2 permet notamment le calcul d'une puissance absorbée par molécule réactive insérée. Tel que mentionné en début de chapitre, un tel paramètre a souvent été utilisé, par exemple, pour établir des liens entre le plasma et les propriétés physiques et chimiques d'un revêtement déposé, de sorte que l'essor des procédés à la PA a ainsi mené à l'apparition de méthodes de calcul spécifiquement consacrées. En particulier, une méthode basée sur des diagnostics électriques a fait l'objet d'articles s'intéressant chacun à des familles de précurseurs pouvant être insérés dans un plasma en vue d'une panoplie d'applications [26, 51–54, 63, 64]. Ainsi, la question de comparer les résultats obtenus selon les deux approches se pose naturellement et c'est l'objectif qui a été visé dans le cadre d'un quatrième article.

Pour parvenir à cette comparaison, les mesures ont été effectuées dans une DBD d'argon à la PA, un tel réacteur permettant l'acquisition simultanée des courbes I-V nécessaires au diagnostic électrique et des spectres d'émission nécessaires au diagnostic optique. Des quantités croissantes de deux précurseurs (anhydride acétique et anhydride isobutyrique) ont été ajoutées à l'argon afin de suivre le pourcentage de puissance prise par eux. Pour de faibles concentrations ($\ll 1\%$), il s'avère que les deux méthodes sont relativement en accord entre elles. Cependant, pour de plus grandes concentrations ($\sim$0.1%), une différence notable est observée et est attribuable aux modifications significatives des caractéristiques du plasma. En effet, ces modifications (augmentation de la densité électronique, diminution de la température électronique et de la densité des états 1s de l'argon) sont prises en compte de manière inhérente par le diagnostic optique mais entièrement ignorées par le diagnostic électrique.

Energy uptake by precursor molecules in dielectric barrier discharges : a comparison between electrical and optical diagnostics

par

Antoine Durocher-Jean[1], Simon Boivin[1], Jacopo Profili[1], et Luc Stafford[1]

([1]) Département de physique, Université de Montréal, Montréal, Québec, Canada

Cet article sera soumis pour publication prochainement.

Les contributions des différents auteurs à cet article sont :

- Antoine Durocher-Jean : Analyses des résultats optiques, comparaison des approches et écriture du premier jet du manuscrit
- Jacopo Profili : Prise des mesures, analyse des résultats électriques, révision du manuscrit
- Simon Boivin : Aide à l'analyse des résultats optiques et électriques
- Luc Stafford : Supervision des travaux, révision du manuscrit

Abstract.

Optical emission spectroscopy combined with collisional-radiative modelling of argon 2p-1s transitions was used to calculate the relative energy uptake by anhydride precursor molecules in argon-based dielectric barrier discharges at atmospheric pressure. For low precursor concentrations, the optical method revealed comparable energy uptakes with respect to those obtained from detailed analysis of the current-voltage characteristics. At higher concentrations, however, variations were noticed. Such discrepancy was mostly ascribed to changes in the electron temperature, electron number density, and population of argon 1s atoms as the precursor concentration in the argon-based discharge increases.

Keywords: Optical emission spectroscopy, collisional-radiative modelling, dielectric barrier discharges, energy uptake by precursor molecules

3.4.1. Introduction

Plasma-enhanced chemical vapour deposition (PECVD) is a well-known process for thin film deposition (for example, nanocomposites [1-3], metallics [4,5], organics [6-8]) on substrates near ambient temperatures. This method relies on the addition of precursor molecules in non-thermal (non-equilibrium) plasmas and the corresponding fragmentation of the precursor molecules by plasma-generated species, in particular high-energy electrons, metastable and resonant atoms and molecules, and UV photons [9,10]. In process development and optimization, significant research efforts are devoted to the relationships between plasma deposition kinetics and gas phase physico-chemistry. From the pioneering studies of Yasuda and Hirotsu [11], the calculation of the energy uptake per precursor molecule can provide very useful insights into such connections. For example, in recent years, Hegemann *et al.* have evidenced a link between the W/F ratio (W being the absorbed power and F the precursor flow rate) and the formation of reactive intermediates in low pressure RF plasma [12-14]. More recently, Wertheimer and co-workers have examined the current-voltage characteristics of argon (Ar)-based dielectric barrier discharges (DBDs) at atmospheric pressure with and without the precursor molecules and have reported values of the energy uptake by precursor molecules for a wide variety of precursors and experimental conditions [15-19]. In parallel to these studies, an optical method based on optical emission spectroscopy (OES) combined with collisional-radiative (CR) modelling of argon 2p-1s transitions was developed and used to analyze the electron kinetics in non-thermal argon plasmas at atmospheric pressure [20,21]. This method was also used to calculate the relative energy uptake by N_2, O_2 or H_2 admixtures in microwave Ar plasmas [20].

The objective of this work is to compare the values of the relative energy uptake by precursor molecules obtained from optical and electrical diagnostics. This is realized in the specific case of acetic anhydride (AA) and isobutyric anhydride (IA) precursors in Ar-based DBDs at atmospheric pressure relevant for the deposition of carboxylic acid groups for biodegradable and biomedical applications [22-25]. While both methods show a good agreement for low precursor concentrations, significant variations are observed at higher concentrations; this feature seems mostly linked to changes in the electron temperature, electron number density, and population of Ar 1s atoms as the number density of precursor molecules in the Ar-based DBD increases.

3.4.2. Description of the electrical method

As suggested by other authors [15-19], the energy uptake by precursor molecules in plane-to-plane dielectric barrier discharges at atmospheric pressure can be obtained through detailed analysis of the current-voltage characteristics. More specifically, this electrical diagnostic requires the calculation of the energy absorbed by electrons from the electric field per cycle of the applied voltage (E_g):

$$E_g = \frac{1}{n} \int_t V_{gap} \, I_d \, dt \tag{1}$$

where n is the number of cycles over which the integration is performed. In Equation (1), the voltage across the gas gap (V_{gap}) and the discharge current (I_d) can be obtained from the measured applied voltage and total measured current (discharge current plus displacement current) using an equivalent circuit model [15]. Then, it is assumed in the approach proposed by other authors [15-19] that the energy uptake by precursor molecules simply corresponds to the difference between the energy absorbed by electrons per cycle of the applied electric field in the nominally pure Ar case ($E_g\,(Ar)$) and the one when precursor molecules are injected into the Ar plasma ($E_g\,(Ar + Prec)$). For comparison purposes with the optical method in the upcoming section, these absolute values can here be expressed as percentages:

$$\Delta E_g^{electrical}\,(\%) = \frac{E_g\,(Ar) - E_g\,(Ar + Prec)}{E_g\,(Ar)} \times 100 \tag{2}$$

In Equation (2), it is worth highlighting that it is implicitly assumed that the fundamental properties of the background Ar plasma remain "unaltered" following the addition of the precursor molecules, such that $\Delta E_g^{electrical}$ goes directly to the precursor molecules. This aspect will be discussed in more details below.

3.4.3. Description of the optical method

As for the optical method, it relies on detailed analysis of the electron power losses using the neutral gas temperature (T_g), the electron temperature (T_e), the electron number density (n_e), and the population of Ar 1s atoms (n_{1s}, Paschen notation) as input parameters (see additional details below). For the Ar-based DBDs examined in this study, T_g can be assumed close to 300 K [15]. As for T_e and n_{1s}, it can be obtained from optical emission spectroscopy combined with collisional-radiative modelling of Ar 2p-1s transitions. Since the method was

detailed elsewhere [21,26], only a summary is presented here. For all operating conditions reported below, an experimental optical emission spectrum was recorded between 700 and 900 nm using a wavelength-calibrated and intensity-calibrated optical emission spectrometer (Avantes AvasSpec-3648-2-USB2). The spectral resolution (full width at half maximum) of this apparatus was about 0.24 nm; this resolution was enough to resolve most of the Ar emission lines in the 700-900 nm wavelength range. The relative line emission intensities from Ar 2p levels obtained from the experiments were then compared to those predicted by a CR model describing the populations of Ar 2p states. In this model, the emission intensity of Ar I line (I_λ) linked to a specific 2p$_i$-to-1s$_j$ transition is given by:

$$I_\lambda = A_{ij} n_{2p_i} \theta_{ij} \tag{3}$$

where A_{ij} is the spontaneous emission Einstein coefficient for the 2p$_i$-to-1s$_j$ transition, n_{2p_i} is the number density of the emitting 2p$_i$ level, and θ_{ij} is the escape factor in optically thick media. Therefore, the role of the CR model is to find the optimal n_{2p_i} and θ_{ij} values that fit the relative line emission intensities obtained in the experiments. As detailed in [26], θ_{ij} can be obtained from the radiative transfer equation averaged over the line of sight while n_{2p_i} can be obtained from the steady-state particle balance equation of the Ar 2p$_i$ state:

$$n_{2p_i} = \frac{n_e\left(k_{g-2p_i}\ n_g + \sum_j k_{1s_j-2p_i}\ n_{1s_j}\right) + \sum_{k\neq i} k_{2p_k-2p_i}\ n_g\ n_{2p_k}}{\sum_j A_{ij}\ \theta_{ij} + k_{2p_i-1s_j}\ n_g + \sum_{k\neq i} k_{2p_i-2p_k}\ n_g + \sum_{Cont.} k_{Quench}\ n_{Prec.}} \tag{4}$$

where n_g is the number density of ground state Ar atoms (2.4×10^{25} m^{-3} at atmospheric pressure for T_g=300 K [15]), $k_{g-2p_i} = k_{g-2p_i}(T_e)$ is the reaction rate for the electron impact excitation of Ar 2p$_i$ states from ground state Ar atoms, $k_{1s_j-2p_i} = k_{1s_j-2p_i}(T_e)$ is the stepwise electron impact excitation of Ar 2p$_i$ states from Ar 1s$_j$ levels, $k_{2p_k-2p_i}$ and $k_{2p_i-2p_k}$ are the reaction rates for excitation transfers among the 2p$_i$ states by collisions with ground state Ar atoms, $k_{2p_i-1s_j}$ and k_{Quench} are the reaction rates for quenching of Ar 2p$_i$ states by collisions with ground state Ar atoms and precursor molecules, and $n_{Prec.}$ is the number density of precursor molecules. Here, $n_{Prec.}$ is calculated with respect to n_g from the concentration fraction of the precursor molecules. For example, in a nominally pure Ar plasma with 0.05% of anhydride precursor, $n_{Prec.} = 0.05\%\ n_g$. Since the quenching rate of Ar 2p$_i$ states by AA and IA could not be found in the literature, the molecules were considered in the particle balance equation of Ar 2p$_i$ states as if they were the sum of CO_2 and CH_3 fragments (1 AA

molecule = 1.5 CO_2 + 2 CH_3; 1 IA = 1.5 CO_2 + 6 CH_3). The quenching rates of Ar 2p$_i$ states by CO_2 and CH_3 were reported in [27]. It is worth highlighting that comparable values of T_e and n_{1s} were obtained with and without the inclusion of these quenching reactions in the collisional-radiative model; this reveals that quenching of Ar 2p$_i$ states by collisions with AA and IA play no significant role in the particle balance equations of Ar 2p$_i$ states. This comment does not hold for Ar 1s states for which Penning excitation and ionisation reactions are known to play a very significant role in the discharge physics and chemistry [9]. In particular, in Ar-based DBDs, Penning ionization processes become the predominant source of electron production for many precursor molecules used for thin film deposition [28].

In Equation (4), n_e appears in every term of the numerator (implicit in all the n_{2p_k} terms). Therefore, the electron number density acts as a scaling factor for the absolute number density of the Ar 2p levels and thus for the absolute line emission intensity (see Equation (4)). In the approach used in this study, relative emission intensities are computed from the CR model as a function of T_e and n_{1s}. These relative emission intensities were then compared to the ones obtained from the experiments. For each experimental spectrum, and thus for each experimental condition, the values of T_e and n_{1s} that yield the most accurate fit of the experimental data is assumed to be the actual electron temperature and population of Ar 1s atoms in the Ar-based plasma. Since only relative emission intensities, and not absolute emission intensities, are compared, the method used to extract T_e and n_{1s} from the best fit of the experimental data is thus independent of n_e [21,26].

In DBDs, the electron number densities are typically too small to be accurately obtained from Stark broadening method [29]. However, as described in [26], the combination of equations (3) and (4) for two sets of experimental conditions can provide relative values of the electron number density according to

$$\frac{n_{e_i}}{n_{e_{Ref}}} = \frac{I_i}{I_{Ref}} \frac{\theta_{Ref}}{\theta_i} \frac{n'_{2p_{2-Ref}}}{n'_{2p_{2-i}}} \tag{5}$$

where I_i/I_{Ref} is the relative emission intensity of the Ar 2p$_1$-1s$_2$ transition at 750.4 nm, θ_{Ref}/θ_i is ratio of escape factors for the Ar 2p$_1$-1s$_2$ transition, and $n'_{2p_{1-i}}/n'_{2p_{1-Ref}}$ is the population ratio of Ar 2p$_1$ states. In Equation (5), I_i/I_{Ref} is obtained from the experimental data while θ_{Ref}/θ_i and $n'_{2p_{1-i}}/n'_{2p_{1-Ref}}$ are obtained from the combination of optical emission spectroscopy and collisional-radiative modelling of Ar 2p$_i$-to-1s$_j$ transitions.

The absolute values of T_e and n_{1s} combined with the relative values of n_e obtained from optical diagnostics can then used to calculate the power being dissipated by the electrons P_{diss} though collisions with neutral Ar atoms. The following collisions were considered: elastic collisions, direct and stepwise ionization, direct excitation of the Ar 1s and Ar 2p levels, and stepwise excitation of the Ar 2p levels via the Ar 1s levels

$$P_{diss} = n_e V \left(k_{el}\ n_g \frac{2m_e M_{Ar}}{(m_e + M_{Ar})^2} \left(\frac{3}{2} T_e - \frac{3}{2} T_g \right) + k_{ion-d}\ n_g\ \Delta E_{ion-d} \right.$$
$$+ \sum_j \left(k_{ion-s}\ n_{1s_j} \left(\Delta E_{ion-d} - \Delta E_{1s_j} \right) + k_{1s_j}\ n_g\ \Delta E_{1s_j} \right)$$
$$\left. + \sum_k \left(k_{2p_k}\ n_g\ \Delta E_{2p_k} + \sum_j k_{1s_j - 2p_k}\ n_{1s} \left(\Delta E_{2p_k} - \Delta E_{1s_j} \right) \right) \right) \quad (6)$$

In Equation (6), k_i=$k_i(T_e)$ are the reaction rates calculated from the corresponding cross-sections [30-32], ΔE_{ion-d}, ΔE_{1s} and ΔE_{2p} are the threshold energies for electron-impact ionization of Ar atoms, electron-impact excitation of Ar atoms leading to 1s atoms, and electron-impact excitation of Ar atoms leading to 2p atoms, respectively, and V is the plasma volume in which the power is dissipated. In Equation (6), only relative values of n_e were used so that only relative values of the power dissipated by electrons through collisions with neutral argon atoms can be determined. The relative values of P_{diss} can then be compared to the corresponding value achieved in nominally pure Ar plasma to obtain the relative power uptake by precursor molecules:

$$\Delta E_g^{optical}\,(\%) = \frac{onP_{diss}^{Ar} - onP_{diss}^{Ar+Prec}}{onP_{diss}^{Ar}} \times 100 \quad (7)$$

In Ar-based DBDs, it is worth highlighting that mostly electrons absorb the energy from the applied electrical field (the ion mass is much larger than the electron mass). As enumerated in Equation (6), these electrons can then directly dissipate their energy through elastic and inelastic collisions to form electrons, Ar ions, excited Ar species, etc. Furthermore, the Ar-species can form other Ar-species by gas-phase collisions, for example, gas-phase recombination between neutral Ar species leading to the formation of Ar_2 species (neutrals and ions) [33,34]. Ultimately, all of these plasma-generated species can produce radiation and heating power losses [35-37]. These aspects are illustrated in Figure 3.10.

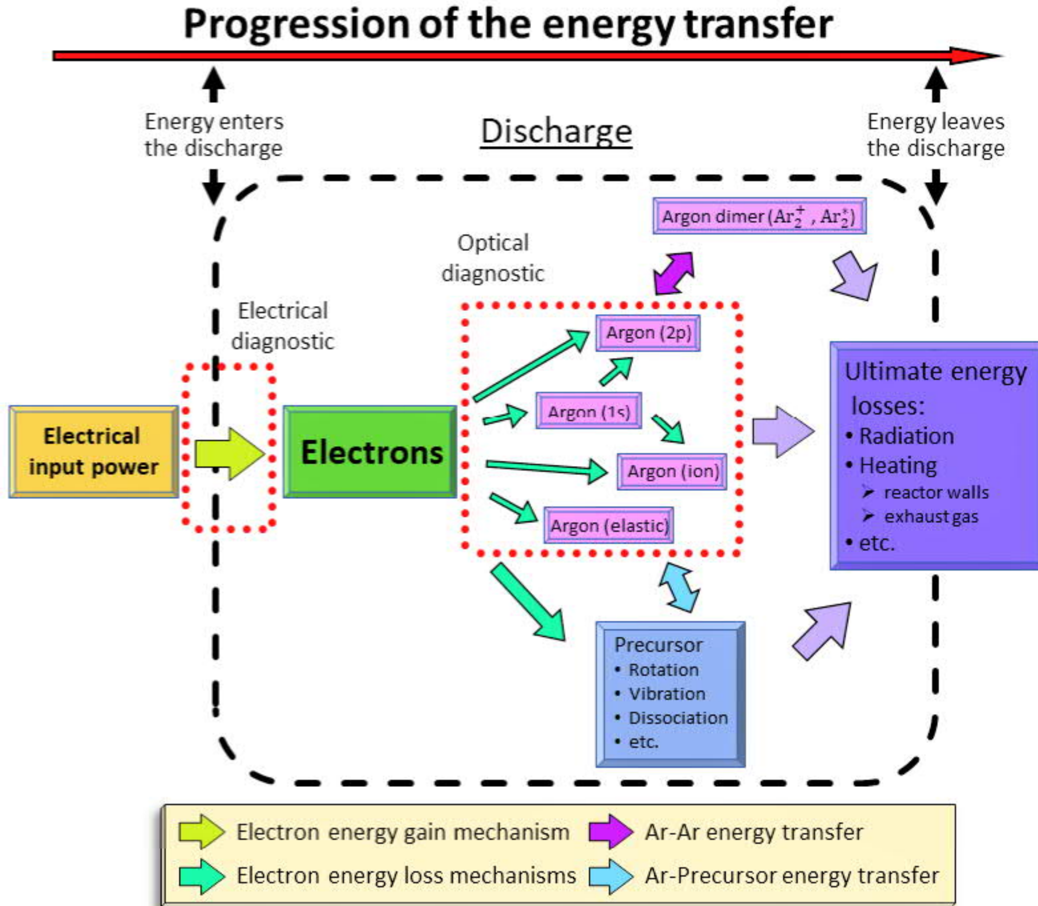

Figure 3.10. Schematics of the power absorption and dissipation in Ar-based DBDs. While the electrical diagnostic defines the absorption of the electrical power by electrons, the optical diagnostic describes the dissipation of the electron energy following their collisions with neutral Ar atoms.

From Figure 3.10, it can be concluded that electrical diagnostics (Equation (1)) thus mainly concern the absorption of the electrical energy by electrons while optical diagnostics (Equation (7)) describe the dissipation of the electron energy following their collisions with neutral Ar atoms. In this framework, since gas-phase collisions between neutral Ar species do not directly consume electron energy, they do not appear in Equation (6). Therefore, since all power that could have gone from the electric field to the electrons and then from the electrons to the neutral Ar atoms to form electrons, ions, excited Ar species, etc. was considered in Equation (6), any difference between onP_{diss}^{Ar} and $onP_{diss}^{Ar+Prec}$ can readily be attributed to the power uptake by the precursor molecules.

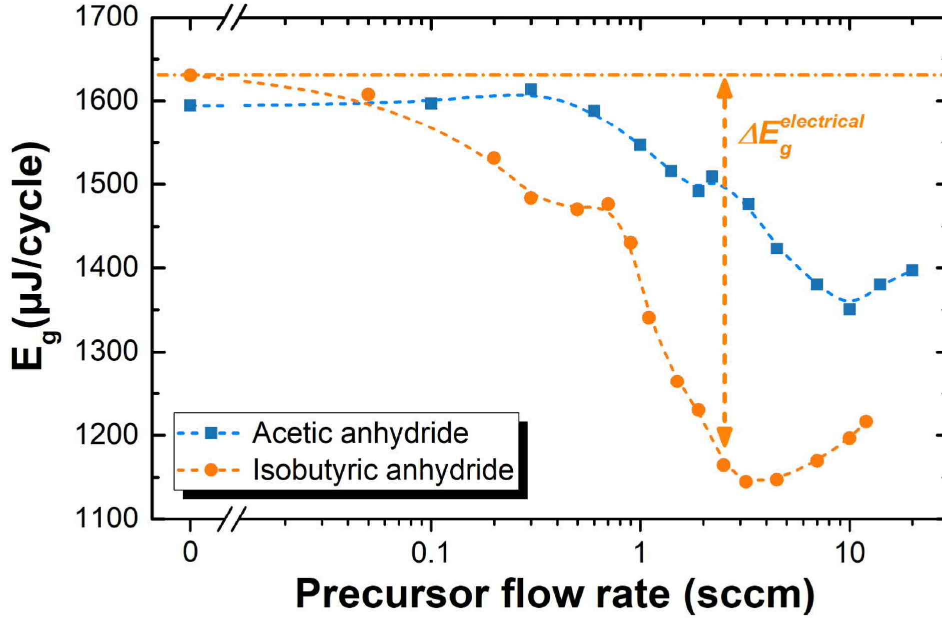

Figure 3.11. Electrical measurements of E_g as a function of the precursor flow rate.

3.4.4. Results and discussion

All electrical measurements of Ar-based DBDs presented in this work were obtained from previous studies realized in the specific case of AA and IA precursors [25]. These experiments were carried out at constant frequency (20 kHz) and applied voltage (8 kV_{pp} peak-to-peak, 2.8 kV_{rms}). Figure 3.11 shows the corresponding E_g values as a function of the precursor flow rate, F_p, for both anhydride precursors, AA and IA.

Every value for a given precursor flow rate is lower than the one for the nominally pure Ar case (0 sccm). As observed for many other precursors [15-17], this absorbed energy E_g typically decreases with F_p at low precursor concentration fractions. In addition, as suggested by other authors [15-17], the energy uptake by precursor molecules can be interpreted as the difference between the energy absorbed by electrons per cycle of the applied electric field in the nominally pure Ar case and the one when precursor molecules are injected into the Ar plasma (denoted as $\Delta E_g^{electrical}$ in Figure 3.10).

In parallel with the electrical characterization, the influence of F_p on T_e, n_e, and n_{1s} values obtained from optical emission spectroscopy and CR modelling of Ar $2p_i$-to-$1s_j$ transitions over the same range of experimental conditions are presented in Figure 3.12.

Decreases in T_e (~0.85 eV to ~0.70 eV) as well as in n_{1s} (~6×10^{16} m^{-3} to ~2×10^{16} m^{-3}) are observed in Figure 3 with increasing F_p. These values are comparable to those reported

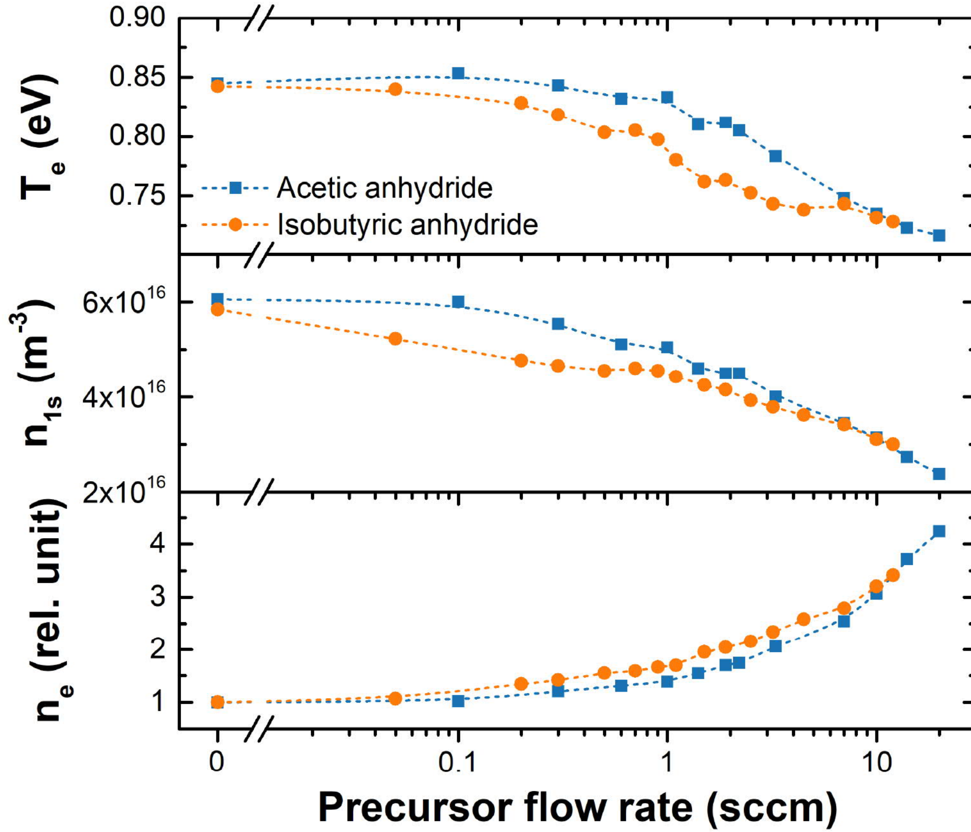

Figure 3.12. Influence of the precursor flow rate on the electron temperature, argon 1s number density and relative electron number density obtained from optical emission spectroscopy combined with collisional-radiative modelling of argon $2p_i$-to-$1s_j$ transitions.

in the literature for similar experimental conditions [21,38,39]. From this set of data, one readily concludes that the addition of anhydride precursors has a meaningful impact on the properties of Ar-based DBDs. This conclusion is further supported by the concomitant rise of the relative electron number density. This increase was also observed by Loffaehen *et al.* in fluid modeling of Ar-based discharges in presence of hexamethyldisiloxane [28]. These trends can be readily explained by the fact that most precursors used for thin film deposition, as well as their elementary hydrogen, oxygen and carbon atoms, have a lower ionization threshold than Ar species. Consequently, electrons are more easily created (rise of n_e) and require less energy to sustain and maintain the plasma (decrease of T_e). In line with these results, the diminution of T_e combined with the rise of the quenching frequency with the increase of the concentration fraction of precursor molecules should lead to a decrease of n_{1s}, as seen in the experiments [26].

Relative values of the energy uptake by precursor molecules ΔE_g obtained from electrical (Equation (2)) and optical (Equation (8)) diagnostics are compared in Figure 3.13. For most of the precursor flow rates, both methods show an increase in ΔE_g with F_p. In addition, both techniques feature variations on smaller scales, for example a small dip can be seen around 1 sccm for the IA precursor. Interestingly, such a dip was also observed for other precursors and was linked to bonded oxygen atoms, especially in precursors with low C/O ratios [17,40]. Figure 4 further reveals that while $\Delta E_g^{optical}$ monotonously increases with F_p, $\Delta E_g^{electrical}$ seems to reach a plateau at higher F_p values. A small maximum of $\Delta E_g^{electrical}$ can even be distinguished at higher flow rates for the IA precursor. In this context, both methods show a good agreement for low precursor concentrations. However, a significant difference between $\Delta E_g^{optical}$ and $\Delta E_g^{electrical}$ occurs at higher precursor concentrations.

In order to better understand the observed discrepancy at higher F_p, it is worth looking at the diagnostics first independently. On the one side, $\Delta E_g^{electrical}$ was hypothesized by other authors to be the amount of energy provided by the background Ar plasma "reservoir" to the precursor molecules [15]. As such, its ascending/descending behaviour observed here (as well as for other precursor molecules) can be ascribed to a shift in the operating regime, going from a monomer-lean/excess-energy regime to a monomer-rich/energy-deficient regime [11,15]. Indeed, for small values of F_p, all precursor molecules are assumed to undergo a certain number of reactions during their residence time in the discharge. In contrast, when they are injected into the Ar-based plasma above a specific threshold amount (corresponding to the value of the flow value at which $\Delta E_g^{electrical}$ reaches a maximum), either the reservoir starts failing to react with all of the precursor molecules or that the number of reaction events per precursor molecule starts to decrease due to a decrease in the population of active species in the plasma reservoir.

On the other side, $\Delta E_g^{optical}$ represents the amount of the injected power being dissipated through electron collisions with the precursor molecules. As also observed in [20], this value increases with the concentration fraction of the precursor molecules in the Ar plasma. Another interesting feature is that even at small flow rates (1-10 sccm versus 10 slm for the Ar carrier gas), the small amounts of anhydride precursors absorb more than 50% of the electrical power. Consequently, in such conditions, the plasma can hardly be considered as an Ar-dominated plasma but rather as a precursor-dominated plasma with the latter

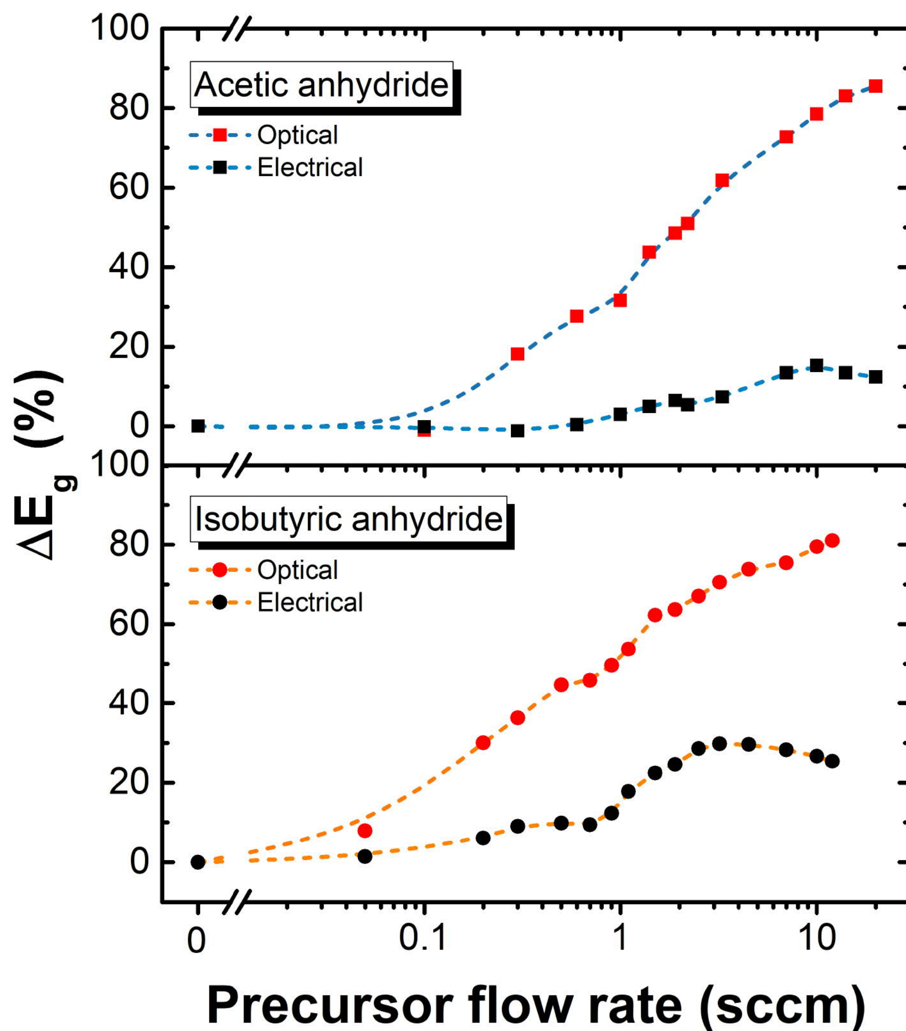

Figure 3.13. Optical and electrical value of ΔE_g as a function of the flow rate for both precursors.

acting as the principal energy recipient. A similar conclusion was reached by Niermann *et al* [41]: the authors noticed that as little as 0.5% of Ar into a He RF plasma at atmospheric pressure was sufficient to dominate the discharge physics. Similar results were reported by Castanos-Martinez in a Ne microwave plasma at atmospheric pressure with small amounts of Ar [42].

In line with this discussion, the two anhydride precursors cannot be responsible for the disparity between electrical and optical methods since they both provide reasonable trends with respect to previous findings reported in literature. Similar results were also observed for other anhydride precursors (not shown here). Instead, such discrepancy can most likely

be linked to gradual changes in the plasma parameters as precursor molecules are added in the Ar-based plasma. From OES analysis combined with CR modelling of Ar 2p$_i$-to-1s$_j$ transitions, T_e and n_{1s} continuously decrease and n_e continuously increases as F_p increases. While these changes of T_e, n_{1s} and n_e were explicitly considered in the electron power dissipation of the optical method described by Equations (6) and (7), the Ar "reservoir" involved in the absorption of the electrical power by electrons was assumed constant for all precursor concentrations in the electrical diagnostics. While this could be a reasonable approximation at very low precursor concentrations, the changes of T_e, n_{1s} and n_e can become significant at higher precursor concentrations, as seen in Figure 3.12 and 3.13. In such conditions, the energy uptake by precursor molecules obtained from electrical measurements can either be underestimated or overestimated. This depends on whether the energy "reservoir" involved in the absorption of the electrical power by electrons for the Ar plasma decreases or increases in presence of the precursor molecules. For the anhydride precursors examined in this work, $\Delta E_g^{electrical}$ measurements seem underestimated by at least a factor of 2 between 1 and 10 sccm due to the corresponding decrease of T_e and n_{1s} and the corresponding increase of n_e as the concentration fraction of precursors in the Ar-based plasma increases. In addition to the inherent changes of T_e, n_e and n_{1s} upon injection of the precursor molecules, discrepancies could also be linked to spatial variations along the gas flow lines. While electrical measurements are averaged over the whole electrode surface, optical measurements are inherently localized over a specific region of the plasma in large-scale deposition tools [28].

3.4.5. Conclusion

In this work, electrical and optical diagnostics were used to determine the relative energy uptake by precursor molecules in Ar-based dielectric barrier discharges in presence of acetic anhydride (AA) and isobutyric anhydride (IA). Individually, both methods provide results that are consistent with previous studies reported in the literature. The electrical diagnostic reveals a transition from a monomer-lean/excess-energy regime to a monomer-rich/energy-deficient regime as the concentration fraction of anhydride precursors in the Ar-based plasma increases. Over the same range of precursor concentrations, the optical diagnostic features a monotonous rise of $\Delta E_g^{optical}$. Consequently, the two methods agree very well for low concentrations of precursors but differ significantly as more precursors are

added to the Ar plasma. Based on optical emission spectroscopy measurements coupled with collisional-radiative modelling of Ar $2p_i$-to-$1s_j$ transitions, this discrepancy can be linked to gradual changes of the electron temperature, electron number density, and population of Ar metastable atoms in presence of precursor molecules such that the energy "reservoir" of the Ar plasma changes significantly as the concentration fraction of the precursor molecules in the Ar plasma increases.

Acknowledgments

The authors are grateful to the Natural Sciences and Engineering Research Council of Canada (NSERC) for the financial support. The authors also thank the "Région Wallonne" and the Fédération Wallonie-Bruxelles for the financial support through the FLYCOAT project and for the travel grant award of J. Mertens in the context of the collaboration between the Université libre de Bruxelles and the Université de Montréal and Polytechnique Montréal.

References

[1] P. Brunet, R. Rincón, Z. Matouk, M. Chaker, and F. Massines, Langmuir 34, 1865 (2018).

[2] J. Profili, O. Levasseur, J. B. Blaisot, A. Koronai, L. Stafford, and N. Gherardi, Plasma Process. Polym. 13, 981 (2016).

[3] J. Profili, O. Levasseur, N. Naudé, C. Chaneac, L. Stafford, and N. Gherardi, J. Appl. Phys. 120, 053302 (2016).

[4] J. L. Hodgkinson, D. Massey, and D. W. Sheel, Surf. Coatings Technol. 230, 260 (2013).

[5] D. W. Sheel and J. L. Hodgkinson, Plasma Process. Polym. 4, 537 (2007).

[6] J. C. Ruiz, A. St-Georges-Robillard, C. Thérésy, S. Lerouge, M. R. Wertheimer, C. The, J. C. Ruiz, S. Lerouge, and M. R. Wertheimer, Plasma Process. Polym. 7, 737 (2010).

[7] N. De Geyter, R. Morent, S. Van Vlierberghe, P. Dubruel, C. Leys, L. Gengembre, E. Schacht, and E. Payen, Prog. Org. Coatings 64, 230 (2009).

[8] O. Levasseur, L. Stafford, N. Gherardi, N. Naudé, V. Blanchard, P. Blanchet, B. Riedl, and A. Sarkissian, Plasma Process. Polym. 9, 1168 (2012).

[9] F. Massines, C. Sarra-Bournet, F. Fanelli, N. Naudé, and N. Gherardi, Plasma Process. Polym. 9, 1041 (2012).

[10] D. Merche, N. Vandencasteele, and F. Reniers, Thin Solid Films 520, 4219 (2012).

[11] H. Yasuda and T. Hirotsu, J Polym Sci Polym Chem Ed 16, 743 (1978).

[12] D. Hegemann, M. M. Hossain, E. Körner, and D. J. Balazs, Plasma Process. Polym. 4, 229 (2007).

[13] D. Hegemann, E. Körner, and S. Guimond, Plasma Process. Polym. 6, 246 (2009).

[14] D. Hegemann, J. Phys. D. Appl. Phys. 46, 205204 (2013).

[15] B. Nisol, H. Gagnon, S. Lerouge, and M. R. Wertheimer, Plasma Process. Polym. 13, 366 (2016).

[16] B. Nisol, S. Watson, S. Lerouge, and M. R. Wertheimer, Plasma Process. Polym. 13, 557 (2016).

[17] B. Nisol, S. Watson, S. Lerouge, and M. R. Wertheimer, Plasma Process. Polym. 13, 900 (2016).

[18] B. Nisol, S. Watson, S. Lerouge, and M. R. Wertheimer, Plasma Process. Polym. 13, 965 (2016).

[19] B. Nisol, S. Watson, S. Lerouge, and M. R. Wertheimer, Plasma Process. Polym. 15, 965 (2018).

[20] A. Durocher-Jean, N. Delnour, and L. Stafford, J. Phys. D. Appl. Phys. 52, 475201 (2019).

[21] E. Desjardins, M. Laurent, A. Durocher-Jean, G. Laroche, N. Gherardi, N. Naudé, and L. Stafford, Plasma Sources Sci. Technol. 27, 015015 (2018).

[22] A. Manakhov, M. Michlí, D. Ne, J. Pol, E. Makhneva, M. Eliá, and L. Zají, 295, 37 (2016).

[23] A. T. A. Jenkins, J. Hu, Y. Z. Wang, S. Schiller, R. Foerch, and W. Knoll, Langmuir 16, 6381 (2000).

[24] G. Mertz, T. Fouquet, C. Becker, F. Ziarelli, and D. Ruch, Plasma Process. Polym. 11, 728 (2014).

[25] J. Mertens, J. Baneton, A. Ozkan, E. Pospisilova, B. Nysten, A. Delcorte, and F. Reniers, Thin Solid Films 671, 64 (2019).

[26] A. Durocher-Jean, E. Desjardins, and L. Stafford, Phys. Plasmas 26, 063516 (2019).

[27] N. Sadeghi, D. W. Setser, A. Francis, U. Czarnetzki, and H. F. Döbele, J. Chem. Phys. 115, 3144 (2001).

[28] D. Loffhagen, M. M. Becker, D. Hegemann, B. Nisol, S. Watson, M. R. Wertheimer, and

C. Klages, Plasma Process. Polym. (2019).

[29] T. Belmonte, C. Noël, T. Gries, J. Martin, and G. Henrion, Plasma Sources Sci. Technol. 24, 064003 (2015).

[30] J. E. Chilton, J. B. Boffard, R. S. Schappe, and C. C. Lin, Phys. Rev. A 57, 267 (1998).

[31] R. K. Gangwar, L. Sharma, R. Srivastava, and A. D. Stauffer, J. Appl. Phys. 111, 053307 (2012).

[32] A. Yanguas-Gil, J. Cotrino, and L. L. Alves, J. Phys D Appl. Phys. 38, 1588 (2005).

[33] A. Sáinz, J. Margot, M. C. García, and M. D. Calzada, J. Appl. Phys. 97, 113305 (2005).

[34] J. Jonkers, M. Van De Sande, A. Sola, A. Gamero, A. Rodero, and J. Van Der Mullen, Plasma Sources Sci. Technol. 12, 464 (2003).

[35] A. Morozov, T. Heindl, R. Krücken, A. Ulrich, and J. Wieser, J. Appl. Phys. 103, 103301 (2008).

[36] S. Hofmann, A. F. H. Van Gessel, T. Verreycken, and P. Bruggeman, Plasma Sources Sci. Technol. 20, 065010 (2011).

[37] M. Archambault-Caron, H. Gagnon, B. Nisol, K. Piyakis, and M. R. Wertheimer, Plasma Sources Sci. Technol. 24, 045004 (2015).

[38] F. Massines, N. Gherardi, A. Fornelli, and S. Martin, Surf. Coatings Technol. 200, 1855 (2005).

[39] Z. S. Chang, C. W. Yao, S. Le Chen, and G. J. Zhang, Phys. Plasmas 23, 093503 (2016).

[40] S. Watson, B. Nisol, S. Lerouge, and M. R. Wertheimer, Langmuir 31, 10125 (2015).

[41] B. Niermann, M. Böke, N. Sadeghi, and J. Winter, Eur. Phys. J. D 60, 489 (2010).

[42] E. Castaños-Martínez, M. Moisan, and Y. Kabouzi, J. Phys. D. Appl. Phys. 42, 12003 (2009).

Chapitre 4

Plasmas d'argon en configuration jet

4.1. Introduction

Les diagnostics optiques dont ceux développés dans le cadre de cette thèse sont aussi tout désignés pour caractériser des jets de plasma, ceux-ci étant un autre exemple typique de plasma incluant des espèces réactives. Bien qu'elles proviennent cette fois-ci principalement de l'environnement, rien n'empêche cependant d'insérer en plus d'autres molécules comme précurseurs pertinents pour le dépôt de couches minces. En effet, selon les applications visées (par exemple la médecine par plasma ou la fonctionnalisation des surfaces), le recours aux jets de plasma est de plus en plus fréquent mais, encore une fois, c'est dans la compréhension de l'impact des espèces réactives sur le plasma que réside l'amélioration de ces procédés. Dès lors, c'est ce dont traite ce quatrième chapitre.

Tout d'abord, un jet de plasma RF à base d'argon est étudié dans le cadre d'un cinquième article. Un tel jet étant propice à des applications biomédicales, il est important qu'il contienne un bon nombre d'espèces actives tout en demeurant à une température tolérable pour le corps humain. Dans ce contexte, la température du gaz et des électrons de même que la densité des états 1s sont étudiées le long du jet, permettant ainsi de mettre en évidence l'impact de l'incorporation de l'air ambiant dans l'admixtion sur ses propriétés fondamentales. Cette étude est effectuée à l'aide de mesures de spectroscopie d'absorption utilisant une lampe spectrale, de la méthode du modèle CR décrivant la population des niveaux émetteurs 2p couplé à des mesures d'émission optique des transitions 2p-1s ainsi que d'une simulation numérique d'écoulement des gaz.

Dans le même ordre d'idées, un jet de plasma microonde est lui aussi analysé dans un sixième article. Dans ce cas, l'objectif consiste à évaluer l'influence de la position d'injection du précurseur organosilicé HMDSO dans le jet de plasma microonde pour le dépôt de revêtements fonctionnels sur verre. En particulier, il y est question d'établir des liens entre

les propriétés physiques et chimiques des revêtements, obtenus par microscopie optique, mouillabilité à l'eau, transmittance et test antibuée, et les propriétés fondamentales du jet de plasma microonde obtenue par spectroscopie d'émission et d'absorption. Ces différentes analyses permettent notamment de comprendre quelles espèces énergétiques issues du jet de plasma sont responsables de la fragmentation du précurseur selon sa position d'insertion et comment les propriétés du dépôt résultant sont tributaires de celle-ci. Les travaux révèlent également des propriétés antibuée dans des conditions opératoires spécifiques, un résultat fort prometteur pour l'industrie du verre.

4.2. Article 5 : Diagnostics optiques d'un jet de plasma RF d'argon en contact avec l'air ambiant

Le premier jet sous étude dans ce chapitre est celui d'un plasma RF (13.56 MHz) à base d'argon s'écoulant dans l'air ambiant. Tel que mentionné dans l'introduction de ce chapitre, ce jet est propice notamment à des applications biomédicales puisqu'il offre le potentiel de fournir une quantité appréciable d'espèces réactives tout en demeurant à une température tolérable pour le corps humain. Basé sur un couplage capacitif entre deux électrodes, c'est un débit élevé de gaz qui se charge de pousser les espèces produites dans le plasma RF hors de l'espace interélectrodes. Avec les conditions expérimentales retenues pour le présent article (débit d'argon de 5 SLM et puissance absorbée de 40 W), ceci a donné lieu à un plasma en contact avec l'air ambiant sur une longueur de l'ordre de quelques millimètres. Conséquemment, l'acquisition des données s'est effectuée à tous les 0.2 mm, cette limite étant imposée par la résolution spatiale du microscope confocal utilisé pour l'obtention des spectres.

D'une part, des mesures d'absorption de différentes raies émises par une lampe spectrale ont permis d'obtenir le profil spatial de la densité d'états métastables de l'argon ($1s_3$ et $1s_5$). D'autre part, des températures rotationnelles de même que la température des électrons, respectivement calculées à partir de l'émission ro-vibrationnelle des niveaux OH(A) et N_2(C) et de spectres d'émission optiques des transitions 2p-1s couplés au modèle CR décrivant la population des niveaux émetteurs 2p, sont elles aussi obtenues en fonction de la position. Pour cet article, l'utilisation du modèle CR a été rendue possible grâce à une simulation numérique de l'écoulement du jet dans l'air ambiant donnant accès au profil de la température du gaz le

long du jet de même qu'à la quantité d'air s'étant mêlée à l'argon, deux paramètres d'entrée primordiaux au modèle CR. Les résultats de cette étude montrent que la température des électrons en sortie de jet avoisine 2.5 eV mais diminue à mesure de la progression du gaz dans l'air. Un comportement similaire est observé pour la densité d'états métastables, celle-ci étant de l'ordre de 10^{18} m^{-3} en sortie. Par ailleurs, la différence entre les températures rotationnelles et celle du gaz telle que calculée par la simulation fluide démontre qu'il n'existe pas d'équilibre translation/rotation dans un tel jet dû à l'intervention des métastables dans le mécanisme de peuplement des molécules émettrices OH(A) et N_2(C).

:

Spatially-resolved spectroscopic diagnostics of a miniature RF atmospheric pressure glow discharge jet in argon

par

Florent Sainct[2], Antoine Durocher-Jean[1], Reetesh Kumar Gangwar[1],
Norma Yadira Mendoza Gonzalez[2], Sylvain Coulombe[2] et Luc Stafford[1]

([1]) Laboratoire de physique des plasmas, Département de physique, Université de Montréal, Montréal, Québec, Canada

([2]) Plasma Processing Laboratory, Department of Chemical Engineering, McGill University, Montréal, Québec, Canada

Cet article a été accepté pour publication dans la revue *Plasma* (plasma-636743).

Les contributions des différents auteurs à cet article sont :

- Antoine Durocher-Jean : Analyse des spectres d'émission avec le modèle CR, écriture de quelques sections de texte, révision globale du manuscrit
- Florent Sainct : Prise des mesures, aide à l'analyse des résultats et écriture de quelques sections de texte
- Reetesh Kumar Gangwar : Aide à la prise des mesures et analyse des spectres d'absorption
- Norma Yadira Mendoza Gonzalez : Élaboration de la modélisation CFD
- Luc Stafford et Sylvain Coulombe : Supervision des travaux, révision du manuscrit

Abstract.

Spatially-resolved electron temperature, rotationnal temperature, and number density of the two metastable Ar 1s levels were investigated in a miniature RF Ar glow discharge jet at atmospheric pressure. The 1s level population densities were determined from optical absorption spectroscopy (OAS) measurements assuming a Voigt profile for the plasma emission and a Gaussian profile for the lamp emission. As for the electron temperature, it was deduced from the comparison of the measured Ar $2p_i \rightarrow 1s_j$ emission lines with those simulated using a collisional-radiative model. Ar $1s$ level population higher than 10^{18} m^{-3} and electron temperature around 2.5 eV are obtained close to the nozzle exit. In addition, both values decrease steadily along the discharge axis. Rotational temperatures determined from OH(A) and N_2(C) optical emission featured a large difference with the gas temperature found from a thermocouple; a feature ascribed to the population of emitting OH and N_2 states by energy transfer reactions involving the Ar 1s levels.

Keywords: Atmospheric pressure plasma jet, optical emission spectroscopy, optical absorption spectroscopy, collisional-radiative model

4.3. Introduction

Understanding non-thermal atmospheric-pressure plasma sources is of increasing interest for a wide range of industrial and biomedical applications as they can provide plasma chemistry without low-pressure conditions [1–3]. As an example for biomedical applications, the electron temperature needs to be hot enough to produce reactive species whereas the neutral gas temperature has to stay near room temperature to avoid excessive heating of the tissues. Over the years, a number of configurations for sustaining non-thermal plasmas at atmospheric pressure have been developed, mainly in the form of dielectric barrier discharges (DBDs), micro-discharge jets, and glow discharges generated in confined space [4–9]. A key advantage of atmospheric pressure plasma jet (APPJ) is the ability to transport various reactive species to a region separated from the plasma generation zone [10–12]. This spatial separation allows objects spanning a wide range of sizes and shapes to be treated, especially for biomedical, surface treatment, and plasma chemical functionalization applications [13–15].

In order to implement these plasma sources as viable options, advanced diagnostics are needed to characterize and optimize their processing efficiency under various operating conditions (*e.g.* power, gas flow rate, choice of feed gas and precursor, etc). In this context, various APPJs have been developed and characterized in the past two decades [16–18]. Nowadays, stable jet devices can operate with various electrical excitations (DC, pulsed DC, kilohertz frequency AC, radio-frequency (RF) and microwave), and in many different gases, from noble gases to diatomic gases to air. Depending on the electrical excitation and the jet geometry, different plasma characteristics can be selected for the application of interest. Some jet devices are able to generate radicals over very large distances [19], or can be bundled together to cover a larger surface [20].

Recently, Léveillé *et al.* [21] designed an APPJ with a hollowed electrode to produce a stable discharge in an inert gas and added an injection source of reactive species downstream of the plasma-forming zone. Such a device is well-suited for atomic species and radicals production and transport for precise bio-applications such as the treatment of skin tissues and cells. Some studies showed, using nanosecond camera imaging, that the jet was formed of fast moving ionization volumes, often called "plasma bullets", and that the bullet velocity and diameter increase with applied voltage [22, 23]. Laser diagnostics have been applied to

obtain more insight on the plasma chemistry, e.g. the concentration and behaviour of OH radicals and O atoms [24, 25].

Although huge improvements have been made in the fundamental understanding of plasma jets, important plasma characteristics such as the metastable and resonant population density of Ar atoms and electron temperature are still under investigation for most configurations. Moreover, highly populated Ar 1s states (Paschen notation) are suspected to play a major role in the chemistry of the flowing afterglow (such as molecule fragmentation) due to the large portion of energy they carry [26, 27]. Therefore accurate information on spatial distribution of Ar 1s levels population is highly required to understand the underlying physics and chemistry of APPJs operated in Ar.

In this work, optical emission spectroscopy (OES) and optical absorption spectroscopy (OAS) are used on an APPJ operating with Ar and open to ambient air. The neutral gas temperature profile is estimated using computational fluid dynamic (CFD) calculations considering a 2D-axisymetric representation of the APPJ. These simulations also allow the observation of the basic flow pattern as well as the mixing of the jet with the surrounding air. Spatially-resolved metastable ($1s_3$, $1s_5$) population density of Ar atoms are estimated from OAS measurements, performed with a standard low-pressure Ar-lamp. Using the estimated gas temperatures and the measured values of the population of metastable Ar atoms, a collisional-radiative model along with OES measurements of Ar 2p-to-1s transitions is used to estimate the spatial distribution of the electron temperature (T_e).

4.4. Experimental setup and methods

4.4.1. Setup configuration

The non-thermal atmospheric pressure plasma jet (APPJ) was produced using a device similar to, but larger than, the original design of Léveillé and Coulombe [21]. A schematic is shown in Fig. 4.1. The coaxial geometry device features a RF-powered capillary electrode at the center, surrounded by a grounded nozzle, both parts being insulated by a PTFE spacer. The device diameter is 2.5 cm, and the nozzle exit diameter is 1 mm. The plasmagen gas is injected in the ring formed by the two coaxial electrodes. The capillary electrode allows injection of a secondary gas in the flowing afterglow discharge. The grounded outer electrode is made of stainless steel while the inner capillary electrode, adjustable in axial position, is

made of brass. This electrode is held in place by an O-ring located between two compressed PTFE sleeves. Argon was used with a flow rate of 5 standard litres per minute (slm). The RF power, set at 40 W, is delivered from a 13.56 MHz 300 W generator (Cesar Generator Model 1312 Advanced Energy) equipped with an automatic matching network (Dressler VM1000 A). Consequently, ~90% (~36 W) is absorbed by the plasma. The discharge forms inside the nozzle throat and the flowing afterglow streaming into the surrounding atmosphere forms the jet.

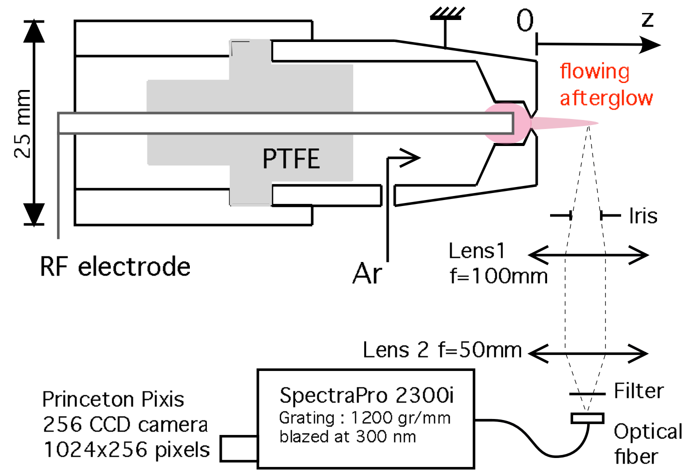

Figure 4.1. Schematics of the APPJ and OES setup.

4.4.2. Optical Emission Spectroscopy

Optical Emission Spectroscopy (OES) measurements were performed using a spectrometer (Princeton Instruments Acton SpectraPro2300) equipped with a CCD camera (Princeton Instruments PIXIS 1024x256). The 25 cm focal length combined with a 1200 lines/mm grating, blazed at 300 nm, provides a spectral resolution of 0.22 nm (full width at half maximum) at $\lambda = 632$ nm. The light emitted by the discharge region is collected using a confocal microscope system with two lenses with f = 50 mm and 100 mm, respectively (Fig. 4.1). With this optical setup, the magnification was 0.5. A 200 μm-diameter optical fibre, located at the focal point of the imaging lens, was connected to the entrance slit of the spectrometer. Considering the magnification, the spatial resolution was 400 μm.

Light was collected from the center of the plasma jet, perpendicularly to the discharge axis, and all the recorded spectra were corrected for the spectral response of the optical fibre, monochromator, and detector. All spectra are averaged over many cycles of the applied

RF power (integration times of tens of milliseconds) and a typical example is presented in Fig. 4.2. Strong Ar-I emission lines are observed in the 700-900 nm wavelength range. Besides these anticipated Ar lines, noticeable emissions from N_2 (second positive system), N_2^+ (first negative system), OH (A-X), O-I (777 nm) and H-I (656.3 nm) are also observed. These are due to the interaction of the APPJ with ambient air.

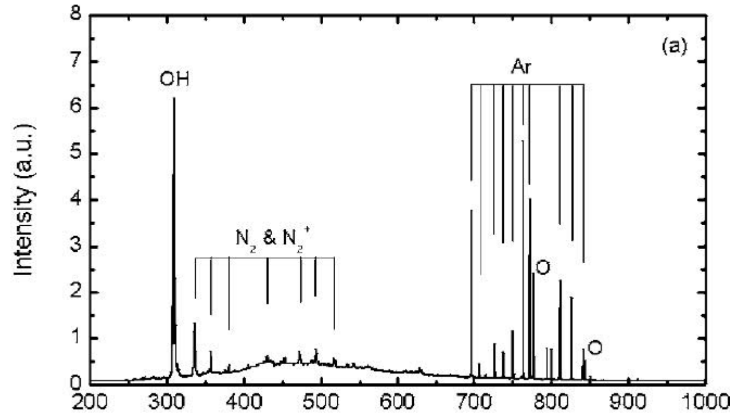

Figure 4.2. Emission spectrum of the Ar APPJ flowing afterglow region, 0.6 mm from the nozzle exit, integrated over 200 ms between 300 and 680 nm, and over 20 ms between 680 and 880 nm.

4.4.3. Optical Absorption Spectroscopy

Optical Absorption Spectroscopy (OAS) measurements were in part performed using the same spectrometer but with a different light collection arrangement. A schematic of the absorption setup is presented in Fig. 4.3. The light emitted by the low-pressure argon spectral lamp (Philips) was collimated by a first lens (f=100 mm) and then went through a first iris to ensure that a parallel beam with a well-controlled diameter (0.5 mm) is obtained. Next, the beam passed through the plasma jet, a second iris, and a second lens (f=100 mm) before finally reaching the optical fiber.

Using this experimental setup, the global optical absorption coefficient, A_L, can be obtained from:

$$A_L = 1 - \frac{I_{p+l} - I_p}{I_l} \tag{1}$$

where I_{p+l} is the emission of the plasma with the lamp on, I_p is the emission of the plasma with the lamp off, and I_l is the emission of the lamp with the plasma off. The analysis method was then adopted from Castaños-Martinez and Moisan [28] to take into account the

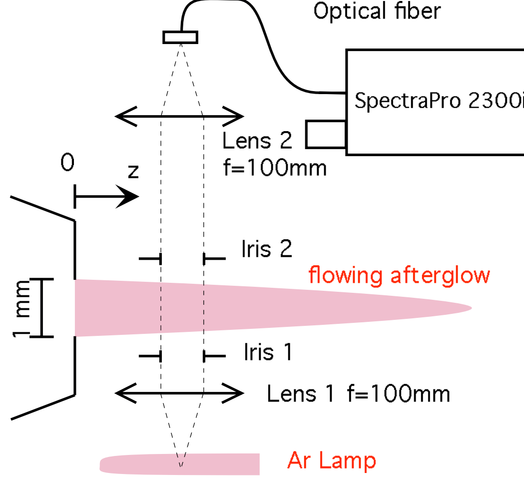

Figure 4.3. Schematic diagram of the optical absorption spectroscopy setup.

difference in pressure broadening between the low-pressure Ar lamp and the atmospheric-pressure Ar plasma. This method assumes a Voigt line profile to carry out the analysis, thus taking into account the pressure broadening of the Ar emission lines from the plasma. As a result, the frequency-integrated absorption coefficient for each individual line can be expressed as [28]:

$$A_L = \frac{\int e^{-(\frac{\omega}{\alpha})^2} \left(1 - e^{-k_0 L \frac{\beta}{\pi} \int_{-\infty}^{\infty} \frac{e^{-y^2} dy}{\beta^2 + (\omega - y)^2}}\right) d\omega}{\int e^{-(\frac{\omega}{\alpha})^2} d\omega} \quad (2)$$

which depends on the central frequency absorption coefficient (k_0) and the absorption length (L). The frequency integration occurs through the variable ω:

$$\omega = \frac{2(\nu - \nu_0)}{\Delta\nu_D} \sqrt{\ln 2} \quad (3)$$

where ν_0 is the central frequency of the transition and $\Delta\nu_D$ the Doppler half-width component of the line broadening. The α and β coefficients are defined as:

$$\alpha = \frac{\Delta\nu_D(\text{lamp})}{\Delta\nu_L(\text{plasma})/2 + \sqrt{(\Delta\nu_L(\text{plasma})/2)^2 + \Delta\nu_D^2(\text{plasma})}}, \quad (4)$$

$$\beta = \frac{\Delta\nu_L(\text{plasma})}{\Delta\nu_D(\text{plasma})} \sqrt{\ln 2} \quad (5)$$

with $\Delta\nu_L$ the Lorentzian half-width component. The Doppler half-width was calculated according to $\Delta\nu_D = 7.16 \times 10^{-7} \nu_0 \sqrt{T_g/M}$, where T_g is the gas temperature and M is the atom mass (in atomic units). This equation allowed the calculation of the plasma Doppler

broadening at each position when taking the neutral gas temperature obtained from CFD simulations (detailed in section 4.5.1). As for the lamp Doppler broadening, it was calculated by estimating a temperature of 600 K as suggested by Moussounda [29]. Afterwards, the Lorentzian half width $\Delta\nu_L$ was obtained again at each position by deconvoluting the Voigt profile of the measured plasma emission lines. To measure with enough precision the broadenings of these emission lines and those of the Ar lamp used for the OAS analysis, a very good spectral resolution is required. For that set of experiments, light was sent via an optical fiber to the entrance slit of a HORIBA Jobin-Yvon THR-1000 monochromator having a focal length of 1 m and a holographic grating of 1800 lines/mm. The exit slit was fitted with a Hamamatsu R-955 photomultiplier tube linked to a picoammeter. The spectral resolution was 0.05 nm at $\lambda = 632$ nm.

Using the resulting α and β values from this procedure, A_L can be obtained for every position as a function of k_0L. In order to highlight the fact that, in our plasma conditions, the pressure broadening was significant, the A_L values assuming a Gaussian profile was also plotted at the same spatial position (z=0, nozzle exit) in Fig. 4.4. It shows that, for given A_L and L values, the assumption of a Gaussian profile would have underestimated the k_0 value and therefore resulted in lower population densities.

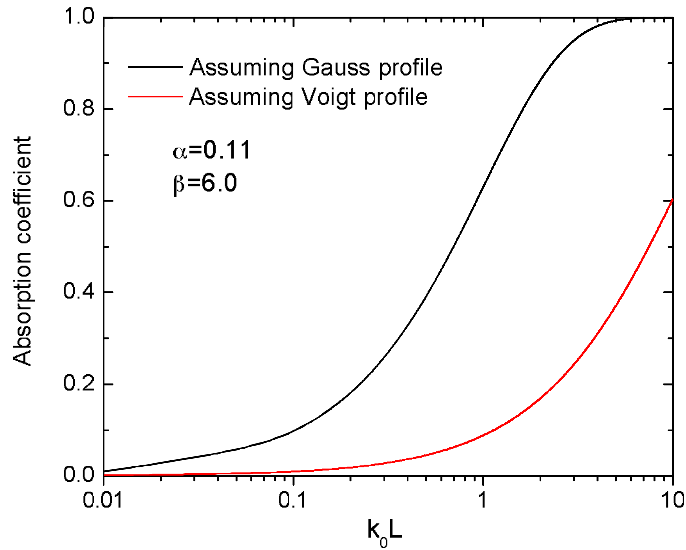

Figure 4.4. Global absorption coefficients as a function of k_0L at the nozzle exit plane (z=0).

Finally, the absorption length of the APPJ was estimated by scanning the averaged absorption of the 751.5 nm line in the plane perpendicular to the jet axis. This profile was

then fitted with a Gauss profile, as presented in Fig. 4.5. The full-width at half-maximum (FWHM) of the fit being 0.6 mm, we used an absorption length of 1.2 mm.

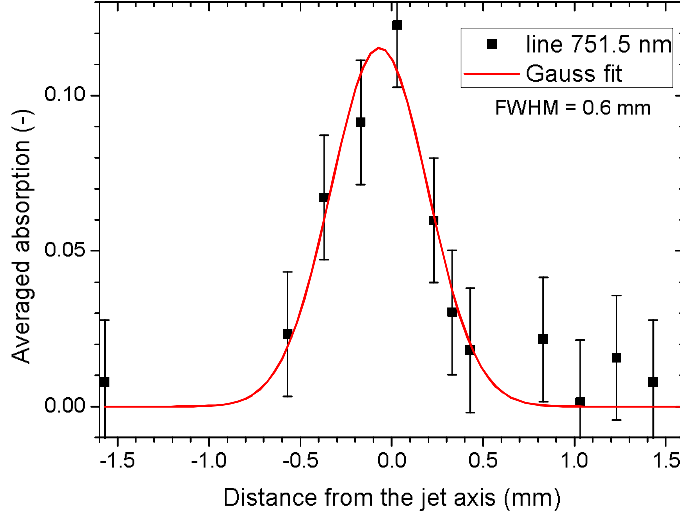

Figure 4.5. Radial profile of the absorption for the 751.5 nm line, 1 cm away from the nozzle exit plane.

Hence, by calculating A_L from equation 2 and using Fig. 4.4 to see at which k_0L this absorption would occur enabled us to extract the value of k_0. This value was then used in equation 6 to find the population density of the lower level involved in the considered emission line

$$N_i = \frac{4}{\sqrt{ln2}} \frac{g_i}{g_j} \frac{\Delta\nu_D}{\lambda_{ji}^2 A_{ji}} \frac{k_0 L}{L} \beta \int\int \frac{e^{-y^2} dy}{\beta^2 + (\omega - y)^2} d\omega \tag{6}$$

The statistical weight (g_j, g_i) and the spontaneous decay coefficients A_{ji} were obtained from NIST database [30] .

4.4.4. Collisional Radiative Model

In order to extract the electron temperature T_e along the discharge axis, the measured Ar $2p_j$-to-$1s_i$ emission line intensities as seen in Fig 4.2 were compared to those predicted by a collisional radiative (CR) model solving the balance equations of the ten $2p$ levels assuming a Maxwell-Boltzmann electron energy distribution function (EEDF) and steady-state. As such, our approach to find T_e is based on fitting the experimental spectra with theoretical ones instead of solely relying on an auto-coherent CR model. The details of this method can be found elsewhere [31]; only an overview is presented in the following lines.

The intensity of a given Ar I line emanating from a $2p_i$ level is given by

$$I_\lambda = f(\lambda) A_{ij} n_i \theta_{ij} \tag{7}$$

where $f(\lambda)$ is the optical response of the optical fiber, monochromator, and detector, θ_{ij} is the escape factor, A_{ij} is the Einstein coefficient for spontaneous emission (taken from NIST database [30]), and n_i is the number density of the Ar 2p state emitting at wavelength λ.

The role of the CR model is to find the optimal n_i and θ_{ij} values by solving for a given number of T_e values the particle balance equations for the 10 2p levels. By comparing up to 24 emission lines from the experimental spectrum to all the simulated ones, a relative standard error calculation is done to evaluate the goodness of the fit [32]. For each experimental spectrum, the T_e value yielding the most accurate simulated spectrum is assumed to be the actual electron temperature. Input parameters found from other diagnostics are the gas temperature, working pressure, plasma length along the line of sight of spectroscopic measurements and the number density of Ar 1s levels. Since OAS measurements performed in this work only provided information about the $1s_3$ and $1s_5$ levels, two CR simulations were made for each spectrum assuming Boltzmann equilibrium of the 1s levels: the first by imposing the $1s_3$ number density and the second by imposing the $1s_5$ number density. The mean T_e value obtained from those two simulations was considered as the actual T_e and the standard deviation provided the error bars.

Figure 4.6 summarizes the different mechanisms that were considered in the particle balance equations. Excitation mechanisms include electron impact from either ground or $1s$ metastable and resonant states, population mixing between two 2p levels induced by a collision with ground state Ar atoms [33] as well as radiation trapping [31]. As represented by the box on top of Figure 4.6, apparent (cascading) cross-sections for electron collisions were used to calculate the corresponding reaction rates, thus ensuring that cascading effects are adequately described without going through the complexity of solving the population of energy levels higher than the 2p. Futhermore, de-excitation mechanisms include radiative decay [30], quenching by neutrals [34, 35], impurities [36] and again population mixing. In our case, we considered the impurities to be nitrogen and oxygen due to the interaction with ambient air (80% N_2, 20% O_2) and their concentrations along the plasma jet axis were deduced from the CFD simulations (see details below). Radiation trapping and collisions

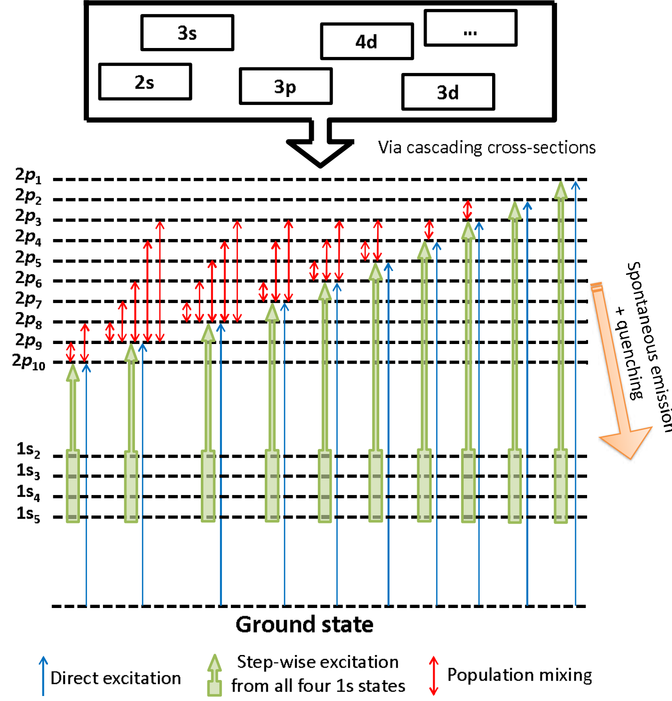

Figure 4.6. Schematic of the reactions considered in the CR model

involving neutrals make the CR model especially suited for non-equilibrium atmospheric-pressure plasma conditions and population mixing by electrons was neglected because their density was assumed to be many orders of magnitude lower than the ground state Ar density.

Based on this framework, the coupled steady-state particle balance equations of the $2p_i$ levels can be expressed as

$$n_{2p_i} = \frac{\left(k_{Gi}n_G + \sum_{j=2}^{5} k_{1s_{ji}} n_{1s_j}\right) n_e + \sum_{j=1(j\neq i)}^{10} k_{2p_{ji}} n_G n_{2p_j}}{\sum_{j=1(j\neq i)}^{10} k_{2p_{ij}} n_G + \sum_{j=2}^{5} A_{ij}\theta_{ij} + k_{Quench_{Ar}} n_G + \sum_{Im} k_{Quench_{Im}} n_{Im}} \tag{8}$$

In equation 8, k_{Gi} denotes the reaction rate of the electron excitation from ground state, $k_{1s_{ji}}$ the step-wise electron excitation from $1s$ levels; $k_{2p_{ji}}$ and $k_{2p_{ij}}$ the population mixing among the $2p$ manifold, k_{Quench_x} the quenching coefficients by neutral argon atoms and impurities and n_{Im} the number density of impurities. Considering that the electron density n_e is in every term of the numerator (indeed it is also hidden in the n_{2p_j} number density), it only acts as a scaling factor for the 2p number densities. Therefore, since only the relative emission line intensities (and thus the relative 2p number densities) are required for the model, the simulations are in fact independent of the electron density.

4.5. Results and Discussion

4.5.1. Gas Temperature and Fluid Flow

To ensure compatibility with temperature-sensitive applications, the plasma jet temperature profile was monitored. A first estimate was made using the OH and N_2 rotational band emissions acquired with the OES setup over the 300-400 nm range. The observed transitions are the second positive system of nitrogen ($N_2(C^3\Pi_u) \rightarrow N_2(B^3\Pi_g)$, $\Delta\nu = 1, 2, 3$) and the OH transition (OH(A) $\rightarrow$OH(X)). The Specair software [37, 38] was used to model the experimental OES results and to determine the corresponding rotational temperature. The results, presented in Fig. 4.7, show a rotational temperature ranging from 500 to 1000 K, both for OH(A) and N_2(C). In this figure, the z=0 mm position is defined as the nozzle exit plane of the APPJ.

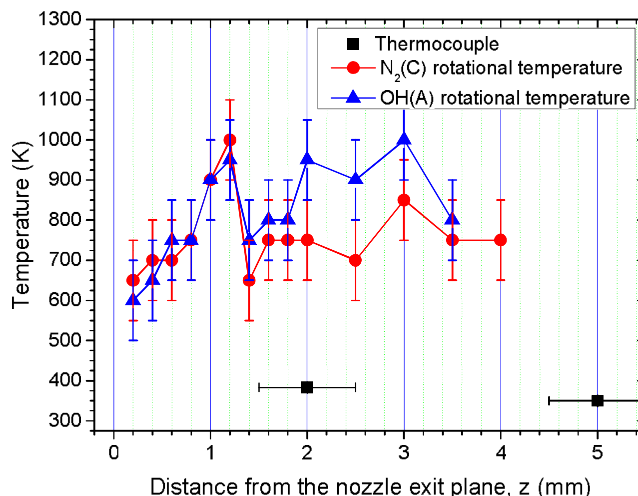

Figure 4.7. Axial distribution of the rotational temperature of OH(A) and N_2(C) obtained using Specair and gas temperature measured with a thermocouple, at 5 L/min of Ar and 40 W.

These temperatures were compared with a 1-mm RF-shielded thermocouple placed in the plasma jet. The gas temperature measured by the thermocouple ranged from 75 to 50 °C, 2 to 8 mm away from the outlet. Thus, OH(A) and N_2(C) molecules feature much higher temperatures; this discrepency most likely results from energy transfer collisions with the Ar 1s states [39]. Indeed, the energy of these levels is close to the excitation energy levels of OH(A) and N_2(C) and, as will be shown later, their density turn to be relatively high.

In order to enhance our understanding of the APPJ investigated, its fluid flow was simulated with the commercial CFD code ANSYS Fluent v.14.5 [40]. Because of the cylindrical symmetry of the APPJ, a two-dimensional $r - z$ computational geometry was used. The geometry included the entire device, as well as an extended area (8 mm in z after the nozzle exit plane, and 8 mm in r) for the analysis of the effect of surrounding air on the plasma jet. The plasma formation was not simulated in this preliminary study. To take into account neutral gas heating by the plasma on the flow pattern, the injection temperature of the argon was set to the temperature of the APPJ metallic nozzle, measured with the thermocouple, 390 K.

The combined incompressible Navier-Stokes and non-reactive species transport equations were solved in the 2D computational domain composed of 80 000 control volumes. As turbulence can be present due to the two geometry expansions adopted for this design, a standard k-epsilon model was used [41]. The number density of the argon-air mixture was calculated with the ideal gas equation. The boundary conditions are the imposed mass flow rate of argon at the inlet, the non-slip conditions at the walls, and atmospheric static pressure at the extended area boundaries.

From the CFD modeling results, Fig. 4.8.(a) shows the axial distribution of the argon mole fraction along the jet axis. It is shown that the argon mole fraction decreases due to the diffusion of the surrounding air into the jet. The 4 mm axial position composition is about 25 % mole air fraction. In theses conditions, and considering that the APPJ is pointing down, the flow is laminar.

Additionally, the CFD modeling results include the temperature evolution along the centerline. As shown in Fig. 4.8.(b), the axial distribution of the gas temperature along the jet axis as predicted by the model is in very good agreement with thermocouple measurements at 2 and 8 mm.

4.5.2. Spatially-resolved Ar 1s level populations

A typical absorption profile for a few of the most visible Ar lines is presented in Figure 4.9. The spatial step size is fixed at 0.2 mm, even though the spatial averaging is set by the iris opening of 0.5 mm. The corresponding horizontal error bars were omitted for clarity. With a flow rate of 5slm, the jet visually appears to be ~4 mm long but for distances larger

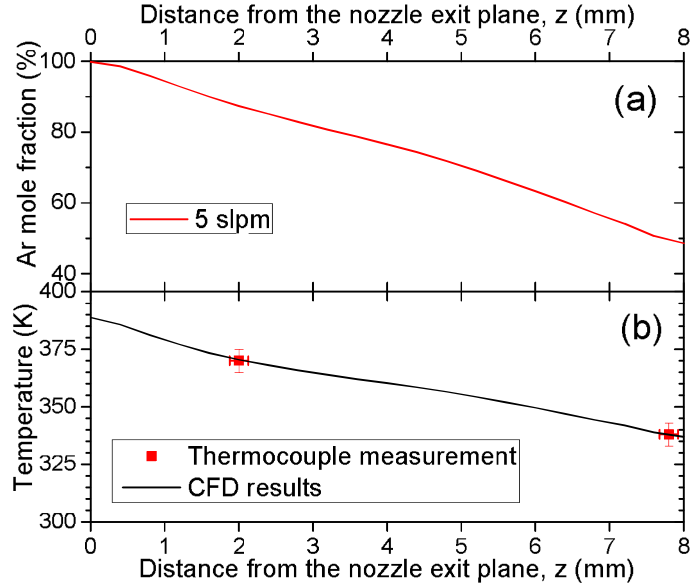

Figure 4.8. Argon mole fraction at 5 slm and temperature from measurement and CFD

than 2.5 mm the absorption coefficient is too low to be significant and thus used in the calculations.

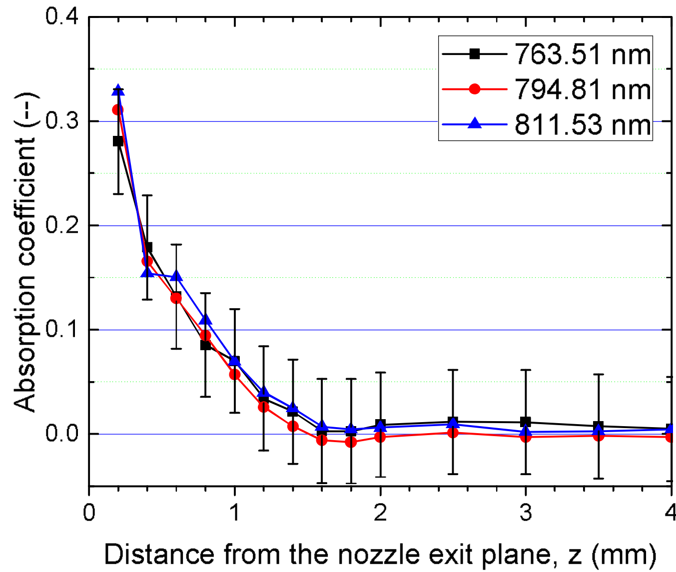

Figure 4.9. Axial distribution of the measured absorption at 5 L/min and 40 W.

Using Equation 6, the spatial distribution of the population densities of both metastable levels ($1s_3$ and $1s_5$) was determined. The results are presented in Figure 4.10. The population of excited states at the exit of the nozzle are found to be ~7x10^{17} m^{-3} for $1s_3$ and ~2x10^{18} m^{-3} for $1s_5$. Not surprisingly, the $1s_5$ number density is higher than the $1s_3$ one, and

both densities decrease along the discharge axis (they are already two orders of magnitude lower 2 mm away from the nozzle exit plane).

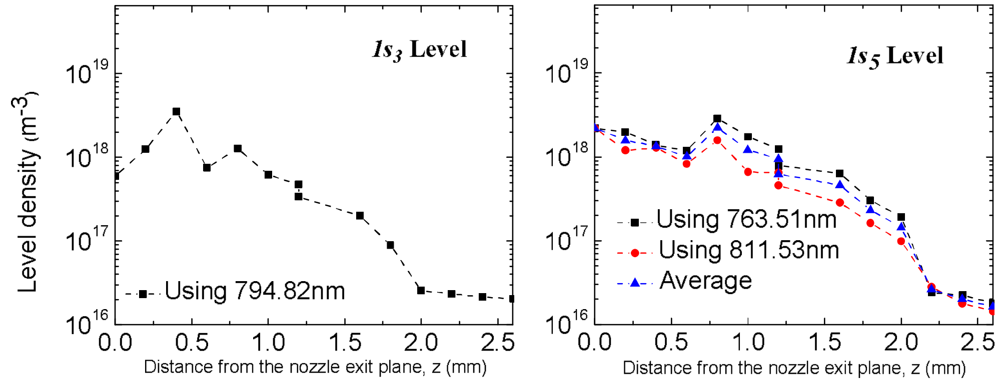

Figure 4.10. Axial distribution of Ar 1s level population at 5 L/min and 40 W.

Similar experiments have been conducted by other research groups to study the Ar excited states, mainly using diode laser absorption spectroscopy. Niermann *et al.* [42] reported maximum densities of ~1x10^{19} m^{-3} for the $1s_5$ level, which is one order of magnitude higher than our values. Additional experimental results have been reported but for Ar/He mixtures, with typically 1-5% Ar. Ar $1s_5$ level densities of ~1x10^{16} m^{-3} [43] and ~1x10^{17} m^{-3} were found [44]. However, no experimental measurements have been reported for the other three Ar $1s$ levels.

Recently, the behaviour of resonant and metastable levels of Ar has been studied by Van Gaens and Bogaerts [36] who performed a kinetic modeling study. The power level reported was 6.5 W with an Ar flow of 2 L/min (compared to 40 W at 5 L/min in our experiment). These values provide roughly a factor 2 lower in power density compared to the present study. It is reasonable to compare the population predicted by the model to our measurement if the exit velocity of the gas is scaled : 29 m/s in the model and 150 m/s in the experiment. The populations of excited states reported at the exit of the nozzle are ~10^{18} m^{-3} for $1s_5$ and ~10^{17} m^{-3} for $1s_3$; these values are in good agreement with our results.

The possible reason for the discrepancy between the prediction of their kinetic model and our experimental results could be the configuration of the experimental setup. In Van Gaens and Bogaerts's study, the tube guiding the plasma is a dielectric, whereas in our setup, the plasma created between the two electrodes is transported during approximately 2 mm in the

grounded metallic nozzle before exiting the system. This configuration greatly reduces the electron density.

As a matter of fact, they explained the decrease in the Ar excited state densities by a drop of the electron density, as well as by quenching reactions by mixing with ambient air. In the present study, since the electron density is already very low, we attribute the decrease in the Ar excited state densities mainly to the mixing with air. The main recombinaison reactions identified in [36], and also valid in the present study, are:

$$Ar^* + O_2 \rightarrow 2O + Ar \quad (1)$$

$$Ar^* + N_2 \rightarrow 2N + Ar \quad (2)$$

$$Ar^* + N_2 \rightarrow N_2(A) + Ar \quad (3)$$

The summarized comparison between data found in the literature and our present study is presented in Table 4.1.

Table 4.1. Comparison of Ar 1s level densities available in the literature. The present study is reported on the last line.

Ref.	Gas	Power [W]	$1s_3$ [m^{-3}]	$1s_5$ [m^{-3}]
[42]	Ar	*n.a.*	-	10^{19}
[44]	He/Ar	*n.a.*	-	10^{17}
[43]	He/Ar	23	-	10^{16}
[36]	Ar	6.5	10^{17}	10^{18}
This work	Ar	40	10^{18}	10^{18}

4.5.3. Spatially-resolved Electron Temperature

Results for the electron temperature as found from the comparison between measured and simulated optical emission spectra from Ar 2p-to-1s transitions are presented in Fig. 4.11. As mentioned above, 1s number densities obtained from OAS experiments (Fig. 4.10) were used as inputs in the CR model. Fig. 4.11 reveals a decay of T_e when moving away from the nozzle, starting roughly around 2.4 eV at the nozzle exit and dropping below 2 eV 2 mm downstream.

Electron temperature is an essential parameter to characterize when studying APPJs, but is nonetheless not always straightforward to estimate. The most common experimental techniques reported are the line-ratio method assuming Boltzmann equilibrium [45–47], the

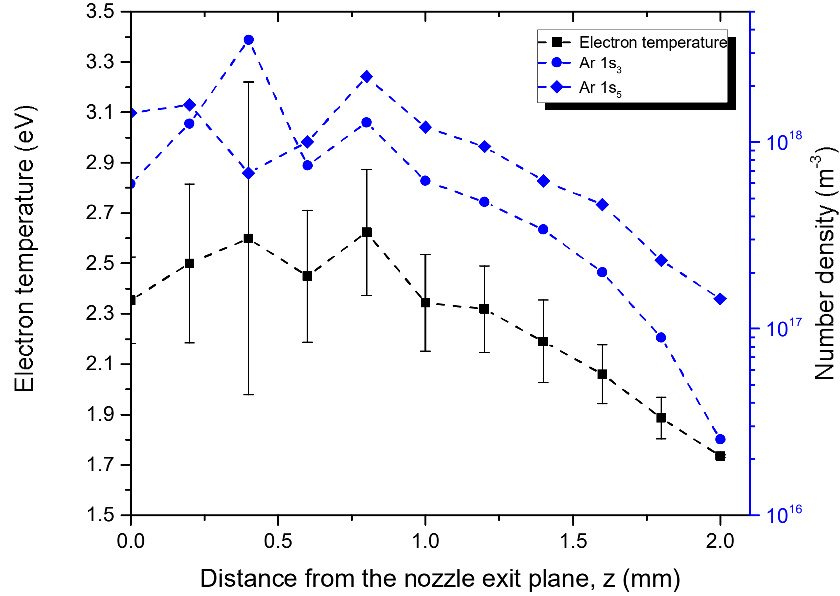

Figure 4.11. Axial distribution of T_e at 5 L/min and 40 W.

Boltzmann-plot method [46, 47], the equivalent circuit model coupled with the power balance equation [48], and CR models similar to the one used in the present study [33, 49, 50]. As can be seen in the next lines, these multiple technique can provide a wide range of T_e values but, depending on the conditions, not all are always reliable.

Li *et al.* [48] estimate a constant 1.4 eV electron temperature for the entire range between 5 and 120 W, for a RF discharge in Ar at 10 L/min based on the equivalent circuit model of the discharge and by making use of the power balance equation. The equation includes the power delivered and the energy losses due to radiation, ionization processes, excited states production, temperature and pressure increase. The uncertainties of this technique arise from numerous sources, and the error on the electron temperature can be difficult to estimate.

Forster *et al.* [46] report an excitation temperature of 1.0 eV at the exit of the tube for a discharge in Ar at 2 W at 4 L/min using a Boltzmann plot method, and the temperature goes down to 0.7 eV after 2 mm. The radial study, using an Abel-inversion, shows a slightly higher electron temperature on the fringe compared to the center of the jet, probably due to the ring-shape of the jet. Using the same technique but in a DC discharge in Ar with 2 %H_2,

Sismanoglu *et al.* [47] measured an excitation temperature of 0.7 eV. This temperature was confirmed by using two Ar I lines, 603.213 and 565.070 nm, and two Cu I lines.

Finally, the modelling study of Van Gaens and Bogaerts [36] predicts T_e values around 3 eV at the exit of an argon plasma jet flowing into humid air. These values are comparable to those obtained by Hubner *et al.* [51] under comparable experimental conditions using temporally and spatially resolved Thomson laser scattering measurements. A summary of these results is presented in Table 4.2, along with the results of the present study. As can be seen, our extracted electron temperature values are somewhere in the middle of everything that can be found in the literature. As for the excited Ar level densities, the drop along the discharge axis is attributed to mixing with ambient air.

Table 4.2. Comparison of electron temperature available in the literature. The present study is reported on the last line.

Ref.	Gas	Power [W]	T_e [eV]
[36]	Ar	6.5	3.0
[46]	Ar	2	1.0 to 0.7
[48]	Ar	0-120	1.4
[47]	Ar/H_2	*n.a.*	0.7
[51]	Ar	*n.a.*	3 to 0.2
[52]	Ar	4	2.2
This work	Ar	40	2.5 to 1.7

4.6. Conclusion

In this investigation, spectroscopic diagnostics combined with a CR model and CFD simulations have been applied to an APPJ to study the Ar 1s levels number density, as well as the electron and neutral gas temperatures along the discharge axis. OAS results revealed densities higher than $\sim$1x10^{18} m^{-3} for the metastable levels at the exit of the mini-torch nozzle. Both densities were found to decrease by two orders of magnitude over a distance of 2 mm. These results, coupled with spatially-resolved OES measurements and a collisional-radiative model, were used to estimate the evolution of T_e along the jet axis. At 40 W and 5 L/min of Ar flow, T_e is around 2.5 eV at the nozzle exit and decreases below 2 eV over 2 mm.

The neutral gas temperature measured with a thermocouple has been compared to the rotationnal temperatures of OH(A) and N_2(C) bands fitted using the Specair software. The

large difference between these species excitation temperatures, the gas temperature and the electron temperature highlights the non-equilibrium nature of the jet.

In future experiments, operation in different plasma-forming gases is foreseen, *e.g.* helium. The injection of reactive gases in the plasma afterglow through the capillary electrode, like O_2 and various organosilicon precursors, will expand the possible applications of the APPJ.

Acknowledgements

The authors wish to thank C. Szalacsi and R. Piché for their technical assistance. The project was funded by the Natural Sciences and Engineering Research Council of Canada (NSERC), the Fonds de recherche du Québec – Nature et technologies (FRQNT), McGill University and Université de Montréal.

References

[1] M. Laroussi and T. Akan, Plasma Processes and Polymers **4**, 777 (2007).

[2] A. Lacoste, A. Bourdon, K. Kuribara, K. Urabe, S. Stauss, and K. Terashima, Plasma Sources Science and Technology **23**, 062006 (2014).

[3] B. Van Gessel, R. Brandenburg, and P. J. Bruggeman, Applied Physics Letters **103**, 064103 (2013).

[4] Y. Sakiyama, D. B. Graves, J. Jarrige, and M. Laroussi, Applied Physics Letters **96**, 41501 (2010).

[5] S. Spiekermeier, D. Schröder, V. S.-v. D. Gathen, M. Böke, and J. Winter, Journal of Physics D: Applied Physics **48**, 35203 (2015).

[6] J. B. Boffard, R. O. Jung, C. C. Lin, and a. E. Wendt, Plasma Sources Science and Technology **18**, 035017 (2009).

[7] J. Benedikt, S. Hofmann, N. Knake, H. Böttner, R. Reuter, A. von Keudell, and V. Schulz-von der Gathen, The European Physical Journal D **60**, 539 (2010).

[8] G. V. Naidis, Plasma Sources Science and Technology **23**, 065014 (2014).

[9] J. L. Walsh and M. G. Kong, Applied Physics Letters **91**, 221502 (2007).

[10] S. Schneider, J. W. Lackmann, D. Ellerweg, B. Denis, F. Narberhaus, J. E. Bandow, and J. Benedikt, Plasma Processes and Polymers **9**, 561 (2012), arXiv:1105.6260 .

[11] S. Schneider, J. W. Lackmann, F. Narberhaus, J. E. Bandow, B. Denis, and J. Benedikt, Journal of Physics D: Applied Physics , 10 (2011), arXiv:1105.2207 .

[12] D. Nečas, V. Čudek, J. Vodák, M. Ohlídal, P. Klapetek, J. Benedikt, K. Rügner, and L. Zajíčková, Measurement Science and Technology **25**, 115201 (2014).

[13] H. M. Joh, J. Y. Choi, S. J. Kim, T. H. Chung, and T.-H. Kang, Scientific Reports **4**, 6638 (2014).

[14] J. F. M. van Rens, J. T. Schoof, F. C. Ummelen, D. C. van Vugt, P. J. Bruggeman, and E. M. van Veldhuizen, IEEE Transactions on Plasma Science **42** (2014), 10.1109/TPS.2014.2328793.

[15] S. Coulombe, V. Léveillé, S. Yonson, and R. L. Leask, Pure and Applied Chemistry **78**, 1147 (2006).

[16] S. Kelly and M. M. Turner, Plasma Sources Science and Technology **23**, 065012 (2014).

[17] M. Leduc, S. Coulombe, and R. L. Leask, IEEE Transactions on Plasma Science **37**, 927 (2009).

[18] J. L. Walsh, F. Iza, N. B. Janson, V. J. Law, and M. G. Kong, Journal of Physics D: Applied Physics **43**, 075201 (2010).

[19] M. Laroussi and X. Lu, Applied Physics Letters **87**, 28 (2005).

[20] J. Y. Kim, J. Ballato, and S. O. Kim, Plasma Processes and Polymers **9**, 253 (2012).

[21] V. Léveillé and S. Coulombe, Plasma Sources Science and Technology **14**, 467 (2005).

[22] J. Jarrige, M. Laroussi, and E. Karakas, Plasma Sources Science and Technology **19** (2010).

[23] L. Chauvet, L. Therese, B. Caillier, and P. Guillot, J. Anal. At. Spectrom. **29**, 2050 (2014).

[24] S. Yonemori, Y. Nakagawa, R. Ono, and T. Oda, Journal of Physics D: Applied Physics **45**, 225202 (2012).

[25] N. Knake, S. Reuter, K. Niemi, V. Schulz-von der Gathen, and J. Winter, Journal of Physics D: Applied Physics **41**, 194006 (2008).

[26] A. Sarani, N. De Geyter, A. Y. Nikiforov, R. Morent, C. Leys, J. Hubert, and F. Reniers, Surf. Coatings Technol. **206**, 2226 (2012).

[27] F. Massines, C. Sarra-Bournet, F. Fanelli, N. Naudé, and N. Gherardi, Plasma Process. Polym. **9**, 1041 (2012).

[28] E. Castaños Martínez and M. Moisan, Spectrochimica Acta Part B: Atomic Spectroscopy **65**, 199 (2010).

[29] P. S. Moussounda and P. Ranson, Journal of Physics B: Atomic and Molecular Physics **20**, 949 (1987).

[30] A. Kramida, Y. Ralchenko, J. Reader, and NIST ASD Team, "NIST Atomic Spectra Database (ver. 5.0), [Online]," (2012).

[31] A. Durocher-Jean, E. Desjardins, and L. Stafford, Physics of Plasmas **26**, 1 (2019).

[32] M. V. Malyshev and V. M. Donnelly, Physical review. E **60**, 6016 (1999).

[33] T. D. Nguyen and N. Sadeghi, Physical Review A **18**, 1388 (1978).

[34] R. S. F. Chang and D. W. Setser, The Journal of Chemical Physics **69** (1978).

[35] X.-M. Zhu and Y.-K. Pu, Journal of Physics D: Applied Physics **43**, 015204 (2009).

[36] W. Van Gaens and A. Bogaerts, Journal of Physics D: Applied Physics **47**, 079502 (2014).

[37] C. O. Laux, T. G. Spence, C. H. Kruger, and R. N. Zare, Plasma Sources Science and Technology **12**, 125 (2003).

[38] "www.specair-radiation.net," .

[39] J.-S. Poirier, P.-M. Bérubé, J. Muñoz, J. Margot, L. Stafford, and M. Chaker, Plasma Sources Sci. Technol. Plasma Sources Sci. Technol **20** (2011), 10.1088/0963-0252/20/3/035016.

[40] "ANSYS FLUENT 14.5, Theory Guide; ANSYS, Inc." .

[41] B. E. Launder and D. B. Spalding, *Lectures in Mathematical Models of Turbulence* (Academic press, London, England, 1972).

[42] B. Niermann, R. Reuter, T. Kuschel, J. Benedikt, M. Böke, and J. Winter, Plasma Sources Science and Technology **21**, 034002 (2012).

[43] B. Niermann, M. Böke, N. Sadeghi, and J. Winter, European Physical Journal D **60**, 489 (2010).

[44] B. L. Sands, R. J. Leiweke, and B. N. Ganguly, Journal of Physics D: Applied Physics **43**, 282001 (2010).

[45] X.-M. Zhu and Y.-K. Pu, Journal of Physics D: Applied Physics **43**, 403001 (2010).

[46] S. Förster, C. Mohr, and W. Viöl, Surface and Coatings Technology **200**, 827 (2005).

[47] B. N. Sismanoglu, J. Amorim, J. a. Souza-Corrêa, C. Oliveira, and M. P. Gomes, Spectrochimica Acta - Part B Atomic Spectroscopy **64**, 1287 (2009).

[48] S. Z. Li, J. P. Lim, and H. S. Uhm, Physics Letters, Section A: General, Atomic and Solid State Physics **360**, 304 (2006).

[49] J. M. Palomares, E. I. Iordanova, A. Gamero, A. Sola, and J. J. a. M. V. D. Mullen, Journal of Physics D: Applied Physics **43**, 395202 (2010).

[50] E. Iordanova, J. M. Palomares, A. Gamero, A. Sola, and J. J. a. M. van der Mullen, Journal of Physics D: Applied Physics **42**, 155208 (2009).

[51] S. Hübner, S. Hofmann, E. M. van Veldhuizen, and P. J. Bruggeman, Plasma Sources Sci. Technol. Plasma Sources Sci. Technol **22**, 65011 (2013).

[52] T. Farouk, B. Farouk, A. Gutsol, and A. Fridman, Plasma Sources Sci. Technol. Plasma Sources Sci. Technol **17**, 35015 (2008).

4.7. Article 6 : Diagnostics optiques d'un jet de plasma microonde d'argon appliqué au dépôt d'un revêtement antibuée sur verre

Le second jet de plasma sous étude dans ce chapitre et faisant l'objet d'un sixième article est celui d'un plasma microonde, lui aussi à base d'argon s'écoulant dans l'air ambiant. Puisqu'un des objectifs de cet article est d'explorer l'influence de la position du précurseur HMDSO dans le jet ainsi que son potentiel à réaliser un dépôt fonctionnel sur verre, toutes les mesures ont été réalisées dans une enceinte hermétique. Celle-ci avait pour but de réguler l'humidité et la température ambiantes via l'insertion et l'évacuation contrôlées d'un flux continu d'air comprimé. Quant au plasma lui-même, il a été produit à l'aide d'un montage similaire à celui des deux articles précédents sur les POS, à la différence près de l'utilisation d'un tube de silice fondue saillant seulement de 2 cm en aval du surfaguide servant au couplage des microondes. Avec un débit d'argon de 1.15 SLM et une puissance absorbée de 185 W, cette configuration a permis d'obtenir un jet de plasma en sortie du tube long de quelques centimètres.

Tel que démontré dans les résultats, la haute température des neutres dans le jet de plasma a entrainé la nécessité de faire défiler les échantillons de verres à 2.5 cm du tube afin d'éviter qu'ils cassent à cause de contraintes thermiques. D'ailleurs, cette température des neutres, de même que le profil spatial de la densité d'états 1s de l'argon, des températures de rotation du niveau OH(A), de vibration du niveau $N_2(C)$ et d'excitation des électrons sont tous obtenus à l'aide d'une caractérisation optique du jet de plasma. Ce faisant, des liens sont établis entre les propriétés fondamentales du jet de plasma, la fragmentation du précurseur selon sa position d'injection, le transport et la recombinaison en phase gaz des fragments qui en résultent et finalement le dépôt obtenu sur le substrat de verre. Plus spécifiquement, des mesures de microscopie optique, de mouillabilité à l'eau et de transmittance des échantillons mettent respectivement en lumière qu'une injection près du tube résulte en un revêtement très hydrophobe, poudreux et opaque dû à une importante fragmentation du précurseur par les électrons, métastables et neutres chauds du plasma, suivie par des réactions d'association en phase gaz favorisées par une grande distance de transport pour parvenir au substrat de verre. Au contraire, une injection loin dans le jet (donc près du substrat) résulte en un revêtement superhydrophile, uniforme et antibuée dû à une fragmentation plus modeste du précurseur par du rayonnement UV et des neutres chauds.

Deposition of anti-fog coatings on glass substrates using the jet of an open-to-air microwave argon plasma at atmospheric pressure

par

Antoine Durocher-Jean[1], Ivan Rodríguez[2], Siavash Asadollahi[1], Gaétan Laroche[2] et Luc Stafford[1]

([1]) Département de physique, Université de Montréal, Montréal, Québec, Canada

([2]) Laboratoire d'Ingénierie de Surface, Centre de Recherche sur les Matériaux Avancés, Département de Génie des Mines, de la Métallurgie et des Matériaux, Université Laval, Québec, Québec, Canada

Cet article a été soumis à la revue Plasmas Processes and Polymers (ppap.201900229.R1)

(La version inclue est celle après un premier retour positif par 4 arbitres) .

Les contributions des différents auteurs à cet article sont :

— Antoine Durocher-Jean : Élaboration du réacteur, prise des mesures, analyse des résultats et écriture du premier jet du manuscrit

— Ivan Rodríguez, Siavash Asadollahi et Gaétan Laroche : Révision du manuscrit

— Luc Stafford : Supervision des travaux, révision du manuscrit

Abstract.

This work reports a one-step process for the formation of anti-fog coatings on commercial glass substrates using the jet of an open-to-air microwave argon plasma at atmospheric pressure with hexamethyldisiloxane (HMDSO) as the precursor for plasma-enhanced chemical vapour deposition. The influence of the injection position of the precursor along the plasma jet was studied with regard to the coating features, including surface topography and wetting behaviour. Optical microscopy and broadband light transmittance measurements revealed significant precursor fragmentation and gas phase association reactions when HMDSO was injected close to the tube outlet, resulting in powder-like, hydrophobic, and semi-opaque glass surfaces. On the contrary, injection of HMDSO close to the substrate led to smoother, homogeneous, hydrophilic, and transparent glass surfaces. In addition, transmittance measurements at 590 nm in humid air according to ASTM standard tests revealed superior anti-fogging properties to plasma-treated glass substrates. Based on optical emission and absorption spectroscopy measurements, electrons, metastable argon atoms, and hot neutral argon atoms were mostly responsible for the significant precursor fragmentation close to the tube outlet, while the contribution of hot neutrals and UV photons became important close to the substrate.

Keywords: anti-fog coatings, microwave argon plasmas, organosilicon precursors, optical emission spectroscopy, optical absorption spectroscopy

4.4.1. Introduction

Over the last few decades, there has been a growing interest in the use of non-thermal plasmas at atmospheric pressure. In particular, they are now widely found in surface engineering applications due to their versatility, controllability, and operability. Because of the wide variety of plasma-generated species such as electrons, ions, excited species, reactive neutrals, and photons, it became possible to finely tune the surface structure and/or the surface chemistry of heat-sensitive materials for various purposes. Typical examples include the elaboration of coatings with wear- or corrosion-resistant features for the aeronautic industry [1-3], the functionalization of polymers and textiles for improved bonding [4,5], the design of water-repellent and UV-blocking surfaces for the wood, pulp, and paper industries [6-8], the development of superhydrophobic and icephobic surfaces with multiple levels of roughness [9-12], the modification of materials for the detection of hazardous molecules [13-15], and the manufacture of inorganic insulators and insulating polymers for the microelectronic and optoelectronic industries [16]. The fabrication of (super)hydrophilic surfaces have also recently attracted enormous attention, in part due to their capacity to eliminate the effects of water condensation (i.e., fogging) [17]. As recently reviewed by Durán and Laroche [18], (super)hydrophilicity causes water drops to spread on the surface to form a continuous or nearly continuous thin film of water (spreading mechanism), resulting in light scattering mitigation. In such case, any light ray at normal incidence with respect to the surface passes through the material without being refracted. In practical terms, the surface remains optically clear even under very humid conditions. In contrast, when water drops lying on the surface remain in their hemispherical or nearly hemispherical shape (hydrophobic surface), incident light is scattered because of refraction phenomenon at the water drop/air interface. As a result, the "see-trough" property becomes dramatically reduced, i.e. objects are seen blurry, if seen at all.

Numerous studies have examined the elaboration of anti-fog surfaces using techniques such as dip-coating, spin-coating, and layer-by-layer deposition [18]. However, approaches based on non-thermal plasmas at atmospheric pressure present clear advantages such as being safe for greenhouse and packaging applications (solvent-free processing), potentially integrable into large-scale mass production, and suitable for treating heat-sensitive materials such as polymers or composite materials [18]. Still, most of the plasma-based approaches

reported in the literature are generally either multi-step or reduced-pressure processes [19-24], two characteristics that hinder their overall cost-effectiveness and applicability.

To overcome these drawbacks, an open-to-air microwave argon plasma jet at atmospheric pressure was developed and used for the one-step deposition of anti-fog coatings on glass substrates. Up to now, atmospheric pressure plasma jets (APPJs) have been used in many different application fields such as surface activation, plasma medicine or thin-film deposition [8,9,25-29]. Similarly, deposition of antifog coatings on glass surfaces using an atmospheric pressure plasma process have also been reported [30,31]. However, as far as the authors are aware of, such one step processes never involved using an APPJ, allowing for a decoupling of the plasma generation zone from the plasma deposition zone. Consequently, the aim of this study is twofold: to examine the influence of the precursor injection position along the microwave argon plasma jet on the fundamental plasma properties, and to correlate the plasma jet characteristics with the plasma deposition dynamics and the micro and macroscopic properties of plasma-deposited coatings. To this end, optical microscopy, water contact angle, broadband light transmittance, and x-ray photoelectron spectroscopy measurements were performed to characterize the plasma-coated glass substrates. Light transmittance measurements at 590 nm in the presence of water vapor at 50°C (ASTM F 659-06 testing protocol [20]) were also used to assess the fogging resistance of plasma-coated glass substrates. Optical emission and absorption spectroscopy measurements performed along the plasma jet axis were realized to examine the populations of the plasma-generated species, in particular electrons, excited argon atoms, and UV photons. These measurements coupled with detailed calculations of the neutral gas, rotational, vibrational, and excitation temperatures, were also used to provide insights into the precursor fragmentation kinetics and plasma deposition dynamics, and thus into the resulting film properties.

4.4.2. Experimental details and data analysis methods

4.4.2.1. *Experimental setup and operating conditions*

Figure 4.12 shows a schematic of the experimental setup used to produce the open-to-air microwave argon plasma at atmospheric pressure. The system relies on a 2 kW Sairem microwave generator operating at 2.45 GHz. Microwave power was transported using WR430 waveguides up to a surfaguide-type wave launcher where the discharge tube was placed. A

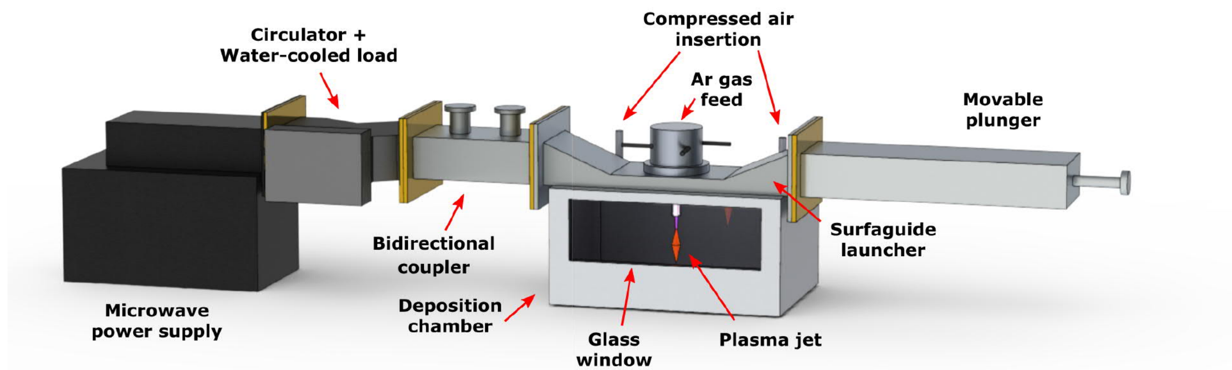

Figure 4.12. Schematics of the apparatus used for the production of an open-to-air argon plasma at atmospheric pressure sustained by microwave electromagnetic fields.

movable plunger located after the surfaguide was used to ensure maximal power transfer to the plasma. As shown in Figure 4.12, a circulator was inserted close to the microwave generator to direct unwanted reflections to a water-cooled load. In addition, a bidirectional coupler paired to a bolometer was used to measure the incident and reflected powers (and thus the absorbed power from the incident minus the reflected powers). In this work, the absorbed power was set at 185 W. A high purity argon flow maintained at 1.15 slm (standard liters per minute) using a mass flow controller was injected into a fused silica discharge tube (6 mm inner diameter, 8 mm outer diameter) in a vortex configuration. A thick brass piece was placed on the upper wall of the surfaguide around the discharge tube to hinder any microwave propagation in the upstream direction. As a result, the microwave power was predominantly absorbed by the downstream plasma column and this most probably resulted in different properties than if the upstream plasma column was not blocked. Furthermore, the discharge tube extended only 2 cm below the wave launcher and was open to ambient air at the outlet. As shown in Figure 4.13, these conditions of input microwave power, argon mass flow rate, and tube length below the surfaguide resulted in the formation of a plasma jet visually stable over short and long periods of time. This configuration was first described by Moisan *et al.* [32]. Regions similar to those later examined by Moon *et al.* were also observed in this study [33]. In particular, three plasma filaments stable in time

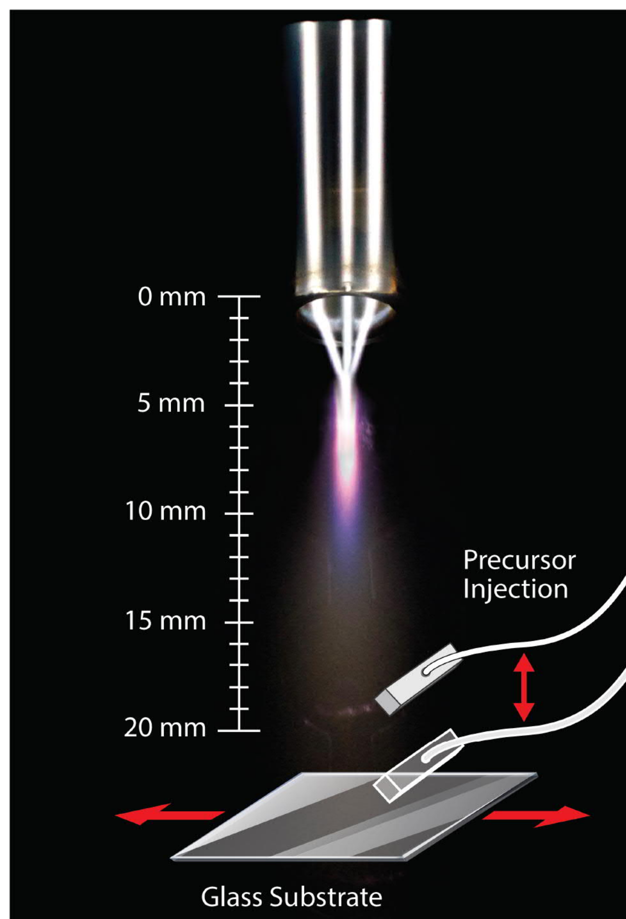

Figure 4.13. Picture of the microwave plasma jet along with the precursor injection system.

and space (not rotating nor visually fluctuating) formed the microwave plasma inside the discharge tube. These plasma filaments then converged at a single, on-axis point located a few millimetres below the tube outlet. Beyond this converging point, an open-to-air plasma jet was observed.

For deposition purposes, this plasma jet configuration offers a great flexibility as the interaction between the plasma-generated species and the precursor molecules can be tuned by varying the injection position along the flowing afterglow. In this study, hexamethyldisiloxane (HMDSO, Aldrich 99.5% purity) was used as the precursor and argon (Ar, Praxair 99.99% purity) was used as the carrier gas. Liquid HMDSO was atomized into the plasma jet at a rate of 4 μL/min using a syringe pump (KD Scientific Legato 110^{TM}, Fisher Scientific, Canada) coupled to a nebulizer (Mira Mist CE^{TM}, Burgener Research Inc., Mississauga, Canada). The mass flow rate of the carrier gas was set at 0.2 slm. As illustrated in Figure

4.13, the precursor was carried toward the plasma zone in a capillary stainless-steel tube. This tube was long enough to ensure that only HMDSO vapors (no droplets) are injected into the plasma jet. HMDSO injection was realized at five different positions beneath the discharge tube. These positions ranged from 16 to 24 mm. Commercial glass samples (Multiver Ltée, Québec, Canada) measuring 40 mm $\times$ 50 mm were placed 25 mm below the tube outlet. Immediately prior to coating deposition, glass samples were successively cleaned once in an ultrasonic bath with methanol and acetone and dried with oil-free compressed air. During the deposition process, samples were continuously moved back and forth laterally under the gas flow lines at a speed of 2 cm/s. Because of the high neutral gas temperatures reached in this microwave plasma jet configuration (see Section 4.4.3.2), substrate displacement prevented shattering of glass samples. Every deposition reported in this work consisted of 50 round trips under the plasma jet, for a total deposition time of approximately 8 min. During this time, the surface temperature of the glass samples was measured by a thermocouple to increase from room temperature ($\sim$293 K) to roughly 470 K.

To ensure reproducible experimental conditions, in terms of humidity and temperature, coating deposition was carried out in a sealed stainless-steel chamber ($35 \times 35 \times 65$ cm^3=$\sim$80 L) continuously filled with 35 slm of oil-free compressed air. A fan placed at the bottom of the chamber ensured gas exhaust. An aluminum plate was also placed a few centimetres above the bottom of the chamber and a few centimetres from the chamber walls to ensure proper distribution of the compressed air and argon gas flow lines, and to minimize perturbation of the plasma jet. Over the range of experimental conditions examined in this study, relative humidity and temperature inside the stainless-steel chamber were maintained at $\sim$10% and $\sim$35°C, respectively. This temperature has been monitored for different locations in the chamber but a temperature gradient is expected close to the plasma jet since, as shown below, neutral gas temperatures obtained by optical emission spectroscopy reveal temperature values much higher than 35°C.

4.4.2.2. *Methods for surface characterization of plasma-coated glass substrates*

Characterization of plasma-coated glass substrates was carried out immediately following the deposition process to minimize natural ageing effects [34-37]. Optical microscopy (OMAX Infinity Trinocular microscope) was performed to obtain qualitative data on the surface

roughness and homogeneity of the coatings. A 1500X magnification made it possible to gather information at the micrometer scale. The wetting behavior was assessed by the sessile drop method (Biolin Scientific Theta optical tensiometer, Gothenburg, Sweden). Here, 3 μL water drops were deposited on the surface at three different locations and the apparent contact angle (ACA) was measured after 1 s. Optical transparency of the plasma-coated-glass substrates was analyzed using a broadband wavelength transmittance test. Briefly, the transmittance of a bare glass sample (I_G) was first measured using a deuterium-halogen lamp and a low-resolution spectrometer in the 200-1600 nm range. The transmittance was obtained from the ratio of the lamp optical spectra with (I_1) and without (I_0) the glass sample, i.e. $I_G=I_1/I_0$. Afterwards, the lamp optical spectra through each plasma-coated sample was measured (I_2). In order to obtain the transmittance of the plasma-deposited coatings exclusively (I_C) and not a combination of glass and coating transmittances, I_G instead of I_0 was considered as the reference intensity, and thus $I_C= I_2/I_G$.

The anti-fogging feature of plasma-coated glass substrates was tested according to the ASTM F659-06 standard [38] using a custom-built anti-fog measuring device. A schematic diagram of a device very similar to the one used can be found in ref [20]. Briefly, glass samples were placed over a bath containing hot water at 50°C and the two-pass transmittance of a 590 nm light beam was recorded as a function of time. According to the standard, a surface can be considered as anti-fog if the minimal transmittance over time is maintained above 80% for more than 30 seconds. Typical transmittance plots for samples obtained for different injection positions in the jet are presented in Figure 4.14. For all conditions, the first few instants correspond to the maximal transmittance possible when no sample is present. Then, the abrupt and noisy transmittance drop corresponds to the moment when the sample is inserted. At this stage, water vapour instantaneously condenses on the surface in the form of micro-droplets, thus accounting for the observed decrease in transmittance. As the glass gets warmer and droplets coalesce to form a sheet-like layer, the transmittance tends to recover despite temporary fluctuations caused by the formation and coalescence of new water droplets. In practice, this translates into rather noisy transmittance plots, as depicted in Figure 4.14 (blue line) for the uncoated, bare glass sample.

X-ray photoelectron spectroscopy (XPS) analysis were performed on selected samples (3 areas per sample) using a Thermo Scientific K-Alpha Photoelectron Spectrometer system.

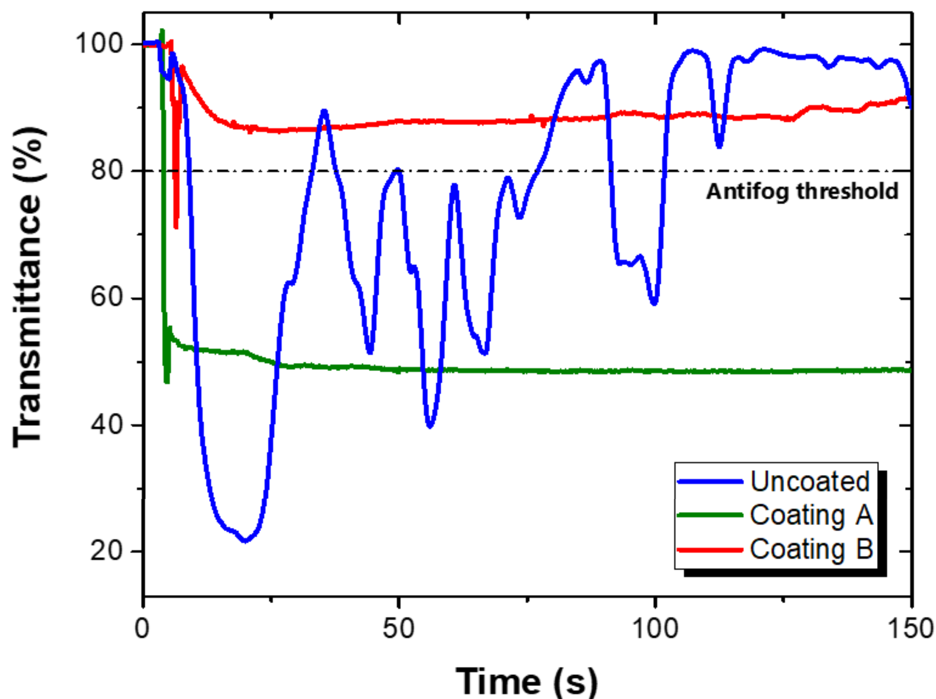

Figure 4.14. Transmittance of different glass samples (before and after plasma treatment) as a function of time when exposed to a warm, humid atmosphere.

The beam size of the Al K_α source was set at 0.4x0.4 mm^2. Survey spectra were taken with a pass energy of 200 eV and an energy step size of 1 eV, while high-resolution spectra of the C1s and Si2p peaks were taken using an energy step size of 0.1 eV. The spectrometer work function was calibrated by the setting the binding energy of the C-C bond at 285 eV. Atomic composition analysis on the survey spectra were performed using the Avantage software. Curve-fitting of the high-resolution spectra using Gaussian-Lorentzian functions and a Shirley-type background were performed using the CasaXPS v.2.3.22 software. The results presented below are the mean of the results for the 3 areas probed in each case.

4.4.2.3. *Methods for plasma jet characterization*

Optical spectroscopy in the UV-visible spectral range was realized along the jet axis to characterize the populations of plasma-generated species. A pinhole (0.5 mm wide × 15 mm long) was placed in front of the optical fibers facing the jet to gather spatially-resolved measurements. For the jet-to-optical fiber distance used in this study, the axial resolution was estimated to 0.8 mm. Optical emission spectra (OES) were recorded every millimetre below the tube outlet down to 20 mm (defined in Figure 4.13). Beyond this position, the

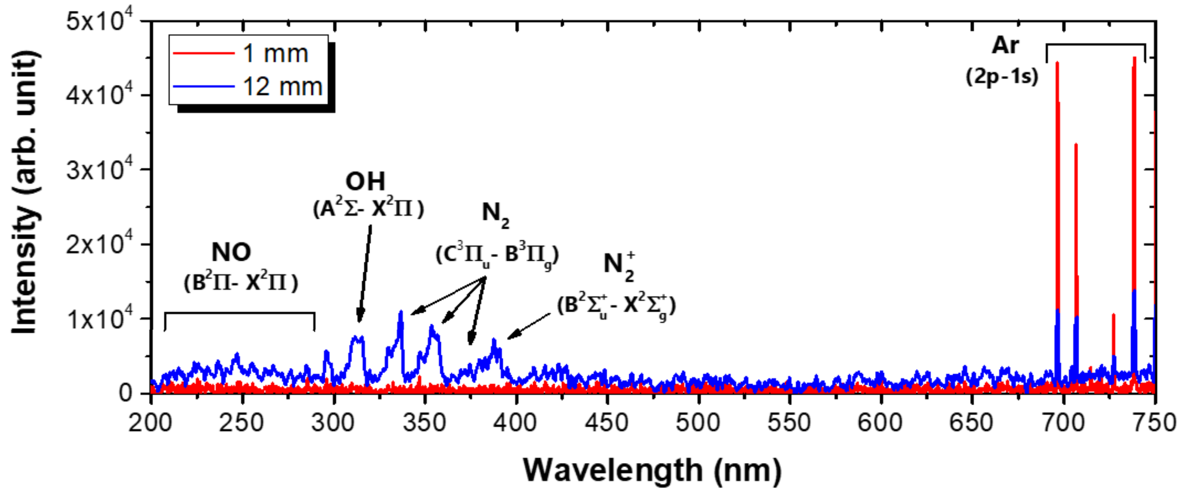

Figure 4.15. Typical OES spectra along the jet of the open-to-air microwave argon plasma. The results are shown at 1 and 12 mm from the tube outlet.

light intensity became too weak to obtain reliable OES data. However, for some of the other analysis based on optical emission and absorption spectroscopy, weaker and thus less reliable signals were observed before the 20 mm position. For this reason, fewer data point are shown in the forthcoming graphs for some properties measured as a function of position. Typical OES spectra taken using a low-resolution Avantes spectrometer are shown in Figure 4.15.

Close to the tube outlet, the fiber was facing directly one of the three filaments (see typical image in Figure 4.13), and the plasma emission was dominated by argon atomic lines. However, as the jet expanded into ambient air, this emission was replaced by those originating from molecular rovibrational systems of N_2, N_2^+, OH, and NO species. These emission bands typical of non-thermal plasmas expanding into ambient air have also been observed by several authors in different plasmas and jet configurations [39-43].

Further OES analyses were realized using a high-resolution spectrometer (HORIBA Jobin Yvon THR1000 monochromator) equipped with a photomultiplier tube (Hamamatsu R636-10) and a 1800 lines/mm holographic grating. This system provided significant spectral resolution to resolve most of the OH $A^2\Sigma$-$X^2\Pi$ molecular bands in the UV region. A typical example of this system is presented in Figure 4.16a. The lines used in the calculation of a rotational temperature (T_{rot}) from the Boltzmann plot [44-46] using the OH rovibrational constants reported by Dieke and Crosswhite [47] are also shown in Figure 4.16a.

The same high-resolution spectrometer was used to measure the line broadening of the Ar $2p_2$-$1s_2$ and $2p_3$-$1s_2$ (Paschen notation) emission lines at 826 nm and 841 nm. These two lines were specifically chosen because, at atmospheric pressure, they are strongly affected by resonance broadening and this results in the Lorentzian portion of their broadening to be completely dominated by mechanisms linked to the neutral gas temperature (T_g) (resonance and van der Waals broadening) [48,49]. With this in mind, for every line broadening measurement, the Lorentzian component of the broadening was deconvoluted from the Gaussian one by fitting a Voigt function. A minimal Gaussian width arising from the instrumental broadening at both the emission lines central frequency (~21.5 pm, measured from the emission of a low-pressure, low-neutral-gas-temperature Ar plasma), was always considered. Typical measurements along with their Voigt fits are presented in Figure 4.16d. Any T_g value reported in this paper is the mean of the temperatures found from both lines and the error is defined as the standard deviation.

OES measurements were also recorded using a 320 mm focal length spectrometer (Princeton Instruments IsoPlane SCT-320) equipped with an intensified charged coupled device camera (Princeton Instruments PI-MAX4 1024x256) and a 2400 lines/mm grating. This system provided a spectral resolution (full width at half maximum) of ~0.061 nm between 360 and 695 nm. A few bands of the N_2 $C^3\Pi_u$-$B^3\Pi_g$ rovibrational system and Ar atomic emission lines originating from high-energy levels (3d, 5s, 5p, etc.) can be observed. The band head emission intensities of the $\Delta v = 2$ sequence together with the N_2 rovibrational constants reported by Lofthus and Krupenie [50] were used to build a Boltzmann plot, and thus to calculate a vibrational temperature (T_{vib}). A typical example is shown in Figure 4.16b; the three band heads identified were the only ones observed throughout the whole microwave argon plasma jet and therefore the only ones considered. Similarly, Ar emission line intensities from Ar high-energy levels were used to obtain an electron excitation temperature (T_{exc}). The data for the Ar lines were taken from the NIST spectral database [51]. A typical spectrum is presented in Figure 4.16c along with the lines that were used in the construction of the Boltzmann plot.

It is worth highlighting that the excitation temperature obtained from the Boltzmann plot is mostly representative of the low-energy part of the electron energy distribution function,

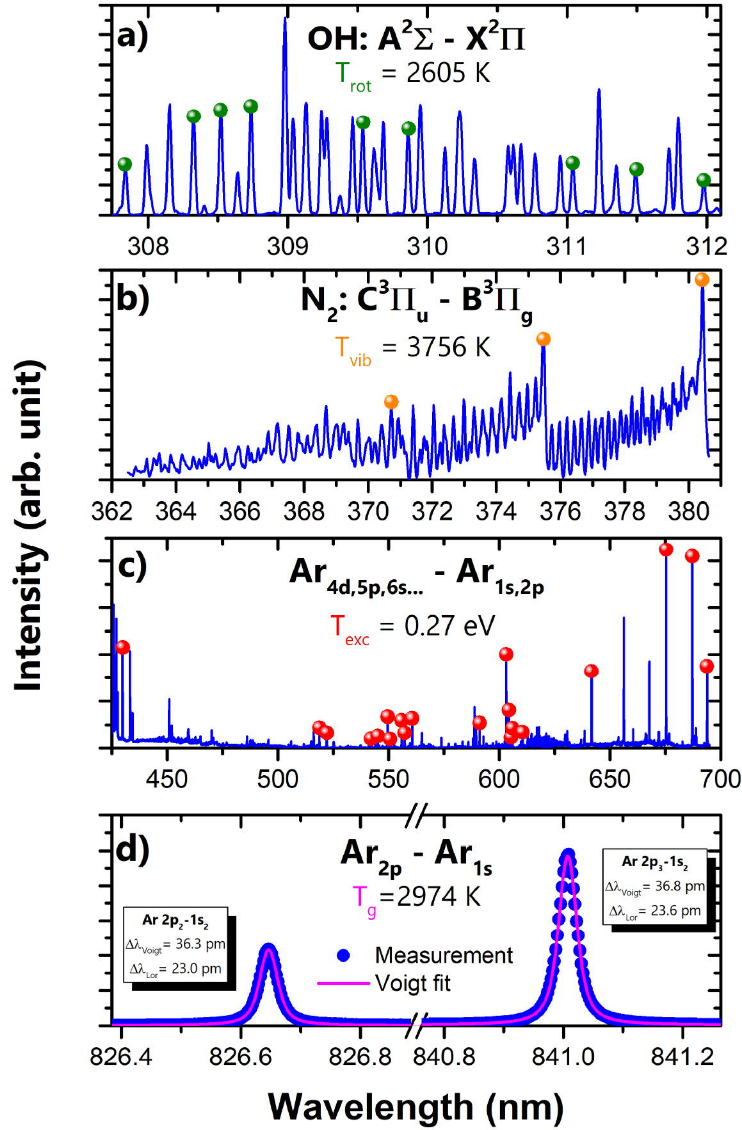

Figure 4.16. a) OH emission used for the calculation of T_{rot}. b) N_2 emission used in the calculation of T_{vib}. c) Ar emission used in the calculation of T_{exc}. d) Ar line broadenings used for the calculation of T_g.

and therefore must not be regarded as the actual electron temperature [40]. Indeed, the high-energy electronic levels behind the observed Ar emission lines (Figure 4.16c) are separated by 1 eV at the most. Given the large number of low-energy electrons, an excitation-de-excitation equilibrium of these levels through electron collisions becomes easily achievable. In sharp contrast, the populations of Ar 2p states yielding to the Ar 2p-1s emission lines above 690 nm cannot be described by a simple Boltzmann distribution [52]. For such transitions, OES measurements need to be coupled with the predictions of a collisional-radiative model

for Ar 2p states to obtain the corresponding electron temperature. This approach has been implemented by quite a number of authors, in argon-based dielectric barrier discharges and in argon plasma columns sustained by electromagnetic surface waves [48,49]. However, several reasons make it difficult to apply this approach over the range of experimental conditions herein reported. In particular, the gas phase composition changes significantly with the axial position because of the open-to-air configuration such that adequately describing quenching reactions of Ar 2p states by collisions with Ar, N_2, and O_2 species is a very challenging task. In addition, the radiative transfer equations of Ar 2p-1s transitions become difficult to solve in spatially-inhomogeneous plasma and flowing afterglows [48]. For this reason, excitation temperatures instead of electron temperatures are presented in the forthcoming graphs.

The population of argon $1s_5$ atoms was determined by optical absorption spectroscopy measurements using a tunable laser diode (Pilot PZ 500, Sacher Lasertechnik, Marburg, Germany) in a Littman/Metcalf configuration (laser linewidth < 100 kHz). A more detailed description of this technique can be found in reference [48]. Briefly, a piezoelectric actuator enabled a periodical frequency sweep of the laser frequency centered on the Ar $2p_9$-$1s_5$ transition and a wavelength meter (HighFinesse GmbH WS6-600) was used to monitor the sweeping process. An oscilloscope (Teledyne-Lecroy HDO6104) connected to two photodiode detectors recorded both the reference (unabsorbed) intensity I_0 of the laser and the absorbed one I_t as a function of time (laser frequency). As the optical transition was periodically swept with the laser frequency first decreasing and then increasing, two absorption spectra were obtained for each measurement. Similar to the high-resolution OES procedure described above, the n_{1s_5} values reported in this work are the average of these two spectra. The error in n_{1s_5} is the standard deviation.

4.4.3. Experimental results and discussion

4.4.3.1. *Surface characterization*

Figure 4.17 shows optical images of the plasma-deposited coatings. While as-received, bare glass samples are smooth and homogeneous, a drastic change in the surface homogeneity and morphology can be observed for the various precursor injection positions. The coatings went from powder-like microstructure at 16 mm (left, injection high in the jet) to much flatter and more uniform microstructure at 24 mm (right, injection close to the glass sample).

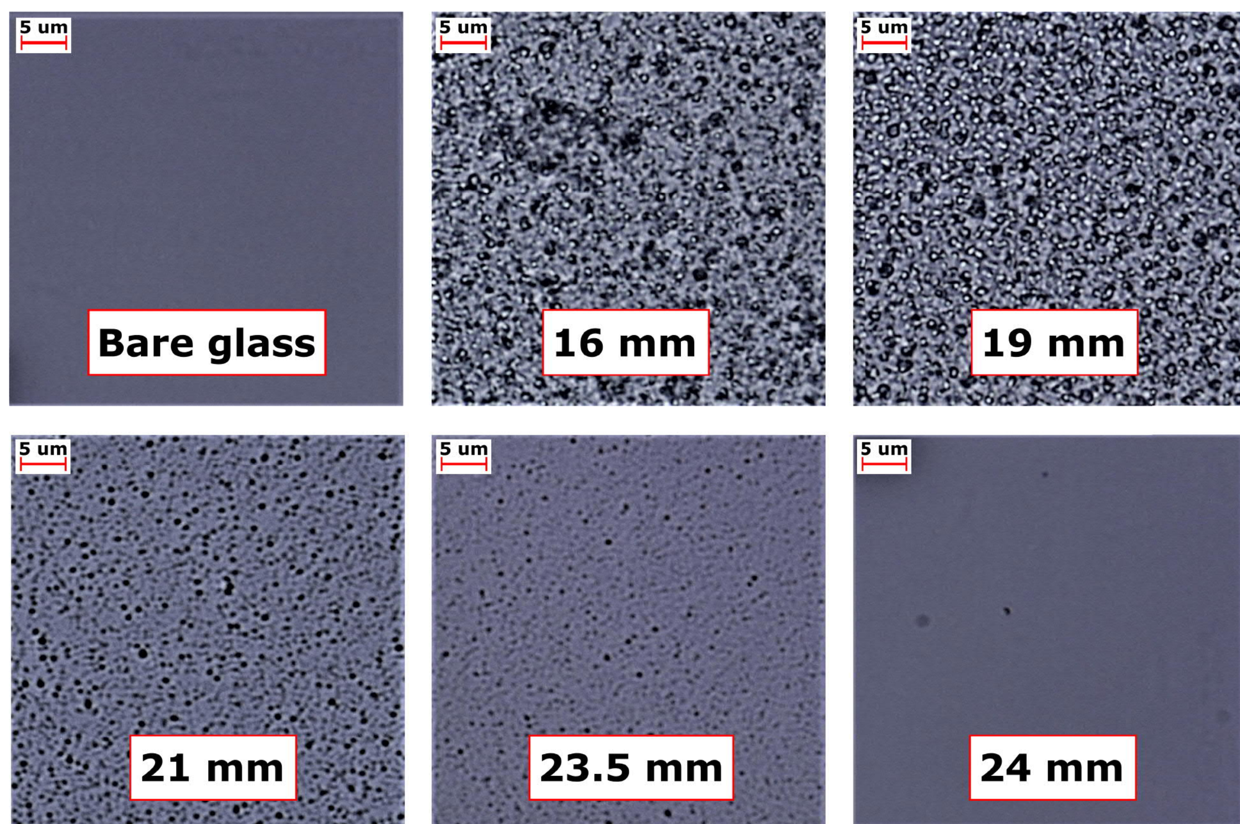

Figure 4.17. Optical images of the plasma-deposited coatings for various precursor injection positions along the jet of the open-to-air microwave argon plasma.

Injection positions closer to the tube outlet (< 16 mm) resulted in a coating homogeneity and morphology very similar to the ones observed at 16 mm (not shown). Changes in the surface roughness were confirmed by profilometry measurements: the root mean square (RMS) roughness of plasma-deposited coatings went from 544±60 nm for the 16 mm sample down to 88±2 nm for the 24 mm sample. As a comparison point, bare glass samples had a roughness of 15±0.5 nm. Powder-like microstructures resulting from the injection of HMDSO in non-thermal argon-based plasmas at atmospheric pressure have also been observed by other authors for high populations of plasma-generated fragments [53-57]. These conditions can be achieved either at low precursor fragmentation levels with high precursor concentrations (precursor-rich/energy-deficient regime) or at high precursor fragmentation levels with low precursor concentrations (precursor-lean/excess-energy regime) [58,59]. In both cases, the high populations of plasma-generated fragments promote gas phase recombination reactions leading to the formation of nanoparticles (dusty plasma) instead of heterogeneous surface reactions leading to the deposition of a thin film (non-dusty plasma). These arguments are

consistent with the topographical images shown in Figure 4.17. When the precursor injection occurs close to the tube outlet, the precursor molecules travel a large distance (high residence time) before they reach the glass sample. This implies a significant interaction with plasma-generated species and thus a large probability for significant fragmentation and gas phase recombination reactions leading to powder formation and deposition. On the contrary, when the precursor injection position is moved closer to the substrate, the precursor molecules travel a short distance (low residence time) before they deposit on the glass sample. This reduces the interaction with plasma-generated species and thus promotes the deposition of relatively smooth and homogeneous thin films with extremely low concentration fractions of plasma-generated particles.

The transition from a powder-like microstructure at 16 mm to a much smoother and more uniform microstructure at 24 mm was accompanied by a significant change in the transmittance of the plasma-coated glass substrates. On the left-hand side of Figure 4.18, the transmittance of the coatings exclusively (I_C) is reported. Additionally, the reference transmittance of a bare glass substrate (I_G) is also presented on the right-hand side to highlight its opacity in the UV range (below 300 nm), and thus to justify why no percent transmittance values for the coatings were reported below this threshold value. Coatings obtained following HMDSO injection at 16 and 19 mm blocked more than half of the visible light (semi-opaque) and performed quite well in the near infrared region (orange and purple lines in Figure 4.18). This result can be linked to the aforementioned powders: their presence provides coatings with an unattractive, whitish appearance visible to the naked eye. However, as the precursor injection position approaches the glass substrate, transmittance rises progressively between 400 and 1600 nm up to more than 90%. For these conditions, visual inspection revealed no noticeable disparity between uncoated and plasma-coated glass samples.

Minimal transmittances at 590 nm obtained in a humid atmosphere are presented in the left-hand side of Figure 4.19. These values correspond to the minimal transmittance observed in the transmittance versus time plots displayed in Figure 4.14. As can be seen, plasma deposition with HMDSO in the jet of the open-to-air microwave argon plasma significantly improves the anti-fog performance of glass substrates. In addition, the minimal transmittance increased with the injection position of the precursor with respect to the tube

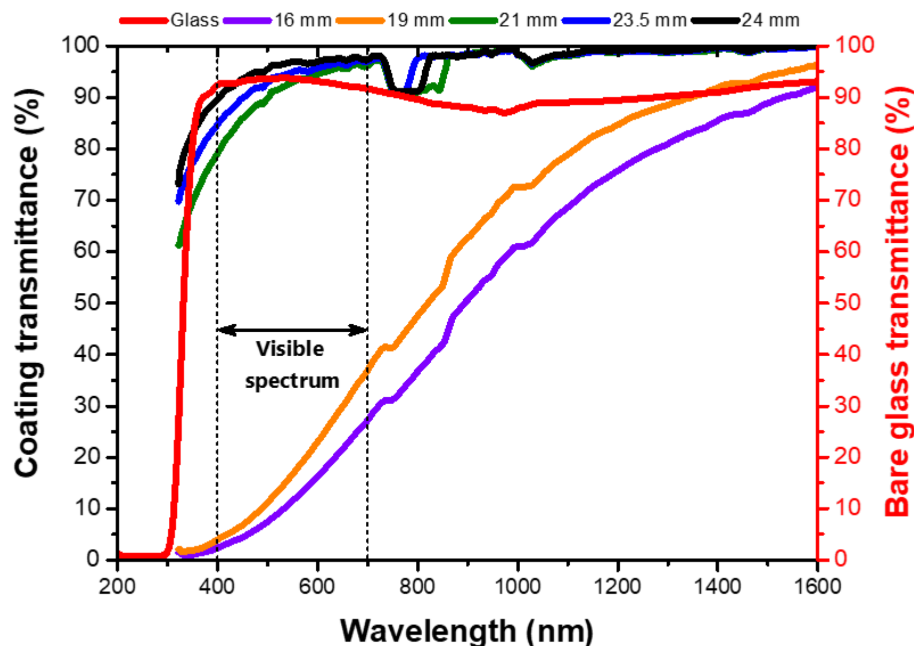

Figure 4.18. Transmittance plots of the coatings for various precursor injection positions along the jet of the open-to-air microwave argon plasma (left) and reference transmittance of the glass substrate (right).

outlet. Moreover, when the precursor was injected very close to the substrate surface (24 mm in Figure 4.19), plasma-deposited coatings were anti-fogging according to the ASTM F659-06 standard [38]. It is worth highlighting that glass samples were not anti-fogging according to the ASTM F659-06 standard [38] in absence of HMDSO in the flowing afterglow; this confirms that the optimal anti-fog behaviour was directly linked to the plasma deposition of a functional coating.

Anti-fog data were correlated with apparent contact angle (ACA) measurements (right side of Figure 4.19). ACA values ranged from 155±3° (highly hydrophobic surface), when the precursor was injected closer to the tube outlet, to 0° (superhydrophilic surface) when the precursor was injected closer to the glass sample. In addition, the plasma-coatings characterized by the lower ACA (at 24 mm) featured the most promising anti-fog performance. This result appears to concur with the theory of minimal light scattering for uniform or continuous films [18].

It is well established in the literature that the contact angle of a liquid on a surface results from the combined effect of the surface chemistry and the surface roughness [60-62].

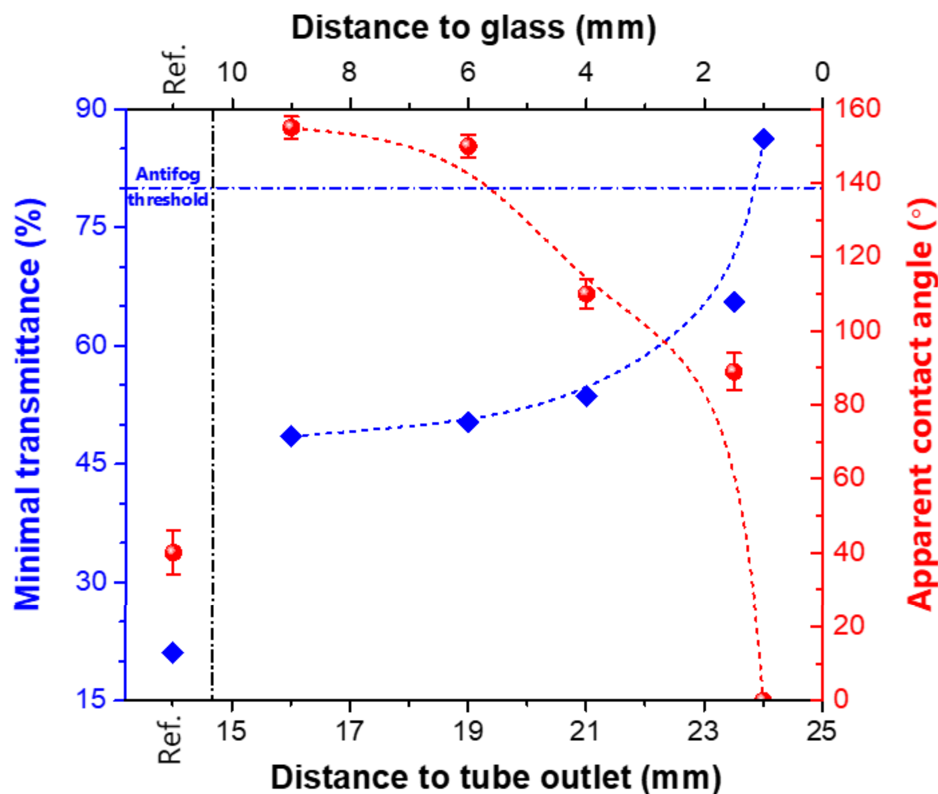

Figure 4.19. Minimal transmittance during the anti-fog test (left) and apparent contact angle (right) of the coatings.

Furthermore, according to both the Wenzel and the Cassie-Baxter theories, surface roughness emphasizes the natural tendency of a surface to be hydrophobic or hydrophilic [63,64]. Experimental data presented in Figures 4.17, 4.18, and 4.19 suggest that both the surface chemistry and the surface roughness are modified. For very high injection positions with respect to the glass sample, the semi-opaque coatings are characterized by ACA values above 150°. The formation of semi-opaque and water-repellent coatings using HMDSO as the growth precursor can be attributed to the deposition of SiO_xC_y:H films with a high concentration of hydrophobic methyl groups [6,10,54,65-68]. However, smooth and homogeneous SiO_xC_y:H films are generally characterized by water contact angles around 130° [6]. In line with Wenzel's theory, the higher values reported in Figure FigAntibuee8 most likely results from the powder-like and very rough microstructure observed in Figure FigAntibuee6 [10,11].

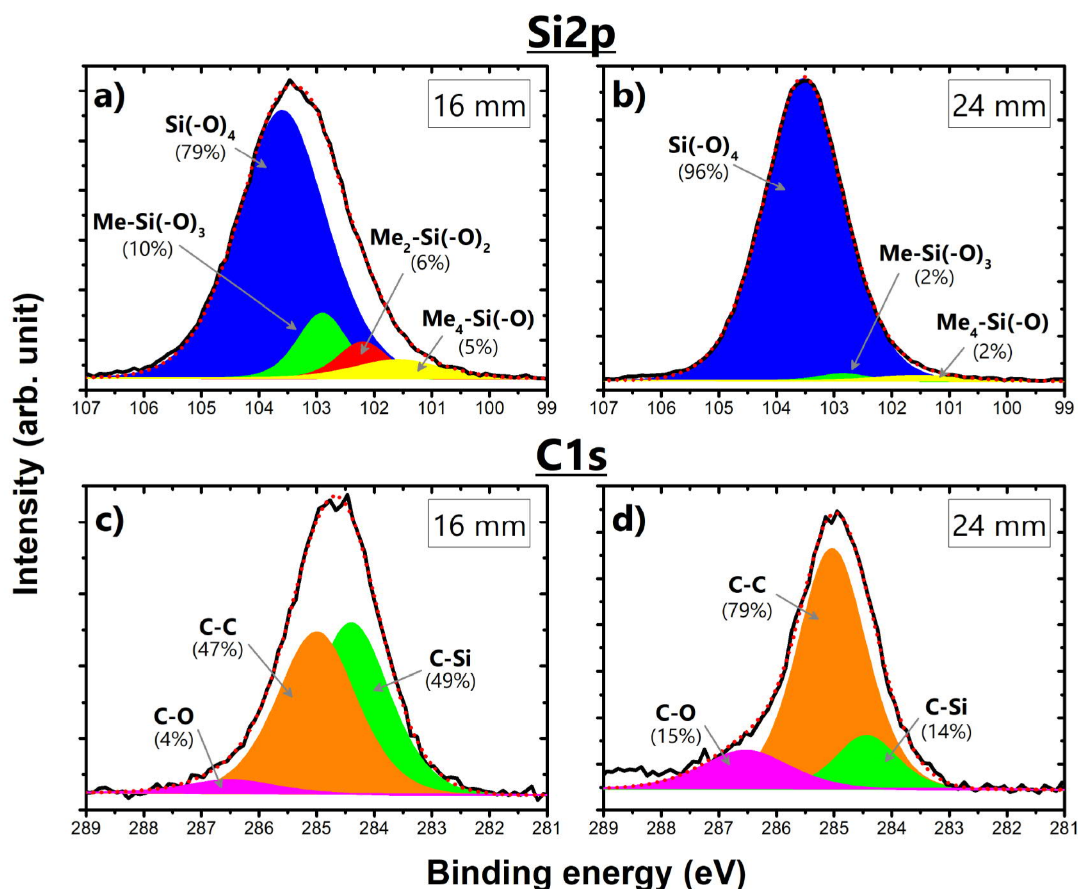

Figure 4.20. XPS high-resolution scans of Si2p(top) and C1s (bottom) peaks of the plasma-deposited coatings for experiments realized at 2 injection positions: 16 mm (left) and 24 mm (right).

On the other hand, for organosilicon precursors in presence of oxygen species, the formation of transparent and hydrophilic coatings can be linked to the plasma deposition of SiO_xC_y:H with very low carbon content [69,70]. In addition, superhydrophilic surfaces have been produced in HMDSO-based plasmas for SiO_xC_y:H coatings with a very high silanol (Si-OH) content (x>2, i.e. oxygen-to-silicon ratio >2) [71,72]. In such cases, it was found that silanol groups were preferentially formed on the substrate surface, and not through gas phase collisions involving HMDSO and plasma-generated fragments. In another study, the anti-fog property of an organosilicon-based coating was linked to the presence of silanol groups [31]. In line with these findings, it can be suggested that the superhydrophilic and anti-fog glass samples obtained when HMDSO was injected very close to the substrate surface results from the plasma deposition of SiO_xC_y:H films with most likely a low carbon content and a high silanol content.

These chemical aspects were verified by XPS analyses for the two limit conditions, namely when the precursor injection position was at 16 mm and 24 mm. On the one side, survey spectra revealed the presence of silicon, oxygen and carbon in proportions of ~25%/60%/15% at 16 mm and ~30%/63%/7% at 24 mm. As expected, the films obtained for an injection position of 24 mm reveal a lower carbon content. However, these carbon values obtained from the survey spectra may be somewhat amplified due to surface contamination that most probably occurred between the plasma deposition process and the XPS analysis. On the other side, high-resolution XPS spectra of the Si2p peak presented in Figure 4.20 a and b also point to a significantly lower carbon content for the 24 mm condition than for the 16 mm one. This conclusion results from the spectral decomposition of the peak into four components, as done by Rodriguez-Duran *et al.* based on the works of O'Hare *et al* and Alexander *et al* [30,73,74]. These components are attributed to Si atoms surrounded by methyl groups (Me) and oxygen atoms, namely Me_3-Si(-O) (or M-units, 101.5 eV), Me_2-Si$(-O)_2$ (or D-units, 102.1 eV), Me-Si$(-O)_3$ (or T-units, 102.8 eV), and Si$(-O)_4$ (or Q-units, 103.4-103.6 eV). Even if the last two components dominate the high-resolution Si2p spectra, a more important concentration fraction of carbon-containing units can be seen at 16 mm than at 24 mm. Additionally, as described in Table 4.3, this spectral decomposition allows for the calculation of an atomic percentage of Si, O and C in the coating. This time, the Si/O/C content is calculated to be 20%/73%/7% at 16 mm and 20%/78%/2% at 24 mm.

Interestingly, the carbon proportions obtained from the high-resolution Si2p peaks (7% at 16 mm and 2% at 24 mm) are significantly lower than those obtained from the survey spectra (15% at 16 mm and 7% at 24 mm). This discrepancy by a factor of ~2 and ~4, respectively, can be understood by looking at the high-resolution C1s peaks presented in Figure 4.20 c and d. By decomposing the peaks into three components (C-Si at 284.4 eV, C-C at 285 eV, and C-O at 286.5 eV [10,11]), it can be seen that the C-C component play an important role in both samples. While C-C and C-Si are almost equal in the 16 mm case, the contribution of C-C represents 80% of the C1s signal in the 24 mm case. Assuming that the C-C component is mainly related to surface contamination and that the C-Si component is mostly due to carbon atoms linked to Si atoms in the plasma-deposited coatings, it becomes clear that the survey results were biased by surface contamination effects. Indeed, in the 16 (24) mm case, if 50% (80%) of the C1s signal is due to surface contamination, the obtained

Table 4.3. Calculation of the Si, C and O atomic percentages in the plasma-deposited coatings for experiments realized at the 16 mm and 24 mm injection positions according to the high-resolution spectra

16 mm condition	Me_3-Si(-O)	Me_2-Si(-O)$_2$	Me-Si(-O)$_3$	Si(-O)$_4$	Total
Relative concentration	0.05	0.06	0.10	0.79	
Si / component	1	1	1	1	
Relative amount in coating	1×0.05=0.05	0.06	0.10	0.79	1
C / component	3	2	1	0	
Relative amount in coating	3 ×0.05=0.15	0.12	0.10	0.0	0.37
O / component	1	2	3	4	
Relative amount in coating	1×0.05=0.05	0.12	0.30	3.16	3.63

Atomic percent in the coating	Si: $100\times\frac{1}{1+0.37+3.63}=20.0\%$	C: 7.4%	O: 72.6 %

24 mm condition	Me_3-Si(-O)	Me_2-Si(-O)$_2$	Me-Si(-O)$_3$	Si(-O)$_4$	Total
Relative concentration	0.02	0.0	0.02	0.96	
Si / component	1	1	1	1	
Relative amount in coating	1×0.02=0.02	0.0	0.02	0.96	1
C / component	3	2	1	0	
Relative amount in coating	3 ×0.02=0.06	0.0	0.02	0.0	0.08
O / component	1	2	3	4	
Relative amount in coating	1×0.02=0.02	0.0	0.06	3.84	3.92

Percentage in coating	Si: $100\times\frac{1}{1+0.08+3.92}=20.0\%$	C: 1.6%	O: 78.4 %

carbon percentage in the coating becomes overestimated by a factor of 2 (5) in the survey spectra, in very good agreement with our experimental data.

This being established, similar atomic percentages of carbon, silicon and oxygen as for the 16 mm condition were reported by Asadollahi *et al.* [10,11] for superhydrophobic and ice-phobic coatings. These coatings were deposited on pre-treated aluminum substrates using a commercial OpenAir AS400 atmospheric pressure plasma jet manufactured by PlasmaTreat, with nitrogen as the ionization and carrier gas, and HMDSO as the growth precursor. In such conditions, due to the high available energy per precursor molecules and the relatively low oxygen content, high fragmentation of HMDSO followed by gas phase recombination of plasma-generated fragments lead to organosilicon coatings with a very high concentration

fraction of hydrophobic methyl groups [10,11]. These conditions of high-available energy per precursor molecules (mainly stored in the plasma in the form of electron kinetic energy) and relatively low oxygen content are similar to those involved in the microwave argon plasma jet at 16 mm. More details on this point are provided in the plasma characterization section.

For the 24 mm condition, XPS analysis showed less carbon on the surface and an oxygen-to silicon atomic ratio slightly above 2. Similar atomic percentages of carbon, silicon and oxygen were reported by Rodriguez-Duran *et al.* [30,31] for superhydrophilic and antifog coatings deposited on glass substrates using a homogeneous Townsend dielectric barrier discharge in N_2/N_2O gas mixtures and tetramethylcyclotetrasiloxane (TMCTS) as the growth precursor. In such conditions, because of the much lower values of available energy per precursor molecules and the presence of oxidant species in the gas phase, low fragmentation level of TMCTS followed by gas-phase and surface oxidation or organosilicon fragments leads to silica-like coatings with a very low carbon content. These conditions are similar to those involved in the open-to-air microwave argon plasma jet at 24 mm. Indeed, the available energy per precursor molecules is not only lower than before (mainly stored in the form of UV photons and hot neutrals), but also is the oxygen content relatively high. Again, more details on this point are provided in the plasma characterization section. Therefore, over the range of experimental conditions examined in this study, plasma deposition of organosilicon coatings relies on a combination of two processes. On one hand, plasma is enhancing the deposition process by fragmenting the HMDSO molecules and creating species from which the coating may grow (plasma as the growth medium, with the precursor fragmentation kinetics being linked to the available energy per precursor molecules). On the other hand, plasma-generated-species and oxidant species are interacting with the substrate surface, breaking some of the less stable surface bonds and modifying surface chemical composition (plasma as the activation medium) [75].

4.4.3.2. *Plasma jet characterization*

The film properties analyzed in the previous section were compared to the plasma properties obtained from optical diagnostics to gain insights into the plasma deposition dynamics along the jet of the open-to-air microwave argon plasma. Spatially-resolved emission intensities are reported in Figure FigAntibuee10. Pure argon plasma generated inside the discharge

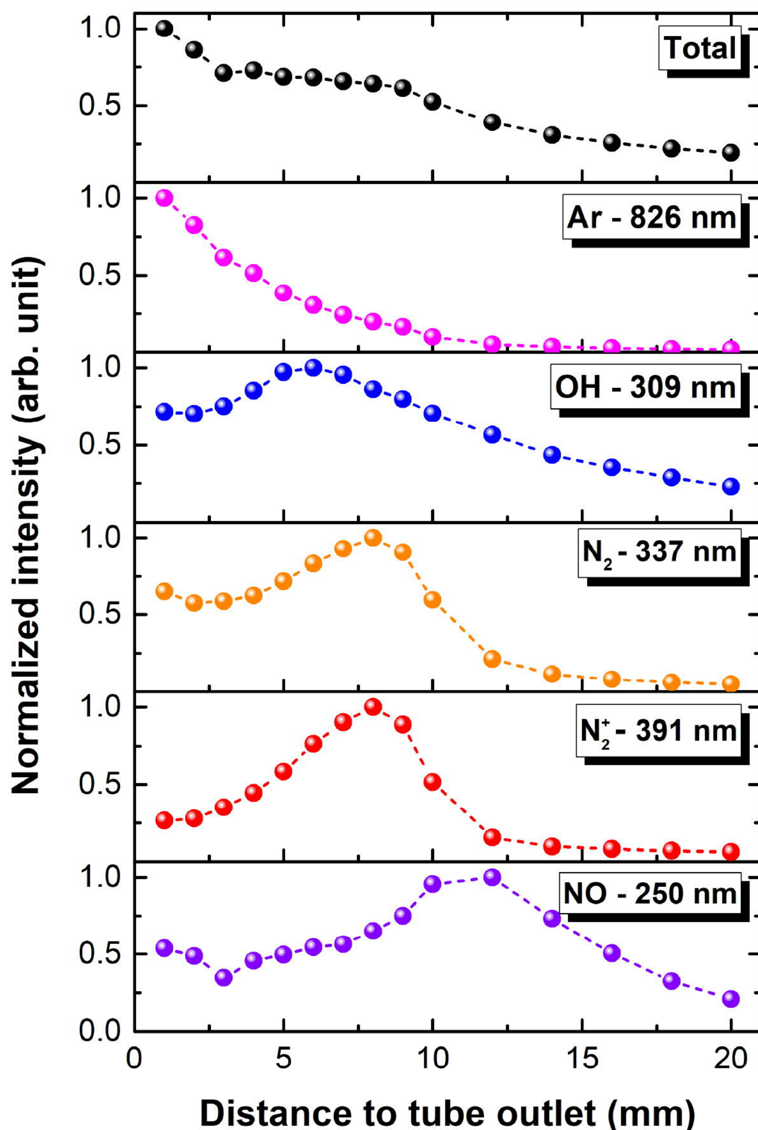

Figure 4.21. Normalized emission intensity from various excited species as a function of position along the jet of the open-to-air microwave argon plasma.

tube was found to rapidly interact with ambient air at the outlet of the tube. This conclusion can be drawn from the rather constant decrease of the Ar line emission intensity to the profit of air-related species, especially N_2 and N_2^+, OH and NO emission bands. Indeed, at atmospheric pressure, OH emission is always observed when trace amounts of water vapor are present in the plasma phase. Excitation of the emitting OH(A) state generally arises either from electron impact on ground state OH(X) or from water dissociation reactions [45]. As for NO, it can be ascribed to Zel'dovich reactions involving nitrogen and oxygen species [76].

Figure 4.21 reveals that, besides argon, all emission intensities exhibit a maximum along the jet, with the first one at 7 mm due to OH and the last one at 12 mm due to NO. A similar trend was reported by other authors in non-thermal argon plasmas jets at atmospheric pressure [25,77]. These features can be explained as follows: close to the tube outlet, most of the kinetic and chemical energy stored in the microwave argon plasma is carried by electrons, metastable argon atoms, and hot neutral argon atoms because of the very low interaction between the jet and ambient air. As the jet/ambient air interaction becomes important, this energy is transferred to the air-related species by collisions (elastic, inelastic, excitation, and charge transfers [25,78]), and consequently the populations of excited N_2, N_2^+, OH and NO increase, as observed in the experiments [49]. This increase is expected to remain up to the point where energy depletion of the microwave argon plasma reservoir occurs. Beyond this point, the creation of excited N_2, N_2^+, OH and NO is expected to decrease concomitantly with their emission intensities. Therefore, much higher values of the available energy per precursor molecules are expected when the precursor injection is realized close to the tube outlet versus close to the substrate surface.

From the results presented in Figure 4.21, it can be inferred that only OH and NO emissions remain very close to the glass sample. This is of interest for two reasons. First, according to Asad *et al.*[37] following the injection of tetramethylsilane (TMS) in an axial injection torch at atmospheric pressure, the presence of silanol groups in plasma-deposited SiO_x films can be attributed to OH species in the gas phase resulting from the interaction of the plasma with ambient air. In line with these findings, the presence of OH close to the glass sample during plasma deposition with HMDSO most likely account for the formation of superhydrophilic and antifog glass samples when HMDSO is injected close to the substrate surface. Second, photons emitted from OH and NO systems have energies ranging from $\sim$4 eV (309 nm) to $\sim$5 eV (250 nm). As these energies are comparable to those of Si-C ($\sim$3.7 eV), Si-O ($\sim$4.6 eV), and C-H ($\sim$4.5 eV) bonds [65], these UV photons are likely to be involved in the fragmentation dynamics of HMDSO molecules when the injection is performed close to the substrate surface.

As underlined above, for the first few millimetres, mostly electrons, metastable argon atoms, and hot neutral argon atoms carry the kinetic and chemical energy stored in the microwave argon plasma. Therefore, for injection positions either inside the microwave argon

plasma or close to the tube outlet, fragmentation of the HMDSO molecules can *a priori* be due to collisions with electrons, metastable argon atoms, and hot neutral argon atoms [56,79]. Beyond this point, however, the population of metastable argon atoms sharply decreased. This aspect is illustrated in the top graph of Figure 4.22. Here, OAS measurements probing the metastable argon $1s_5$ level could only be realized in the first 5 mm; beyond the 6 mm position, the number density was too low to absorb any noticeable laser light. These values of Ar $1s_5$ number density were compared to those obtained in a previous study [49] (tubular configuration with 99% Ar/ 1% N_2). The results are also shown on the left of Figure 4.22. On the one hand, the reference value was in agreement with the one measured at the 1 mm position (position for which the interaction with ambient air remained small, hence the comparison with 1% N_2 in pure argon plasma column). On the other hand, the set of data reported in [49] evidenced that an increase in the amount of nitrogen translated into a reduction in the Ar $1s_5$ number density. Since the Ar $1s_5$ level is the lowest lying level in the argon energy diagram and hence should be the most populated one, the results presented in Figure 4.22 indicates that metastable argon atoms could only have participated to the precursor fragmentation dynamics in the first few millimetres of the jet, after which their number density becomes too low to play any significant role.

Similarly, the contribution of electrons to the precursor fragmentation dynamics can be analyzed by examining their population along the microwave argon plasma jet open to ambient air. In this context, high-resolution OES measurements of the H_α and H_β lines were performed in order to extract their Stark broadening and thus to obtain the corresponding electron number density. However, either insufficient emission intensities for H_α and H_β lines or their overlap with nitrogen emission bands made the acquisition of reliable results unfeasible. Adding hydrogen to the plasma as alternative was ruled out since this procedure greatly increases the neutral gas temperature, even in small amounts [49]. Based on the results of Timmermans *et al.* [77], the electron number density sharply decreases with increasing position along the jet. Over the range of experimental conditions examined by the authors, the electron population decreased from $\sim 5\times10^{21}$ m^{-3} into the plasma source to under the detection threshold in barely 10 mm. In line with this study, it is reasonable to assume that the electron number density in the microwave argon plasma jet open to ambient air can only be much smaller than the one at the tube outlet. For the reference condition

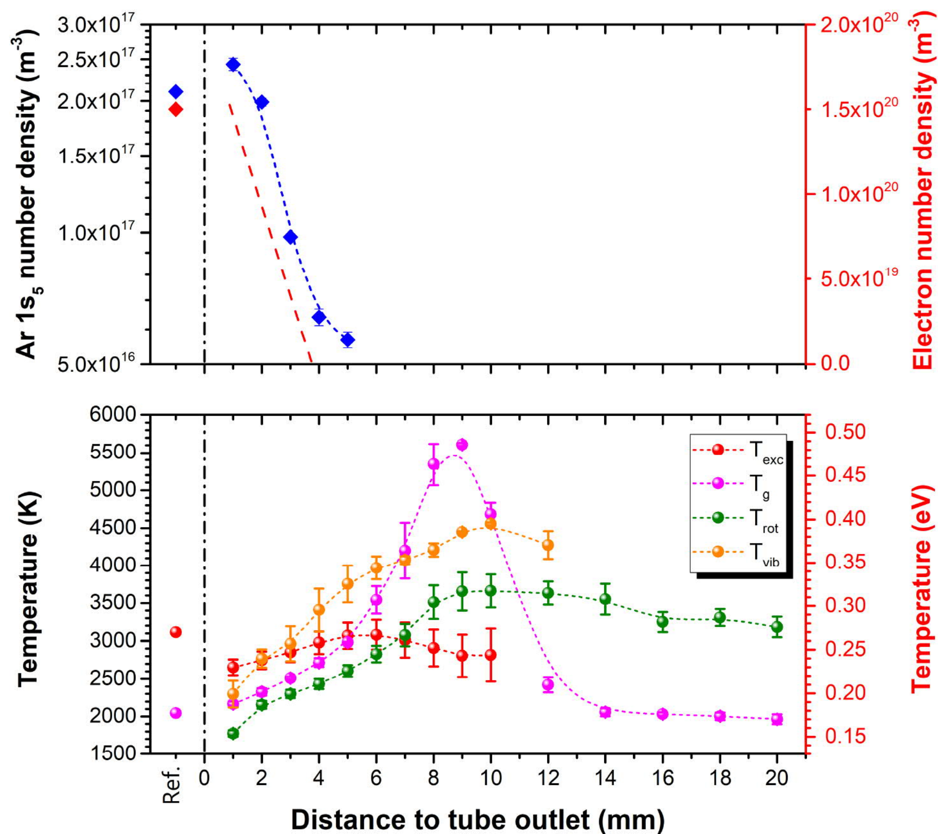

Figure 4.22. Ar $1s_5$ and electron number density profiles (top) and gas, rotational, vibrational and excitation temperature profiles (bottom).

presented in Figure 4.22 (tubular configuration with 99% Ar/ 1% N_2), the electron number density was in the range of 1-2$\times10^{20}$ m^{-3} [49]. Therefore, it can be concluded that, as for the metastable argon species, the electrons played no significant role in the precursor fragmentation dynamics when the injection was realized relatively far from the tube outlet.

Neutral species carrying kinetic, rotational, or vibrational energy can also be involved in HMDSO fragmentation. This aspect is examined in Figure 4.22 where the evolution of T_g, T_{rot}, T_{vib} and T_{exc} along the axis of the plasma jet is illustrated. The difference in the spatial profiles between all of these temperatures confirms the non-equilibrium nature of microwave argon plasma jets open to ambient air. Furthermore, the excitation temperature describing the population of low-energy electrons remained virtually unchanged. Coupled with the previous conclusion that the electron number density sharply decreases when moving away from the microwave plasma region, this result confirms that energy is being transferred from the electrons to the other species contained in ambient air. Regarding T_g, Figure

4.22 reveals that it rises to 5500 K at 10 mm, decreases to ~2000 K 10 and 12 mm, and then remains fairly constant between 14 and 20 mm. T_{rot} rises until the same position but only very slowly goes down afterward. Finally, T_{vib} also rises up to 10 mm. From these results, it can be concluded that, as one moves further down the microwave plasma jet, the available power not only decreases but is also being gradually transferred from electrons and Ar excited states to neutrals, including those mixed from ambient air, and stored in the form of translation, vibration, and rotation [49]. Considering a Maxwell-Boltzmann energy distribution function for neutral Ar atoms and a neutral gas temperature of 2000 K for the last measured positions, more than 5×10^{19} atoms/m^3 have sufficient energy to break Si-C bonds (>3.7 eV). This number can only be higher when adding rotational and vibrational energy in the energy balance equation. Within this framework, hot neutral atoms certainly play an important role in the fragmentation of HMDSO molecules.

From this plasma jet characterization study, it can be concluded that the powder-like and water-repellent organosilicon-based coatings obtained when the precursor injection was carried out closer to the tube outlet results from significant precursor fragmentation (due to the high values of the available energy per precursor molecules) by plasma-generated electrons, metastable argon atoms, and hot neutral argon atoms in a mostly argon atmosphere and the subsequent gas phase recombination reactions of plasma-generated fragments. This plasma configuration is very similar to the one used by Kilicaslan *et al.* [56] and Asadollahi *et al.* [10,11] who also deposited SiO_xC_y:H powders with high carbon content. In sharp contrast, the much smoother, more homogeneous, superhydrophilic, and anti-fog organosilicon coatings achieved when the precursor injection was carried out very close to the substrate can be attributed to a much lower precursor fragmentation level by hot neutrals and UV photons in a mostly air atmosphere. In this regime, the presence of OH could promote the formation of silanol groups on the glass surface. In addition, the overall kinetic, rotational, or vibrational energy involved in HMDSO fragmentation is much lower than the one involved inside microwave argon plasmas (not in the plasma jet) with comparable precursor and oxygen concentration fractions. This feature explains why much smoother and more homogenous SiO_xC_y:H films with low carbon content are obtained in this study while silica-like powders were reported for experiments in microwave Ar/HMDSO/O_2 plasmas [56].

Finally, it is relevant to mention here that deposition tests were also performed with the plasma turned off. In such cases, only intact HMDSO molecules were blown onto the glass surface from the 24 mm injection position. As it turned out, these deposition tests did not result in any of the aformentionned surface properties, thus evidencing the need for precursor fragmentation and confirming the essential role of the plasma-generated hot neutrals and UV photons during the coating procedure in the microwave argon plasma jet. Similarly, additional tests were performed without any HMDSO injection: only hot neutrals and UV photons were impinging onto the glass sample. This time, a modification in the water contact angle was observed but it decreased to a minimum of 15° and not 0°. Consequently, the performance to the antifog test was improved with regards to bare glass samples but was never as good as the 24 mm condition, thus again attesting the need of HMDSO fragmentation by plasma-generated species and the corresponding plasma deposition of an organosilicon coating.

4.4.4. Conclusion

Anti-fog coatings on commercial glass substrates were obtained in a one-step process from the injection of HMDSO in the jet of an open-to-air microwave argon plasma at atmospheric pressure. The influence of the precursor injection position in the jet was studied with regard to the coating features. It is found that precursor injections close to the tube outlet produced semi-opaque, powder-like, and highly hydrophobic coatings while injections closer to the substrate produced transparent, smooth, homogeneous, and superhydrophilic coatings. This latter condition resulted in an organosilicon coating endowed with the anti-fogging property, as revealed by the ASTM F659-06 testing protocol (transmittance above 80% when exposed to water vapor at 50°C). Gas phase recombination favored by longer travel lengths and stronger interactions between HMDSO and plasma-generated species was shown to be responsible for the formation of powder-like microstructures. Conversely, hydroxyl groups formed directly on the glass surface by plasma-generated OH was proposed as a mechanism for the formation of silanol groups, and therefore for the observed superhydrophilic/anti-fogging behavior.

Acknowledgments

The authors are grateful to the Natural Sciences and Engineering Research Council of Canada (NSERC), Prima-Québec, Multiver Ltée, and Plasmionique inc. for the financial support. The equipment used in this work was acquired through the Leaders Opportunity Fund of the Canadian Foundation for Innovation (CFI).

References

[1] M. Vennekamp, I. Bauer, M. Groh, E. Sperling, S. Ueberlein, M. Myndyk, G. Mäder, and S. Kaskel, Beilstein J. Nanotechnol. 2, 665 (2011).

[2] C. Tendero, C. Tixier, P. Tristant, J. Desmaison, and P. Leprince, Spectrochim. Acta Part B At. Spectrosc. 61, 2 (2006).

[3] Y. Wu, M. Bekke, Y. Inoue, H. Sugimura, H. Kitaguchi, C. Liu, and O. Takai, Thin Solid Films 457, 122 (2004).

[4] J. Friedrich, The Plasma Chemistry of Polymer Surfaces: Advanced Techniques for Surface Design (John Wiley & Sons, 2012).

[5] R. D'Agostino, P. Favia, C. Oehr, and M. R. Wertheimer, Plasma Processes and Polymers: 16th International Symposium on Plasma Chemistry Taormina, Italy June 22-27, 2003 (Wiley, 2006).

[6] O. Levasseur, L. Stafford, N. Gherardi, N. Naudé, V. Blanchard, P. Blanchet, B. Riedl, and A. Sarkissian, Plasma Process. Polym. 9, (2012).

[7] J. Profili, O. Levasseur, A. Koronai, L. Stafford, and N. Gherardi, Surf. Coatings Technol. 309, 729 (2017).

[8] O. Levasseur, M. Vlad, J. Profili, N. Gherardi, A. Sarkissian, and L. Stafford, Wood Sci. Technol. 51, 1339 (2017).

[9] S. Asadollahi, M. Farzaneh, and L. Stafford, J. Appl. Phys. 123, 073302 (2018).

[10] S. Asadollahi, J. Profili, M. Farzaneh, and L. Stafford, Materials (Basel). 12, 219 (2019).

[11] S. Asadollahi, M. Farzaneh, and L. Stafford, Coatings 9, 679 (2019).

[12] R. Jafari, S. Asadollahi, and M. Farzaneh, Plasma Chem. Plasma Process. 33, 177 (2013).

[13] C. Wang, L. Yin, L. Zhang, D. Xiang, and R. Gao, Sensors 10, 2088 (2010).

[14] J. Kong, N. R. Franklin, C. Zhou, M. G. Chapline, S. Peng, K. Cho, and H. Dai, Science

(80-.). 287, 622 (2000).

[15] L. Lan, Y. Yao, J. Ping, and Y. Ying, Biosens. Bioelectron. 91, 504 (2017).

[16] W. W. H. Wong, S. Rudd, K. Ostrikov, M. Ramiasa-MacGregor, J. Subbiah, and K. Vasilev, Org. Electron. 32, 78 (2016).

[17] J.-B. Chemin, S. Bulou, K. Baba, C. Fontaine, T. Sindzingre, N. D. Boscher, and P. Choquet, Sci. Rep. 8, 9603 (2018).[18] I. R. Durán and G. Laroche, Prog. Mater. Sci. 99, 106 (2019).

[19] R. Di Mundo, R. d'Agostino, and F. Palumbo, ACS Appl. Mater. Interfaces 6, 17059 (2014).

[20] P. Chevallier, S. Turgeon, C. Sarra-Bournet, R. Turcotte, and G. Laroche, ACS Appl. Mater. Interfaces 3, 750 (2011).

[21] M. Nie, P. Patel, K. Sun, and D. D. Meng, in 2009 4th IEEE Int. Conf. Nano/Micro Eng. Mol. Syst. (2009), pp. 1017-1020.

[22] L. Yao and J. He, Chinese J. Chem. 32, 507 (2014).

[23] D. M. Sim, M.-J. Choi, Y. H. Hur, B. Nam, G. Chae, J. H. Park, and Y. S. Jung, Adv. Opt. Mater. 1, 428 (2013).

[24] A. Shoji, T. Fukushima, D. S. Kumar, K. Kashiwagi, and Y. Yoshida, J. Photopolym. Sci. Technol. 19, 241 (2006).

[25] L. Potočňáková, J. Hnilica, and V. Kudrle, Open Chem. 13, 541 (2014).

[26] K. Weltmann and T. Von Woedtke, Plasma Phys. Control. Fusion 59, 014031 (2017).

[27] V. Raballand, J. Benedikt, S. Hoffmann, M. Zimmermann, and A. von Keudell, J. Appl. Phys. 105, 083304 (2009).

[28] J. Hnilica, J. Schäfer, R. Foest, L. Zajíčková, and V. Kudrle, J. Phys. D. Appl. Phys. 46, 335202 (2013).

[29] S. E. Babayan, J. Y. Jeong, A. Schütze, V. J. Tu, M. Maryam, G. S. Selwyn, and R. F. Hicks, Plasma Sources Sci. Technol. 10, 573 (2001).

[30] I. R. Durán, J. Profili, L. Stafford, and G. Laroche, Prog. Org. Coatings 141, 105401 (2020).

[31] I. Duran, A. Durocher-Jean, J. Profili, L. Stafford, and G. Laroche, Plasma Process. Polym. e1900186 (2020).

[32] M. Moisan, R. Pantel, J. Hubert, E. Bloyet, P. Leprince, J. Marec, and A. Ricard, J.

Microw. Power 14, 57 (1979).

[33] S. Y. Moon, W. Choe, H. S. Uhm, Y. S. Hwang, and J. J. Choi, Phys. Plasmas 9, 4045 (2002).

[34] S. Takeda and M. Fukawa, Mater. Sci. Eng. B Solid-State Mater. Adv. Technol. 119, 265 (2005).

[35] S. Takeda, K. Yamamoto, Y. Hayasaka, and K. Matsumoto, J. Non. Cryst. Solids 249, 41 (1999).

[36] S. Takeda and M. Fukawa, Thin Solid Films 444, 153 (2003).

[37] S. Takeda, M. Fukawa, Y. Hayashi, and K. Matsumoto, Thin Solid Films 339, 220 (1999).

[38] F659-06 ASTM Standard, Https://Www.Astm.Org/Standards/F659.Htm (2004).

[39] J. Winter, R. Brandenburg, and K.-D. Weltmann, Plasma Sources Sci. Technol. 24, 064001 (2015).

[40] E. A. H. Timmermans, J. Jonkers, I. A. J. Thomas, A. Rodero, M. C. Quintero, A. Sola, A. Gamero, and J. A. M. Van Der Mullen, Spectrochim. Acta - Part B At. Spectrosc. 1553 (1998).

[41] X. Lu and S. Wu, Plasma Sci. IEEE Trans. 41, 2313 (2013).

[42] M. Dünnbier, A. Schmidt-Bleker, J. Winter, M. Wolfram, R. Hippler, K.-D. Weltmann, and S. Reuter, J. Phys. D. Appl. Phys. 46, 435203 (2013).

[43] C. O. Laux, T. G. Spence, C. H. Kruger, and R. N. Zare, Plasma Sources Sci. Technol. 12, 125 (2003).

[44] T. Belmonte, C. Noël, T. Gries, J. Martin, and G. Henrion, Plasma Sources Sci. Technol. 24, 064003 (2015).

[45] P. J. Bruggeman, N. Sadeghi, D. C. Schram, and V. Linss, Plasma Sources Sci. Technol. 23, (2014).

[46] C. Chun-Ku and P. Jonathan, J. Phys. D. Appl. Phys. 35, 998 (2002).

[47] G. H. Dieke and H. M. Crosswhite, J. Quant. Spectrosc. Radiat. Transf. 2, 97 (1962).

[48] A. Durocher-Jean, E. Desjardins, and L. Stafford, Phys. Plasmas 26, 063516 (2019).

[49] A. Durocher-Jean, N. Delnour, and L. Stafford, J. Phys. D. Appl. Phys. 52, 475201 (2019).

[50] A. Lofthus and P. H. Krupenie, J. Phys. Chem. Ref. Data 6, 113 (1977).

[51] A. Kramida, Yu. Ralchenko, J. Reader, and NIST ASD Team, (2015).

[52] M. D. Calzada, M. Saez, and M. C. Garcia, J. Appl. Phys. 88, 34 (2000).

[53] A. Pfuch and R. Cihar, Surf. Coatings Technol. 183, 134 (2004).

[54] S. S. Asad, J. P. Lavoute, C. Dublanche-Tixier, C. Jaoul, C. Chazelas, P. Tristant, and C. Boisse-Laporte, Plasma Process. Polym. 6, S508 (2009).

[55] T. Belmonte, T. Gries, R. P. Cardoso, G. Arnoult, F. Kosior, and G. Henrion, Plasma Sources Sci. Technol. 20, 24004 (2011).

[56] A. Kilicaslan, O. Levasseur, V. Roy-Garofano, J. Profili, M. Moisan, C. Cote, A. Sarkissian, and L. Stafford, J. Appl. Phys. 115, 113301 (2014).

[57] The 1998 Ice Storm: 10-Year Retrospective - RMS Special Report (New Ark, CA, 2008).

[58] H. Yasuda and T. Hirotsu, J Polym Sci Polym Chem Ed 16, 743 (1978).

[59] B. Nisol, H. Gagnon, S. Lerouge, and M. R. Wertheimer, Plasma Process. Polym. 13, 366 (2016).

[60] J. Drelich, Surf. Innov. 1, 248 (2013).

[61] J. Drelich and A. Marmur, Surf. Innov. 2, 211 (2013).

[62] P. Dimitrakellis and E. Gogolides, Adv. Colloid Interface Sci. 254, 1 (2018).

[63] R. N. Wenzel, J. Phys. Colloid Chem. 53, 1466 (1949).

[64] A. B. D. Cassie and S. Baxter, Trans. Faraday Soc. 40, 546 (1944).

[65] D. Hegemann, U. Schütz, and A. Fischer, Surf. Coatings Technol. 200, 458 (2005).

[66] R. Barni, S. Zanini, and C. Riccardi, Adv. Phys. Chem. 2012, (2012).

[67] D. Magni, C. Deschenaux, C. Hollenstein, A. Creatore, and P. Fayet, J. Phys. D. Appl. Phys. 34, 87 (2001).

[68] X. Landreau, C. Dublanche-Tixier, C. Jaoul, C. Le Niniven, N. Lory, and P. Tristant, Surf. Coatings Technol. 205, S335 (2011).

[69] O. Levasseur, L. Stafford, N. Gherardi, N. Naudé, E. Beche, J. Esvan, P. Blanchet, B. Riedl, and A. Sarkissian, Surf. Coatings Technol. 234, 42 (2013).

[70] M. Bashir and S. Bashir, Plasma Chem. Plasma Process. 35, 739 (2015).

[71] E. C. Muñoz, C. Díaz, E. Navarrete, R. Henríquez, R. Schrebler, R. Córdova, R. Marotti, and C. Heyser, Arab. J. Chem. (2016).

[72] J. Drelich, E. Chibowski, D. Desheng Meng, and K. Terpilowski, Soft Matter 7, 1 (2011).

[73] L. A. O'Hare, B. Parbhoo, and S. R. Leadley, Surf. Interface Anal. 36, 1427 (2004).

[74] M. R. Alexander, R. D. Short, F. R. Jones, W. Michaeli, and C. J. Blomfield, Appl.

Surf. Sci. 137, 179 (1999).

[75] S. Asadollahi, J. Profili, M. Farzaneh, and L. Stafford, Plasma Process. Polym. Submitted, (2019).

[76] A. F. H. van Gessel, B. Hrycak, M. Jasiński, J. Mizeraczyk, J. J. A. M. van der Mullen, and P. J. Bruggeman, J. Phys. D. Appl. Phys. 46, 095201 (2013).

[77] E. A. H. Timmermans, M. J. van de Sande, and J. J. A. M. van der Mullen, Plasma Sources Sci. Technol. 12, 324 (2003).

[78] J. Jonkers, A. Hartgers, L. J. M. Selen, J. A. M. van der Mullen, and D. C. Schram, Plasma Sources Sci. Technol. 8, 49 (1999).

[79] F. Fanelli, S. Lovascio, R. D'Agostino, F. Arefi-Khonsari, and F. Fracassi, Plasma Process. Polym. 7, 535 (2010).

Conclusion générale et perspectives

Les travaux effectués dans le cadre de cette thèse ont permis de mettre au point un ensemble cohérent de diagnostics spectroscopiques pour la caractérisation des propriétés fondamentales des plasmas froids d'argon à la pression atmosphérique en présence d'espèces réactives. En lien avec le premier objectif décrit dans l'introduction, cet ensemble comprend des mesures d'élargissement de raies pour obtenir la température du gaz et la densité des électrons, des mesures de spectroscopie optique d'absorption avec une diode laser pour obtenir la densité des niveaux métastables et résonnants, de même qu'une méthode couplant un modèle collisionnel-radiatif décrivant la population des niveaux émetteurs 2p de l'argon à des mesures d'émission optiques des transitions 2p-1s pour obtenir la température des électrons (en supposant une fonction de distribution en énergie de type Maxwell-Boltzmann). Par le biais de deux articles publiés dans la littérature scientifique, l'un concernant un plasma d'onde de surface et l'autre une décharge à barrière diélectrique en régime homogène, les capacités et la fiabilité de ces diagnostics ont été démontrées. Dans les deux cas, les travaux révèlent des résultats cohérents avec ceux d'autres études s'étant intéressées aux mêmes genres de plasmas.

En capitalisant sur cet ensemble cohérent de diagnostics spectroscopiques, le second objectif était d'étudier l'influence de l'ajout d'espèces réactives dans un plasma d'argon sur ses propriétés fondamentales. À nouveau, cet objectif a été atteint par la rédaction de deux autres articles soumis pour publication. Le premier s'est intéressé à l'influence de l'ajout des molécules diatomiques N_2, O_2 et H_2 dans un plasma d'onde de surface d'argon à la pression atmosphérique. Il a été observé qu'un tel ajout augmentait la température du gaz et diminuait la densité électronique. Cependant, les comportements de la température des électrons et de la densité des états métastables de l'argon dépendaient de la nature du gaz ajouté. De plus, à l'aide d'une analyse détaillée du bilan de puissance des électrons dans le plasma, il a été démontré que ces gaz en venaient rapidement à dominer la cinétique de la décharge en absorbant la majorité de la puissance fournie au plasma. D'ailleurs, cette analyse a par

le fait même expliqué l'augmentation de la température du gaz puisqu'il a été déterminé qu'une portion de cette puissance s'en allait en chauffage des neutres via l'excitation par impact électronique de niveaux rotationnels. Quant au second article, il a été voué à comparer cette analyse du bilan de puissance des électrons déduit des diagnostics optiques à celui déduit de diagnostics électriques maintes fois rapporté dans la littérature. Cette comparaison a été effectuée à partir de mesures dans une décharge à barrière diélectrique d'argon à la pression atmosphérique dans laquelle des précurseurs anhydrides étaient injectés. Il est ressorti de cette étude que les deux méthodes donnaient des résultats comparables pour des basses concentrations de précurseur mais présentaient des écarts plus importants pour de plus grandes concentrations. Cet effet a été attribué au changement des propriétés fondamentales du plasma (augmentation de la densité électronique, diminution de la température électronique et de la densité d'états métastables de l'argon en présence des précurseurs) mis en évidence par les diagnostics optiques et donc considérés ceux-ci, contrairement aux analyses électriques qui ne le permettent pas.

Par ailleurs, le troisième objectif impliquait d'examiner des plasmas froids d'argon à la pression atmosphérique en configuration jet dans le but d'établir des liens entre ses propriétés fondamentales et les propriétés physiques et chimiques des matériaux traités par plasma. Dans ce contexte, un cinquième article concernant la caractérisation des propriétés d'un jet de plasma RF d'argon s'écoulant dans l'air ambiant a été présenté. L'étude d'un tel jet étant pertinente pour le domaine de la médecine par plasma, il y a été observé que l'interaction avec l'air ambiant avait pour effet de diminuer autant la température des électrons que la densité des atomes d'argon dans les états métastables tout en gardant l'ensemble à une température de gaz tolérable pour les tissus biologiques. Dans le même ordre d'idées, un jet de plasma microonde en contact avec l'air ambiant a fait l'objet d'un sixième article. Cette fois, les propriétés fondamentales du plasma ont permis d'expliquer les différences obtenues quant aux propriétés des revêtements déposés sur des substrats de verre lorsque le précurseur HMDSO était inséré à différents endroits le long de l'axe du jet de plasma. Plus particulièrement, l'injection de HMDSO en amont du jet de plasma impliquait une importante fragmentation du précurseur par les électrons, métastables et neutres chauds du plasma et donnait ainsi lieu à des réactions d'association en phase gaz favorisées par une grande distance de transport pour parvenir au substrat de verre. Ceci résultait en un

revêtement très hydrophobe, poudreux et opaque. Au contraire, une injection de HMDSO en aval dans le jet impliquait une fragmentation nettement plus modeste du précurseur par le rayonnement UV et les neutres chauds du plasma. Pour de courtes distances de transport pour parvenir au substrat de verre, ceci résultait en un revêtement superhydrophile, uniforme et antibuée selon la norme ASTM F659-06[114].

À la lumière de tous ces résultats de grande importance pour les études fondamentales de la physique des plasmas froids à la pression atmosphérique, plusieurs questions restent néanmoins en suspens et offrent ainsi quelques perspectives quant aux suites à donner à cette thèse. Tout d'abord, il a maintes fois été question de la méthode développée pour trouver la température des électrons à partir de mesures d'émissions optiques des transitions 2p-1s de l'argon couplées à un modèle collisionnel-radiatif décrivant la population des niveaux émetteurs 2p. Dans tous les cas, dû au nombre important de collisions inhérent à la pression atmosphérique et favorisant ainsi l'équilibre des vitesses pour chacune des espèces, il a été supposé que cette température des électrons était associée à une fonction de distribution en énergie des électrons de type Maxwell-Boltzmann. Or, la question se pose évidemment à savoir si, selon les cas, cette hypothèse est systématiquement justifiée ou non et, pour cette raison, certains tests ont déjà été réalisés à ce sujet. Le modèle CR a récemment été modifié afin de permettre de considérer des fonctions de distribution en énergie des électrons généralisées, c'est-à-dire ayant une dépendance en $exp(-E/\langle E \rangle)^n$, et où la distribution de Maxwell-Boltzmann s'avère être le cas particulier pour lequel $n = 1$ et $\langle E \rangle = T_e$. Dans le cas où $n = 2$, la distribution est plutôt connue sous le nom de distribution de Druyvesteyn. Les résultats préliminaires montrent que pour le plasma microonde en argon pur comme celui abordé dans le premier article, un meilleur accord théorie/expérience est obtenu pour une distribution avec un $n < 1$, c'est-à-dire avec une proportion d'électrons chauds relativement plus grande que celle décrite dans le cas d'une distribution de Maxwell-Boltzmann. Ce résultat est appuyé par un calcul de T_{exc} décrivant la distribution des électrons froids qui s'accorde bien avec la portion de basse énergie de la fonction de distribution généralisée optimale. Dès lors, une meilleure compréhension de l'écart à la distribution de Maxwell-Boltzmann est de mise pour pouvoir plus adéquatement employer la méthode développée dans cette thèse sur une gamme étendue de conditions opératoires.

Dans un autre ordre d'idée, les travaux sur l'impact de l'ajout de molécules diatomiques sur les propriétés fondamentales d'un plasma d'onde de surface d'argon ont permis de jeter les bases d'études complémentaires dans des chimies plus complexes comme celles utilisées dans le dépôt de couches minces. Dans ce contexte, il serait maintenant intéressant de recourir aux diagnostics spectroscopiques mis au point dans cette thèse pour effectuer des études fondamentales de pointe de la densité et de la température des électrons, de la densité des atomes d'argon dans des niveaux métastables et résonants, ainsi que de la température du gaz dans des plasmas hautement réactifs en conditions de dépôt. Inspirés de travaux similaires effectués dans les plasmas à pression réduite [115, 116], ces informations pourraient ensuite être couplées à des mesures de taux de fragmentation des précurseurs, par exemple par spectrométrie de masse [50]. Il deviendrait alors possible d'obtenir un meilleur portrait de l'ensemble des phénomènes physiques et chimiques gouvernant la dynamique de fragmentation des précurseurs dans les plasmas hautement réactifs d'argon à la pression atmosphérique. À ce jour, aucune étude de ce genre n'a pu être réalisée de sorte que l'état des connaissances dans ce domaine demeure à un niveau embryonnaire. Ceci est particulièrement vrai dans le cas des décharges à barrière diélectrique et des plasmas produits par des ondes de surface mais l'est encore plus dans les plasmas en configuration jet pour lesquels, tel que montré, l'interaction avec l'air ambiant joue un rôle prépondérant.

Finalement, les diagnostics optiques développés dans le cadre de cette thèse l'ont été dans le but d'offrir une meilleure compréhension des propriétés fondamentales des plasmas froids à la pression atmosphérique afin de permettre d'améliorer les procédés pour lesquels ils sont utilisés. Le sixième article offre justement un exemple concret de la mise en application de ceci puisqu'il y est question d'établir des liens entre les propriétés fondamentales d'un jet de plasma microonde et celles des dépôts obtenus sur des substrats de verre. Ainsi, ultimement, il serait pertinent d'employer cet ensemble de diagnostics cohérents plus amplement pour définir de tels liens dans le contexte plus général des procédés par plasma froid à la pression atmosphérique, non seulement pour le dépôt mais aussi pour l'activation de surface ou encore pour le traitement de tissus biologiques en médecine par plasma.

Références

[1] L. Stafford, J. Margot, S. Delprat, M. Chaker, and S. J. Pearton, J. Appl. Phys. **101** (2007), 10.1063/1.2719015.

[2] V. M. Donnelly and A. Kornblit, J. Vac. Sci. Technol. A **31** (2013), 10.1116/1.4819316.

[3] O. Levasseur, L. Stafford, N. Gherardi, N. Naudé, V. Blanchard, P. Blanchet, B. Riedl, and A. Sarkissian, Plasma Process. Polym. **9**, 1168 (2012).

[4] T. Belmonte, T. Gries, R. P. Cardoso, G. Arnoult, F. Kosior, and G. Henrion, Plasma Sources Sci. Technol. **20**, 24004 (2011).

[5] S. Asadollahi, M. Farzaneh, and L. Stafford, J. Appl. Phys. **123**, 073302 (2018).

[6] J. Prégent, L. Vandsburger, V. Blanchard, P. Blanchet, B. Riedl, A. Sarkissian, L. Stafford, and L. V. V. Blanchard, Cellulose **22**, 3397 (2015).

[7] Z. Pan, D. Ding, B. Wu, D. Cuiuri, H. Li, and J. Norrish, in *Trans. Intell. Weld. Manuf.*, edited by S. Chen, Y. Zhang, and Z. Feng (Springer Singapore, Singapore, 2018) pp. 3–24.

[8] M. Hrabovsky and I. J. van der Walt, "Plasma Waste Destruction," in *Handb. Therm. Sci. Eng.*, edited by F. A. Kulacki (Springer International Publishing, Cham, 2017) pp. 1–57.

[9] M. Vandamme, E. Robert, S. Lerondel, V. Sarron, D. Ries, S. Dozias, J. Sobilo, D. Gosset, C. Kieda, B. Legrain, J.-M. Pouvesle, and A. L. Pape, Int. J. Cancer **130**, 2185 (2012).

[10] O. Levasseur, J. Profili, R. K. Gangwar, N. Naudé, R. Clergereaux, N. Gherardi, and L. Stafford, Plasma Sources Sci. Technol. **23** (2014), 10.1088/0963-0252/23/5/054006.

[11] K.-D. Weltmann and T. V. Woedtke, Plasma Phys. Control. Fusion **59**, 014031 (2017).

[12] N. Naudé, *Etude Electrique de la Physique d'une Décharge de Townsend à la Pression Atmosphérique et de son Interaction avec un Générateur : Modèle et Expérience*, Ph.D.

thesis, Université Paul Sabatier (2005).

[13] J. S. Boisvert, N. Sadeghi, J. Margot, and F. Massines, J. Appl. Phys. **121**, 043302 (2017).

[14] H. Luo, Z. Liang, B. Lv, X. Wang, Z. Guan, and L. Wang, Appl. Phys. Lett. **91**, 2013 (2007).

[15] M. I. Boulos, IEEE Trans. Plasma Sci. **19**, 1078 (1991).

[16] M. Moisan and Z. L. B. M. Zakrzewski, J. Phys. D. Appl. Phys. **24**, 1025 (1991).

[17] A. R Hoskinson and J. Hopwood, Plasma Sources Sci. Technol. **21**, 52002 (2012).

[18] M. Moisan and H. Nowakowska, Plasma Sources Sci. Technol. **27**, 073001 (2018).

[19] J. Golda, J. Held, B. Redeker, M. Konkowski, P. Beijer, and A. Sobota, J. Phys. D. Appl. Phys. **084003**, 84003 (2016).

[20] M. Moisan, Z. Zakrzewski, and J. C. L. B. M. Rostaing, Plasma Sources Sci. Technol. **10**, 387 (2001).

[21] J.-S. Boisvert, *Transition des basses fréquences aux hautes fréquences d'une décharge à barrière diélectrique en hélium à la pression atmosphérique*, Ph.D. thesis, Université de Montréal (2016).

[22] U. Kogelschatz, IEEE Trans. Plasma Sci. **30**, 1400 (2002).

[23] R. Bazinette, R. Subileau, J. Paillol, and F. Massines, Plasma Sources Sci. Technol. **23** (2014), 10.1088/0963-0252/23/3/035008.

[24] F. Massines, C. Sarra-Bournet, F. Fanelli, N. Naudé, and N. Gherardi, Plasma Process. Polym. **9**, 1041 (2012).

[25] J. J. Shi and M. G. Kong, Appl. Phys. Lett. **90**, 111502 (2007).

[26] B. Nisol, H. Gagnon, S. Lerouge, and M. R. Wertheimer, Plasma Process. Polym. **13**, 366 (2016).

[27] M. D. Calzada, M. Saez, and M. C. Garcia, J. Appl. Phys. **88**, 34 (2000).

[28] A. Phys, S. Park, W. Choe, S. Youn Moon, and J. Park, Appl. Phys. Lett. **104** (2014), 10.1063/1.4866804.

[29] A. F. H. van Gessel, E. A. D. Carbone, P. J. Bruggeman, and J. J. A. M. van der Mullen, Plasma Sources Sci. Technol. **21**, 15003 (2012).

[30] S. Hübner, J. S. Sousa, J. Van Der Mullen, and W. G. Graham, Plasma Sources Sci. Technol. **24** (2015), 10.1088/0963-0252/24/5/054005.

[31] S. Hübner, J. S. Sousa, V. Puech, G. M. Kroesen, and N. Sadeghi, J. Phys. D. Appl. Phys. **47** (2014), 10.1088/0022-3727/47/43/432001.

[32] B. Van Gessel, R. Brandenburg, and P. Bruggeman, Appl. Phys. Lett. **103**, 1 (2013).

[33] M. Huang, D. S. Hanselman, P. Yang, and G. M. Hieftje, Spectrochim. Acta Part B At. Spectrosc. **47**, 765 (1992).

[34] J. J. van der Mullen, M. J. van de Sande, N. de Vries, B. Broks, E. Iordanova, A. Gamero, J. Torres, and A. Sola, Spectrochim. Acta - Part B At. Spectrosc. **62**, 1135 (2007).

[35] M. Christova, E. Castaños Martínez, M. D. Calzada, Y. Kabouzi, J. M. Luque, and M. Moisan, Applied spectroscopy **58**, 1032 (2004).

[36] C. Yubero, M. S. Dimitrijevi, M. C. García, and M. D. Calzada, Spectrochim. Acta - Part B At. Spectrosc. **62**, 169 (2007).

[37] C. Yubero, A. Rodero, M. S. Dimitrijevic, A. Gamero, and M. C. García, Spectrochim. Acta - Part B At. Spectrosc. **129**, 14 (2017).

[38] E. Castaños Martínez and M. Moisan, Spectrochimica Acta Part B: Atomic Spectroscopy **65**, 199 (2010).

[39] R. K. Gangwar, O. Levasseur, N. Naudé, N. Gherardi, F. Massines, J. Margot, and L. Stafford, Plasma Sources Sci. Technol. **25** (2016), 10.1088/0963-0252/25/1/015011.

[40] X.-M. Zhu and Y.-K. Pu, Journal of Physics D: Applied Physics **43**, 015204 (2009).

[41] Y. Kabouzi, D. B. Graves, E. Castaños-Martínez, and M. Moisan, Phys. Rev. E **75**, 16402 (2007).

[42] E. Castaños-Martínez, M. Moisan, and Y. Kabouzi, J. Phys. D. Appl. Phys. **42**, 12003 (2009).

[43] G. R. Nowling, S. E. Babayan, V. Jankovic, and R. F. L. B. N. Hicks, Plasma Sources Sci. Technol. **11**, 97 (2002).

[44] C. R. Seon, W. Choe, H. Y. Park, J. Kim, S. Park, D. J. Seong, and Y. H. Shin, Appl. Phys. Lett. **91**, (2007).

[45] Y. L. B. W. Watanabe, J. Phys. D. Appl. Phys. **39**, R329 (2006).

[46] S. E. Babayan, J. Y. Jeong, A. Schütze, V. J. Tu, M. Maryam, G. S. Selwyn, and R. F. Hicks, Plasma Sources Sci. Technol. **10**, 573 (2001).

[47] F. Fanelli, S. Lovascio, R. D'Agostino, F. Arefi-Khonsari, and F. Fracassi, Plasma Process. Polym. **7**, 535 (2010).

[48] J. Vallade and F. Massines, J. Phys. D. Appl. Phys. **46** (2013), 10.1088/0022-3727/46/46/464007.

[49] A. Kilicaslan, O. Levasseur, V. Roy-Garofano, J. Profili, M. Moisan, C. Cote, A. Sarkissian, and L. Stafford, J. Appl. Phys. **115**, 113301 (2014).

[50] J. Benedikt, D. Ellerweg, S. Schneider, K. Rügner, R. R, H. Kersten, T. Benter, R. Reuter, H. Kersten, and T. Benter, J. Phys. D. Appl. Phys. **46**, 464017 (2013).

[51] B. Nisol, S. Watson, S. Lerouge, and M. R. Wertheimer, Plasma Process. Polym. **13**, 557 (2016).

[52] B. Nisol, S. Watson, S. Lerouge, and M. R. Wertheimer, Plasma Process. Polym. **13**, 900 (2016).

[53] B. Nisol, S. Watson, S. Lerouge, and M. R. Wertheimer, Plasma Process. Polym. **13**, 965 (2016).

[54] B. Nisol, S. Watson, S. Lerouge, and M. R. Wertheimer, Plasma Process. Polym. **14**, 1600191 (2017).

[55] B. Nisol, S. Watson, S. Lerouge, and M. R. Wertheimer, Plasma Process. Polym. **15**, 965 (2018).

[56] J. Margot-Chaker, M. Moisan, M. Chaker, V. M. M. Glaude, P. Lauque, J. Paraszczak, and G. Sauve, J. Appl. Phys. **66**, 4134 (1989).

[57] Z. S. Chang, C. W. Yao, S. L. Chen, and G. J. Zhang, Phys. Plasmas **23** (2016), 10.1063/1.4962183.

[58] H. Yasuda and T. Hirotsu, J Polym Sci Polym Chem Ed **16**, 743 (1978).

[59] D. Hegemann, M. M. Hossain, E. Körner, and D. J. Balazs, Plasma Process. Polym. **4**, 229 (2007).

[60] A. M. Coclite and K. K. Gleason, Plasma Process. Polym. **9**, 425 (2012).

[61] D. Hegemann, J. Phys. D. Appl. Phys. **46**, 205204 (2013).

[62] J. Schäfer, J. Hnilica, J. Šperka, A. Quade, V. Kudrle, R. Foest, J. Vodák, and L. Zajičková, Surf. Coatings Technol. **295**, 112 (2015).

[63] S. Watson, B. Nisol, S. Lerouge, and M. R. Wertheimer, Langmuir **31**, 10125 (2015).

[64] B. Nisol, S. Watson, A. Meunier, D. Juncker, S. Lerouge, and M. R. Wertheimer, Plasma Process. Polym. **15**, e1700132 (2018).

[65] M. Laroussi and T. Akan, Plasma Processes and Polymers **4**, 777 (2007).

[66] A. Lacoste, A. Bourdon, K. Kuribara, K. Urabe, S. Stauss, and K. Terashima, Plasma Sources Science and Technology **23**, 062006 (2014).

[67] B. Van Gessel, R. Brandenburg, and P. J. Bruggeman, Applied Physics Letters **103**, 064103 (2013).

[68] Y. Sakiyama, D. B. Graves, J. Jarrige, and M. Laroussi, Applied Physics Letters **96**, 41501 (2010).

[69] S. Spiekermeier, D. Schröder, V. S.-v. D. Gathen, M. Böke, and J. Winter, Journal of Physics D: Applied Physics **48**, 35203 (2015).

[70] J. B. Boffard, R. O. Jung, C. C. Lin, and a. E. Wendt, Plasma Sources Science and Technology **18**, 035017 (2009).

[71] J. Benedikt, S. Hofmann, N. Knake, H. Böttner, R. Reuter, A. von Keudell, and V. Schulz-von der Gathen, The European Physical Journal D **60**, 539 (2010).

[72] G. V. Naidis, Plasma Sources Science and Technology **23**, 065014 (2014).

[73] J. L. Walsh and M. G. Kong, Applied Physics Letters **91**, 221502 (2007).

[74] S. Schneider, J. W. Lackmann, D. Ellerweg, B. Denis, F. Narberhaus, J. E. Bandow, and J. Benedikt, Plasma Processes and Polymers **9**, 561 (2012), arXiv:1105.6260 .

[75] S. Schneider, J. W. Lackmann, F. Narberhaus, J. E. Bandow, B. Denis, and J. Benedikt, Journal of Physics D : Applied Physics , 10 (2011), arXiv:1105.2207 .

[76] D. Nečas, V. Čudek, J. Vodák, M. Ohlídal, P. Klapetek, J. Benedikt, K. Rügner, and L. Zajíčková, Measurement Science and Technology **25**, 115201 (2014).

[77] H. M. Joh, J. Y. Choi, S. J. Kim, T. H. Chung, and T.-H. Kang, Scientific Reports **4**, 6638 (2014).

[78] J. F. M. van Rens, J. T. Schoof, F. C. Ummelen, D. C. van Vugt, P. J. Bruggeman, and E. M. van Veldhuizen, IEEE Transactions on Plasma Science **42** (2014), 10.1109/TPS.2014.2328793.

[79] S. Coulombe, V. Léveillé, S. Yonson, and R. L. Leask, Pure and Applied Chemistry **78**, 1147 (2006).

[80] S. Kelly and M. M. Turner, Plasma Sources Science and Technology **23**, 065012 (2014).

[81] M. Leduc, S. Coulombe, and R. L. Leask, IEEE Transactions on Plasma Science **37**, 927 (2009).

[82] J. L. Walsh, F. Iza, N. B. Janson, V. J. Law, and M. G. Kong, Journal of Physics D: Applied Physics **43**, 075201 (2010).

[83] M. Laroussi and X. Lu, Applied Physics Letters **87**, 28 (2005).

[84] J. Y. Kim, J. Ballato, and S. O. Kim, Plasma Processes and Polymers **9**, 253 (2012).

[85] V. Léveillé and S. Coulombe, Plasma Sources Science and Technology **14**, 467 (2005).

[86] J. Jarrige, M. Laroussi, and E. Karakas, Plasma Sources Science and Technology **19** (2010).

[87] L. Chauvet, L. Therese, B. Caillier, and P. Guillot, J. Anal. At. Spectrom. **29**, 2050 (2014).

[88] S. Yonemori, Y. Nakagawa, R. Ono, and T. Oda, Journal of Physics D: Applied Physics **45**, 225202 (2012).

[89] N. Knake, S. Reuter, K. Niemi, V. Schulz-von der Gathen, and J. Winter, Journal of Physics D: Applied Physics **41**, 194006 (2008).

[90] A. Sarani, N. De Geyter, A. Y. Nikiforov, R. Morent, C. Leys, J. Hubert, and F. Reniers, Surf. Coatings Technol. **206**, 2226 (2012).

[91] P. S. Moussounda and P. Ranson, Journal of Physics B : Atomic and Molecular Physics **20**, 949 (1987).

[92] A. Kramida, Y. Ralchenko, J. Reader, and NIST ASD Team, "NIST Atomic Spectra Database (ver. 5.0), [Online]," (2012).

[93] A. Durocher-Jean, E. Desjardins, and L. Stafford, Physics of Plasmas **26**, 1 (2019).

[94] M. V. Malyshev and V. M. Donnelly, Physical review. E **60**, 6016 (1999).

[95] T. D. Nguyen and N. Sadeghi, Physical Review A **18**, 1388 (1978).

[96] R. S. F. Chang and D. W. Setser, The Journal of Chemical Physics **69** (1978).

[97] W. Van Gaens and A. Bogaerts, Journal of Physics D: Applied Physics **47**, 079502 (2014).

[98] C. O. Laux, T. G. Spence, C. H. Kruger, and R. N. Zare, Plasma Sources Science and Technology **12**, 125 (2003).

[99] "www.specair-radiation.net," .

[100] J.-S. Poirier, P.-M. Bérubé, J. Muñoz, J. Margot, L. Stafford, and M. Chaker, Plasma Sources Sci. Technol. Plasma Sources Sci. Technol **20** (2011), 10.1088/0963-0252/20/3/035016.

[101] "ANSYS FLUENT 14.5, Theory Guide; ANSYS, Inc." .

[102] B. E. Launder and D. B. Spalding, *Lectures in Mathematical Models of Turbulence* (Academic press, London, England, 1972).

[103] B. Niermann, R. Reuter, T. Kuschel, J. Benedikt, M. Böke, and J. Winter, Plasma Sources Science and Technology **21**, 034002 (2012).

[104] B. Niermann, M. Böke, N. Sadeghi, and J. Winter, European Physical Journal D **60**, 489 (2010).

[105] B. L. Sands, R. J. Leiweke, and B. N. Ganguly, Journal of Physics D: Applied Physics **43**, 282001 (2010).

[106] X.-M. Zhu and Y.-K. Pu, Journal of Physics D: Applied Physics **43**, 403001 (2010).

[107] S. Förster, C. Mohr, and W. Viöl, Surface and Coatings Technology **200**, 827 (2005).

[108] B. N. Sismanoglu, J. Amorim, J. a. Souza-Corrêa, C. Oliveira, and M. P. Gomes, Spectrochimica Acta - Part B Atomic Spectroscopy **64**, 1287 (2009).

[109] S. Z. Li, J. P. Lim, and H. S. Uhm, Physics Letters, Section A: General, Atomic and Solid State Physics **360**, 304 (2006).

[110] J. M. Palomares, E. I. Iordanova, A. Gamero, A. Sola, and J. J. a. M. V. D. Mullen, Journal of Physics D: Applied Physics **43**, 395202 (2010).

[111] E. Iordanova, J. M. Palomares, A. Gamero, A. Sola, and J. J. a. M. van der Mullen, Journal of Physics D: Applied Physics **42**, 155208 (2009).

[112] S. Hübner, S. Hofmann, E. M. van Veldhuizen, and P. J. Bruggeman, Plasma Sources Sci. Technol. Plasma Sources Sci. Technol **22**, 65011 (2013).

[113] T. Farouk, B. Farouk, A. Gutsol, and A. Fridman, Plasma Sources Sci. Technol. Plasma Sources Sci. Technol **17**, 35015 (2008).

[114] F659-06 ASTM Standard, "Standard Specification for Skier Goggles and Faceshields," (2004).

[115] V. Garofano, R. Bérard, S. Boivin, C. Joblin, K. Makasheva, and L. Stafford, Plasma Sources Sci. Technol **28**, 055019 (2019).

[116] V. Garofano, R. Bérard, X. Glad, C. Joblin, K. Makasheva, and L. Stafford, Submitt. to Plasma Process. Polym. (2019).

Annexe : Article 2

Time-resolved study of the electron temperature and number density of argon metastable atoms in argon-based dielectric barrier discharges

par

Edouard Desjardins[1], Morgane Laurent[2,3,4], Antoine Durocher-Jean[1], Gaétan Laroche[2,3], Nicolas Gherardi[4], Nicolas Naudé[4] et Luc Stafford[1]

([1]) Département de physique, Université de Montréal, Montréal, Québec, Canada

([2]) Laboratoire d'Ingénierie, Centre de recherche sur les Matériaux Avancés, Département de génie des mines, de la métallurgie et des matériaux, Université Laval, Québec, Québec, Canada

([3]) Centre de recherche du CHU de Québec, Hôpital St-François, Québec, Québec, Canada

([4]) LAPLACE, Université de Toulouse, CNRS, INPT, UPS, France

Cet article a été publié dans la revue *Plasma Sources Science and Technology*

(Plasma Sources Sci. Technol. 27 (2018) 015015) .

Les contributions des différents auteurs à cet article sont :

- Edouard Desjardins : Analyse des résultats optiques, écriture du premier jet du manuscrit
- Morgane Laurent : Prise des mesures, analyse des résultats électriques, révision du manuscrit
- Antoine Durocher-Jean : Élaboration et adaptation du modèle CR, aide à l'analyse des résultats
- Gaétan Laroche, Nicolas Gherardi, Nicolas Naudé et Luc Stafford : Supervision des travaux, révision du manuscrit

Abstract.

A combination of optical emission spectroscopy and collisional-radiative modelling is used to determine the time-resolved electron temperature (assuming Maxwellian electron energy distribution function) and number density of Ar 1s states in atmospheric pressure Ar-based dielectric barrier discharges in presence of either NH_3 or ethyl lactate. In both cases, T_e values were higher early in the discharge cycle (around 0.8 eV), decreased down to about 0.35 eV with the rise of the discharge current, and then remained fairly constant during discharge extinction. The opposite behaviour was observed for Ar 1s states, with cycle-averaged values in the 10^{17} m^{-3} range. Based on these findings, a link was established between the discharge ionization kinetics (and thus the electron temperature) and the number density of Ar 1s state.

Keywords: plasma diagnostics, dielectric barrier discharges, electron temperature

A.1.1. Introduction

Ar-based dielectric barrier discharges (DBDs) at atmospheric pressure in presence of reactive precursors are routinely used for the growth of functional, nanostructured coatings on polymeric substrates, including those relevant for biomedical and photovoltaic device applications [1–9]. In such processes, a good control of the precursor fragmentation kinetics is crucial to ensure optimal macro and microscopic properties of the film for specific technological applications. During plasma-enhanced chemical vapour deposition (PECVD) of functional, nanostructured coatings in Ar-based DBDs, many plasma-generated species can participate in the precursor fragmentation and plasma deposition dynamics, including electrons, positive ions, Ar metastable species (Ar 1s states in Paschen notation), and UV photons. While many authors have examined the role of specific operating parameters on the macro and microscopic properties of the film, much less efforts were devoted to fundamental investigations of the precursor fragmentation kinetics and more specifically on the specific role of each plasma-generated species on the plasma deposition dynamics. Part of this scarcity can be related to the difficulty of characterizing with high accuracy plasma-generated species in non-equilibrium atmospheric-pressure plasmas, in particular in highly reactive plasma conditions relevant for PECVD applications.

In this study, a combination of optical emission spectroscopy (OES) and collisional-radiative (CR) modelling is used to determine the electron temperature (T_e) and the Ar 1s populations as a function of time in Ar-based DBDs at atmospheric pressure operated in the kHz regime. Experiments are performed in either Ar/NH_3 (this Penning mixture is useful to obtain a homogeneous discharge instead of the commonly observed filamentary discharge in nominally pure Ar-based DBDs [10–16]) or Ar/ethyl lactate (this mixture is relevant for the growth of biodegradable plasma polymers on heat-sensitive substrates [1,17]) gas mixtures.

A.1.2. Experimental conditions

Experiments were performed in a plane-to-plane DBD. A schematic is presented in figure A.1 and details can be found in [1]. Briefly, two 0.64 mm thick alumina plates with 3.9×3 cm^2 area were used as square parallel dielectrics and a 1.1 mm thick glass plate was used as a substrate. The distance between the top dielectric surface and the substrate surface (discharge gap) was set to 1 mm. The Ar/NH_3 and Ar/ethyl lactate gas mixtures are injected

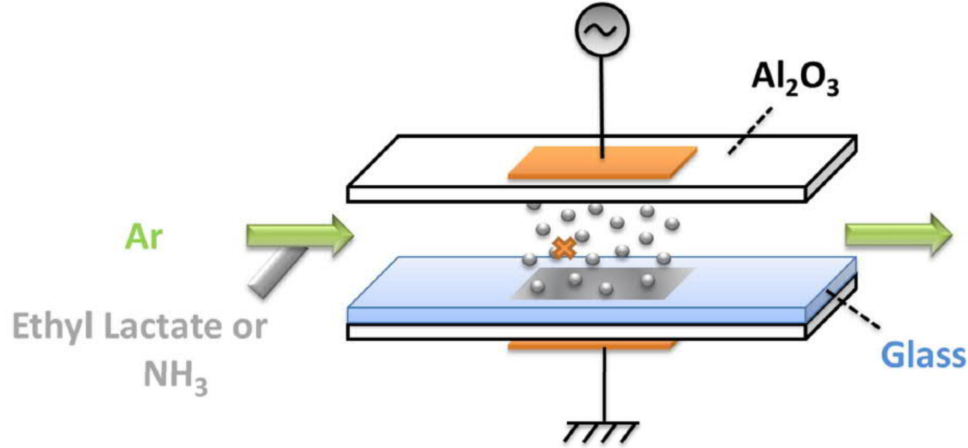

Figure A.1. Schematic of the DBD used in this study with the x representing the position of the optical fibre.

longitudinally between the two dielectric plates. For Ar/NH_3 plasmas, the concentration of NH_3 was set to 200 ppm whereas for Ar/ethyl lactate plasmas, the amount of ethyl lactate was set to 450 ppm. All experiments were performed with a sinusoidal voltage input frequency of 35 kHz (period of 28.6 μs). Over the range of experimental conditions investigated, the average power absorbed and then dissipated by electrons in the discharge was fixed to 1.5 W cm^{-3}. In such conditions, Ar DBDs with impurities such as NH_3 or ethyl-lactate are homogeneous (glow-like) [18], with a single and broad discharge current peak per half cycle of the applied voltage. The system used to collect the optical emission spectra comprised a monochromator from Princeton Instruments coupled with a PI-Max3 intensified charged-coupled device camera also from Princeton Instruments. An optical fibre was used to collect the light from the plasma; this fibre was placed perpendicularly to the gas flow lines at about 1 cm from the gas entrance in the glow discharge region. Photons were collected over a line-of-sight (discharge width) of 3.9 cm. It is worth mentioning that in our conditions, the light emission is fairly uniform on the xy plane (coplanar to the electrodes) but is non-uniform in the transverse direction (normal to the electrode's surface). Given the small discharge gap (1 mm), the size of the optical fibre (200 μm), and the distance between the output of the fibre and the discharge cell (2 cm), light emission is spatially-averaged over the discharge gap and along the line-of-sight. Time-resolved measurements were obtained using a 100 ns gate width. The wavelength calibration of the optical system was done using a spectral lamp for which the spectrum is known.

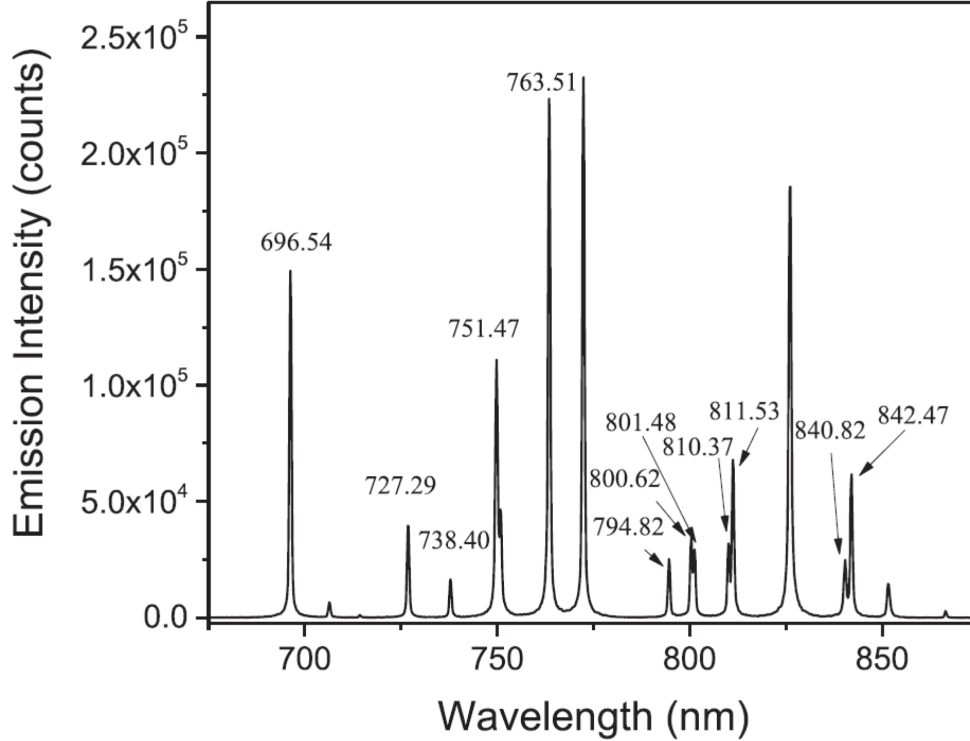

Figure A.2. Typical optical emission spectrum of Ar/NH_3 DBDs with Ar lines identified. All wavelengths for Ar 2p to 1s transitions are in nm.

As for the intensity calibration of the spectrometer, optical fibre and camera, it was realized using a calibration lamp for which the theoretical spectrum is known. From there, a response function was calculated taking into account the discrepancy of units between the theoretical spectrum and the measured data from the optical system.

A typical spectrum in the 650–850 nm wavelength range is presented in figure A.2. Many lines ascribed to Ar 4p-to-4s transitions (2p-to-1s in Paschen notation) can be observed. The non-ascribed lines were either not from Ar 2p states or where overlaping with lines from other species in the discharge, rendering them impossible to incorporate in our analysis. As described below, the emission intensity from this set of lines is used to extract the electron temperature (assuming Maxwellian EEDF (electron energy distribution function)) and the number densities of Ar 1s states.

A.1.3. Description of the model

In order to analyse time-resolved optical emission spectra of Ar-based DBDs, we have developed a CR model. In recent years, many CR models have been proposed, including

some relevant for Ar/NH_3 plasmas [19–21]. In this work, intensity of argon emission $I(\lambda)$ (corrected for the optical response of the optical fibre, monochromator and detector) is given by (1)

$$I(\lambda) = A_{ij} n_{(2p)i} \theta_{ij}, \tag{1}$$

where A_{ij} is the spontaneous emission Einstein coefficient of the i-to-j level transition, $n_{(2p)i}$ is the number density of the emitting i level, and θ_{ij} is the radiation escape factor (between 0 and 1). $n_{(2p)i}$ values were calculated from the coupled steady-state 2p levels balance equations using as inputs the gas temperature, the operating pressure, and the plasma length along the line of sight. Population of emitting $2p_i$ states was assumed to occur by electron-ground state collisions (i.e. direct electron excitation processes with cross sections obtained from [22]), electron-1s collisions (i.e. stepwise electron excitation processes from every 1s states with cross sections obtained from [21,23,24]), 2p-ground state collisions (excitation transfer processes from all $2p_x$ levels to the emitting $2p_i$ level with cross sections extracted from [25]), and radiation trapping using Mewe's formula [26]. On the other hand, de-excitation of a given 2p level was assumed to occur by spontaneous emission (A_{ij} values taken from [27]), $2p_i$-ground state collisions (excitation transfer leading to both 2p and 1s states; cross sections in [25,28,29]), and quenching by collisions with impurities (cross sections taken from [30,31]). This last mechanism will be discussed in more details later on. It is worth mentioning that the EEDF was assumed Maxwellian throughout this study. In the absence of a full kinetic treatment of the electron population, without further study on the matter, Maxwellian EEDF certainly represents the most reasonable assumption. Even if deviation from the Maxwellian form would occur, one would expect comparable trends for the mean electron energy of the EEDF and the electron temperature of a Maxwellian EEDF.

Compared to other CR models [19–21], the one used in this study considers the radiation trapping of Ar emission lines, the population transfer processes between neutral species, all the stepwise excitation processes and solves the particle balance equation for every 2p argon level. Instead of using pre-calculated values for the metastable and resonant number densities as input parameters, the model is also capable, through a comparison with experimental data, to extract these populations as a function of the various operating conditions. Finally, through such comparison between modelled and measured emission intensities, it becomes possible to extract the dominant population and depopulation mechanisms for each

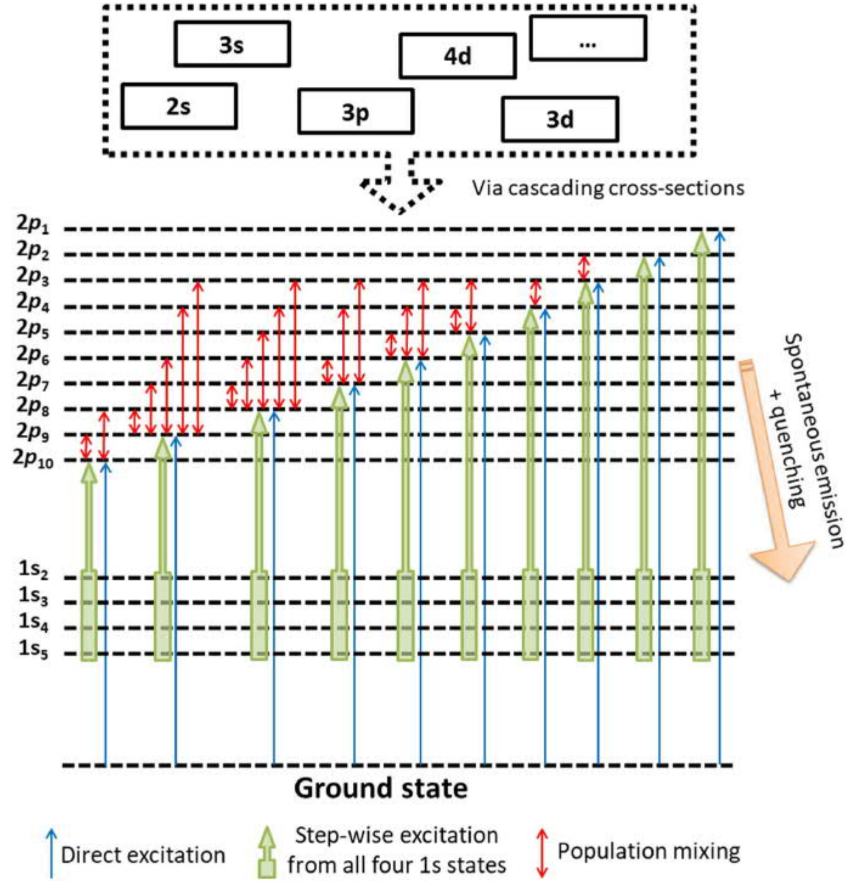

Figure A.3. Schematics of the population and depopulation mechanisms considered for Ar 2p levels.

2p state. These population and depopulation processes are illustrated in figure A.3. Note that the model resolves only the population of argon 2p states. Ar-based ions, even if present in relatively significant amount, cannot contribute to the population and depopulation of argon 2p states. Therefore, these species can completely be omitted from the data analysis. Similarly, the populations of metastable and resonant argon 1s state are treated as an adjustable parameter in the population/depopulation dynamics of argon 2p states. Thus, the model does not explicitly resolve the populations of these states. Any mechanism influencing the population of argon 1s states, including the quenching with impurities and super-elastic collisions, would thus play an important role in the particle balance equation of argon 1s states but not directly in those of argon 2p states.

In this framework, $n_{(2p)i}$ the population of the 2p level i, can be obtained from equation (2), with T_e and $n_{(1s)k}$ being the only adjustable parameters.

$$\frac{d}{dt}n_{(2p)i} = 0 = n_e \left\{ k_{1i}(T_e)n_g + \sum_{k=2}^{5} k_{2ki}(T_e)n_{(1s)k} \right\} + n_g \sum_{j,j\neq i} k_{3ji}(T_g)n_{(2p)j} - k_{4ji}(T_g)n_{(2p)i}\}$$
$$- n_{(2p)i} \sum_{k=2}^{5} \{A_{ik} - k_{5ji}(T_g)n_g + A_{ik}\{1 - 0ik\}\} \quad (2)$$

Here, n_g is the number density of ground-state Ar atoms, $n_{(1s)k}$ is the number density of the Ar 1s state k (metastable and resonant states), and k_{xji} are the rate constants associated with each mechanism ($x = 1$ refers to direct electronic excitation of the i level, $x = 2$ refers to stepwise electronic excitation of the i level, $x = 3$ refers to 2p population transfers from the j levels to the i level, $x = 4$ refers to 2p population transfers from the i level to the j levels, and $x = 5$ refers to de-excitation of the i level by 2p-ground state collisions). For electron–atom collisions, these rate constants were calculated as a function of the electron temperature (assuming a Maxwell– Boltzmann electron energy distribution function) using the set of cross sections described above. For simplicity, Ar 1s states were treated as a block (same number density for Ar $1s_2$,$1s_3$, $1s_4$ and $1s_5$). It is worth highlighting that this assumption had only a minor effect on the results described below. Indeed, similar values of T_e and Ar 1s populations were obtained from the comparison between measured and simulated optical emission spectra when assuming a Boltzmann distribution of the 1s states.

As mentioned above, the model considers the de-excitation of emitting 2p states by collisions with impurities. In Ar/NH_3 and Ar/ethyl lactate DBDs, impurities obviously include NH_3 and ethyl lactate, but also all plasma-generated fragments. It is worth mentioning that quenching probabilities for most of these impurities are poorly documented in literature. In addition, the population of most plasma-generated fragments is very difficult to establish. In this context, we have assumed that Ar states are mostly quenched by collisions with plasma-generated H_2 (0.25%) for Ar/NH_3 mixture and CO_2 (1.5%) in Ar/ethyl lactate mixture for which literature is readily available. The heavy concentrations of these impurities were used to compensate for the lack of literature on other possible fragments present in the discharge. It is pertinent to note that changes in the concentration fraction of these impurities had only

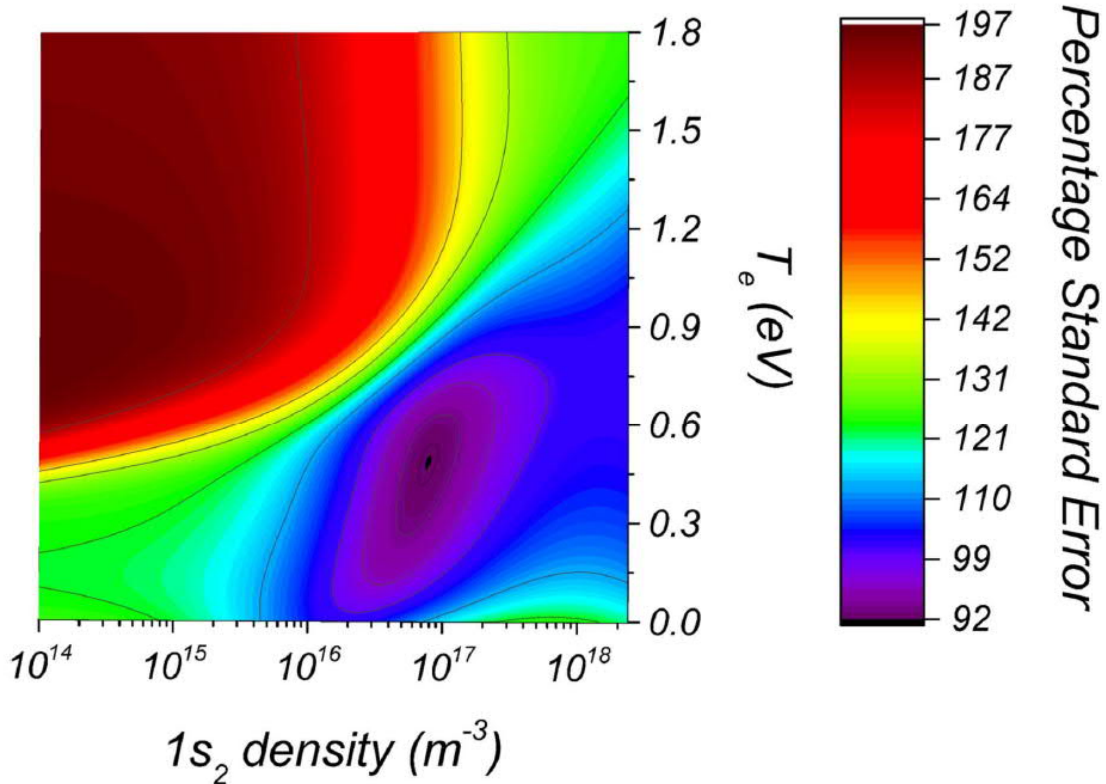

Figure A.4. Typical surface plot of the percentage standard error between measured and calculated emission intensities for various values of T_e and number density of Ar $1s_2$ state. The black dot represents the minimum for PSE.

a minor effect (less than 5%) on the values of T_e and and Ar 1s populations obtained from the comparison between measured and simulated optical emission spectra.

As mentioned above, radiation trapping effects were considered using the empirical formula for θ_{ij} provided by Mewe [26]. This factor is calculated using Mewe's definition which takes into account different gaussian and lorentzian broadening mechanisms. Because of the high pressure, van der Waals [32] and resonant [33] broadening mechanisms were considered in addition to Doppler broadening [34]. Stark broadening effects are neglected because of the relatively low charged particles number densities in DBDs. In those calculations, the neutral gas temperature (T_g) was assumed equal to 300 K; this is a reasonable assumption for Ar-based DBDs [35].

The coupled set of 10 equations for $2p_1$ to $2p_{10}$ states was solved using the electron temperature T_e and the number density of Ar $1s_2$ level (assumed equal to Ar $1s_3$, $1s_4$, and $1s_5$ since these species were treated as a block) as the only input parameters. Note that, in

(2), the population of all $2p_i$ states scales linearly with the electron density n_e; therefore, relative number densities of emitting 2p states can be obtained without precise knowledge of n_e. From this approach, the relative emission intensities were computed over a wide range of T_e and $1s_2$ number density values and then compared to those obtained from the measured optical emission spectra. For each T_e and $1s_2$ number density value, the difference between simulated and measured spectra was calculated using a percentage standard error (PSE) method [20]. More precisely, both the experimental and simulated spectra were first normalized by dividing each line's intensity in a spectrum with the sum of the intensities of all considered lines in the same spectrum. Afterwards, the PSE was calculated for the ratio of experimental over simulated intensities of each lines and then summed over all analysed lines in the spectrum. For each spectrum, the results can be plotted on a 3D graph; a typical example is presented in figure A.4. It can be seen that the PSE displays a well-defined unique minimum for precise values of T_e and $1s_2$ population. This minimum thus represents the closest possible fit between the observed and the simulated optical emission spectra. Figure A.4 shows the corresponding example of the fit between the observed emission intensities at a given time in the discharge and the model's reconstruction at optimal T_e and $n_{(1s)2}$ values. This approach was used to determine those parameters for various operating conditions.

A.1.4. Experimental results and discussion

Figure A.6 presents the time-evolution of the electron temperature and number density of Ar $1s_2$ state in an Ar/NH_3 (200 ppm) plasma over the 35 kHz sinusoidal excitation for the negative half-cycle (top electrode is cathode). In this case, T_e peaks early in the discharge cycle (0.8 eV) and then decreases down to about 0.35 eV until discharge extinction (above 8 μs, emission intensities were too low to obtain a significant number of lines and thus reliable data). The opposite trend can be observed for the number density of Ar $1s_2$ state. This population first rises early in the discharge cycle and then stabilizes at around 2×10^{17} m^{-3}. Similar results were observed for the positive half-cycle (bottom electrode is cathode). Note that the oscillation-like variations between 2 and 8 μs are not repeatable and mostly come from uncertainties in both measurements and data analysis. Error bars obtained from the average over three subsequent temporal data points are used to support this aspect.

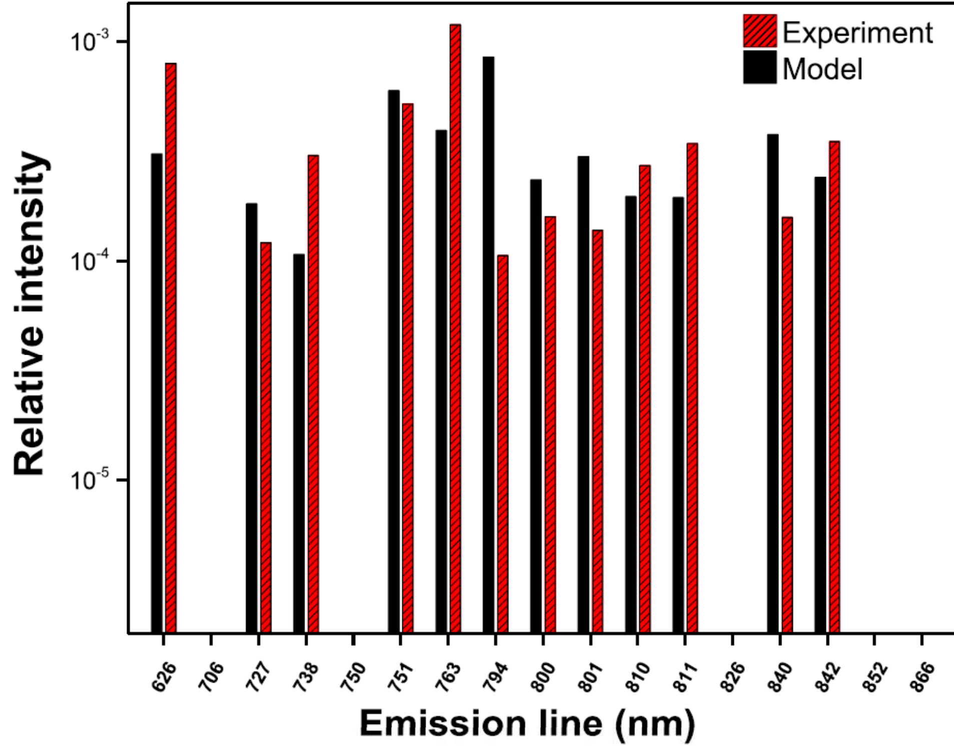

Figure A.5. Comparison of normalized emission intensities obtained from the experiment and the model at optimum T_e and $n_{(1s)2}$ values.

Figure A.7 displays the time-evolution of the electron temperature and number density of Ar $1s_2$ state in Ar/ethyl lactate (450 ppm) plasmas for the negative half-cycle (top electrode is cathode) of the sinusoidal applied voltage. As in Ar/NH_3 plasmas, the electron temperature decreases from 0.7 to 0.3 eV while the population of Ar $1s_2$ increases from 4×10^{16} to 2×10^{17} m^{-3} during discharge ignition and then remains fairly constant. In addition, Ar/ethyl lactate plasmas reveal slightly higher cycle-averaged T_e (0.4 eV) values than Ar/NH_3 plasmas (0.35 eV). On the other hand, the cycle-averaged number density of Ar $1s_2$ is higher in Ar/NH_3 plasmas than in Ar/ethyl lactate plasmas. Such behaviour can probably be attributed to the difference in the impurity concentration between Ar/ethyl lactate plasmas (450 ppm of ethyl lactate) and Ar/NH_3 plasmas (200 ppm of NH_3). Also, the mass ratios between impurities and pure Ar change with the reactive gas used. Since ethyl lactate (118.13 g/mol) is 7 times heavier than NH_3 (17.031 g/mol), 450 ppm of ethyl lactate represents a much higher concentration than 200 ppm of ammonia.

Similar results were recently reported for He DBDs operated under comparable experimental conditions [36]. High T_e values were observed early in the discharge cycle when the

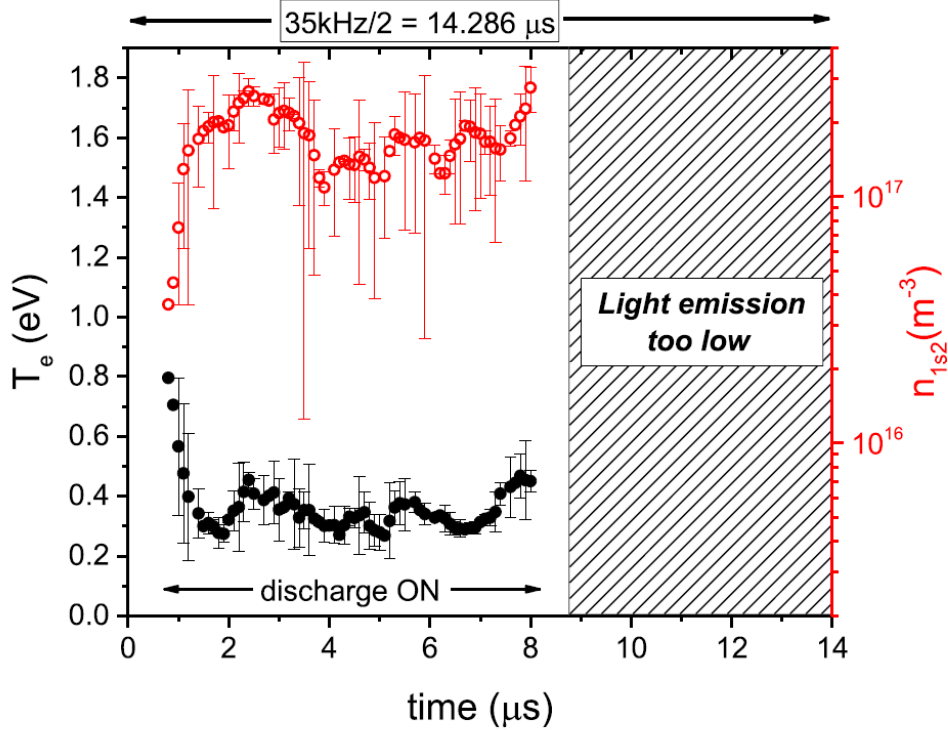

Figure A.6. Time evolution of T_e (black) and Ar $1s_2$ population (red) during the negative half cycles of the 35 kHz excitation for an Ar/NH_3 DBD. On the time axis, 0 μs represents the beginning of the negative half-cycle of the applied voltage. The error bars represent the variance on T_e and Ar $1s_2$ populations with respect to their mean values obtained over three subsequent data points.

discharge current is small and the gas voltage is high. T_e then decreased rapidly with the decrease in the gas voltage (linked to the development of a cathode fall and the formation of a positive column region) and the corresponding increase of the discharge current. T_e values were also compared to those obtained by other authors in Ar/NH_3 plasma jets open to ambient air (0.9 eV) [19]. Higher T_e values were observed by these authors, which can most likely be attributed to the presence of N_2 and O_2 due to the open-air-configuration (this aspect was already described by Levasseur et al in He based discharges [37]). Metastable number densities reported in figure A.6 are also comparable to those obtained by Massines and co-workers using diode laser optical absorption spectroscopy under comparable experimental conditions [38].

In order to compare the results displayed in figures A.6 and A.7 with those expected for DBDs operated in nominally pure Ar (without NH_3 or ethyl lactate), average electron energies were computed using the BOLSIG+ solver as a function of the reduced electric

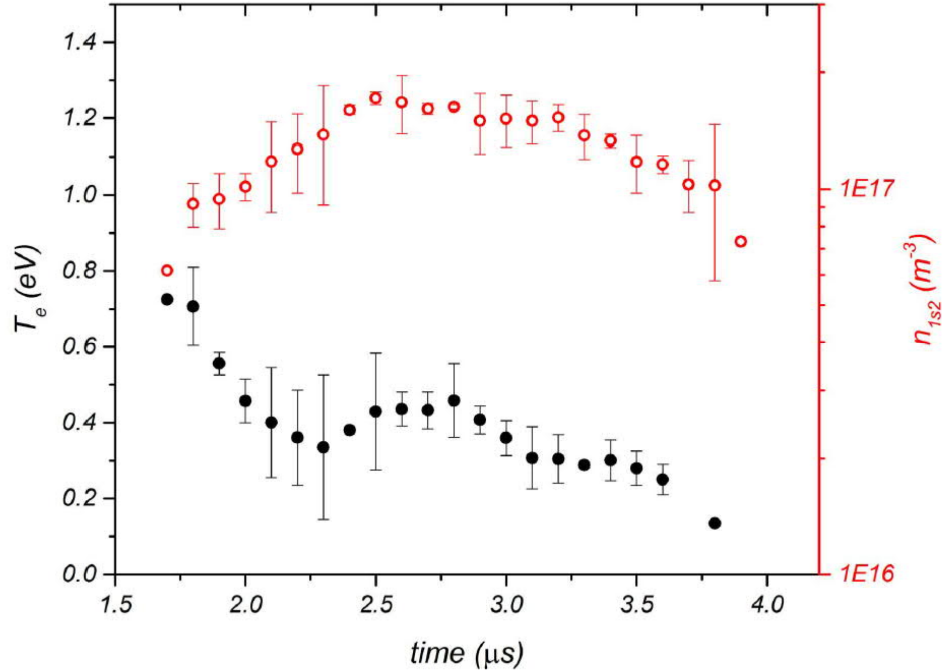

Figure A.7. Time evolution of the electron temperature (black) and Ar $1s_2$ population (red) during the negative DBD half cycle of the 35 kHz sinusoidal excitation for an Ar/ethyl lactate DBD. On the time axis, 0 μs represents the beginning of the negative half-cycle of the applied voltage. The error bars represent the variance on T_e and Ar $1s_2$ populations with respect to their mean values obtained over three subsequent data points.

field (E/N). This programme relies on numerical solutions of the Boltzmann equation for electrons in weakly ionized gases in uniform electric fields [39]. Although the electric field in glow discharges of DBDs strongly varies in time and space from the cathode to the anode, it can be assumed fairly constant before discharge ignition (in absence of positive and negative charges) as well as in the positive column region. Over the range of experimental conditions examined in this study, breakdown voltages for Ar/NH_3 and Ar/ethyl lactate plasmas were between 1 and 2 kVpp. At atmospheric pressure, assuming a neutral gas temperature of 300 K, this corresponds to reduced electric fields between 10 and 20 Td. Using these values, the electron temperatures deduced from the BOLSIG+ code (assuming that the average electron energy is equal to 3/2 T_e) were between 3 and 5 eV, respectively. These values are much higher than those observed in figures A.6 and A.7, even early in the discharge cycle. However, it is worth mentioning that BOLSIG+ [39] simulations only consider electron-impact ionization on ground state Ar atoms for the production of charged species. When stepwise ionization processes or Penning ionization processes become important, much lower

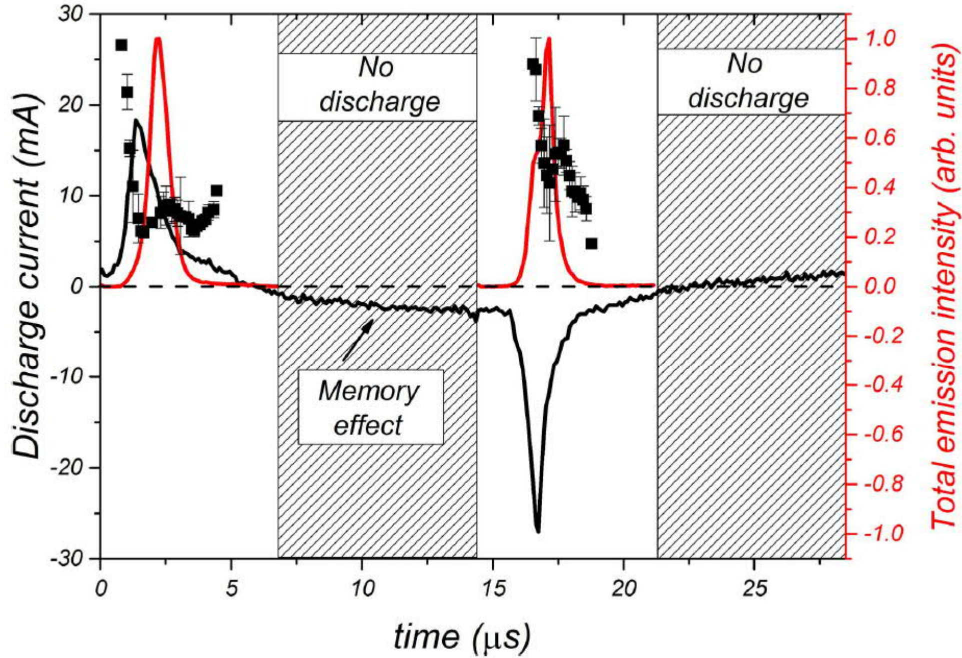

Figure A.8. The discharge current (black), the integrated emission intensity (red) and the electron temperature (black dots) for Ar/ethyl lactate (450 ppm) DBD during both positive and negative halfcycles.

T_e values are expected for a given applied electric field, as obtained in this study. This effect should also be exacerbated in the presence of other electron energy losses in the electron kinetics, for example elastic and inelastic electron collisions with fragments and impurities.

The importance of stepwise processes involving metastable and resonant Ar atoms on the physics driving Ar-based DBDs was examined in more details by comparing T_e values with the discharge current as well as the total emission intensity (integration over all wavelengths). As shown in figure A.8, for both positive and negative half cycles, T_e peaks slightly before the discharge current (and thus before the electron number density) whereas the total emission peaks a few microseconds after the discharge current. This indicates that most of the levels giving rise to the observed emission intensities are populated by stepwise excitation reactions involving metastable and resonant Ar atoms. This result is in sharp contrast to those reported by Ricard et al [40] in pulsed He discharges at atmospheric pressure. In this specific case, He $n = 3$ emission intensities peaked before the discharge current. In [36, 37], this behaviour was explained by a change in the excitation dynamics with increasing current, going from electron-impact excitation on ground state He atoms early in the discharge cycle to electron-impact excitation reactions on metastable He atoms later in the discharge

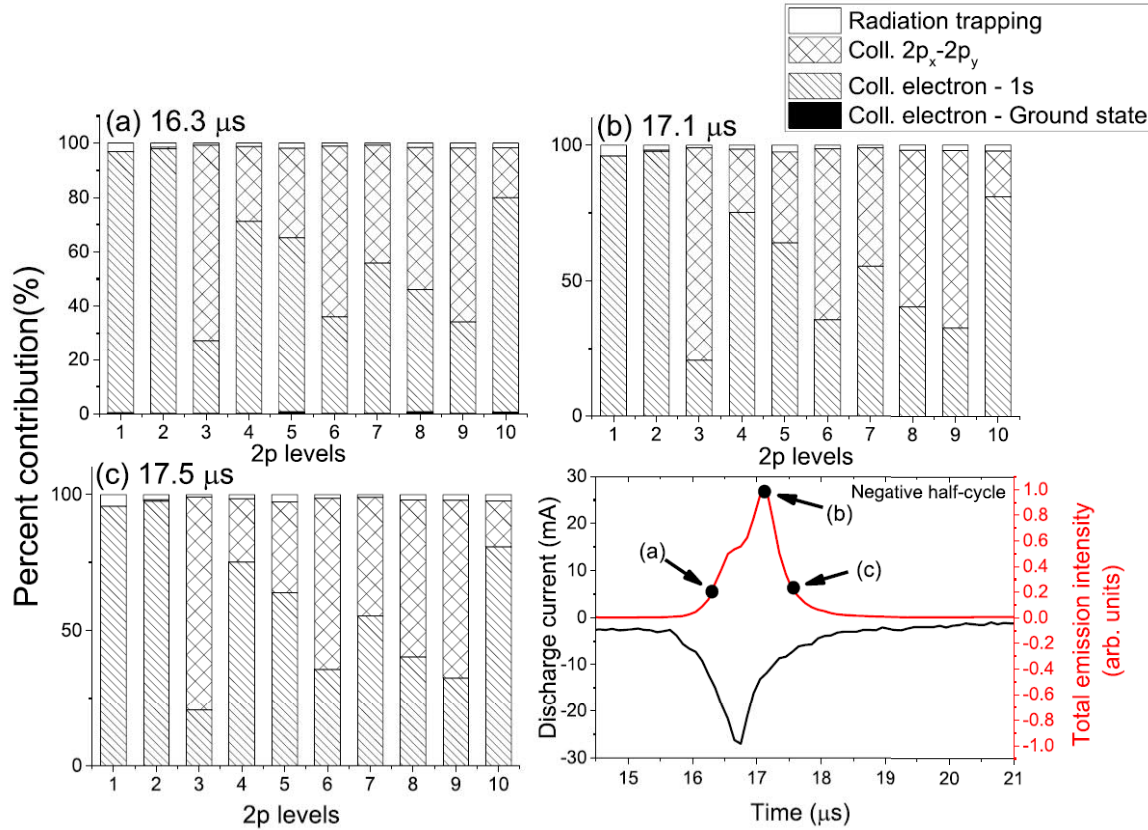

Figure A.9. Percent contribution of each populating mechanism for Ar 2p levels at different times during the negative half-cycle of an Ar/ethyl lactate (450 ppm) plasmas.

cycle. Note that in figure A.8, only a single and broad discharge current peak is observed per half cycle of the applied sinusoidal voltage; this is typical for homogeneous, glow-like DBDs operated in rare gases [6].

The dominance of stepwise excitation processes for Ar 2p states was confirmed by examining the relative contributions of all population and depopulation mechanisms of Ar 2p emitting levels, as obtained from the CR model. The results are presented in figure A.9. It can be seen that even at the very beginning of the discharge (figure A.9(a)), electron-impact excitation on ground state Ar atoms plays a negligible role (less than 1%). Based on these findings, one thus expects that stepwise or Penning ionization reactions would dominate the creation dynamics of charged species in Ar-based DBDs, even early in the discharge cycle. In many studies, the creation of charged species is assumed to occur by electron impact ionization on ground state Ar atoms and the losses by ambipolar diffusion (and recombination) to the reactor walls. In such cases, the electron temperature becomes solely governed by the reactor dimensions and the number density of ground state neutral atoms [41]. For

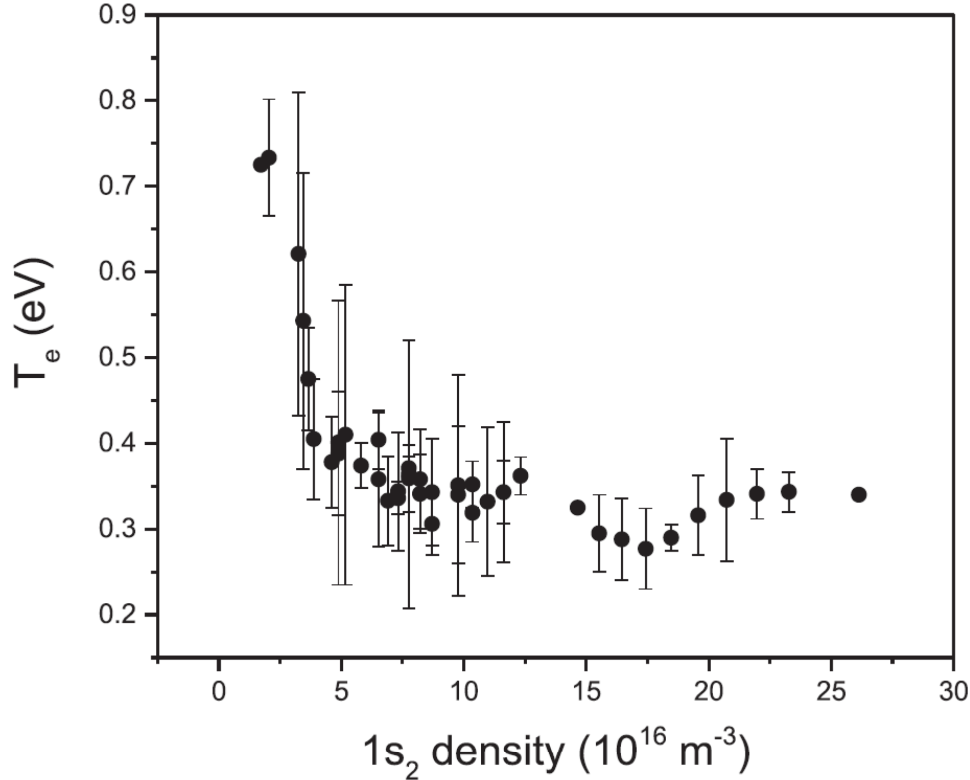

Figure A.10. Relation between T_e and $n_{(1s)}$ for Ar/ ethyl lactate and Ar/NH_3 plasmas in the conditions studied in this paper. These values were obtained from those presented in figures A.6 and A.7. The error bars represent the variance on T_e with respect to the mean value obtained over nearby data points for the Ar $1s_2$ populations.

example, in nominally pure Ar at atmospheric pressure, for a 1 mm gas gap (plane-to-plane configuration assuming a homogenous discharge regime), this yields a T_e value of 1.6 eV. On the other hand, when stepwise or Penning ionization processes govern the discharge ionization dynamics, the behaviour of T_e for given reactor dimensions must become dependent on the population of Ar 1s states. Over the range of experimental conditions examined, figure A.10 confirms this hypothesis that there seems to be a link between T_e and $n_{(1s)}$ for both Ar/ethyl lactate and Ar/NH_3 plasmas. More precisely, using the time-resolved measurements presented above, when the populations of metastable or resonant Ar atoms increase, the electron temperature first sharply decreases and then reaches a plateau, strengthening our belief in the importance of stepwise processes in these discharges.

A.1.5. Conclusion

In this work, a combination of OES and collisional radiative modelling was used to analyse the time-resolved behaviour of the electron temperature and number density of Ar metastable and resonant species in Ar-based DBDs. Both Ar/NH_3 and Ar/ethyl lactate plasmas revealed a decrease of T_e combined with an increase in the Ar $1s_2$ population early in the discharge cycle with more or less constant values until discharge extinction. It was also observed that the electron temperature peaks before the discharge current whereas the emission intensity and the number density of Ar 1s states peaks several microseconds after the discharge current. Over the range of experimental conditions examined in this work, it was found that stepwise and Penning processes play a very important role on the discharge kinetics. In such plasmas, the behaviour of the electron temperature becomes linked to the population of metastable and resonant Ar atoms.

Acknowledgments

The authors acknowledge the Conseil Franco-Québécois de Coopération Universitaire, the Laboratoire International Associé—Science et TEchnologies des Plasmas (LIA-STEP), and the National Science and Engineering Research Council (NSERC) for their financial support.

References

[1] Laurent M, Desjardins E, Meichelboeck M, Naudé N, Stafford L, Gherardi N and Laroche G 2017 J. Phys. D: Appl. Phys. 50 475205

[2] Ceiler M F Jr, Kohl P A and Bidstrup S A 1995 J. Electrochem. Soc. 142 2067

[3] Ikeda K, Nakayama S and Maeda M 1995 J. Electrochem. Soc. 143 1715

[4] Massines F, Sarra-Bournet C, Fanelli F, Naudé N and Gherardi N 2012 Plasma Process Polym. 9 1041–73

[5] Silva J A, Lukianov A, Bazinette R, Blanc-Pélissier D, Vallade J, Pouliquen S, Gaudy L, Lemiti M and Massines F 2014 Energy Proc. 55 741–9

[6] Massines F, Ségur P, Gherardi N, Khamphan C and Ricard A 2003 Surf. Coat. Technol. 174–175 8–14

[7] Elam F M, Starostin S A, Meshkova A S, van der Velden-Schuermans B C A M, Bouwstra

J B, van de Sanden M C M and de Vries H W 2016 Plasma Process. Polym. 14 1600143

[8] Starostin S A, Creatore M, Bouwstra J B, van de Sanden M C M and de Vries H W 2015 Plasma Process. Polym. 12 545–54

[9] Starostin S A, Premkumar P A, Creatore M, van Veldhuizen E M, de Vries H W, Paffen R M J and van de Sanden M C M 2009 Plasma Sources Sci. Technol. 18 4

[10] Babaeva N Y and Kushner M J 2014 Plasma Sources Sci. Technol. 23 015007

[11] Kogelschatz U 2002 IEEE Trans. Plasma Sci. 20 1400

[12] Gherardi N, Croquesel E and Massines F 2003 Proc. 16th Int. Symp. on Plasma Chemistry, (ISPC 16) (Taormina, Italy, 22–27 June)

[13] Kloc P, Wagner H-E, Trunec D, Navràtil Z and Fedoseev G 2010 J. Phys. D: Appl. Phys. 43 345205

[14] Gherardi N and Massines F 2001 IEEE trans. plasma Sci. 29 536

[15] Okazaki S, Kogoma M, Uehara M and Kimura Y 1993 J. Phys. D: Appl. Phy 26 889

[16] Arakoni R A, Bhoj A N and Kushner M 2007 J. Phys. D: Appl. Phys. 40 8

[17] Ligot S, Renaux F, Denis L, Cossement D, Nuns N, Dubois P and Snyders R 2013 Plasma Process. Polym. 10 999–1009

[18] Bazinette R, Paillot J and Massine F 2015 Plasma Sources Sci. Technol. 24 055021

[19] Chang Z, Yao C, Chen S and Zhang G 2016 Phys. Plasma 23 093503

[20] Meulenbroeks R F G, Engeln R A H, Beurskens M N A, Paffen R M J, van de Sanden M C M, van der Mullen J A M and Schram D C 1995 Plasma Sources Sci. Technol. 4 74

[21] Donnelly V M 2004 J. Phys. D: Appl. Phys. 37 19

[22] Yanguas-Gil A, Cotrino J and Alves L L 2005 J. Phys. D: Appl. Phys. 38 1588–98

[23] Boffard J B, Piech G A, Gehrke M F, Anderson L W and Lin C C 1999 Phys. Rev. A 59 2749

[24] Bartschat K and Zeman V 1999 Phys. Rev. A 59 R2552

[25] Nguyen T D and Sadeghi N 1978 Phys. Rev. A 18 1388–95

[26] Mewe R 1967 Br. J. Appl. Phys. 18 107–18

[27] Kramida A, Ralchenko Y, Reader J and (NIST ASD Team) 2015 NIST Atomic Spectra Database (ver. 5.3), http://physics.nist.gov/asd (27 February 2017). National Institute of Standards and Technology, Gaithersburg, MD

[28] Zhu X-M and Pu Y-K 2010 J. Phys. D: Appl. Phys. 43 015204

[29] Chang R S F and Setser D W 1978 J. Chem. Phys. 69 3885–97

[30] Van Gaens W and Bogaerts A 2014 J. Phys. D: Appl. Phys. 47 079502

[31] Sadeghi N and Setser D W 2001 J. Chem. Phys. 115 3144

[32] Yubero C, Dimitrijevic M S, García M C and Calzada M D 2007 Spectrochim. Acta B 62 169–76

[33] Kunze H-J Introduction to Plasma Spectroscopy (Berlin: Springer) p 157

[34] Moisan M, Kéroack D and Stafford L 2016 Physique Atomique et Spectroscopie Optique (Les Ulis: EDP Sciences) p 27

[35] Wei G-D, Ren C-S, Qian M-Y and Nie Q-Y 2011 IEEE Trans. Plasma Sci. 39 1842–8

[36] Kumar Gangwar R, Levasseur O, Naudé N, Gherardi N, Massines F, Margot J and Stafford L 2016 Plasma Sources Sci. Technol. 25 015011

[37] Levasseur O, Kumar Gangwar R, Profili J, Naudé N, Gherardi N and Stafford L 2016 Plasma Process. Polym. 14 1–7

[38] Massines F, Gherardi N, Fornelli A and Martin S 2005 Surf. Coat. Technol. 200 1855–61

[39] Hagelaar G J M and Pitchford L C 2005 Plasma Sources Sci. Technol. 14 722–33

[40] Richard A, Décomps P and Massines F 1999 Surf. Coat. Technol. 112 1–4

[41] Moisan M and Pelletier J 2006 Physique des Plasmas Collisionnels, Applications au Décharges Hautes Fréquences (Les Ulis: EDP Sciences) p 125